Dissertation

submitted to the

Combined Faculties for the Natural Sciences and for Mathematics

of the Ruperto-Carola University of Heidelberg, Germany

for the degree of

Doctor of Natural Sciences

presented by

Markus Heinrich Lamm

born in Korbach

Oral examination: November 26, 2003

Angular Momentum Evolution of Young Stars

Referees: Prof. Dr. Reinhard Mundt
Prof. Dr. Immo Appenzeller

Zusammenfassung

Diese Dissertation enthält eine ausführliche Untersuchung des Rotationsverhaltens junger Vor-Hauptreihensterne (VHSt) mit dem Ziel, ein klareres Bild über die Drehimpulsentwicklung während dieser Entwicklungsphase zu erhalten. Als Grundlage dafür habe ich ein umfangreiches photometrisches Beobachtungsprogramm durchgeführt, das es mir ermöglichte, insgesamt 405 periodisch variable und 184 irregulär variable VHSt im jungen offenen Sternenhaufen NGC 2264 (Alter: 2–4 Mio. Jahre) zu identifizieren. Damit ist es mir gelungen, die Zahl der bekannten VHSt in NGC 2264 um mehr als das Dreifache und die Zahl der veröffentlichten Rotationsperioden in NGC 2264 um mehr als das Zehnfache erhöhen.
Neben dem Orion-Nebel-Haufen (ONC, Alter: 1 Mio. Jahre), mit ca. 370 bekannten Rotationsperioden, ist NGC 2264 damit der einzige junge Haufen für den eine statistisch signifikante Anzahl von Rotationsperioden für VHSt bekannt ist. Somit war es erstmals möglich, das Rotationsverhalten von Sternen zweier junger Haufen miteinander zu vergleichen. Es zeigte sich, dass die Periodenverteilung der Sterne in NGC 2264 stark masseabhängig ist und qualitativ der Verteilung im ONC gleicht. Die Sterne in NGC 2264 rotieren im Durchschnitt jedoch mit kürzeren Rotationsperioden. Eine quantitative Analyse unter Berücksichtigung des Altersunterschiedes und der unterschiedlichen Radien der Sterne beider Haufen zeigte, dass die zeitliche Entwicklung der Rotationsperioden für die meisten Sterne mit der Erhaltung des Drehimpulses im Einklang ist. Im Gegensatz dazu zeigte sich aber auch, dass einige Sterne trotz zunehmendem Alters weiter mit deutlich längerer Periode rotieren. Diese Sterne verlieren offensichtlich Drehimpuls, was als Folge einer magnetischen Ankopplung der Sterne an ihre zirkumstellare Scheibe ("disk-locking") interpretiert wird. Die resultierende Kopplungsperiode betrgt ca. 8 Tage. Meine Analyse ergab ferner, dass in NGC 2264 oder dem ONC "disk-locking" nur für massereichere Sterne ($M \gtrsim 0.3\ M_{\odot}$) von Bedeutung ist. Zwar gibt es auch bei massearmen Sternen ($M \lesssim 0.3\ M_{\odot}$) Anzeichen für eine magnetische Wechselwirkung mit der Scheibe, diese ist aber nur in wenigen Fällen stark genug, um eine Ankopplung mit einer festen Rotationsperiode zu ermöglichen.
Diese Ergebnisse stehen in engem Zusammenhang mit einem überraschenden Ergebnis. Die auftretenden Helligkeitsvariationen der Sterne in NGC 2264 (hervorgerufen durch Sternflecken) unterscheiden sich für die beiden hier untersuchten Massebereiche. Während die Helligkeit der massereicheren Sterne typischerweise um bis zu 0.2 mag schwankt, zeigen die masseärmeren Sterne nur Helligkeitsschwankungen bis zu 0.06 mag, was auf unterschiedliche Magnetfeldstrukturen hindeutet, die durch verschiedene Dynamoprozesse erzeugt werden. Dies könnte für das unterschiedliche Rotationsverhalten der massereicheren und masseärmeren Sterne von Bedeutung sein.

Abstract

This thesis presents a detailed investigation of the rotational behaviour of young pre-main sequence (PMS) stars in order to achieve a better understanding of their angular momentum evolution during this evolutionary stage. For that purpose I have carried out an extensive photometric monitoring program which enabled me to identify a total of 405 periodic and 184 irregular variable PMS stars in the young open cluster NGC 2264 (age: 2–4 Myr). Hence, I could increase the number of known PMS stars in NGC 2264 by more than a factor of three and the number of published periods by more than a factor of ten.
Apart from the Orion Nebular Cluster (ONC, age: 1 Myr), with about 370 known rotation periods, NGC 2264 is therefore the only cluster for which a statistically significant number of rotation periods of PMS stars is known. For the first time it was possible to compare the rotational behaviour of stars of two young clusters with each other. I have shown that the period distribution of stars in NGC 2264 strongly depends on mass and quantitatively agrees with that of the ONC. However, the stars in NGC 2264 rotate with shorter rotation periods on average. A quantitative analysis which took into account the age ratio and the different stellar radii showed that a large fraction of stars spin up with conserved angular momentum while increasing in age. However, I also found that some stars clearly rotate with longer rotation periods even though they are aging. Apparently, these stars lose angular momentum, which is interpreted as a result of magnetic coupling to their circumstellar disk ("disk-locking"). The resulting locking period is about 8 days. My analysis further showed that "disk-locking" in NGC 2264 or the ONC is important only for higher mass stars ($M \gtrsim 0.3\ M_{\odot}$). There is evidence that also the lower mass stars ($M \lesssim 0.3\ M_{\odot}$) interact magnetically with their disks, but this interaction is in most cases not strong enough to remove angular momentum with sufficiently high rates to lock the star with a constant rotation period.
These findings are closely connected with a surprising result. The typical brightness variations of the stars in NGC 2264 (caused by star spots) differ for the two mass regimes considered here. While the peak-to-peak variation of the higher mass stars is typically up to 0.2 mag, the lower mass stars show brightness modulations only up to 0.06 mag. I argue that this is evidence for a different magnetic field structure, caused by different dynamo processes, and could be the decisive factor for the different rotational behaviour of the lower mass stars.

Wer nicht eine Million Leser erwartet,
sollte keine Zeile schreiben.

J. W. von Goethe

Contents

Chapter 1

Introduction

1.1 Star Formation and Pre-Main Sequence Evolution

The formation of stars is determined by several physical processes. Although theory and observations have made substantial progress in the last 30 years many details of the star formation process are still unclear.

It is generally accepted that stars form by gravitational contraction in rotating molecular cloud cores. It is believed that low mass (i. e. $M \lesssim 2\ M_{\odot}$) star formation begins with the fragmentation of a molecular cloud into a number of gravitationally-bound condensations. Initially these condensations are supported against gravity by thermal, magnetic, and turbulent pressures (e. g. Shu et al., 1987). At some point in this pre-stellar phase the condensations become gravitationally unstable and quickly collapses to form a protostar inside the molecular cloud core which is surrounded by a disk. From the continuously infalling (optically thick) envelope matter is accreted onto the protostar and the disk which results in a continuously increasing mass of the star-disk system.

Various scientists have suggested that the evolution from a deeply embedded and mass accreting protostar to a visible pre-main sequence (PMS) stars with little or no mass accretion (e. g. weak-line T Tauri stars) is characterised by a corresponding change in the spectral energy distribution (SED). During this main accretion phase the central object is called a Class 0 protostar (André et al., 1993) or "extreme Class I" object (Lada, 1991). The luminosity of Class 0 objects is generated entirely from the gravitational accretion. Phenomenologically Class 0 objects are characterised by high ratios of submillimetre to bolometric luminosity (André et al., 1993; Barsony, 1995) and are also the driving sources of powerful jet-like outflows (see e. g. Eislöffel et al., 2000, or Bachiller, 1996, for a review). The radius of low mass protostars ($\sim 5\ R_{\odot}$ for $1\ M_{\odot}$) is set by a mass-radius relation which is believed to depend mainly on the nuclear burning of interstellar deuterium in the accreted gas (Stahler, 1983; Palla & Stahler, 1990). During the main accretion phase the accretion rate is estimated to be typically between $10^{-5}\ M_{\odot}$/yr and $10^{-4}\ M_{\odot}$/yr (Palla & Stahler, 2000). Adopting such high mass accretion rates, a $1\ M_{\odot}$ star has assembled most of its stellar mass after 10000–100000 yr.

Class 0 objects are believed to proceed into Class I objects which are also near infrared sources and show a rising SED longer than $2.2\,\mu$m. The SEDs are broader than that of a single blackbody and are probably resulting from a warm dusty envelope around a hot

stellar object. In addition Class I objects show apparently weaker outflows than Class 0 objects and the mass of the circumstellar envelope is well below the stellar mass (e. g. André & Montmerle, 1994). They are interpreted as protostars at a late accretion phase.

Once the forming star is also optically visible it is called a Class II object which can be placed in the Hertzsprung-Russell (HR) diagram. In this diagram the stars first appear as Class II on the so-called birthline (Stahler, 1983; Shu et al., 1987). Low mass Class II objects are presumably T Tauri stars (TTSs) which are surrounded by a dusty circumstellar disk (classical TTSs). Their SEDs are broader than a single blackbody function and show large infrared excess radiation. The SEDs of Class III objects are slightly reddened blackbody functions. These stars are presumably TTSs which are surrounded by optically thin disks (weak-line TTSs). T Tauri stars represent a pivotal class of low mass ($M \leq 2\ M_{\odot}$) stars between deeply embedded sources, which can be studied only at infrared and radio wavelength, and solar-type main sequence stars. They are a sub-group of the (low mass) PMS stars. TTSs were first recognised as a distinct group of late type emission line objects associated with dark clouds and related nebulosity by Joy (1945) in the Taurus Auriga dark cloud and are named after the "prototype" T Tauri while their physical nature was first recognised by Ambartsumian (1947). The basic features of these stars have been reviewed by Bertout (1989) and Appenzeller & Mundt (1989).

During the last two decades we have obtained a consensus picture of what we call a classical TTS (CTTS). The basic components are first a low mass pre-main sequence star ($M \leq 2\ M_{\odot}$) with strong surface magnetic activity resulting in large spots and some chromospheric emission and second a circumstellar disk from which matter is accreting onto the central star. The dust in the disk causes the infrared excess of the spectrum by reradiating the absorbed optical radiation of the star at longer wavelengths. The strong Hα emission and UV excess which is inherent in CTTSs is believed to arise from magnetically driven accretion in funnel flows onto the stars in which the gas is accelerated to free-fall velocity (Cabrit et al., 1990; Calvet & Hartmann, 1992; Muzerolle, Calvet & Hartmann, 2001) and from chromospheric activity. Accretion in CTTSs is also connected to magnetically driven winds (see Sect. 1.3). CTTSs have stellar winds with mass loss rates ranging from $10^{-9}\ M_{\odot}$/yr to $10^{-7}\ M_{\odot}$/yr while the accretion rates of these stars are typically between $10^{-8}\ M_{\odot}$/yr and $10^{-7}\ M_{\odot}$/yr (e. g. Hartmann, 1998). At least at larger distances from the stars many of these outflows have been collimated into bipolar jet-like flows (Hirth, Mundt & Solf, 1997; Mundt & Eislöffel, 1998; Eislöffel et al., 2000). In contrast PMS stars are called "naked" of "weak-line" TTSs (WTTSs) if they do not show large infrared or ultraviolet excesses and only weak Hα emission which is believed to arise in active stellar chromospheres (Najita et al., 2000). These features suggest that accretion disks have almost disappeared (at least the inner parts) in WTTSs. It has become the norm to distinguish between the two sub-classes of TTSs using the strength of the Hα emission. According to this definition TTSs with equivalent widths of $W_{\lambda}(H\alpha) > 10$ Å are called CTTSs while those with $W_{\lambda}(H\alpha) < 10$ Å are called WTTSs (Walter, 1986; Appenzeller & Mundt, 1989; Strom et al., 1990).

During the PMS evolution the luminosity of these stars is generated almost entirely by gravitational contraction with nearly constant effective temperature. This evolution is described by the classical PMS theory of Hayashi (1962). According to the PMS evolution models of D'Antona & Mazzitelli (1997) the stellar radius of a 1 Myr old PMS star of $1\ M_{\odot}$ decreases from $2\ R_{\odot}$ to $1\ R_{\odot}$ within 10 Myr. The luminosity is also decreasing with decreasing stellar radius but the effective temperature stays nearly constant as long as the

star follows the convective tracks in the HR diagram. Later it evolves along the so-called radiative Henyey tracks toward the main sequence and thereby increases the effective temperature. Low mass TTSs ($M \lesssim 0.25\ M_\odot$) are expected to be fully convective and follow the Hayashi tracks until they reach the main sequence (MS) with an age of about 30–50 Mry. However, in both cases the PMS stars are always located below the birthline and above the MS in the HR diagram.

1.2 The Angular Momentum Problem

An important open questions in the theory of star formation outlined above is the evolution of the angular momentum of the stars. It has been recognised for many decades that the specific angular momenta of interstellar clouds are many orders of magnitude higher than that of the Sun and other MS or PMS stars. In the literature this observational fact is often called the angular momentum problem which was first well expressed by Spitzer (1978): Suppose we consider a interstellar cloud with a length of $d \approx 10\,\mathrm{pc}$ and a radius of $R \approx 0.2\,\mathrm{pc}$ which is rotating about the long axis with the same angular velocity as our galaxy (i. e. $\omega = 10^{-15}\,\mathrm{s}^{-1}$). If we further assume a mass of 1 $M_\odot$ its density is $\rho = 5 \times 10^{-23}\,\mathrm{g/cm}^3$ or equivalently 30 particles per cm^3. If the cloud collapses to form a star of radius $R_\star = 6 \times 10^{10}\,\mathrm{cm}$ the radius of the cloud has to decrease by a factor of 10^7 from 0.2 pc to the stellar radius $R_\star$. Conservation of angular momentum ($J \propto M\omega R^2$) would require that the angular velocity increases by a factor of 10^{14}. This yields $\omega = 10^{-1}\,\mathrm{s}^{-1}$ and a maximum rotational velocity at the stellar equator of $v = 6 \times 10^8\,\mathrm{cm\,s}^{-1}$, i. e. 20% of the speed of light. The centrifugal force at the equator would exceed the gravity by a factor of 10^4. Obviously angular momentum can not be conserved during the star formation process, since it would be impossible for molecular clouds to be incorporated into a star.

Although it is likely that stars form in filaments with a different structure than it was assumed by Spitzer the basic argument still holds. Observations of molecular clouds (Goodman et al., 1993; Goldsmith & Arquilla, 1985; Blitz, 1993) show that their specific angular momenta ($j = J/M$) are typically $j = 10^{21}\,\mathrm{cm}^2\mathrm{s}^{-1}$ on the small scales ($r = 0.05\,\mathrm{pc}$) and $j = 10^{24}\,\mathrm{cm}^2\mathrm{s}^{-1}$ on the largest scales ($r = 10\,\mathrm{pc}$). In contrast the specific angular momentum of a PMS star is $j = 10^{16} - 10^{17}\,\mathrm{cm}^2\mathrm{s}^{-1}$. Thus, the specific angular momentum of the material that forms the star has to be reduced at least by a factor of $10^4 - 10^5$. It is believed that during the different evolutionary steps of a star several mechanisms remove angular momentum from the molecular cloud, the protostar, and later even from the visible TTS and in this way the specific angular momentum is continuously reduced (for a review see Bodenheimer, 1989). Table 1.2 lists some characteristic values of specific angular momenta for different evolution stages during the star formation process.

It is often stated that the angular momentum problem is solved by the formation of stellar companions and circumstellar disks. In this scenario angular momentum of the cloud is transferred to the orbital motion of the companions and the disk. However, only the specific (orbital) angular momenta of wide binaries are of the same order as the specific angular momenta of molecular clouds. In contrast the specific angular momenta of close binaries are typically two orders of magnitude smaller. In addition not all stars form in multiple systems. The specific angular momenta of circumstellar disks are also typically one order of magnitude smaller than those of molecular cloud cores. Hence, the

Tab. 1.1: Characteristic values of specific angular momenta taken from Bodenheimer (1989), Herbst et al. (2002) and the open cluster data base by Prosser & Stauffer.

Object	J/M (cm^2 s^{-1})
Dense molecular cloud cores ($\leq$ 1pc)	10^{21} – 10^{22}
Binary (period $\leq 10^4$ yr)	10^{20} – 10^{21}
Binary (period $\leq$ 10 yr)	10^{19} – 10^{20}
Binary (period $\leq$ 3 yr)	10^{18} – 10^{19}
100 AU disk (1 $M_\odot$ central star)	10^{20}
Planet (Jupiter orbit)	10^{20}
PMS star (median ONC)	10^{17}
ZAMS (median young clusters)	3×10^{16}
Sun	10^{15}

angular momentum problem is only partly solved by the formation of binary systems and circumstellar disks. Another mechanism which causes angular momentum loss of molecular clouds in the early phase of star formation is magnetic braking. In this scenario angular momentum is transfered to the ambient medium by magnetic stress (Spitzer, 1978).

Angular momentum loss during the star formation phases also originate from bipolar outflows which are believed to be driven by magnetic fields. The outflow gas is able to carry angular momentum away from the forming star and/or its surrounding disk (see e. g. Blandford & Payne, 1993; Shu et al., 1988; Königl, 1989; Wardle & Königl, 1993). There are also observational indications for angular momentum loss between the protostellar and TTS phase from measured $v \sin i$ values of protostars which were recently obtained for Class I objects (Greene & Lada, 1997, 2002a,b). These data indicate that these objects rotate considerably faster than most TTSs and have higher specific angular momenta.

When the stars are in the PMS stage of their evolution the angular momentum problem is solved to a large degree, but the typical specific angular momentum of PMS star is still a factor three higher than that of a zero-age main sequence (ZAMS) star (see Tab. 1.2 for details). With spectroscopic observations of line broadening it was first shown by Vogel & Kuhi (1981) and later confirmed by Hartmann et al. (1986) and Bouvier et al. (1986) that the youngest (solar mass) TTSs are slow rotators with rotation velocities $\lesssim 10\%$ of their breakup velocity. Further observations (e. g. by Stassun et al., 1999; Rebull, 2001; Herbst et al., 2002, see below) have provided rotation rates for hundreds of TTSs mainly in young open clusters (e. g. the ONC). These observations show that the typical angular momenta of PMS stars are of the order of 10^{16}–10^{17}cm^{2}s^{-1} depending on the rotation periods of the stars which typically vary between 1 and 10 days (see also Fig. 1.1).

Not only during the PMS phase, but also on the MS late type stars experience strong and continuing angular momentum loss, resulting from a magnetised stellar wind (Weber & Davis, 1967) but the involved time scales are much longer than during the PMS phase. Observational evidence for this slow down is provided for example by the fastest rotators in ZAMS clusters, such as α Per (age: 50–80 Myr), which have equatorial velocities of about 200 km s^{-1} while these values have fallen to below 10 km s^{-1} at the age of the Hyades ($\sim$ 600 Myr) (Radick et al., 1987). The loss rate of specific angular momentum

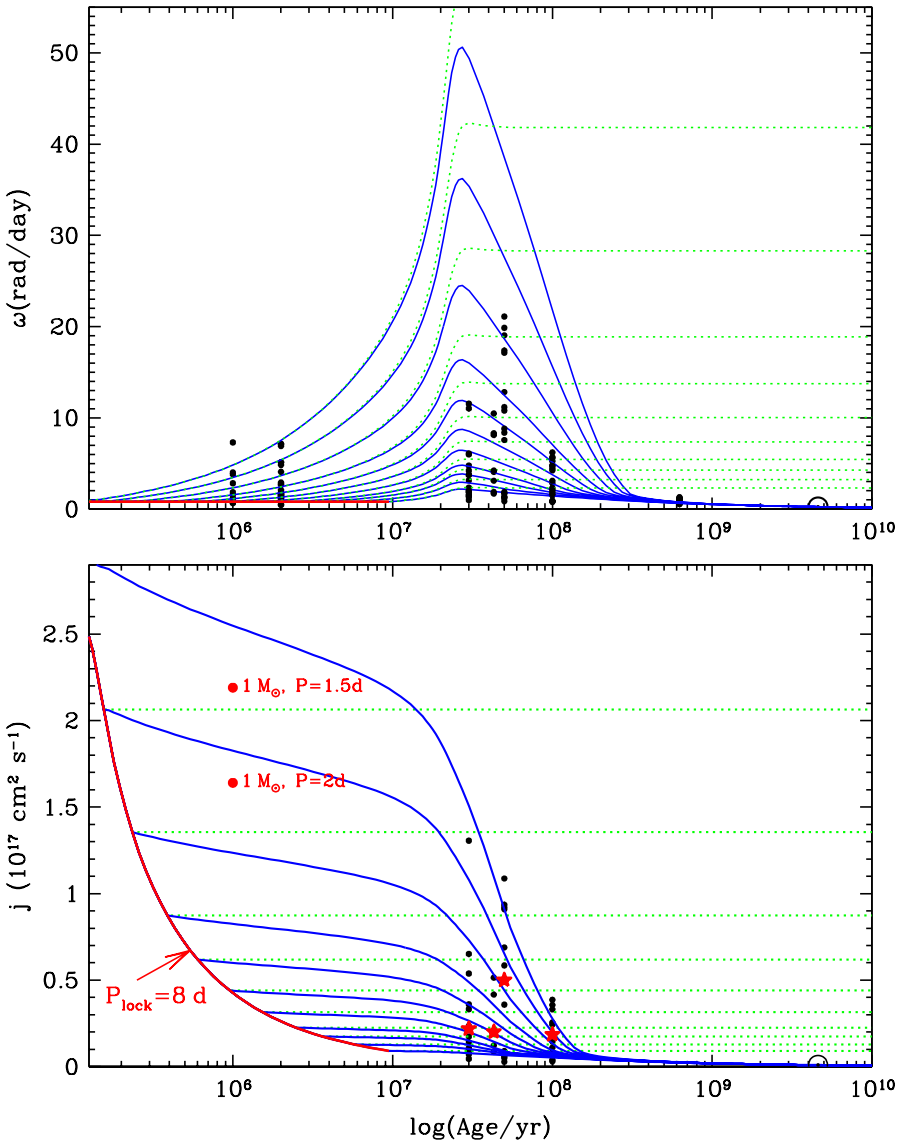

Fig. 1.1: Top panel: Measured rotation periods of PMS stars in the ONC (Herbst et al., 2002), the open cluster NGC 2264 (this study), and young stars in IC 2391, IC 2602, IC 46665, NGC 6475, αPer, the Pleiades, and the Hyades cluster (provided by . Prosser & Stauffer in the open cluster data base) with masses between 0.83 $M_{\odot}$ and 1.2 $M_{\odot}$. The lines represent rotational evolution tracks for 1 $M_{\odot}$ stars based on the PMS evolution models by D'Antona & Mazzitelli (1997). Green dashed lines represent models without angular momentum loss while for the compilation of the solid blue lines angular momentum loss via Skumanich like winds was adopted. The solid red lines represents a constant rotation period (disk-locking) at a 8 day period. **Bottom panel:** The evolution of the specific angular momentum of a 1 $M_{\odot}$ star for the rotational evolution tracks shown in the top panel. The black filled circles represent the specific angular momentum of the ZAMS stars. The red stars indicate the median of these data. Filled red circles indicate the specific angular momentum of a 1 Myr old star with the rotation period given at each data point. The red solid line shows the loss of angular momentum in the disk-locking scenario where the rotation period is fixed at 8 days.

$\mathrm{d}j/\mathrm{d}t$ of MS stars scales as ω^3 for slow rotators which is in agreement with the relationship of Skumanich (1972), $\omega(t) \propto t^{-1/2}$. Observations of stellar activity (Krishnamurthi et al., 1998) and theoretical arguments lead to the idea of a saturation threshold (Kawaler , 1988) where the loss of angular momentum scales as $\omega_{\mathrm{sat}}^2\omega$ for fast rotating stars with $\omega \geq \omega_{\mathrm{sat}}$. The saturation threshold depends on the stellar mass and is lower for lower mass stars (Krishnamurthi et al., 1997). These (Skumanich-like) magnetised winds operates on typical time scale of hundreds of Myr and play therefore only a minor role in the evolution of angular momentum in the PMS phase (in contrast to disk winds, see below). Therefore, if no other mechanism removes angular momentum from PMS stars, the rotational evolution of these stars is determined mostly by the shrinking of their stellar radius and they correspondingly spin up until they reach the MS (see Fig. 1.1).

Observationally, our best hope of constraining the angular momentum evolution of young stars is to obtain stellar rotation rates (beside stellar radii) for objects at a variety of ages and masses. In the last two decades the determination of stellar rotation rates for both PMS and MS stars has made substantial progress which was the basis for our current picture of the angular momentum evolution of solar-like stars outlined in the following. Since the studies of Van Leeuwen & Alphenaar (1982) in the Pleiades numerous subsequent rotational studies have been carried out in the young (30–50 Myr) clusters IC 2602 (Barnes et al., 1999) and IC2391 (Allain et al., 1996), the medium age (50–100 Myr) clusters Alpha Persei (Prosser et al., 1993; Prosser & Grankin, 1997) and the Pleiades (e. g. Van Leeuwen & Alphenaar, 1982; Krishnamurthi et al., 1998; Queloz et al., 1998) or the older (150–600 Myr) clusters M 7 (=NGC 6475; James & Jeffries, 1997), NGC 2516 (Terndrup et al., 2002), M34 (=NGC 1039; Soderblom, Jones, & Fischer, 2001) and Hyades (Radick et al., 1987; Terndrup et al., 2000). To date a variety of slow rotating stars have been detected in several young main sequence clusters (e. g. Stauffer, 1987).

In Fig. 1.1 I show the angular velocity and the specific angular momentum of solar type (0.83 – 1.2 $M_\odot$) main sequence stars derived from rotation periods taken from the open cluster data base provided by Prosser & Stauffer[1]. The measurements include rotation periods of stars in IC 2391, IC 2602, IC 4665, NGC 6475, αPer, the Pleiades, and the Hyades cluster. In addition the angular velocity of PMS stars in the Orion Nebular Cluster (ONC) determined by Herbst et al. (2002) and the open cluster NGC 2264 (this study) are shown. The large dispersion among the rotation rates of the ZAMS stars is evident. Stars at the ZAMS have the largest rotation rates, while PMS stars and older MS stars rotate at slower rates. Slow rotators are present in all PMS and MS clusters.

Fig. 1.1 also shows the evolution of the angular velocity and the specific angular momentum of a 1 $M_\odot$ star for two different models (blue and green lines). For the blue lines angular momentum loss via (Skumanich-like) winds was adopted while for the calculation of the green lines no wind was assumed. In both cases the radii and moment of inertia resulting from PMS evolution models by D'Antona & Mazzitelli (1997) were used for the calculation of ω and j. The difference between the blue and between the green lines is the time from which on the angular velocity was allowed to evolve. Prior to this time the rotation period was adopted to be fixed at 8 days and both the angular velocity and the angular momentum follow the red line (see also Sect. 1.3).

The existence of fast rotating stars on the ZAMS, i. e. the spin up of stars from the PMS phase to the ZAMS, can simply be explained by gravitational contraction of the stars

[1] Available at http://cfa-www.harvard.edu/ stauffer/opencl/index.htm

and only marginal loss of angular momentum. However, the existence of slow rotators and the broad period distribution of ZAMS stars in general can be only explained if during the TTS phase angular momentum loss is rather different from star to star. A magnetic interaction between stellar magnetospheres and circumstellar disks (disk-locking) has been proposed to cause the spin down the stars during the PMS evolution (Edwards et al., 1993). Details on this process and how it explains the period distribution of ZAMS stars are given in Sect. 1.3. This means that classical (i. e. Skumanich-like) winds alone are unable to explain these rotational evolution because of the large dispersion of rotational velocities among ZAMS stars (Krishnamurthi et al., 1997).

The angular momentum loss of older MS stars resulting from magnetised winds depends on their angular velocity in the sense that fast rotating stars lose more angular momentum. Therefore, the resulting angular velocity of the stars is comparable when they are about 1 Gyr old regardless of whether they were fast or slow rotators at the ZAMS. Thus, the dispersion of the angular velocity in older clusters is small.

1.3 The Disk-locking Scenario

To date it is widely accepted that magnetic star-disk interaction controls the PMS winds and therefore the angular momentum evolution of the stars during the PMS phase. This assumption is supported by the observational result that CTTSs with inner disks are rotating more slowly than WTTSs without inner disks (Edwards et al., 1993; Bouvier et al., 1993). Since the pioneering work of Ghosh & Lamb (1979a,b) and Camenzind (1990) several models for a disk-star interaction were developed (Königl, 1991; Shu et al., 1994; Ostriker & Shu, 1995).

The detailed mechanism for braking differs among the models. Figure 1.2 illustrates schematically the basic features of the standard model by Shu et al. (1994) where the star is *locked* into co-rotation with the inner disk which is truncated at some radius $R_{\rm T}$. The rotation period of the star is equal to the Keplerian rotation period of the material in the disk at the "co-rotation radius" ($R_{\rm C}$) which is slightly larger than $R_{\rm T}$ and is set by the balance of accretion ($\dot{M}$) and magnetic field strength ($B_\star$) of the star. Angular momentum is transferred from the star to the disk via the torque of the magnetic field. The circumstellar disk itself and therefore the whole system (disk + star) loses angular momentum through a disk wind which is driven by (quasi) open magnetic field lines.

The disk-locking scenario together with (Skumanich-like) winds are able to explain the observed periods of PMS stars, (ZA)MS stars, and the sun. As it is indicated by Fig. 1.1 (top panel) solar mass stars attain the solar rotation rate regardless of their rotation periods at the ZAMS. The large dispersion of rotation periods at the ZAMS is produced by a different time on which individual stars are locked to their disk. Stars which are locked for short times and therefore lose a smaller amount of angular momentum by disk-locking arrive at the ZAMS as fast rotators. The angular momentum evolution of such stars is represented in the bottom panel of Fig. 1.1 by the blue lines which branch off the solid red line at early times and larger specific angular momentum. Their excess angular momentum (compared with the sun and older MS clusters) is carried away by Skumanich-like disk winds. On the other hand, stars that are locked for longer times lose most of their excess angular momentum during this locking phase. These stars branch off the solid red line with larger ages and Skumanich-like winds carry away only a small

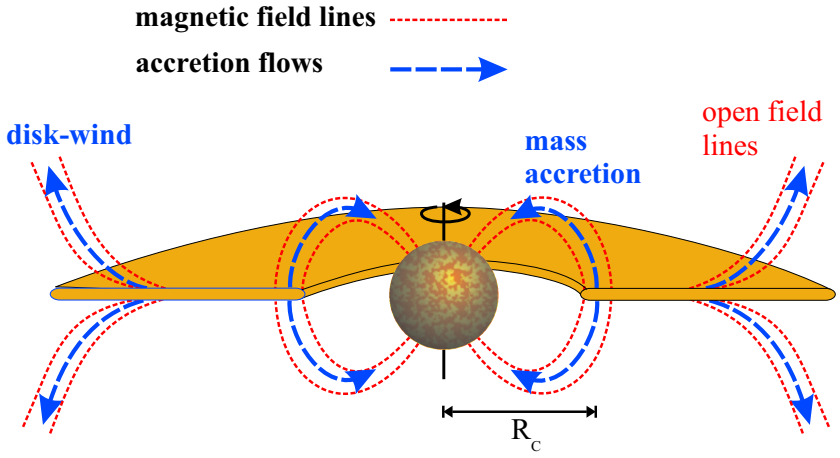

Fig. 1.2: Schematic illustration of the basic features of the disk-locking model by Shu et al. (1994). The star is surrounded by a disk which is truncated at the radius $R_{\rm T}$. The magnetic field locks the star into co-rotation with the disk. Angular momentum is transported from the star to the disk.

amount of specific angular momentum.

The disk-locking scenario is observationally supported by rotation period studies in the Orion Nebular Cluster (ONC, age $\approx 1\,$Myr) where Attridge & Herbst (1992) have first discovered a bimodal period distribution for higher mass stars ($M \geq 0.25\ M_{\odot}$, using the evolution tracks of D'Antona & Mazzitelli 1994) which was later confirmed by Herbst, Bailer-Jones & Mundt (2001) and Herbst et al. (2002). The period distribution of these stars peaks at two distinct periods of $P = 2$ days and $P = 8$ days. In contrast, the period distribution of stars with lower masses was found to be unimodal with a peak at about $P = 2$ days. The bimodality of the higher mass stars is interpreted as an effect of disk-locking. Stars with periods of about 8 days are believed to be locked to their disks. This interpretation is supported by infrared data which show a correlation of the angular velocity and the $(I_{\rm C} - K)$ infrared excess in the sense that stars with circumstellar disks (CTTSs) tends to rotate with larger periods than stars without disks (Herbst et al., 2002). This is consistent with the disk-locking scenario since only stars with circumstellar disks can be locked and therefore rotate with longer periods. Disk-locking is not possible for stars without disks and these stars are expected to rotate at faster rates due to the contraction of the stars. The period distribution of Herbst et al. (2002) suggests that the locking period of higher mass stars in the ONC is about $P = 8$ days while stars with shorter periods are presumably not locked to their disks. The locking period of 8 days is in agreement with the rotation periods measured for CTTSs in other stars forming regions (Bouvier et al., 1993).

Stassun et al. (1999) were not able to confirm the existence of a bimodal period distribution in the ONC. Furthermore, they did not find any differences of the rotation period for WTTSs and CTTSs. Therefore, Stassun et al. (1999) suggested that a large spread in initial rotation periods may be much more important than the effect of disk-locking. However, their study is biased towards periods with $P \leq 8$ days and towards lower mass stars which is probably the reason for their non-detection of a bimodal distribution.

Assuming that disk-locking exits, several questions naturally arise from the results of the rotational studies in the ONC:

- Is the period distribution similar in other young clusters, i. e. does environment play a role in setting up the initial period distribution?
- How many PMS stars interact with their disks? Is disk-locking inefficient for lower mass stars and can their unimodal distribution observed in the ONC result from a lower fraction of locked stars?
- How does the period distribution evolve with time and what is the typical age, $t_{\rm lock}$, at which the stars decouple from their disks? Herbst et al. (2002) have estimated a star-disk interaction half-life of $t_{1/2}\approx 0.7$ Myr and stellar evolution models require disk-locking times of 3–10 Myr in order to reproduce the observed rotation period distribution of ZAMS stars (e. g. Krishnamurthi et al., 1997).

To answer these questions it is necessary to measure rotation periods of large samples of PMS stars in clusters with different ages. The answers to these questions may not only help us to address the angular momentum problem in the PMS phase but should also provide insight in the production and evolution of magnetic fields in this early evolution stage of the stars since magnetic activity is closely connected with disk-locking.

1.4 About this Thesis

The aim of this thesis is to answer the questions raised in the previous Section. On the PMS, photometric monitoring programs for the determination of rotation periods were mainly focused on the ONC where a multiplicity of rotation periods were measured (Attridge & Herbst, 1992; Herbst, Bailer-Jones & Mundt, 2001; Herbst et al., 2002; Rebull, 2001; Stassun et al., 1999). In addition, a few rotation periods are available for stars in the Taurus Auriga Cloud (Bouvier et al., 1993), IC 348 (Herbst, Maley, & Williams, 2000) and NGC 2264 (Kearns & Herbst, 1998; Kearns et al., 1997). However, a statistically significant set of known periods exists only for the ONC. For a better understanding of the angular momentum evolution it is essential to know the rotation periods of more stars with a different age than the ONC stars.

Aside from the ONC, the open cluster NGC 2264 is perhaps the best target for a detailed rotational study of low-mass PMS stars, since it is sufficiently nearby (760 pc, Sung, Bessel & Lee 1997), fairly populous, and with an estimated of 2 – 4 Myr (Park et al., 2000) it is about a factor of 2 – 4 older than the ONC. Therefore I selected the young open cluster NGC 2264 for an extensive photometric monitoring program.

Prior to my study a few monitoring programs have been carried out in the young open cluster NGC 2264 (e. g. Kearns & Herbst, 1998) which altogether yielded only about 30 published rotation periods for PMS stars. Vogel & Kuhi (1981) have measured rotational velocities ($v \sin i$) for 46 stars in NGC 2264. Recently, circumstellar disk candidates have been identified in NGC 2264 by (Rebull et al., 2002). About 200 PMS stars have been identified in NGC 2264 prior to our study using a variety of methods including $H\alpha$ spectroscopy (Herbig, 1954; Marcy, 1980; Ogura, 1984), $H\alpha$ narrow band photometry (Sung, Bessel & Lee, 1997; Park et al., 2000) or ROSAT X-ray flux measurements (e. g. Flaccomio et al., 2000). A PMS membership catalogue that summarises these results is available in Park et al. (2000).

I monitored about 10600 stars in the area of NGC 2264 over a very broad magnitude

range ($9.8 \leq I_{\rm C} \leq 21$) corresponding to stars with masses from about 1.2 $M_{\odot}$ down into the substellar regime. This extensive monitoring program allowed me to discover about 600 new PMS stars in the cluster and in addition I could measure the rotation periods of 405 PMS stars. The monitoring program, its results, and the resulting conclusions for the disk-locking scenario are described in this thesis which has the following structure:

In the following **Chapter 2** I describe the method which was used for the determination of rotation periods, the observational strategy and the basic CCD data reduction.

In **Chapter 3** I describe the astrometry and methods I have used for obtaining relative and absolute photometry.

Chapter 4 describes the time series analysis including the periodogram analysis techniques and the χ^2-test which were used for identifying periodic and irregular variables respectively.

In **Chapter 5** I discuss the selection of PMS stars among the detected periodic and irregular variables in detail. This results in the final sample of periodic and irregular variable PMS members of the cluster.

In **Chapter 6** the nature of the different kinds of stellar variability is examined.

Chapter 7 describes the identification of additional PMS members for which no variability could be detected. Using the complete sample of PMS stars the completeness level of this study is estimated.

In **Chapter 8** the rotational evolution of low mass stars in the case of NGC 2264 is discussed in detail. Here the distribution of rotation periods will be presented and the dependence of the rotation periods from the stellar mass, age, and Hα emission will be discussed.

In **Chapter 9** I present evidence for a quite surprising change in the magnetic field morphology of the stars indicated by the peak-to-peak variation of the stars.

Finally in **Chapter 10** the main results and conclusions of the extensive photometric monitoring program are summarised.

Chapter 2

Observations & Data Acquisition

2.1 Photometric Monitoring as a Tool for Measuring Rotation Periods

Beside the stellar radius and mass, the rotation period of a star is the basic quantity for the study of the angular momentum evolution. Fortunately, it is possible to measure the rotation periods of many stars simultaneously by photometric monitoring.

TTSs are variable at all wavelengths on time scales ranging from hours to decades and amplitudes up to several magnitudes (see e. g. the reviews by Appenzeller & Mundt, 1989 and Bertout, 1989). Originally, time variability was even introduced by Joy (1945) as one classification criterion of TTSs. Later this classification criterion was dropped because spectroscopic criteria are sufficient for classifying this class of PMS stars. Early studies reported quasi-periodic variations of some TTSs with cycle lengths of several days (Wenzel, 1956; Herbig, 1962). Hoffmeister (1965) was the first to suggest that these variations might be due to rotational brightness modulations produced by dark (i. e. cold) spots on the stellar surface. Those spots exist on (late type) PMS stars and are interpreted as the "footprints" of strong surface magnetic fields (e. g. Feigelson & Montmerle, 1999). Fig. 2.1 schematically illustrates how cool surface spots accomplish temporal brightness modulations of a rotating PMS star.

Hoffmeister's interpretation was confirmed by the observations of several groups which also demonstrated that if the spot pattern on TTSs is sufficiently asymmetric and stable enough, the rotation period can be found by photometric monitoring (e. g. Rydgen & Vrba, 1983; Bouvier & Bertout, 1989; Vrba et al., 1989, 1993; Herbst et al., 1994; Stassun et al., 1999; Herbst et al., 2002). The advantage of this photometric method compared with $v \sin i$ measurements is that it yields directly the rotation period independent of the inclination of the star. In addition with period errors $\lesssim 1\%$ it can be very accurate even for slow rotating stars for which $v \sin i$ measurements yield only poor results.

However, I also mention a principal limitation of the photometric method for studying the rotation periods of TTSs. As I will show the photometric method can much more easily measure the periods among the WTTSs but only for a fraction of the CTTSs. The reason for this is the higher irregular variability which is inherent in most CTTSs. This "photometric noise" often prevents the detection of a periodic signal due to cold spots in the photometric data. In some rare cases periods can be measured also for such CTTSs

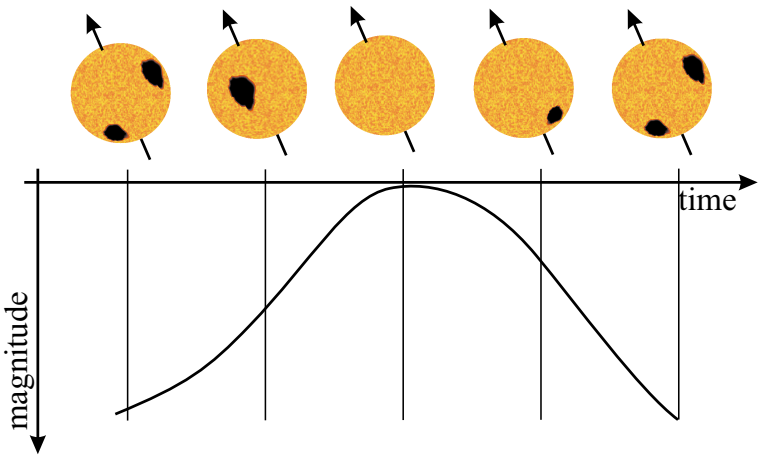

Fig. 2.1: Schematic illustration of a rotating PMS stars with two cool surface spots. The apparent stellar brightness changes periodically depending on the total spot area which is visible by the observer. The period of the brightness modulation is equal to the (surface) rotation period of the star assuming no differential rotation. The amplitude of the variations also depends on the effective temperature of the spots relative to the stellar atmosphere and the distribution of the spot pattern. Note that the cyclic variations of the stellar brightness are not necessarily sinusoidal.

with periodic modulation of larger amplitude which can be produced by bright (i. e. hot) spots resulting from accretion phenomena. Therefore, any photometric monitoring of young open clusters (like the ONC or NGC 2264) will be biased towards WTTSs in the sense that for these stars the fraction of measurable periods will be higher.

2.2 Observations

The rotational study of PMS stars in NGC 2264 described here is based on a photometric monitoring program which was carried out in the I_C band on 44 nights during a period of two month between 30 Dec. 2000 and 01 Mar. 2001 using the Wide Field Imager (WFI) on the MPG/ESO 2.2 m telescope on La Silla (Chile). The WFI consists of a mosaic of four by two CCDs with a total array size of 8 k × 8 k. The field of view is $34' \times 33'$ and the scale is $0.238''$/pixel. In Fig. 2.2 I show a 500 sec R_C exposure of the observed field from which the positions of the eight CCDs is evident.

To avoid highly saturated images and light scattering from the very bright star S Mon ($V = 4.7$ mag) this star was located near the northern end of the $23\farcs3$ (96 pixels) wide central gap between two chips. The central position on the sky was close to RA(2000) = $6^h\,40^m\,59^s$ and DEC(2000) = $9^\circ\,38'\,59''$ for most frames. The typical deviation from this nominal position is $2''$. About 5% of the imaged area is lost due to the gaps between the chips and the small dithering of the frames. In order to increase the dynamical range of the observations, three consecutive exposures of 5 sec, 50 sec and 500 sec were taken with the I_C filter. This series of three exposures is defined here as one data point. In total I obtained 110 data points and between 1 and 18 data points per night. The observing time distribution of the time series is shown in Fig. 2.3. The typical seeing – measured by the full width at half maximum (FWHM) of the point-speared-function (PSF) – in these images

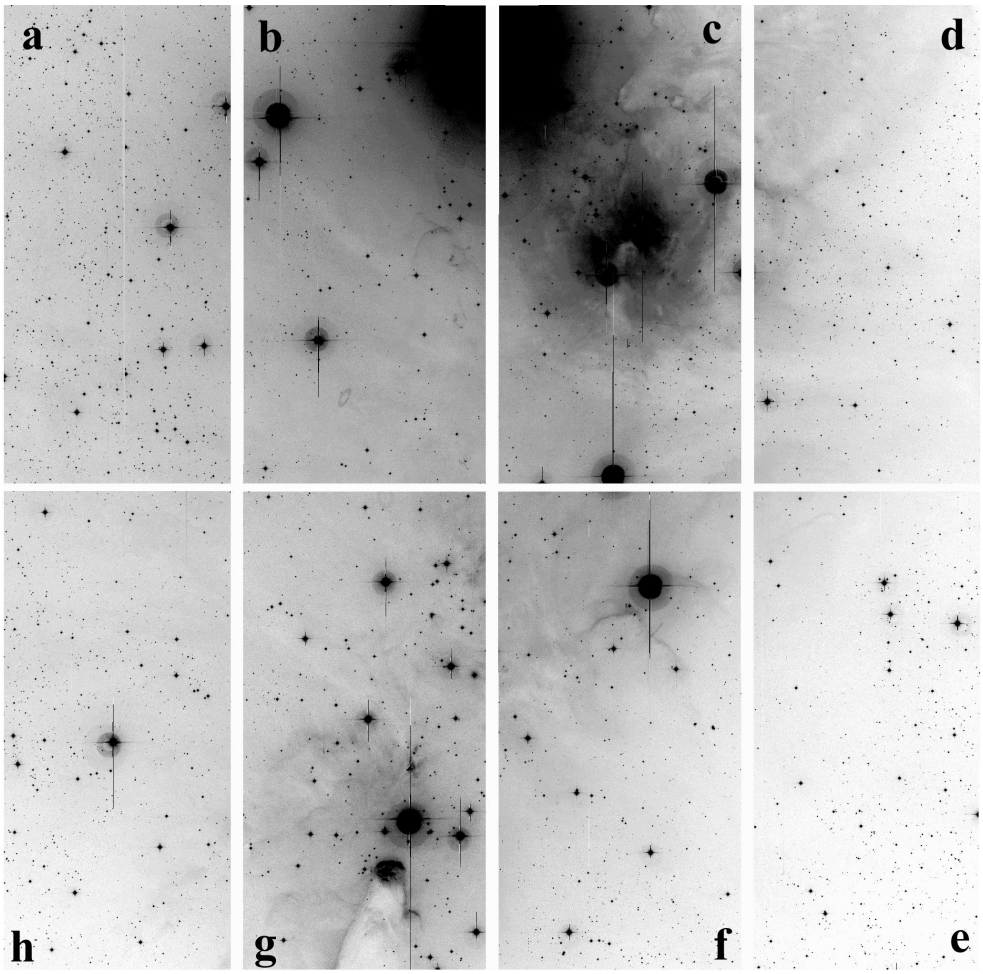

Fig. 2.2: Reproduction of a 500 sec R_C band exposure of the observed field. North is up and east is left. The observed field size is $34' \times 33'$. The area imaged by the individual chips a – h is quite evident. The bright star near the northern end of the gap between chip b and c is S Mon (V=4.7). In chip g the famous cone nebular is visible, which is hardly evident on our I_C band images as is the case for the nebulosity in the centre of chip e.

was of the order of $0\farcs8$–$1\farcs2$. The observations were carried out for air masses between 1.2 and 2.3. Since my aim was to perform differential photometry, which is less sensitive to temporal variations in the Earth's atmosphere (see Sect. 3.2), even observations with high airmass yield reliable results.

In addition to the I_C observations the cluster was observed through V and R_C filters on six nights during the 2000/2001 season. In R_C the exposure times were 5 sec, 50 sec and 500 sec, while the exposure times through the V filter were set to 5 sec, 60 sec and 720 sec. I_C observations were obtained directly before or after an observation in V or R_C. This allows me to determine the $(V - I_C)$ and $(R_C - I_C)$ colours from nearly simultaneous measurements in the two filters, i. e. the colours should not be affected by variability to any substantial extent.

In order to improve the absolute photometry, additional V, R_C and I_C WFI data were obtained between October 2001 and March 2002 using the same exposure times. In order

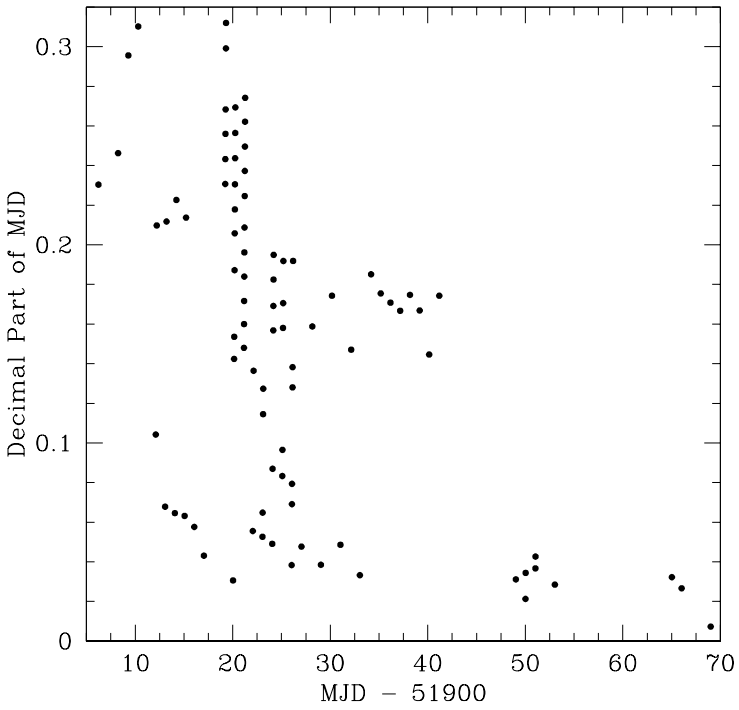

Fig. 2.3: Distribution of observation times of the I_C band time series (between 30 Dec. 2000 and 01 Mar 2001). The time (expressed as a fraction of a day) as a function of the modified Julian day (MJD) is shown.

to search for Hα emission, three consecutive Hα observations of 150 sec, 1200 sec and 1200 sec exposure time were taken directly before or after the observations in R_C in order to obtain nearly simultaneously observations in these two filters for a determination of the (R_C – Hα) colour. A detailed list of observations in filters other than I_C is given in Table 2.1.

2.3 CCD Processing

The image processing was done for each of the eight WFI chips separately using the standard IRAF tasks. A one-dimensional bias was subtracted from each frame using the overscan region in each frame. A small two-dimensional residual remained which was removed using zero integration time (bias) frames. For images through V, R_C and Hα filters the variable sensitivity across the chips was corrected using the median combination of typically 10 – 15 twilight flats taken in the beginning and the end of two or three different nights.

Since the twilight flats taken through the I_C filter showed interference fringes (see below) I used illumination-corrected dome flats for flatfielding the I_C images. The illumination-corrected dome flats were created as follows. Dome flats are sufficient to remove pixel-to-pixel sensitivity variations but they will not correct for large scale variations because of the different global illumination from the telescope dome and the night sky. The global

Tab. 2.1: Dates of observations with the V, $R_{\rm C}$ and Hα filter for the two observing seasons 2000-2001 and 2001-2002. Listed are the number of data points (i. e. three images of three different exposure times) for each night in a given filter. The observations in V and R_C were take directly before or after a set of three images in $I_{\rm C}$.

	Date of observation	data points in V	$R_{\rm C}$	$H\alpha$
first observing season	9 Jan 2001	1	...	...
	10 Jan 2001	1	...	...
	11 Jan 2001	1	...	...
	12 Jan 2001	1	1	...
	15 Jan 2001	..	1	...
	16 Jan 2001	..	1	...
second observing season	25 Nov 2001	1	1	1
	11 Dec 2001	1	...	...
	4 Jan 2002	1	1	1
	13 Jan 2002	1	...	...
	17 Jan 2002	1	...	...
	2 Mar 2002	1	1	1
total		10	6	3

illumination of the night sky was determined by a low order fit to the median combination of long exposure (≥ 500 sec) images which were taken at different sky positions. Finally, the global illumination of the combined dome flats was replaced with this night sky by dividing through a low-order fit and multiplying with the night sky fit. For each observing run a single night sky image was created while illumination-corrected dome flats were created for each night separately.

The science images in the $I_{\rm C}$-band were affected by fringing caused by narrow band emission from the Earth's atmosphere and it was essential that these fringes be removed. I note that fringing is an additive effect and therefore the fringe pattern has to be subtracted from the science images. Since the fringe pattern was found to be stable over a given observation run I created only one fringe image for each chip per observing season. The fringe images were created using the flatfielded nightsky images. See Bailer-Jones & Mundt (2001) for a more detailed discussion.

Chapter 3

Photometry & Astrometry

3.1 Target Identification and Astrometry

My principal objective was to measure the rotation periods of as many stars as possible in the cluster. Since any star in the field is potentially a cluster member (whose PMS nature has to be checked in a later step) I had to examine each star for periodic brightness modulations. Therefore, my goal was to perform relative and absolute photometry for every star in the observed field with a sufficient signal-to-noise ratio, i. e. $S/N = 10$ or better. The relative and absolute photometry is described in the following subsections separately. As a common first step I had to identify the positions of all sources in the field. Therefore I first created a source list for all 8 chips employing the DAOFIND task, with a separate list for the 5 sec, 50 sec and 500 sec exposures. For this source search I selected for each of the three 5 sec, 50 sec and 500 sec exposures one frame with a position very close to the nominal central location of all frames. These images I designate here as reference frames. The number of sources detected in each chip of these reference images is listed in table 3.1.

The coordinates of each source in all other frames were calculated by applying a derived linear offset between the reference images and these frames. The offsets were calculated for each chip separately by measuring the pixel position of a bright star close to the chip's centre in all frames.

The IRAF tasks CCXYMATCH and CCMAP were used to cross-identify my sources in the reference frames with objects in the USNO-A2.0 catalogue (Monet et al., 1998) and to calculate the plate transformations to the sky positions. Using these plate solutions the final J2000 coordinates of the sources were calculated with the task CCTRAN. These

Tab. 3.1: Number of detected sources in the various chips of the reference images.

Exposure	Number of sources in Chip								
time	a	b	c	d	e	f	g	h	total
5 sec	505	268	445	311	405	278	286	334	2832
50 sec	864	447	586	883	814	546	432	648	5220
500 sec	2220	900	1187	1535	1754	1054	654	1645	10940

coordinates are listed in Table 3.5. The typical astrometric (random) error is of the order of $0\farcs3$.

3.2 Relative Photometry

All the variability studies described here are based on differential photometry relative to a set of non-variable reference stars. In this way I reduced the sensitivity to temporal variations in the Earth's atmosphere through which the stars must be observed. Before the final analysis and after various tests, I rejected some frames from the further analysis. These were usually frames that were taken under poor transparency conditions, poor seeing or with a bright background due to scattered moon light. In total I rejected 22 of the 110 data points before the final analysis, so that relative photometry was performed on 88 remaining data points.

The DAOPHOT/APPHOT task was used to measure the brightness of each object in the source lists. The aperture was chosen to be 8 pixels ($1\farcs9$) in diameter for all measurements in order to maximise the signal-to-noise ratio. The sky was calculated for each source separately as the median of an annulus with an inner diameter of 30 pixel ($7\farcs1$) and a width of 8 pixel centred on the source. During the measurement the sources were re-centred. Measurements with any pixel in the annulus entering the $\geq 1\%$ nonlinearity region of the CCD photometric response (i. e. $\gtrsim 35000$ counts) were rejected.

The differential magnitudes for all sources were formed as follows. First a set of non-variable comparison stars was selected from all sources in each chip for each of the three different exposures. Comparison stars were chosen according to the following criteria:

1. present on every of the 88 frames,
2. isolated from other sources and the corners of the field (see below),
3. the photometric error given by APPHOT (i. e. Poisson error in the source and scatter in the background) is on average less than 0.01 mag.

Only stars that passed all of these three tests were selected as candidate comparison stars. Possible variables among the candidate comparison stars were identified by comparing the flux of each candidate with the mean flux of all other candidates at the different epochs. Stars that showed the largest variability were rejected from the candidate sample and the procedure was performed again with the remaining stars. After a few iterations, typically 10–60 non-variable comparison stars were identified in each chip such that the mean standard deviation in the relative light curves of the comparisons stars (relative to the other comparison stars) was typically $\sigma_{\rm comp} = 0.009$ mag. In the best cases I achieved $\sigma_{\rm comp} = 0.007$ mag which is therefore the maximum precision one can expect for the relative photometry. This limit is most likely set by flat fielding errors and not by photon noise. Tab. 3.2 summarises the results of the comparison star selection. For the 5 sec exposures $\sigma_{\rm comp}$ is always larger than for longer exposure times. The reason therefore is that most of the stars measured by the 5 sec exposures are bright stars and cluster members of NGC 2264 which are in most cases variable (see Chapter 4). Therefore the number of non-variable comparison stars is very low for the 5 sec exposures and some variables with low amplitudes had to be included in the sample of comparison stars.

Tab. 3.2: Number of comparison stars (no.) in the various chips for each of the three exposure times. Also listed is $\sigma_{\rm comp}$ which is the mean of the standard deviations of the relative light curves of the comparisons stars (calculated relative to the other comparison stars and given in mag).

	5 sec		50 sec		500 sec	
Chip	no.	$\sigma_{\rm comp}$	no.	$\sigma_{\rm comp}$	no.	$\sigma_{\rm comp}$
a	20	0.018	15	0.008	65	0.008
b	32	0.022	10	0.008	25	0.007
c	17	0.017	30	0.010	48	0.007
d	23	0.019	15	0.010	40	0.008
e	20	0.017	18	0.008	60	0.008
f	18	0.018	10	0.008	51	0.008
g	23	0.023	9	0.007	24	0.008
h	22	0.018	13	0.009	48	0.008

The selected comparison stars were used for the calculation of the relative magnitude $m_{\rm rel}(t_j)$ of each source in the field at the different epochs t_j. The relative magnitude and its error $\delta m_{\rm r}(t_j)$ were calculated as follows. First I calculated the reference flux $F_{\rm r}$ of the comparison stars at each epoch which is defined as

$$F_{\rm r} = \frac{1}{N} \sum_{i=1}^{N} F_i, \tag{3.1}$$

where N is the number of comparison stars in the chip of the source and F_i is the flux of the ith comparison star given in collected electrons. The reference flux yields the reference magnitude which is given by

$$m_{\rm r} = -2.5 \log_{10} F_{\rm r} \; . \tag{3.2}$$

Finally the relative magnitude of the source is defined as

$$m_{\rm rel} = m - m_{\rm r} = m + 2.5 \log_{10} F_{\rm r}, \tag{3.3}$$

where m is the measured magnitude of the source. The fact that I used averages fluxes rather than magnitudes for the determination of the reference magnitude gives more weight on the brighter stars with higher signal-to-noise ratios. The relative magnitudes of each source $m_{\rm rel}(t_1), \ldots, m_{\rm rel}(t_{88})$ form the relative light curve of the source. As a last step I subtracted the mean of the light curve from each data point so that $\sum_j m_{\rm rel}(t_j) = 0$.

In order to decide whether the variations in the light curve are due to photometric noise or intrinsic variability of the star it is important to know the photometric errors, $\delta m_{\rm r}$, as accurately as possible. The photometric error of a data point in the light curve is given by

$$(\delta m_{\rm rel})^2 = (\delta m)^2 + (\delta m_{\rm r})^2, \tag{3.4}$$

where δm and $\delta m_{\rm r}$ are the magnitude errors of the source (measured by APPHOT) and the reference magnitude respectively. For small errors the latter is given by

$$\delta m_{\rm r} \simeq \left| \frac{{\rm d}\, m_{\rm r}}{{\rm d}\, F_{\rm r}} \right| \delta F_{\rm r} = \frac{2.5}{\ln(10)} \frac{\delta F_{\rm r}}{F_{\rm r}}. \tag{3.5}$$

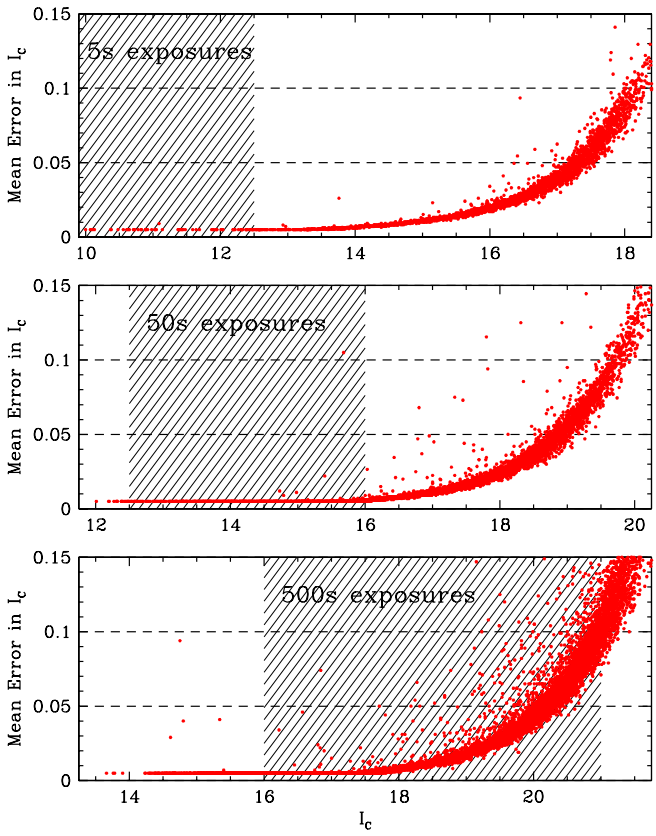

Fig. 3.1: The average error of the data points in the light curves ($\overline{\delta m_{\rm rel}}$) of the stars. These typical errors are shown for the measurements with the three different exposure times of 5s (top), 50s (mid) and 500s (bottom) as a function of stars' $I_{\rm C}$ magnitude. The shaded regions indicate which exposure time I used for the further analysis of a star with a given magnitude (see text). Note the different magnitude scales in the three plots.

The error of the reference flux, $\delta F_{\rm r}$, is given by the flux errors of the reference stars, δF_i, as

$$(\delta F_{\rm r})^2 \simeq \frac{1}{N^2}\sum_{i=1}^{N}(\delta F_i)^2 \simeq \frac{1}{N^2}\left(\frac{ln(10)}{2.5}\right)^2 \sum_{i=1}^{N}(\delta m_i)^2\, F_i^2, \tag{3.6}$$

where δm_i is the magnitude error of the ith comparison star. Inserting Eqs. (3.5) and (3.6) in Eq. (3.4) yields

$$(\delta m_{\rm rel})^2 = (\delta m)^2 + \left(\frac{1}{N\ F_{\rm r}}\right)^2 \sum_{i=1}^{N}(\delta m_i)^2\, F_i^2 \tag{3.7}$$

for the error of the relative magnitude of the source at epoch t_j.

For each star in the field I have determined the typical magnitude error in the light curve. This was done by calculating the average error, $\overline{\delta m_{\rm rel}}$, of all (88) data points in the light curve. In Fig. 3.1 I show these mean errors for the measurements with the

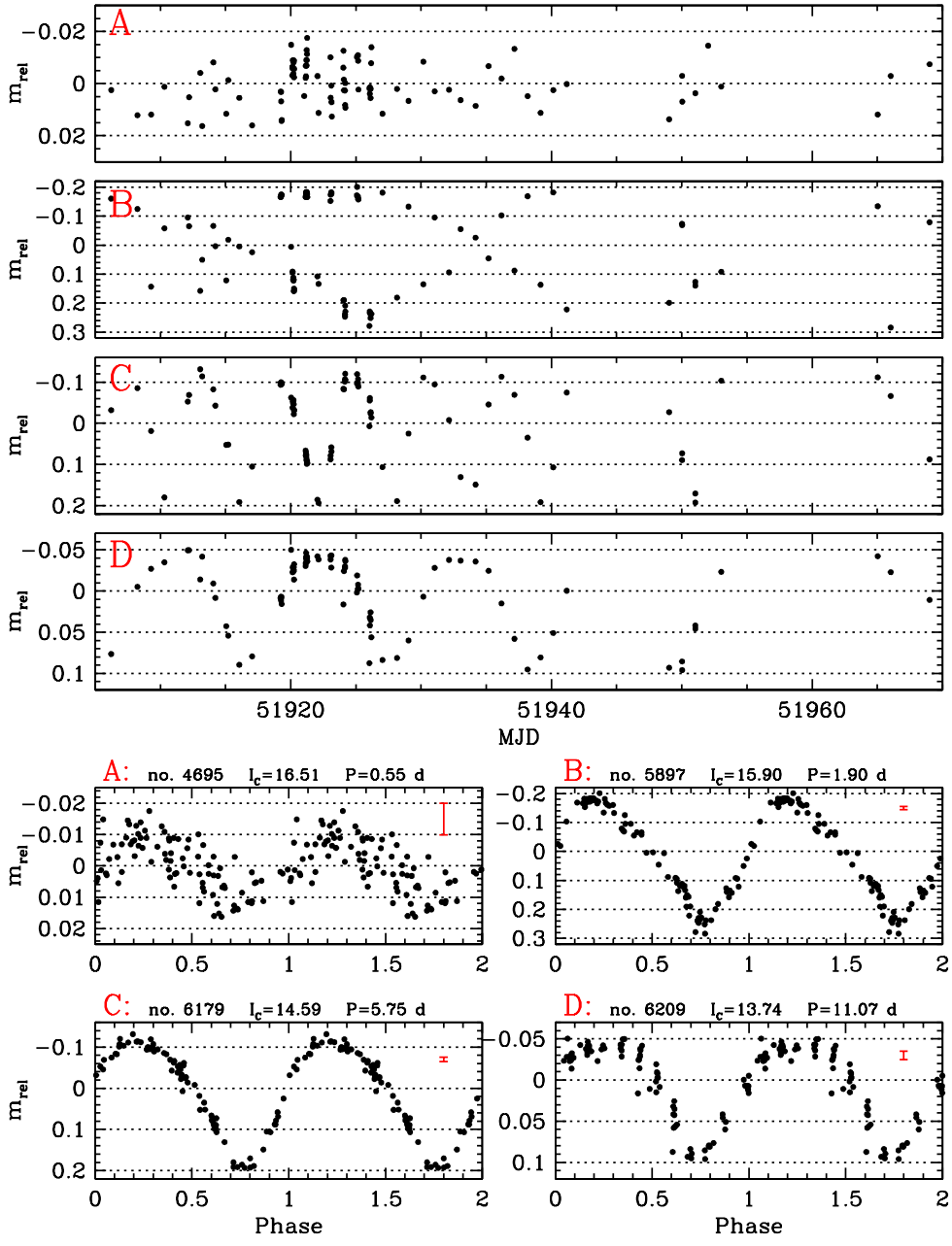

Fig. 3.2: Examples of relative light curves (mean subtracted) of four stars and the resulting phased light curve for each of the four stars. The light curves were phased with the period found by the Scargle periodogram analysis technique (see Chapter 4). For each star I also list the identification number (no.), the mean I_C magnitude, and the period P (in days). In the upper right corner of the four bottom panels the typical photometric error of the data points in each light curve is indicated by the error bar.

three different exposure times as a function of the stars' magnitude (for the magnitude determination see Sect. 3.3). Example light curves of four stars are shown in Fig. 3.2.

3.3 Absolute Photometry

In order to obtain additional constraints on the nature of the observed stars, in particular on their PMS membership, I obtained absolute photometry in V, $R_{\rm C}$ and $I_{\rm C}$. In contrast to the relative photometry described in the previous section, absolute photometry is defined here as the determination of the apparent magnitudes in these filters. As I will outline below, all of the photometry is done relative to secondary standards in the observed field. The result of the absolute photometry is reported in Table 3.5.

Many of the stars in the field are expected (and found, see Chapter 4) to be variable. The peak-to-peak variations of the variable stars are in most cases $\lesssim 0.2$ mag in $I_{\rm C}$ (see Fig. 6.3). Therefore, a single measurement of the magnitude of a star depends on the phase and amplitude of the star's brightness modulation. On the other hand single measurements of the colour of a PMS star with cool (or hot) surface spots also differ at different epochs. That is because the spectral energy distribution of the light coming from the area of the spot differs from the spectral energy distribution of the light radiated from the other part of the stellar atmosphere because of the different effective temperatures. The difference between the two energy distributions is wavelength dependent and larger for shorter wavelengths. Therefore, if cool spots cause the variability of a star the peak-to-peak variation in its light curve increases to shorter wavelength, i. e. it is larger in the V-band and smaller in the $I_{\rm C}$ band.

Observations of T Tauri stars confirm this expected colour behaviour of the stars (Vrba et al., 1989; Herbst et al., 1994). The relations between the peak-to-peak variations ΔV, $\Delta R_{\rm C}$ and $\Delta I_{\rm C}$ in the different filters are given by the colour slopes

$$S_R = \frac{{\rm d}(\Delta R_{\rm C} - \Delta I_{\rm C})}{{\rm d}(\Delta I_{\rm C})} \qquad \text{and} \qquad S_V = \frac{{\rm d}(\Delta V - \Delta I_{\rm C})}{{\rm d}(\Delta I_{\rm C})}.$$

Herbst et al. (1994) calculated these slopes for several WTTSs with a mean value of $S_R = 0.31 \pm 0.23$ and $S_V = 0.55 \pm 0.36$. Since the typical peak-to-peak variations of the stars in my sample are $\Delta I_{\rm C} \simeq 0.2$ (see Sect. 6.2) the expected maximal colour changes are $\Delta(R_{\rm C} - I_{\rm C}) \simeq 0.06$ mag and $\Delta(V - I_{\rm C}) \simeq 0.1$ mag but in some extreme cases the variations in the colour may be higher.

To take into account these magnitude and colour changes I determined the $I_{\rm C}$ magnitude as well as the $(V - I_{\rm C})$ and $(R_{\rm C} - I_{\rm C})$ colours at different epochs. The colours and magnitudes which are listed in Table 3.5 are average values of these different measurements. In the following I describe the calculation of the $I_{\rm C}$ on the one hand and the $(R_{\rm C} - I_{\rm C})$ and $(V - I_{\rm C})$ colours on the other hand separately.

3.3.1 Determination of the $I_{\rm C}$ Magnitude

For the calculation of the $I_{\rm C}$ magnitude only the measurements taken during the first observing run in Jan. 2001 were used because for this measurements the phases of the stars' variability were known from the analysis described in Sect. 3.2. The dates of the employed measurements are listed in the top part of Table 2.1. In the first observing season

I obtained three nearly simultaneous measurements in I_C and R_C (i. e. three images in I_C with different exposure times followed by three images of different exposure times in R_C) and four nearly simultaneous measurements in I_C and V. The final I_C magnitudes listed in Table 2.1 were calculated by averaging the results of these seven independent measurements.

The I_C magnitudes were calculated in three steps: First a colour correction was performed for each of the seven measurements separately. Second, the (mean subtracted) relative magnitudes at each of the seven data points was subtracted from these corrected measurements. In this way the variability of the stars was taken into account. Finally, in the third step the obtained magnitudes in step two were averaged.

Since I did not observe any flux standards during any of the observing seasons I had to use secondary standard stars located in the field for calibrating my measurements. The photometric calibration coefficients were determined using magnitudes and colours of stars in NGC 2264 measured by Rebull et al. (private communication). Their photometric data include the photometry of PMS stars in the cluster from Rebull et al. (2002) and in addition unpublished photometry of foreground and background objects in their observed field. This extended data set, including the unpublished data, compared to a data set consisting only of PMS stars, has the advantage of a smaller fraction of variable stars. My objects were cross-identified with the 2924 objects in this extended Rebull et al. catalogue which are located in my field. The 2227 (76%) stars which I could identify were used as secondary photometric standard stars.

In the first step I performed the colour correction and transformed the instrumental magnitudes $I_{C,instr}$ into the Cousins I system by applying the linear transformation equations of the form

$$\begin{aligned} I_{cor} &= a_1 + b_1 \times (R_{C,instr} - I_{C,instr}) + I_{C,instr} \qquad \text{and} \\ I_{cor} &= a_2 + b_2 \times (V_{instr} - I_{C,instr}) + I_{C,instr}. \end{aligned}$$

The first equation was used for the three observations nearly simultaneous in I_C and R_C while the second equation was used for four nearly simultaneously observations in I_C and V. An air mass correction was not necessary since the calibration coefficients were calculated separately for each measurement and the used secondary photometric standard stars were measured with the same exposures. The coefficients a_1 and a_2 therefore account for the air mass dependence of the colour correction. A simultaneous colour correction with two colours (i. e. using only one transformation equation with two colour terms) was not possible because the measurements where taken at different air masses and when the stars were in different phases of their variability.

The coefficients a_1 and b_1 were calculated by applying a linear least squares fit to the points in the $(I_{C,Rebull} - I_{C,instr})$ vs $(R_{C,instr} - I_{C,instr})$ plane, where $I_{C,Rebull}$ is the magnitude in the secondary standard catalogue. The coefficients a_2 and b_2 were calculated in the same way using the $(I_{C,Rebull} - I_{C,instr})$ vs $(V_{instr} - I_{C,instr})$ plane. I typically used between 100 and 200 stars per chip and exposure time (minimum 42, maximum 392) for calculating the linear transformation coefficients. Thus, even though many of the standard stars are variable this large number ensures a robust transformation. Obvious outliers were rejected before the calculation of the coefficients was done. Since the variable stars were in different phases of their brightness modulation for a given epoch the related data points scatter around the true transformation function. The uncertainties of the transformation

coefficients results from this scatter. The median values of the slopes are $b_1 = 0.18$ and $b_2 = 0.10$. As mentioned above the coefficients a_1 and b_1 depend on the air mass and a_1 varies between -1.8 mag and -1.5 mag while b_2 ranges from -2.1 mag to -1.7 mag. The typical uncertainties of the transformation coefficients are $\delta a_1 = 0.005$ and $\delta b_1 = 0.010$ for the first and $\delta a_2 = 0.015$ and $\delta b_2 = 0.010$ for the second equation.

To improve the results I made use of the fact that the phase and amplitude of each star at the seven epochs is known from the relative photometric analysis described in Sect. 3.2. These results were used in the second step. Here, the relative magnitude of the corresponding data point in the light curve of each star was subtracted from each of the the seven colour corrected measurements, i.e.

$$I_{\rm cor,sub}=I_{\rm cor}(t) - m_{\rm rel}(t), \tag{3.8}$$

where t is the epoch of the seven measurements and $m_{\rm rel}(t)$ is given by Eq. 3.3.

In the last step the seven different values of $I_{\rm cor,sub}$ for each star were averaged. These average values are listed in Table 3.5. The errors of these final $I_{\rm C}$ magnitudes were estimated in two different ways. First, I calculated the expected 1σ error, $\delta I_{\rm C,exp}$, from the measured IRAF/APPHOT errors[1] and the errors of the transformation coefficients. Second, I calculated the standard deviation σ_7 of the 7 independent $I_{\rm C}$ measurements. The final assigned error to the magnitude of each star is the maximum of this two error estimations for each star: $\delta I_{\rm C} = \max(\delta I_{\rm C,exp}, \sigma_7)$.

3.3.2 Determination of the $(R_{\rm C} - I_{\rm C})$ and $(V - I_{\rm C})$ Colours

The $(R_{\rm C} - I_{\rm C})$ and $(V - I_{\rm C})$ colours of the stars were corrected and averaged in a similar way as described in the previous section for the $I_{\rm C}$ magnitudes. For the calculation of these colours I used six nearly simultaneous measurements in $R_{\rm C}$ and $I_{\rm C}$ and ten such measurements in V and $I_{\rm C}$ respectively. The measurements were obtained during both observing seasons (see Table 2.1).

The colour correction of the instrumental $(V - I_{\rm C})_{\rm inst}$ and $(R_{\rm C} - I_{\rm C})_{\rm inst}$ colours was done by using the following transformation equations:

$$\begin{aligned} (R_{\rm C} - I_{\rm cor}) &= c_1 + d_1 \times (R_{\rm C,instr} - I_{\rm C,instr}) \qquad \text{or} \\ (V - I_{\rm cor}) &= c_2 + d_2 \times (V_{\rm instr} - I_{\rm C,instr}). \end{aligned}$$

The transformation coefficients were calculated using a linear least squares fit. The median values of the slopes are $d_1 = -0.26$ and $d_2 = -0.17$. The (air mass dependent) offsets c_1 and c_2 ranging from 0.9 to 1.1 and from 0.6 to 0.9 respectively. The final colours for each star which are listed in Table 3.5 were obtained by calculating the mean of the different corrected colours. The errors were derived in the same way as described above.

3.4 Final Photometry Database

The absolute photometric calibration described in the previous section was done for each chip and exposure time separately. The objects that were measured in the same chip

[1] The IRAF/APPHOT errors were adjusted to somewhat higher values as described in section 4.2.

Tab. 3.3: Comparison of my photometry with those of other authors. I list the offsets in the sense "results of other author minus results of this study". I also show the number of stars which were used for the comparison with other studies. These numbers differ for a single publication because not all magnitudes or colours were available for all stars. Stars with close neighbours were not used for the calculation of the offsets, since these stars are not separated in the other studies.

Publication	stars	I_C	stars	$(R_C - I_C)$	stars	$(V - I_C)$
Rebull et al.(2002)	1344	0.003 ± 0.002	1047	-0.019 ± 0.002	767	-0.010 ± 0.002
Park et al. (2000)	147	-0.009 ± 0.012	.....	.....	147	-0.041 ± 0.002
Flaccomio et al. (1999)	236	0.070 ± 0.003	236	-0.072 ± 0.008	221	-0.147 ± 0.007
Sung et al. (1997)	117	-0.000 ± 0.002	.....	.....	116	0.001 ± 0.010

with two (or three) different exposure times were identified in order to make sure that they do not appear twice in the final catalogue. For each star the colours and magnitudes listed in Table 3.5 were taken from the measurements with the highest signal-to-noise ratio taking into account possible pixel saturation in images with the best seeing: The colours and magnitudes of stars with $I_C \geq 16.0$ mag were taken from the 500 sec exposures. The measurements for stars with 12.5 mag $\leq I_C \leq$ 16.0 mag and with 10 mag $\leq I_C \leq$ 12.5 mag were taken from the 50 sec and 5 sec exposures respectively (see Fig. 3.1).

I compared the results of my photometry with those of other authors. In Tab. 3.3 I report the mean offsets in the photometry between my study and those of other studies. The reported uncertainties are the errors of the mean offsets. I did not find any significant difference in I_C between my results and those reported by Rebull et al. (2002), Park et al. (2000), and Sung, Bessel & Lee (1997). The differences in the $(R_C - I_C)$ and $(V - I_C)$ colours compared with these studies can be explained by slightly different filter transmission curves and intrinsic stellar variability. There is a significant offset in the photometry compared to the study of Flaccomio et al. (2000) (also for the I_C magnitude). The reason therefore could also be different transmission curves of the used filters and a different average colour of the employed flux standards. In Table 3.4 I list the limiting magnitudes in the different pass-bands for different signal-to-noise levels.

A small part of the final photometric catalogue is shown in Table 3.5. The complete table contains all 10554 stars and is available electronically only (see Lamm et al., 2003a). In this Table I also list the $(R_C - H\alpha)$ colour of the stars. Since no $H\alpha$ standard star measurements were available only the instrumental colour is given (a calibration of these instrumental colours in terms of emission equivalent width can be done by using Fig. 6.4).

Tab. 3.4: Limiting magnitudes for signal-to-noise ratios of 20 and 50 for each of the filters V, R_C and I_C resulting from the average of seven different measurements. Stars brighter than the listed magnitudes could be measured with the appropriate signal-to-noise or better.

Filter	20σ	50σ
V	22.1	21.1
R_C	21.5	20.4
I_C	20.7	19.6

Tab. 3.5: Photometric data of the stars in the observed fiel, the complete table is available electronically (see Lamm et al., 2003a). Also listed are the results of the time series analysis described in Chapter 4 (vari) where pv refers to periodic and iv to irregular variables, the standard deviation in the light curve (σ), the peak-to-peak variation in the light curves ($\Delta m_{\rm ptp}$), and, if available, the spectral type (SpT) taken from Rebull et al. (2002), indicated by the index 1, or from Joung et al. (private communication), indicated by the index 2. The identifications in the last column are the catalogue numbers of Y: Young (private communication), R: Rebull et al. (2002,private communication), S: Sung, Bessel & Lee (1997), P: Park et al. (2000), F: Flaccomio et al. (1999), FX: Flaccomio et al. (2000), W: Walker (1956), LkHα: Herbig (1954).

Star	$\alpha(J2000)$	$\delta(J2000)$	$I_{\rm C}$	err	$(V-I_{\rm C})$	err	$(R_{\rm C}-I_{\rm C})$	err	$(R_{\rm C}-{\rm H}\alpha)$	err	vari	σ	$\Delta m_{\rm ptp}$	SpT	cross id
6000	6:41:8.16	9:30:4.4	8137	0.02	...	...	2.0104		-2.908	iv		0.070	0.260	.....	
001	6:41:8.19	9:36:5.8	6101		4.006		2.001		-3.82	pv		0.050	0.170	.....	R3588
2		1.60	0.01		-3.008	0.01	.....		0.010	0.050	.....	R3591			
		0.074		0.270	.....	R3590									

Chapter 4

Time Series Analysis & Period Determination

In order to get a large sample of PMS stars with known periods my aim was to check all 10554 stars in the field for both periodic and irregular variability. In addition all stars in the field were checked for irregular variability, too. For detecting these two types of variability I have used different analysis techniques which are described in the following subsections. I first discuss the search for periodic variables.

4.1 Periodic Variables

Two different periodogram analysis techniques were used to search for significant periodicity in the light curves of each of the 10554 monitored stars. Those stars which have fewer than 15 data points in their light curves were rejected from this analysis. 96% of the remaining 10503 stars have 80 or more data points in their light curves. In the following I describe the two used periodogram algorithms separately.

4.1.1 The Scargle Periodogram & False Alarm Probability

First I used the periodogram technique for unevenly sampled data described Scargle (1982) and Horne & Baliunas (1986) to search for significant periodicity in all monitored stars. For this purpose I have created a *C* routine of the Scargle periodogram technique. First, this algorithm calculates the normalised power $P_{\rm N}(\nu)$ for a set of given frequencies, ν. The normalisation factor of the periodogram is the total variance of the light curve, i. e. $P_{\rm N}(\nu) = P_X(\nu)/\sigma^2$, where $P_X(\nu)$ is the non-normalised power which is given by Eq. (10) of Scargle (1982). In this way the power of any peak in the periodogram indicates the significance that there is a periodic signal with the corresponding frequency in the light curve.

In the second step, the algorithm identifies for each star the frequency of the highest peak in the calculated periodogram. The light curve of each star is then phased with the period according to this frequency. In order to decide whether there is a significant signal of this period in the light curve, the power of the corresponding peak has to be related with a false alarm probability (FAP) which is the probability that a peak of this power

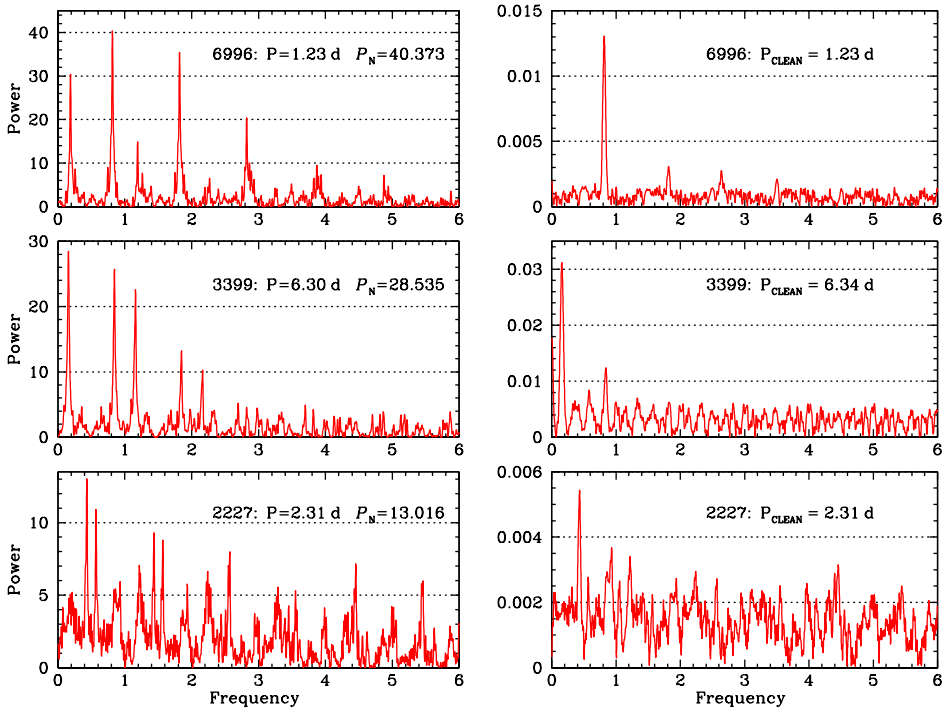

Fig. 4.1: Example periodograms of three stars which represent the highest, the median and the lowest power levels of stars which were finally accepted to be periodic variable. The left hand panels show the Scargle periodograms while the right hand panels show the corresponding CLEAN periodograms (see Sect. 4.1.2). In each periodogram the stars' identification number and the period (P) which corresponds to the frequency of the highest peak are indicated. For the Scargle periodograms also the normalised power of the highest peak (P_N) is listed. The phased light curves of the three stars are shown in the right hand panels of Fig. 4.3 in the first, third, and fifth row respectively.

is due simply to statistical variations, i. e. noise. In Fig. 4.1 (left panels) I show three example periodograms for stars at different power levels.

The standard procedure for determining the FAP is to use light curves created with Monte Carlo simulations. It is necessary that the time sampling of the simulated light curves is identical with that of the measured light curves. The simulated light curves consist only of noise and represent non-variable (or more precisely non-periodic variable) stars. These light curves are used to answer the question what fraction of non-variable stars is erroneously classified as periodic variable. Therefore, the periodogram has to be calculated for each simulated light curve and the power of the highest peak in that periodogram has to be determined. After typically 10 000 simulations (as specified below) the cumulative power distribution of the highest peak is used to determine the FAP as follows: The FAP of a given power P_N is set to be the fraction of simulated (non-variable) stars which have a highest peak power that exceeds P_N; i. e. if one has simulated for example 10 000 light curves, the 1% FAP power $P_{FAP=1\%}$ is the power which was exceeded by the highest peak in 100 simulations.

The critical point in this procedure is the simulation of non-periodic variable stars.

The simplest approach for doing this is to assume that the data points are statistically independent of each other. This is only true if the typical time scale for intrinsic variations of the sources is not larger than the (typical) time difference of the data points. Strictly speaking this assumption is not valid for our sample since the significant time scale for variations in PMS stars is about 1 day (Herbst et al., 1994) and in some nights the data points were obtained at closely spaced intervals of much shorter length; i. e. about 0.5 hour. Therefore I calculated the FAP using different types of simulations.

First, I made the simplified assumption of uncorrelated data points. Gaussian distributed random variables with zero mean and standard deviation σ were assigned to the dates of the real light curves. I set $\sigma = 0.01$ mag since the mean standard deviation in the light curves of the (non-variable) comparison stars which I used for calculating the relative light curves is of the same order (see Tab. 3.2). Therefore one expects a standard deviation of $\sigma \approx 0.01$ in the light curve of a non-variable star. After 10 000 simulations I calculated the cumulative power distribution of the highest peak which is shown in Fig. 4.2 for the time sampling of the 50 sec exposure as the red curve. This distribution yields a 1% FAP power value of $P_{\mathrm{FAP=1\%}} = 10.2$. I note that this level depends only slightly on the standard deviation used for simulating the light curves. For standard deviations of 0.02–0.3 mag the 1% FAP power value is only by a power of 0.2 – 0.5 smaller.

To allow for correlations between the data points a second type of simulation was carried out. Instead of simulating pure Gaussian noise, the measured light curves of the monitored stars were used. For the simulations I kept the time sampling the same as in the measured light curves but the relative magnitudes were randomly reassigned to the real dates. The resulting cumulative distribution of the maximum peak power of this second type of simulation is shown in Fig. 4.2 for the time sampling 50 sec exposures. This distribution yields a 1% FAP power value of $P_{\mathrm{FAP=1\%}}= 9.8$.

To be more conservative the higher power value of the two FAP simulations was used to define a cutoff level for the detection of periodic variables. Since the time sampling of the 5 sec and 500 sec exposures differ slightly from that of the 50 sec exposures also the 1% FAP power of the light curves measured with these exposure times differ slightly from that of the 50 sec exposures. I obtained a 1% FAP power of $P_{\mathrm{FAP=1\%}} = 10.1$ and $P_{\mathrm{FAP=1\%}} = 10.5$ for the light curves measured with 5 sec and 500 sec exposure time respectively. These values were also derived from the simulations of the first type.

Out of the 10554 analysed stars, 1192 were brighter than $I_{\mathrm{C}} = 19.5$ mag (i. e. $\mathrm{S/N} \lesssim 30$ per single measurement) and had a peak power $P_{\mathrm{N}} \geq P_{\mathrm{FAP=1\%}}$. As an example Fig. 3.2 shows the complete light curves and resulting phased light curves for four stars. In Fig. 4.3 I show a sample of phased light curves at different power levels.

4.1.2 The CLEAN Periodogram

The Scargle periodogram technique makes no attempt to account for the observational *window function*, $W(\nu)$, i. e. some peaks in the Scargle periodogram may be a result of the data sampling (see Fig. 4.1). This effect is called aliasing and even the highest peak could be an artifact. The CLEAN periodogram technique by Roberts, Lehar & Dreher (1987) tries to overcome this shortcoming of the Scargle periodogram.

The effect of the data sampling on the periodogram analysis can be understood as follows. Let $d(t_1), d(t_2), ..., d(t_N)$ be the finite number of measurements of the (continuous)

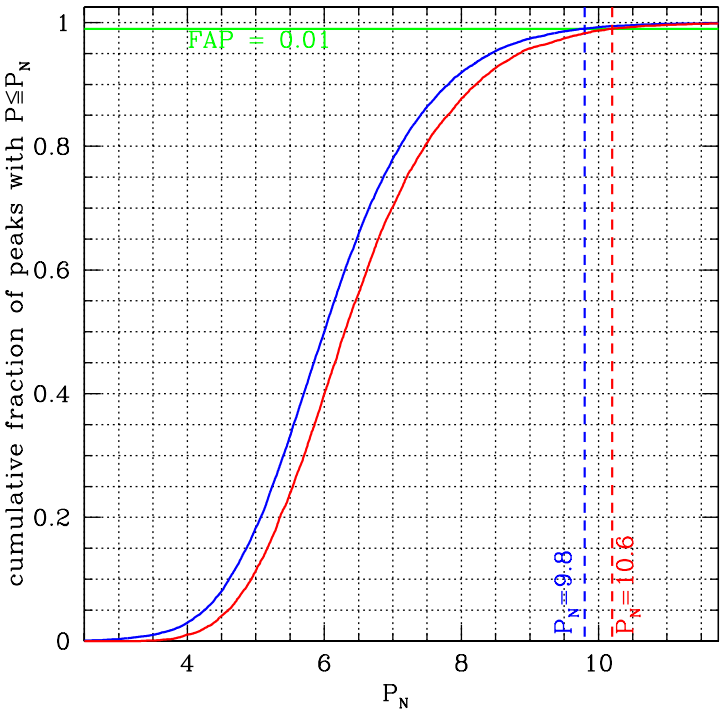

Fig. 4.2: The cumulative power distribution of the highest peak in the power spectrum for light curves with the time sampling of the 50 sec exposures. The red solid line represents 10000 simulations of Gaussian distributed random variables with zero mean and standard deviation $\sigma = 0.01$ mag. The blue solid line represents 16280 light curves which were generated from measured light curves by randomly reassigning the real dates to the relative magnitudes. The green line represents the 99% level of the distribution, i. e. the 1% FAP level. The blue and red dashed lines indicate the 1% FAP power for the two simulations of non-correlated and correlated data points respectively.

stellar brightness, $m(t)$, of a star at (discrete) epochs $t_1, t_2, ..., t_N$. This discrete data set can be described by $d(t) = m(t)\, s(t)$, where $s(t)$ is the (discrete) sampling function which is equal to zero if $t \neq t_i$ with $i = 1, \ldots, N$ and equal to one otherwise. The observed power spectrum $|D(\nu)|^2$ of the (complex) Fourier transformation of this data set is given by

$$D(\nu) \equiv FT[d] = FT[m\, s] \tag{4.1}$$

$$= \int_{-\infty}^{\infty} M(t)\, W(\nu - t)\, dt \tag{4.2}$$

$$= M(\nu) \otimes W(\nu), \tag{4.3}$$

where $\otimes$ is the convolution operator, $M(\nu) = FT[m]$ is the (complex) Fourier transformation of $m(t)$ and

$$W(\nu) = FT[s] = \int_{-\infty}^{\infty} s(t)\, e^{-2\pi i \nu t}\, dt \tag{4.4}$$

is the *spectral window function* of the data set. Hence, we do not observe the power spec-

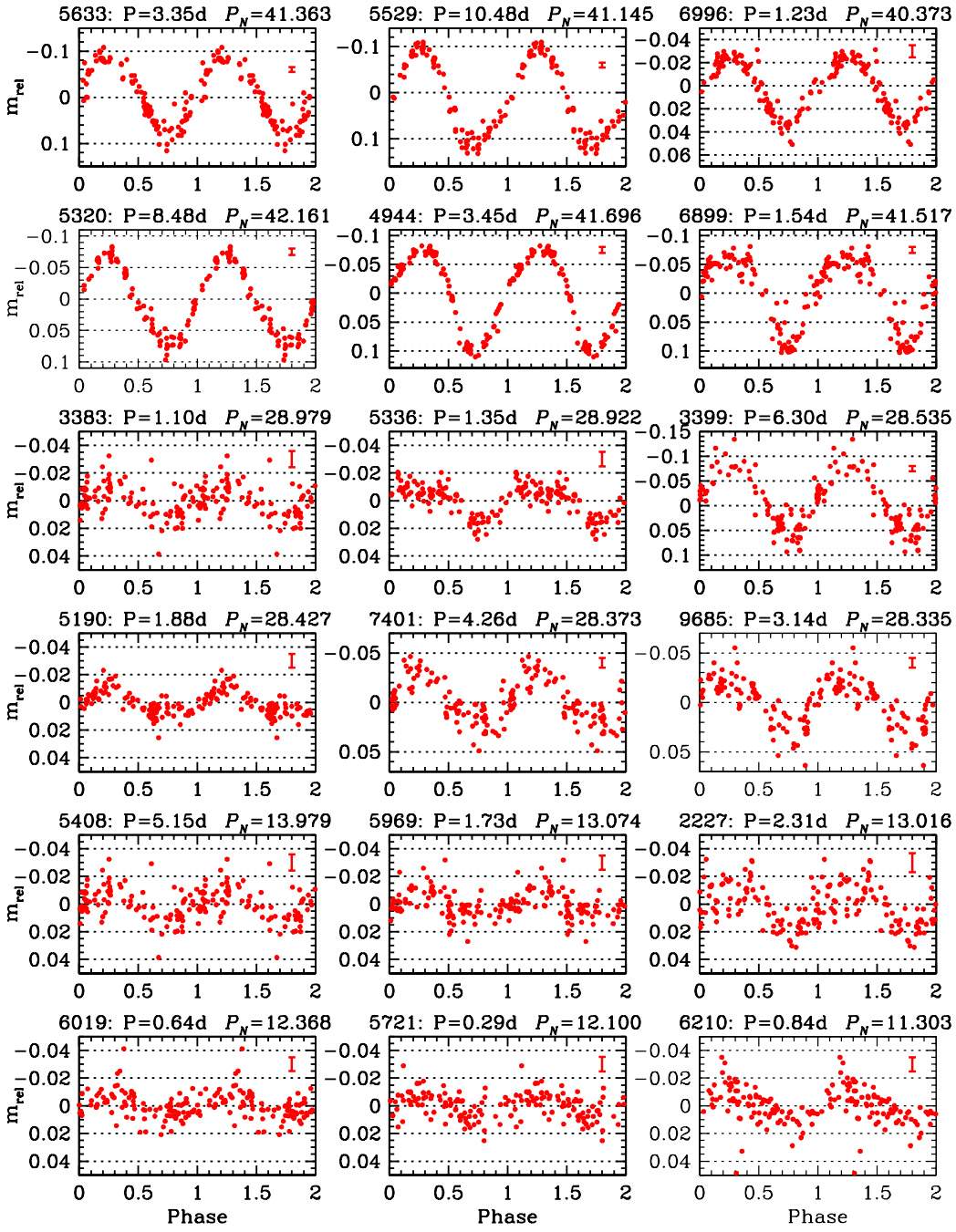

Fig. 4.3: Examples for phased light curves using the period $P_{\rm Scargle}$ found by the Scargle periodogram technique. The peak power P_N in the periodograms of these examples decreases from the upper left to the lower right panel. The examples in the two top rows represent the highest power values ($P_N \simeq 40, \ldots, 42$) I found, the examples in the two middle rows represent median power values ($P_N \simeq 28$) and the lower two rows represent the lowest power values I accepted ($P_N \simeq 11, \ldots, 14$). The peak power P_N, the period $P_{\rm Scargle}$ and the star's identification number are given for each example. The error bar in the upper right corner of each panel indicates the mean photometric error in the light curves.

trum of the continuous signal from the star (i. e. $|M(\nu)|^2 = |FT[m]|^2$). This can have serious consequences for an analysis since the shape of the spectral window function introduces features in the observed power spectrum (see e. g. Brault & White, 1971; Deeming, 1975; Roberts, Lehar & Dreher, 1987). Consider measuring a sinusoidal light curve with frequency ν_s at equally spaced times separated by intervals of Δt over a total time span T. According to Eq. (4.4) this will introduce peaks in the spectral window function at the frequencies $\nu = l/\Delta t$, where l is an integer. The complex Fourier transformation of the signal, $F(\nu)$, consists of delta functions centred at the frequencies $\pm\nu_s$. Thus, the convolution of the window function introduces peaks in the observed spectrum at the frequencies $\nu_p = \pm\nu_s + l/\Delta t$. This effect is called aliasing. For unevenly sampled data $W(\nu)$ can have considerable power at different frequencies which can lead to detections of wrong periods in the observed power spectrum.

Even if the spectral window function is known it is not possible to de-convolve $D(\nu)$ directly. Therefore, Roberts, Lehar & Dreher (1987) modified the CLEAN algorithm that is known from the reconstruction of two-dimensional images from interferometric data. Based on their publicly available Fortran code I have created a *C* realization of the CLEAN algorithm which was used for calculating the CLEAN periodogram for each of the 10554 stars. After the identification of the highest peak in each of these periodograms each light curve was phased with the appropriate period P_{CLEAN}.

In order to compare the results of the Scargle and CLEAN periodogram techniques with each other one has to know the uncertainty in the determined periods. Therefore I first discuss the period error in the following section before I compare the periods resulting from both periodogram techniques.

4.1.3 The Error in the Measured Periods

The uncertainty in a measured period is set by two fundamental limits. First, it is related to the finite frequency resolution of the power spectrum ($\Delta\nu$) which makes it impossible to distinguish between closely separated periods. It is only possible to distinguish between two peaks if they are separated by more than $\Delta\nu/2$ which is therefore equal to the error in the frequency, i.e. $\delta\nu \simeq \Delta\nu/2$. For a discrete data set the frequency resolution $\Delta\nu$ is given by the width of the main peak of the window function $W(\nu = 0)$. If the time sampling is not too non-uniform this is related to the total time span, T, of the observations by $\Delta\nu \simeq 1/T$ (Roberts, Lehar & Dreher, 1987). Since for small errors $\delta\nu/\delta P \simeq \mathrm{d}\nu/\mathrm{d}p = 1/P^2$ the error in the period is given by

$$\delta P \simeq \delta\nu\, P^2 \simeq \frac{\Delta\nu\, P^2}{2}. \tag{4.5}$$

For larger errors (i. e. larger periods) this is only a lower limit on the period error. Second, for very short periods when the finite time span between the data points is comparable to the period the uncertainty in a period is given by the sampling error which is related to the typical spacing between the data points. Both of these fundamental limits leave their footprints in the main peak of the window function.

Since the time sampling of the used light curves is not very uniform (see Fig. 2.3) I estimated the error of the periods directly from the width of this peak for each star separately. Fig. 4.4 shows the main peak of the window function for a typical light curve (i. e. for a star with 88 data points). As indicated by a fit of a Gaussian, the full width at

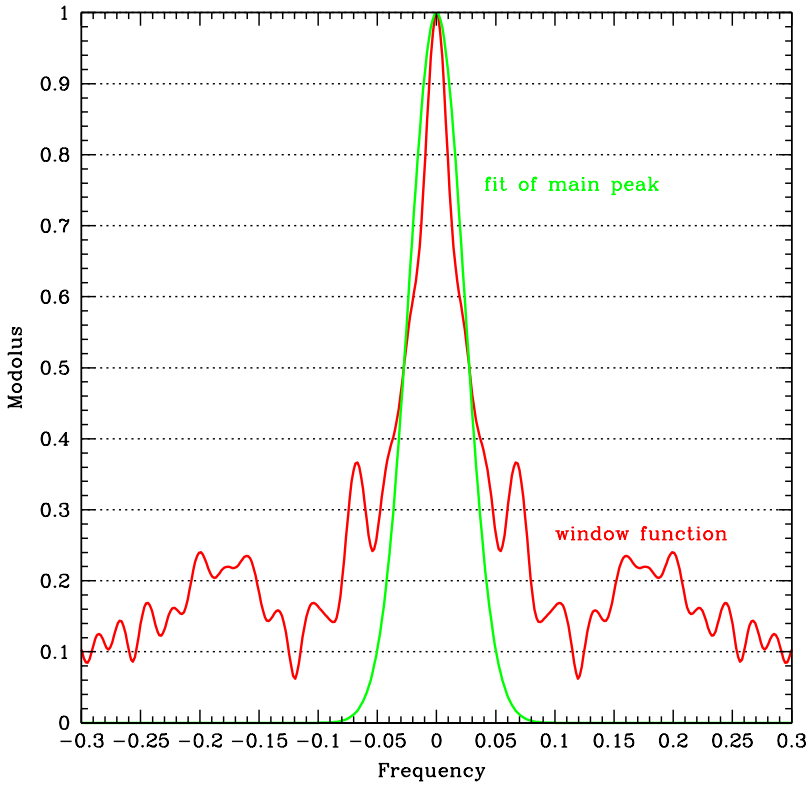

Fig. 4.4: The window function of a typical light curve with 88 data points (red curve). The green curve is a Gaussian (normalised to have a modulus of 1 at $\nu = 0$) with zero mean and standard deviation $\sigma = 0.015$/day. This latter function represents a fit of the main peak of the window function. The corresponding full width at half maximum of the main peak is $\nu_{FWHM} = 0.0521$/day.

half maximum of this main peak is $\nu_{FWHM} = 0.0521$/day which is 3.3 times larger than what one would expect from the total duration of the observations. This can be explained by the non-uniform sampling. For a light curve with 88 data points I finally assigned an error to the period P which is given by $\delta P = 0.026 \times P^2$. For light curves with less data points the factor differs depending on the width of the main peak of the appropriate window function.

4.1.4 Final Period Determination

For all of the 1192 stars which have a normalised peak power in the Scargle periodogram of $P_N \geq P_{\mathrm{FAP}=1\%}$ (i. e. FAP $\leq 1\%$) both the light curve and the light curves phased with the periods found by both periodogram techniques were checked by eye and obvious wrong detections (e. g. due to light contamination from a close-by neighbour) were rejected from the further analysis.

I also only accepted periods if they are larger than a fundamental lower limit. The highest frequency which may be recovered from a sample with data points spaced at intervals of Δt is the Nyquist frequency $\nu_{\mathrm{N}} = 1/(2\Delta t)$ (e. g. Roberts, Lehar & Dreher,

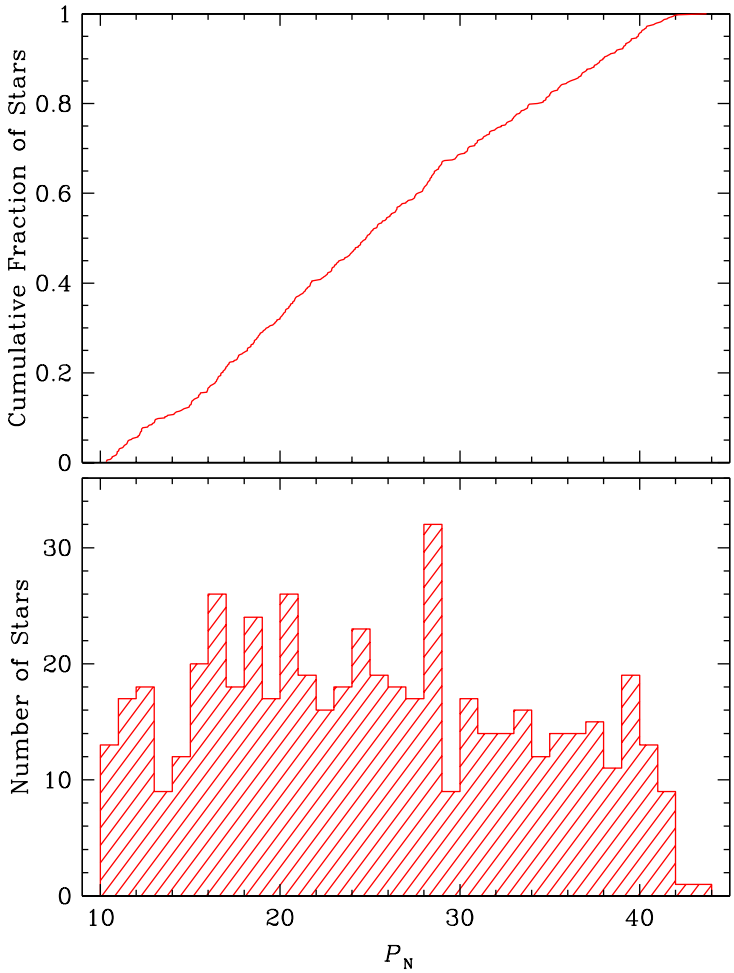

Fig. 4.5: The cumulative distribution (top panel) and the histogram (bottom panel) of the normalised highest peak power P_N of all 543 periodic variable stars.

1987). Since the median time difference of the data points in the light curves is $\Delta t = 0.107\,\mathrm{day}$ I accepted only periods with

$$P \geq \frac{1}{\nu_{\mathrm{N}}} = 2\,\Delta t = 0.21\,\mathrm{day}. \tag{4.6}$$

However, nearly all of the rejected stars were rejected because of obvious wrong detections and only about 10-15 stars were rejected because of failing the criterion given by Eq. (4.6). In total I found 543 periodically variable stars. These stars are marked in Table 3.5 with a *pv* in the column "*vari*". For 520 (95.8%) of these periodic variables, the periods determined with the two different periodogram techniques agree within the estimated errors. In all cases where the periods determined with both methods did not agree, the two periods were beat periods of each other and I assigned one of the two periods to those stars. I always choose the period for which the scatter in the phased light curve was lowest. For 17 of these 23 stars I assigned the CLEAN period but the Scargle period was kept in six cases.

The periodic variables I found are not necessarily PMS stars and I will check the PMS nature of these stars later in Sect. 5. Those periodic variables that passed the PMS tests

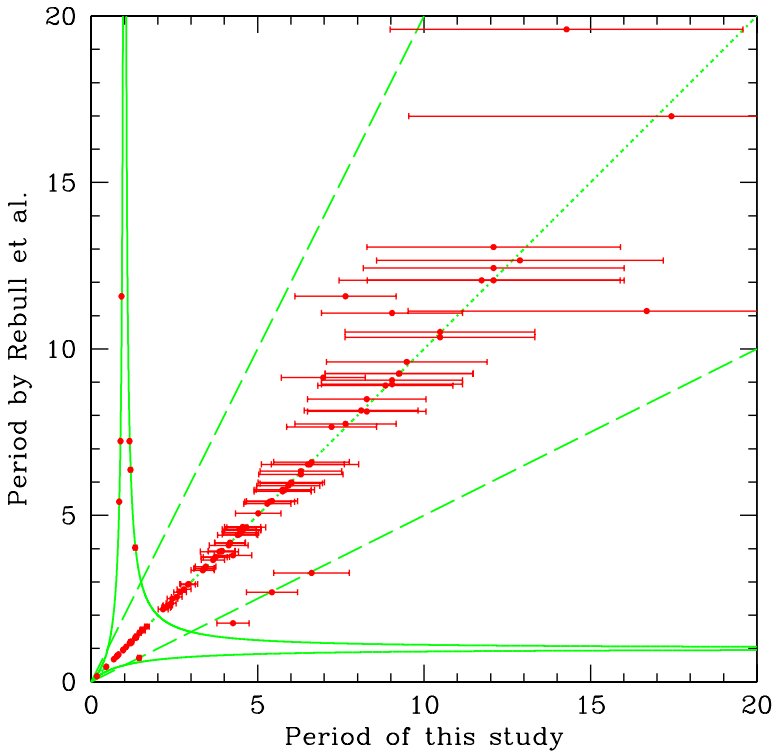

Fig. 4.6: Comparison of periods found in this study with those found by Rebull et al. (private communication). Also shown are the estimated period errors of our periods. Stars with the same period in both studies are located on the doted green line. The dashed lines represent harmonics. The solid green lines represent beat periods, i. e. a relation of $1/\ P_{\rm Rebull} = \mp 1 \pm 1/P$, where P and $P_{\rm Rebull}$ are the periods found by this study and by Rebull et al. respectively.

are listed in Tab. 5.2 while those periodic variables that did not pass the PMS tests are listed in Tab. D.1 in the Appendix D. Out of the 543, stars 501 (91.9%) have a peak power in the Scargle periodogram of $P_N \gtrsim 12.40$ which corresponds to a FAP of $\lesssim 0.1\%$. Fig. 4.5 shows the histogram and the cumulative distribution of P_N for all 543 stars.

The locations of the periodic variables in the observed field are shown together with the positions of irregular variables (see below) in Fig. 4.8. Their distribution shows that there are two concentrations of young stars in NGC 2264 which I call NGC 2264 N (north) and NGC 2264 S (south). The stars located in these two concentrations will be used in Sec. 5.1 to determine the region in the colour-magnitude diagram where the PMS stars are located.

Out of the stars which were rejected after the visual inspection another 136 were classified as possible periodic variables. These stars are marked with a *pv?* in the column "*vari*" of Tab. 3.5 but are not listed in Tab. 5.2 (or Tab. D.1), because they are not used for any further analysis.

I have compared the results of my period study with unpublished periods measured by Rebull et al. (private communication). I could identify 104 periodic variables from my study study which were also periodic variable according to Rebull et al. Fig. 4.6 shows a

comparison of these periods determined in both studies. It is evident that 87 of the periods (84%) agree within the estimated errors. The periods which do not agree are in most of the cases beat periods of each other or differ by a factor of 0.5 (i. e. $P_{\rm Rebull} = 0.5 \times P$). These latter periods are called harmonics. The beat periods are due to the first side peak in the window function of the data set which is located at about 1 day since the observations are done more or less in a daily cycle. The resulting beat periods of $1/P_{\rm beat} = \pm 1 \mp 1/P$ are indicated in Fig. 4.6 by the green solid lines.

I note that always the periods of my study are used for the further analysis because my time series are less evenly sampled than the time series of Rebull et al. and therefore the impact of the beat phenomenon on my analysis should be smaller. In addition, the CLEAN algorithm takes the data sampling into account and provides a more reliable period determination.

4.2 Irregular Variables

Many of the PMS stars this study show non-periodic brightness modulations with peak-to-peak variations up to 1 mag. Here I define any variable star for which no period could be detected as an irregular variable. All stars which are not periodically variable were tested for this irregular variability using a χ^2 test which is described in the following.

4.2.1 The Chi-Square Test

Only stars which are brighter than $I_{\rm C} = 19.5$ mag (i. e. S/N per single measurement ≥ 30) and have at least 20 data points in their light curve were tested for irregular variability. In addition, stars with close neighbours were rejected from this analysis because the fixed-size aperture could lead to seeing-dependent overlapping with a (bright) neighbour, and hence imitate variability. Since the impact of a faint neighbour is negligible I used a rejection criterion that is magnitude dependent: If two stars were separated by less than $2\farcs5$ from each other, both of them were rejected from the analysis if the magnitude difference between the two objects was less than 2.0 mag. If the magnitude difference of such two stars was larger than 2.0 mag only the fainter star was removed and the brighter stars was kept.

In total 5927 non-periodic stars were analysed and 90.6% of these stars have more than 70 data points in the light curve. For detecting the irregular variables I used a χ^2 test, in which one calculates the probability that the deviations in the light curve are consistent with the photometric errors, i.e the probability that the star is not variable. Therefore one evaluates

$$\chi^2 = \sum_{j=1}^{N} \left(\frac{m_{\rm rel}(j)}{\delta m_{\rm rel}(j)} \right)^2 \tag{4.7}$$

where $m_{\rm rel}(j)$ and $\delta m_{\rm rel}(j)$ are the (mean subtracted) relative magnitude and the error of the jth data point in the light curve of a star respectively. The probability that the light curve of a non-variable star with N data points results in a value for chi-square that

exceeds the measured value χ^2 is given by [1] (Press et al., 1992)

$$Q(\chi^2|N) = \frac{\Gamma\left(\frac{N-1}{2}, \frac{\chi^2}{2}\right)}{\Gamma\left(\frac{N-1}{2}\right)} \equiv \frac{\int_{\chi^2/2}^{\infty} t^{(N-3)/2} e^{-t} dt}{\int_0^{\infty} t^{(N-3)/2} e^{-t} dt}. \quad (4.8)$$

The probability $p_{\rm vari}$ that the star is variable is therefore $p_{\rm vari}= 1 - Q(\chi^2|N)$.

4.2.2 Error & Aperture Correction

I note that the χ^2 test is very sensitive to an over- or underestimation of the errors. For example if the error in the single measurements is underestimated by a factor of 2 the value for χ^2 is overestimated by a factor of 4 and we therefore deduce a overestimated probability $p_{\rm vari}$ that the star is variable. In order to check whether the errors in the light curves are over- or underestimated I made a comparison of the scatter σ and the average of the errors $\overline{\delta m_{\rm rel}} = (1/N) \sum_{j=1}^{N} \delta m_{\rm rel}$ in the light curves, where $\delta m_{\rm rel}$ is given by Eq. (3.7).

In Fig. 4.7 I show the scatter (σ) and the mean photometric error ($\overline{\delta m_{\rm rel}}$, see also Fig. 3.1) in the light curve of each star for the different exposure times. For both quantities I have determined the median in different $I_{\rm C}$ magnitude bins. Both medians were fitted by a two component fit: In both cases I fitted an exponential function in the fainter regime and a constant in the brighter regime. The blue dotted line for each exposure time is the fit $M(I_{\rm C})$ of the median of $\overline{\delta m_{\rm rel}}$. The solid blue line represents the fit $S(I_{\rm C})$ of the median of σ. Analytical equations of the fitting functions $S(I_{\rm C})$ and $M(I_{\rm C})$ for the different exposure times are given in Appendix A.

It is evident that the estimated errors $\delta m_{\rm rel}$ are systematically underestimated for each of the three different exposure times. Therefore I corrected the errors measured for each star by calculating the ratio of the two functions for each of the three exposure times to give a correction function $C(I_{\rm C}) = S(I_{\rm C})/M(I_{\rm C})$. The photometric error of each data point in the light curve of a given star was corrected using the equation

$$\delta m_{\rm rel,cor}(j) = C(I_{\rm C})\ \delta m_{\rm rel}(j) \quad (4.9)$$

where I applied the mean $I_{\rm C}$ magnitude of the star (Sec. 3.3) to $C(I_{\rm C})$. By correcting the errors in this way I ensure that the relative distribution of the errors in a given light curve is conserved.

Note that I used a conservative fit for the standard deviation in the sense that the standard deviation may be overestimated by the fit (see Fig. 4.7). Since the same is the case for the fit $M(I_{\rm C})$ of the mean errors this effect is minimised (but maybe not completely canceled) for the ratio $C(I_{\rm C}) = S(I_{\rm C})/M(I_{\rm C})$. However, a conservative estimate of the true error reduces the false detections of the χ^2-test. On the other hand the test is less sensitive for low amplitude variations.

From Eq. (4.7) it is clear that a single outlier in the light curve (e. g. caused by a cosmic ray) could produce a very high value for the χ^2. Since I was looking only for persistent variability I have applied a sigma clipping algorithm to the light curves before the χ^2-test was performed. This algorithm uses the standard deviation σ of a given light curve and removes all data points from this light curve that are located more than 2.5σ

[1] Since the time series has been mean subtracted the number of degrees of freedom is N-1.

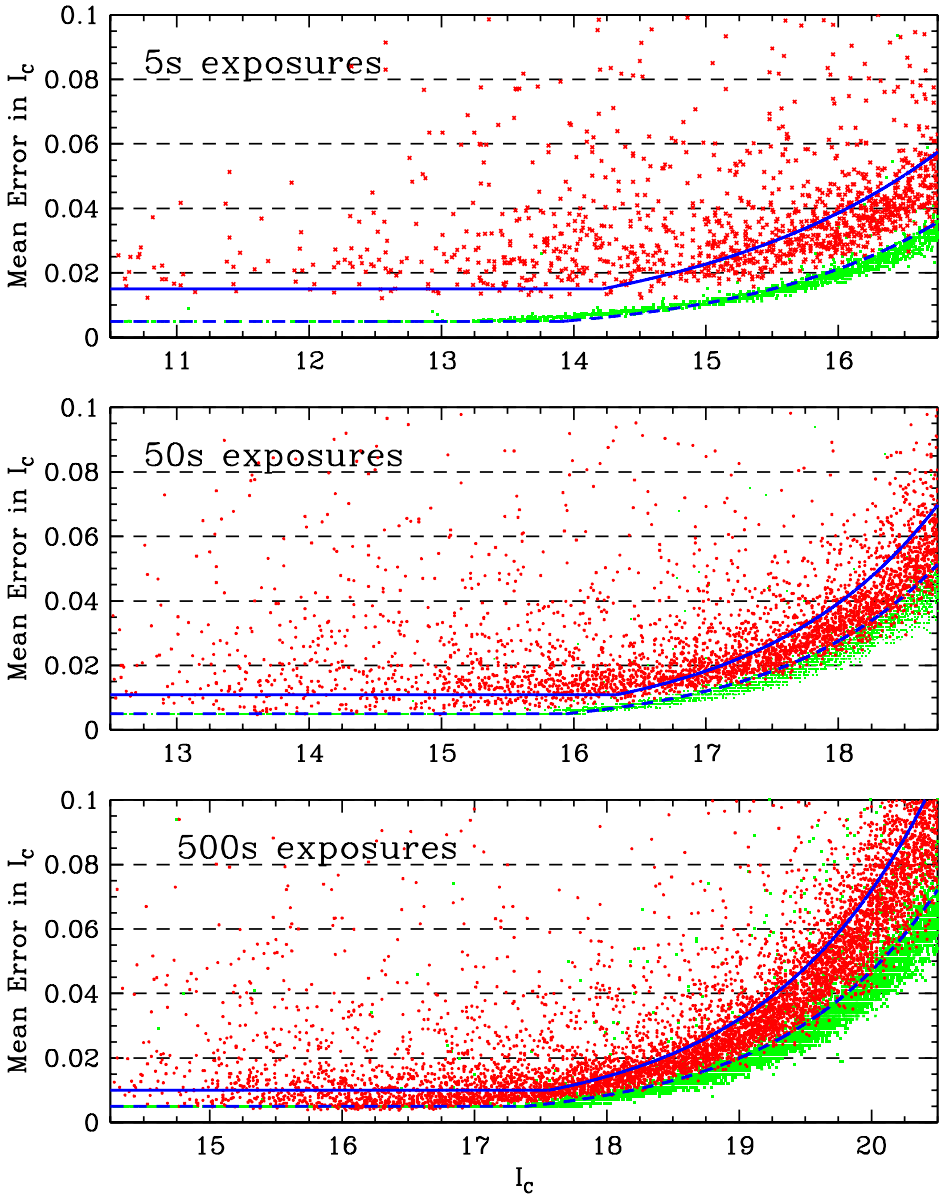

Fig. 4.7: Standard deviation σ (red dots) and the mean of the photometric errors $\overline{\delta m_{\mathrm{rel}}}$ (green dots, see also Fig. 3.1) in the light curve of each star as a function of magnitude. For each of the three exposure times the solid blue line represents a two component fit ($S(I_{\mathrm{C}})$) to median values of σ while the dashed blue line represents a two component fit ($M(I_{\mathrm{C}})$) of the median of the mean photometric error $\overline{\delta m_{\mathrm{rel}}}$. The medians for both quantities were calculated in equally spaced magnitude bins.

above or below zero (note that the mean value was subtracted from the light curves). The resulting standard deviation in the light curve is listed for of each star in Tab. 3.5.

After all stars had been analysed I found that many of the detected variable stars are located in the corners of our field. The light curves of these stars looked very similar and were well correlated with the changing seeing. A possible explanation for this is that the pixel scale of the WFI is different in the corners of the field. A similar result was recently found by Koch et al. (private communication) for the WFI. This leads to variations in the photometry of the stars located in the corners because the flux in the aperture of these stars changes with the seeing in a different way from the flux in the apertures of the comparison stars (the latter are not located in the corners, see Sec. 3.2). As a result the relative magnitudes of the stars in the corners become fainter for worse seeing. Therefore non-variable stars can mimic variability. In order to avoid this problem I performed the relative photometry again in exactly the same way as described in Sec. 3.2 but this time a significantly larger aperture diameter of 20 pixels ($4\farcs76$) instead of 8 pixels was used. In this way it was made sure that much more of the star's light falls into the aperture and the measurement is much less dependent on the seeing, i. e. the photometric errors dominate the changes due to seeing variations. The errors in the relative magnitudes were corrected in the same way as described above. The correction functions employed are also given in Appendix A.

4.2.3 Identification of Irregular Variables

In order to decide whether any star in the whole observed field is irregular variable I used the results of the χ^2-tests based on the measurements with both aperture sizes. Only the stars that have a probability of $p_{\rm vari} \geq 99.9\%$ in *both* tests were assumed to be irregular variable. I used both aperture sizes and not only the measurements with the larger aperture because with the large aperture the probability that the measurement of the stellar brightness is contaminated by the light of a close neighbour was increased and the star can therefore mimic variability with the changing seeing. This effect is minimised for the photometry with the smaller aperture radius. On the other hand stars that do mimic variability because of the variable pixel scale do not pass the χ^2-tests based on the measurements with a bigger aperture radius. Hence, a star that passes both tests is not affected by the variable pixel scale and light contamination from a close-by neighbour and therefore the variability is intrinsic to the star.

In total I found 484 irregular variables out of the analysed 5927 non-periodic stars. The irregular variables are listed in column "*vari*" of Table 3.5 as *iv*. The spatial positions of the irregular variable stars are shown in Fig. 4.8. I remind the reader that irregular variables are defined here as variables with $p_{\rm vari} \geq 99.9\%$ for which I could not find any significant period in the periodograms.

With the χ^2 test I am able to detect variability for stars brighter than $I_{\rm C} \leq 17.5$ mag if the standard deviation σ in the light curves is larger than 0.02 mag. Since I used images with 500 sec exposure time for stars fainter than $I_{\rm C} \leq 16.0$ mag, the sensitivity of the χ^2 test is somewhat better for stars with 16.0 mag $\leq I_{\rm C} \leq 17.25$ mag. In this magnitude range I am able to detect irregular variability for stars with $\sigma \geq 0.015$ mag. For stars with $I_{\rm C} = 18$ mag I am able to detect variability if $\sigma \geq 0.03$ mag. The sensitivity for stars fainter than $I_{\rm C} = 18$ mag decreases as it is indicated by Fig. 4.7.

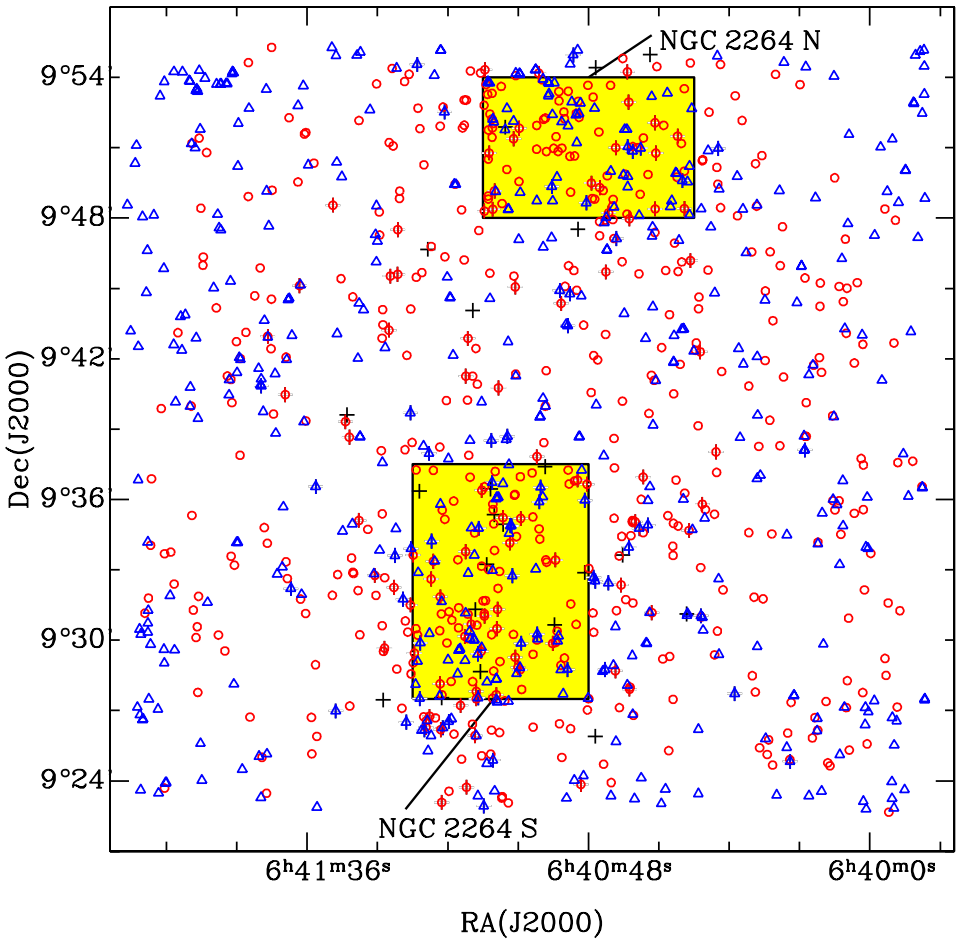

Fig. 4.8: The locations of all 543 periodic (red ◯) and 484 irregular (blue △) variables from our survey (including non-PMS stars). Those variable stars which were previously known as PMS stars are indicated by a vertical red or blue line (◯, △ respectively) while previously known PMS members which are not periodic or irregular variable according to my investigations are marked by a black cross (+). The two regions NGC 2264 N & S with the highest concentration of (periodic) variables are marked by the yellow boxes.

Only 48.3% of the periodically variable stars are variable according to the χ^2-test. It is not surprising that not all periodic variable stars are variable according to this test because the periodogram analysis is much more sensitive to low amplitude variations than the χ^2 test (see Sec. 6). Furthermore relatively conservative errors were adopted for the χ^2 test. This also decreases the sensitivity to small amplitude variations.

I note that the different pixel scale in the corners of the field has only weak or no effect on the results of our periodic variability study. Since the seeing changes randomly, this contributes to all powers in the power spectrum and not only to a single peak. Only about 5–10 periodic variable stars are located in the affected regions of the field. However, the variations in the corners of the field might have caused me to miss detecting a small number of periodic variables.

Chapter 5

Variable PMS Members

The periodic and irregular variable stars I found in the observed field are not necessarily all PMS stars and therefore I had to disentangle variable PMS stars from variable background or foreground stars. This was done in two steps, namely using first the I_C vs $(R_C - I_C)$ colour-magnitude diagram (CMD) and second the $(R_C - H\alpha)$ vs $(R_C - I_C)$ colour-colour diagram. These two tests were applied to *all* variable stars regardless of whether they are periodic or irregular variable. In the following subsections I describe the two discrimination procedures in detail.

5.1 PMS test I: The Colour-Magnitude Diagram and Determination of the PMS Region

In a CMD the PMS stars are located in a region above the main sequence (MS). This is due to their larger stellar radii and correspondingly larger brightness compared to MS stars of the same spectral type or colour (see Sect. 1.1). In order to determine the borders of the PMS region in the observed CMD I placed a well-defined sample of PMS stars in the CMD. This sample was selected in such a way that it is contaminated as little as possible by background and foreground stars. It consists of two subsamples:

1. previously known cluster members selected from the catalogues of Park et al. (2000) and Sung, Bessel & Lee (1997) and

2. a well selected subsample of the newly found periodic and irregular variables.

The second subsample consists of the newly found periodic and irregular variables located in the two dense concentrations of periodic variables in the cluster. These two concentrations are called NGC 2264 N & S and are marked in Fig. 4.8. The two regions are a part of the so called "on cloud region" defined by Rebull et al. (2002) based on the physical projected position of a star compared with the background dark cloud in order to limit their sample "more effectively to actual cluster members".

Determining the borders of the PMS region in the CMD only from the variable stars in NGC 2264 N & S (and previously known members) has the advantage of a maximum fraction of PMS stars relative to any background stars. This is due to high extinction of the dust located behind the cluster stars (Herbig, 1954; Walker, 1956). This is shown by

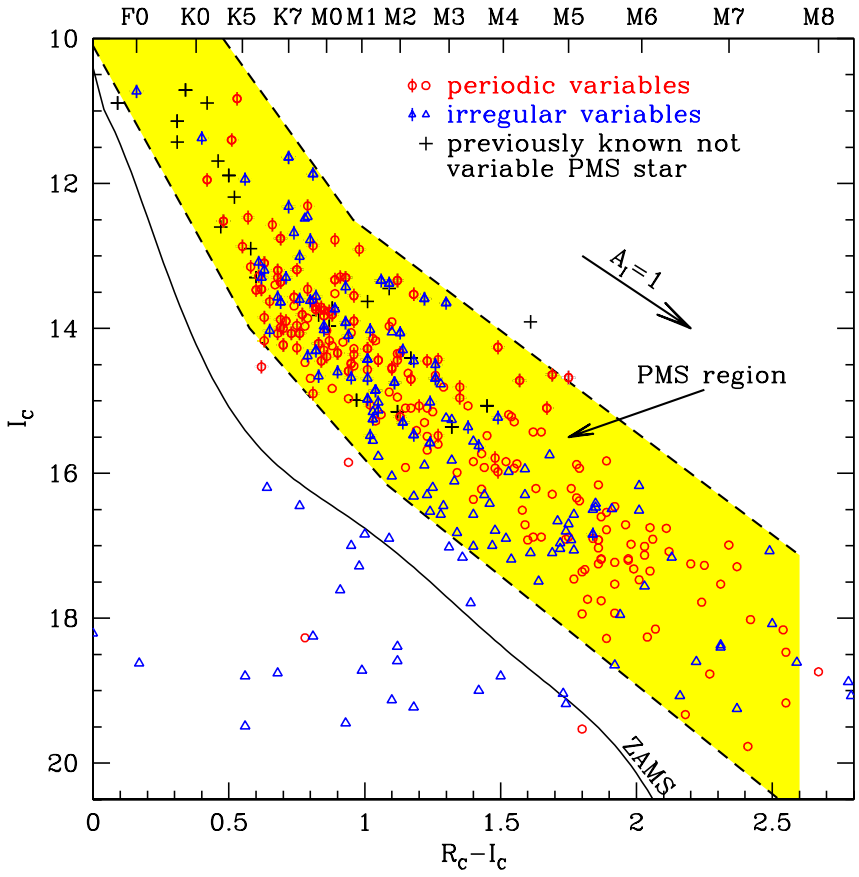

Fig. 5.1: Determination of the PMS region in the CMD. Only the variables in NGC 2264 S & N (see Fig. 4.8) and all previously known PMS stars in the whole NGC 2264 field are plotted. The symbols are the same as in Fig. 4.8. The two dashed lines indicate the deduced lower and upper borders of the PMS region. The indicated reddening vector for $A_{I_C} = 1$ assumes $R_V = 3.1$. The spectral types indicated at the top are derived from the colours of ZAMS stars (see Appendix C for further details).

Fig. 5.4 which also illustrates that in particular for NGC 2264 S a very large background extinction is present. Since I selected only *variable* stars located in these regions the contamination of this subsample by (non-variable) MS foreground stars is also negligible. Therefore the selected variable stars in the two regions NGC 2264 S and N are most likely PMS cluster members.

The CMD of all variable stars in NGC 2264 N & S and all previously known PMS stars in the whole NGC 2264 field is shown in Fig. 5.1. From this plot I defined the PMS region in the CMD by placing an upper and lower border in the the CMD in such a way that most of the stars of the selected sample are inside of the defined region. The lower and upper borders of this region are indicated by the dashed lines. The equations for these border lines are given in Appendix B.

The defined PMS region will obviously eliminate MS stars which are at the same distance as NGC 2264 or further away. Such stars are located in the CMD at or below

the ZAMS indicated in Fig. 5.1 and are therefore well outside the PMS region. Because of their larger apparent I_C magnitude, foreground MS stars with a distance between ~ 300 pc and ~ 600 pc could be located in the PMS region (the distance of NGC 2264 is about 760 pc). However, as already mentioned above the contamination with these stars is probably negligible.

On the other hand it is *not possible* to discriminate between variable PMS stars and variable background giants using the PMS region in the CMD. K or M giants are typically between 3 and 10 magnitudes brighter than PMS stars at the same distance with the same spectral type. Therefore, background giants with a corresponding smaller apparent I_C magnitude could be located in the PMS region of Fig. 5.1. Since the reddening vector is nearly parallel to the borders of the PMS region even these (highly) reddened giants will stay in the PMS region. In addition several types of giants are variable (e. g. RR Lyrae stars) and therefore it is necessary to eliminate these stars from the sample of variable stars using a different selection criterion. This will be done in Sect. 5.2

Of the 543 periodic variable stars I found in the whole NGC 2264 field, 451 stars were located in this PMS region and only these stars were used for the further analysis. These numbers together with the few (only 3) periodic variables outside the PMS region in Fig. 5.1 confirm that the regions NGC 2264 S & N are very little contaminated with foreground or background MS stars compared to the rest of the observed field. That furthermore indicates that the above described procedure to define the PMS region in the CMD provides relatively reliable borders.

5.2 PMS test II: The $(R_C - H\alpha)$ vs $(R_C - I_C)$ Colour-Colour Diagram

As outlined in the previous section it is essential to eliminate background giants from the sample of variables I found. Therefore I used the location of the stars in the $(R_C - H\alpha)$ vs $(R_C - I_C)$ colour-colour diagram (Fig. 5.2) as the second selection criterion for classifying a star as a PMS star, i. e. all stars which passed the first test have also to pass the second one to be classified as a PMS star. Many PMS stars, in particular CTTSs, show large $H\alpha$ emission. Thus their $(R_C - H\alpha)$ colour is larger than the $(R_C - H\alpha)$ colour of a MS star of the same spectral type. There also exist WTTSs or "naked" TTSs with weak or no detectable $H\alpha$ emission (e.g. see Appenzeller & Mundt, 1989). The locus of these latter stars is similar to the MS in the $(R_C - H\alpha)$ vs $(R_C - I_C)$ colour-colour diagram. Here I call this locus the PMS/MS locus (Fig. 5.2).

On the other hand giants with spectral types later than ~K3 have smaller $(R_C - H\alpha)$ colours than MS stars of the same $(R_C - I_C)$ colour. The differences in $(R_C - H\alpha)$ between giants and PMS/MS stars result from stronger molecular bands in the giants' spectra causing different spectral energy distributions in the R_C band. In addition giants are typically at larger distances and are therefore highly reddened. Since reddening affects mainly the $(R_C - I_C)$ colour they are shifted further away (i. e. to the right) from the slightly increasing PMS/MS locus with increasing distance. This behaviour was confirmed by a simulated colour-colour diagram: As a test I created a $(R_C - H\alpha)$ vs $(R_C - I_C)$ colour-colour diagram using simulated stars which were obtained by multiplying the filter transmission curves of the WFI with the spectral energy distribution of standard spectra for stars of different spectral type and luminosity class.

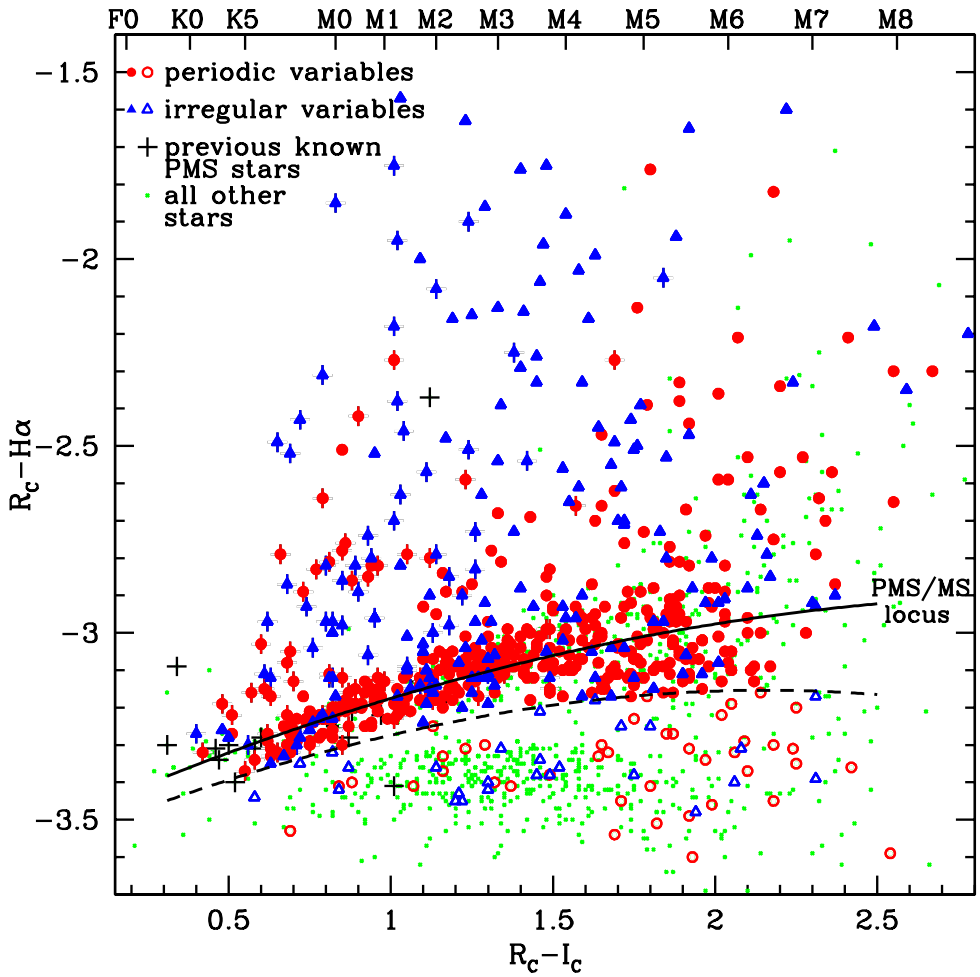

Fig. 5.2: The $(R_C - H\alpha)$ vs $(R_C - I_C)$ colour-colour diagram for all stars (including non-variables) which passed the first PMS test. Red circles and blue triangles represent periodic and irregular variables respectively. Filled symbols indicate the stars which passed both PMS tests. Variables which were previously known as PMS are indicated by a vertical line. Non-variable previously known PMS stars are indicated by a cross. The solid line represents the fit of the locus stars with no or weak $H\alpha$ emission. Variable stars below the dashed line (open symbols) were rejected from the further analysis because they are probable background giants.

Therefore it is possible to discriminate between (background) giants and PMS stars using the $(R_C - H\alpha)$ vs $(R_C - I_C)$ colour-colour diagram because the giants are located below the PMS/MS locus in that diagram. I determined the median $(R_C - H\alpha)$ colour as a function of $(R_C - I_C)$ for PMS/MS locus stars using the data shown in Fig. 5.2. The median was calculated in different $(R_C - I_C)$ colour bins of 0.05 magnitude width using a sigma clipping algorithm after extreme values were removed from this diagram. In Tab. 5.1 I list the median $(R_C - H\alpha)$ colour as a function of $(R_C - I_C)$ for the stars on the PMS/MS locus. I have fitted a quadratic function to these medians and obtained a locus relation of the form

$$(R_C - H\alpha)_{\rm locus} = -0.061\times (R_C - I_C)^2 + 0.382\times (R_C - I_C) - 3.497. \qquad (5.1)$$

This relation is shown in Fig. 5.2 as the solid line. In order to discriminate between PMS stars and background giants I defined a lower discrimination level which shown in Fig. 5.2

Tab. 5.1: The relation between $(R_C - I_C)$ and $(R_C - H\alpha)$ colours for PMS/MS locus stars. The listed $(R_C - H\alpha)$ colours are the median values calculated in bins of 0.05 mag width. σ is the standard deviation of the $(R_C - H\alpha)$ colours (relative to the median) in each bin.

$(R_C - I_C)$	$(R_C - H\alpha)$	σ	$(R_C - I_C)$	$(R_C - H\alpha)$	σ	$(R_C - I_C)$	$(R_C - H\alpha)$	σ
0.38	-3.36	0.05	0.98	-3.22	0.05	1.58	-3.06	0.10
0.43	-3.33	0.04	1.03	-3.20	0.06	1.63	-3.04	0.10
0.48	-3.33	0.05	1.08	-3.17	0.06	1.68	-3.05	0.10
0.53	-3.34	0.05	1.13	-3.16	0.07	1.73	-3.02	0.12
0.58	-3.30	0.04	1.18	-3.13	0.07	1.78	-3.03	0.13
0.63	-3.30	0.06	1.23	-3.12	0.08	1.83	-2.99	0.15
0.68	-3.30	0.05	1.28	-3.10	0.08	1.88	-3.02	0.11
0.73	-3.26	0.04	1.33	-3.10	0.07	1.93	-3.02	0.14
0.78	-3.24	0.04	1.38	-3.08	0.08	1.98	-2.92	0.15
0.83	-3.22	0.06	1.43	-3.09	0.07	2.03	-3.03	0.11
0.88	-3.24	0.05	1.48	-3.07	0.10	2.08	-2.89	0.13
0.93	-3.22	0.06	1.53	-3.07	0.10	2.13	-2.87	0.20

as a dashed line. This line is intended to represent the lower envelope of the PMS/MS locus and is given by

$$(R_C - H\alpha)_{\rm low} = (R_C - H\alpha)_{\rm locus} - 1.65 \times \delta s, \tag{5.2}$$

where δs is a exponential fit of the standard deviation (σ, see Tab. 5.1) of $(R_C - H\alpha)$ in each $(R_C - I_C)$ bin and is given by

$$\delta s = e^{0.60\,(R_C - I_C) - 3.42}. \tag{5.3}$$

If the $(R_C - H\alpha)$ colours of the locus stars are Gaussian distributed in each bin, the factor 1.65 in Eq. (5.2) means that 95% of the locus stars are located above the lower discrimination level. Therefore the intention that the dotted line in Fig. 5.2 represents a lower envelope of the PMS/MS locus is fulfilled. Any variable star (periodic or irregular) which passed the first selection criterion described in Sect. 5.1 and that is located above this level is kept for the final analysis while stars below this level are rejected.

Of the 451 periodic variable stars that passed the first selection criterion another 46 were rejected because of their $(R_C - H\alpha)$ colour, i. e. due to this second PMS test. I finally have a total of 405 periodic and 184 irregular variables (with $p_{\rm vari} \geq 99.9\%$) which are all very likely PMS members of the NGC 2264 star forming region. Hence, I call these stars variable PMS members. The periodic and irregular variable PMS members are listed in Tab. 5.2 and Tab. 5.3 respectively. Those periodic variables which did not pass both PMS tests are listed in a separate Tab. D.1 in the Appendix D.

Tab. 5.2: All 405 periodic variable stars that passed both PMS tests and are therefore assumed to be genuine PMS stars. Listed is for each star the identification number, period obtained from the Scargle periodogram, $P_{\rm Scargle}$, the period obtained from the CLEAN periodogram, $P_{\rm CLEAN}$, the period determined by Rebull et al. (private communication), $P_{\rm Rebull}$, if available, the period finally adopted, $P_{\rm adopt}$, the error of this period, δP, the probability,$p_{\rm vari}$, that the star is variable deduced from the χ^2 test, and the estimated peak-to-peak variation in the $I_{\rm C}$ band ($\Delta m_{\rm ptp}$, see Sect. 6.1). All listed periods are given in days.

Star	$P_{\rm Scargle}$	$P_{\rm CLEAN}$	$P_{\rm Rebull}$	$P_{\rm adopt}$	δP	$p_{\rm vari}$	$\Delta m_{\rm ptp}$	$\Delta(R_{\rm C}-{\rm H}\alpha)$
71	1.36	1.36	1.36	1.36	0.05	1.000	0.11	0.02
249	2.14	2.14	.....	2.14	0.13	0.273	0.03	0.02
503	20.09	19.62	.....	20.09	11.03	6.778e−03	0.02	0.10
616	2.44	2.41	2.50	2.44	0.16	1.000	0.17	0.26
731	0.95	0.95	.....	0.95	0.02	0.390	0.04	0.19
1025	1.29	1.29	.....	1.29	0.04	1.000	0.05	0.01
1146	1.56	1.56	.....	1.56	0.07	0.205	0.03	0.09
1168	9.04	9.10	.....	9.04	2.12	0.998	0.05	0.03
1177	3.92	3.92	3.92	3.92	0.40	1.000	0.07	-0.00
1211	1.81	1.80	.....	1.81	0.09	0.049	0.03	0.12
1316	4.55	4.55	4.65	4.55	0.54	0.675	0.03	0.32
1317	10.31	10.29	.....	10.31	2.76	1.000	0.05	0.01
1473	0.82	0.82	0.82	0.82	0.02	1.000	0.07	0.01
1476	3.73	3.74	.....	3.73	0.36	1.000	0.10	0.04
1490	1.29	1.29	.....	1.29	0.05	0.935	0.04	0.03
1573	6.30	6.28	.....	6.30	1.03	1.000	0.10	0.07
1698	3.16	3.15	.....	3.16	0.26	1.000	0.28	0.03
1704	8.28	8.26	8.12	8.28	1.78	1.000	0.11	0.23
1743	0.78	0.78	.....	0.78	0.02	1.600e−04	0.03	0.08
1748	6.21	6.17	.....	6.21	1.31	1.000	0.05	-0.04
1792	7.22	7.22	7.66	7.22	1.35	1.000	0.06	0.06
1944	1.66	1.66	.....	1.66	0.08	2.000e−06	0.02	0.06
1968	0.96	0.96	0.95	0.96	0.02	1.000	0.29	-0.04
2024	3.73	3.71	3.74	3.73	0.36	1.000	0.07	0.06
2027	5.43	5.41	2.69	5.43	0.77	1.000	0.08	0.05
2204	0.92	0.92	.....	0.92	0.02	1.000	0.05	-0.00
2205	11.73	11.84	.....	11.73	3.81	1.000	0.17	0.05
2219	10.48	10.29	.....	10.48	2.85	1.000	0.05	-0.02
2227	2.31	2.31	.....	2.31	0.15	0.921	0.05	0.00
2465	5.02	4.94	.....	5.02	0.77	1.000	0.17	0.04
2558	0.81	0.81	.....	0.81	0.02	0.341	0.03	-0.03
2605	3.47	3.47	.....	3.47	0.34	1.000	0.05	0.01
2608	1.77	1.77	.....	1.77	0.09	0.740	0.03	-0.06
2676	3.63	3.61	.....	3.63	0.36	1.000	0.92	0.62
2734	3.07	3.06	.....	3.07	0.26	0.996	0.03	-0.03
2750	0.78	0.78	0.78	0.78	0.02	1.000	0.14	-0.02
2756	3.94	3.98	.....	3.94	0.60	1.000	0.06	-0.12
2768	26.97	26.16	26.47	26.97	18.90	1.000	0.06	0.02
2829	1.08	1.08	.....	1.08	0.03	1.000	0.05	0.07
2867	1.56	1.56	.....	1.56	0.07	0.241	0.03	0.05
2883	1.56	1.56	.....	1.56	0.07	0.687	0.03	-0.14
2931	2.27	0.69	.....	0.69	0.01	1.000	0.04	0.03
2963	1.03	1.03	.....	1.03	0.03	1.000	0.06	-0.01
2973	3.32	3.34	.....	3.32	0.29	7.000e−06	0.01	0.12
2989	4.77	4.79	.....	4.77	0.61	1.000	0.04	0.06
3013	3.84	3.90	.....	3.84	0.38	0.976	0.03	-0.01
3071	5.75	5.76	5.72	5.75	0.86	1.000	0.13	0.05
3165	0.62	0.62	.....	0.62	0.01	1.000	0.05	0.01
3299	4.72	4.68	.....	4.72	0.56	0.201	0.03	-0.09
3332	3.14	3.14	.....	3.14	0.26	1.000	0.20	0.01
3340	31.23	29.89	.....	31.23	26.37	1.000	1.75	0.39
3379	2.38	2.37	.....	2.38	0.16	6.027e−03	0.04	0.29
3383	1.10	1.10	.....	1.10	0.03	0.916	0.05	0.32
3390	3.96	3.97	.....	3.96	0.41	1.000	0.10	-0.00
3399	6.30	6.34	6.33	6.30	1.23	1.000	0.14	0.01
3421	0.71	0.71	.....	0.71	0.01	6.270e−04	0.02	-0.13
3424	5.29	5.32	5.35	5.29	0.71	0.868	0.03	-0.00

Tab. 5.2:(continued)

Star	$P_{\rm Scargle}$	$P_{\rm CLEAN}$	$P_{\rm Rebull}$	$P_{\rm adopt}$	δP	$p_{\rm vari}$	$\Delta m_{\rm ptp}$	$\Delta(R_C - H\alpha)$
3494	1.14	1.14	.....	1.14	0.03	0.908	0.05	0.09
3512	1.65	1.65	.....	1.65	0.08	0.812	0.03	0.20
3546	12.09	12.07	12.06	12.09	3.80	1.000	0.09	-0.02
3586	3.88	3.88	.....	3.88	0.47	1.000	0.38	0.38
3592	4.55	4.55	4.57	4.55	0.54	1.000	0.19	-0.03
3603	7.49	7.56	.....	7.49	1.49	1.000	0.06	0.03
3612	0.76	0.76	0.76	0.76	0.02	1.000	0.09	0.04
3615	7.22	7.30	.....	7.22	1.35	1.000	0.06	0.01
3636	4.00	1.32	4.03	1.32	0.05	1.000	0.10	0.30
3666	1.09	11.21	.....	11.21	3.27	1.000	0.75	0.37
3734	0.88	0.88	7.23	0.88	0.02	0.988	0.05	-0.01
3736	3.11	3.12	.....	3.11	0.27	1.000	0.25	0.43
3748	12.09	12.31	.....	12.09	3.92	1.000	1.74	0.45
3803	1.76	1.76	.....	1.76	0.09	0.856	0.03	-0.09
3809	4.17	4.19	.....	4.17	0.45	1.000	0.08	0.36
3814	25.24	1.04	.....	1.04	0.03	1.000	0.05	0.05
3874	4.72	4.76	.....	4.72	0.63	0.366	0.02	-0.00
3907	3.44	3.43	3.46	3.44	0.31	1.000	0.08	0.01
3918	0.30	0.30	.....	0.30	0.00	0.995	0.12	1.13
3966	0.76	0.76	.....	0.76	0.02	1.000	0.08	0.03
3972	16.69	16.97	11.14	16.69	7.17	1.000	0.17	0.16
3973	1.04	1.04	.....	1.04	0.03	0.021	0.03	-0.06
4026	2.07	2.07	.....	2.07	0.12	2.120e−04	0.02	0.02
4035	28.94	26.16	.....	28.94	23.65	1.000	1.42	0.04
4048	3.88	3.85	.....	3.88	0.39	1.000	0.07	0.05
4070	3.16	3.20	.....	3.16	0.27	0.000	0.01	0.10
4098	2.71	2.69	.....	2.71	0.19	0.950	0.05	0.22
4118	4.77	4.76	.....	4.77	0.65	1.000	0.05	-0.08
4184	7.79	7.85	.....	7.79	1.58	1.000	0.24	0.53
4188	16.69	16.97	.....	16.69	7.24	0.545	0.04	0.00
4192	7.79	7.85	.....	7.79	1.58	1.000	0.25	0.90
4207	1.81	1.81	.....	1.81	0.09	0.226	0.03	-0.13
4235	1.15	1.15	7.23	1.15	0.03	0.848	0.03	-0.02
4271	5.82	5.84	.....	5.82	1.07	1.000	0.06	0.01
4281	14.81	14.60	.....	14.81	5.70	0.391	0.04	0.02
4345	1.62	1.62	.....	1.62	0.07	0.988	0.05	-0.11
4348	1.18	1.18	.....	1.18	0.04	8.000e−06	0.02	0.10
4349	1.32	1.32	1.32	1.32	0.05	0.988	0.03	-0.01
4367	4.55	4.55	4.55	4.55	0.54	1.000	0.12	-0.05
4379	3.14	3.15	.....	3.14	0.27	3.000e−05	0.02	-0.04
4397	0.86	0.86	.....	0.86	0.02	0.801	0.04	-0.08
4412	1.90	1.90	.....	1.90	0.10	1.000	0.13	1.25
4443	4.50	4.52	.....	4.50	0.57	1.000	0.06	0.14
4468	1.89	1.90	.....	1.89	0.10	1.000	0.03	-0.06
4471	8.11	8.15	8.15	8.11	1.71	1.000	0.14	0.05
4474	2.55	2.55	.....	2.55	0.17	0.892	0.04	-0.02
4475	2.46	2.46	.....	2.46	0.16	1.000	0.19	0.18
4490	0.62	0.62	.....	0.62	0.01	0.078	0.03	0.08
4503	1.22	1.22	.....	1.22	0.04	2.060e−04	0.03	-0.04
4511	12.47	12.31	.....	12.47	4.04	1.000	0.10	0.12
4517	14.28	14.27	19.60	14.28	5.30	1.000	0.18	0.10
4525	11.39	11.63	.....	11.39	3.37	1.000	0.16	0.35
4547	3.42	3.43	.....	3.42	0.42	0.997	0.05	0.14
4552	4.72	4.72	.....	4.72	0.58	1.000	0.10	0.01
4568	0.60	0.60	.....	0.60	0.01	0.086	0.02	-0.08
4575	1.05	1.05	1.05	1.05	0.03	1.000	0.10	-0.00
4602	6.97	7.05	9.14	6.97	1.26	1.000	0.17	0.71
4605	1.14	1.14	.....	1.14	0.04	0.859	0.03	-0.16
4610	7.09	7.05	.....	7.09	1.31	0.986	0.05	-0.03
4615	14.81	15.31	.....	14.81	5.70	1.000	0.10	-0.03
4635	0.92	0.92	.....	0.92	0.02	1.000e−05	0.02	-0.04
4638	2.50	2.50	.....	2.50	0.16	1.000	0.43	0.05
4664	8.46	8.37	.....	8.46	1.86	0.995	0.04	-0.02
4676	9.04	9.10	.....	9.04	2.12	1.000	0.09	0.02

Tab. 5.2:(continued)

Star	$P_{\rm Scargle}$	$P_{\rm CLEAN}$	$P_{\rm Rebull}$	$P_{\rm adopt}$	δP	$p_{\rm vari}$	$\Delta m_{\rm ptp}$	$\Delta(R_{\rm C}-{\rm H}\alpha)$
4682	9.25	9.23	9.26	9.25	2.22	1.000	0.10	0.03
4695	0.55	0.55	.....	0.55	0.01	3.210e−04	0.02	-0.11
4700	1.96	1.96	.....	1.96	0.11	1.000	0.05	0.09
4701	5.36	5.37	.....	5.36	0.78	1.000	0.31	0.62
4703	1.29	1.29	.....	1.29	0.04	1.000	0.09	-0.04
4718	1.75	1.74	.....	1.75	0.08	0.425	0.02	0.17
4721	0.69	0.69	.....	0.69	0.01	3.352e−03	0.02	0.01
4723	0.96	0.96	0.96	0.96	0.02	0.968	0.05	0.02
4749	2.27	2.27	2.26	2.27	0.13	1.000	0.07	-0.01
4757	3.57	3.59	.....	3.57	0.33	0.219	0.03	0.03
4777	4.95	4.94	.....	4.95	0.64	0.944	0.05	0.02
4793	6.62	6.61	6.60	6.62	1.14	1.000	0.07	0.05
4807	4.61	4.62	.....	4.61	0.55	1.000	0.08	0.01
4823	3.38	3.38	.....	3.38	0.32	1.000	0.05	-0.14
4886	2.35	2.36	.....	2.35	0.15	0.999	0.06	-0.04
4887	6.01	5.98	.....	6.01	0.94	0.000	0.02	0.02
4896	3.70	3.71	.....	3.70	0.37	1.000	0.05	0.55
4944	3.44	3.45	.....	3.44	0.31	1.000	0.17	0.01
4956	5.51	5.56	.....	5.51	0.79	1.000	0.18	0.24
4962	2.30	2.30	.....	2.30	0.14	1.000	0.09	0.09
4967	9.71	9.66	.....	9.71	2.48	1.000	0.04	-0.09
4975	4.12	4.10	.....	4.12	0.44	1.000	0.05	0.02
4986	4.26	4.24	3.80	4.26	0.56	1.000	0.15	0.21
4991	1.57	1.57	.....	1.57	0.07	1.000e−06	0.02	-0.02
5015	2.57	2.56	2.55	2.57	0.16	0.999	0.05	0.04
5030	5.43	5.41	5.43	5.43	0.77	0.999	0.05	0.02
5035	3.09	3.09	.....	3.09	0.25	0.000	0.02	-0.02
5041	1.67	1.67	1.66	1.67	0.07	1.000	0.13	-0.04
5074	9.04	9.10	.....	9.04	2.12	1.000	0.37	0.07
5108	6.40	6.34	.....	6.40	1.06	1.000	0.19	0.37
5125	1.57	1.57	.....	1.57	0.07	1.000	0.04	0.05
5134	7.09	7.05	.....	7.09	1.31	1.000	0.10	0.08
5143	7.64	7.66	11.58	7.64	1.52	1.000	0.11	0.41
5149	4.50	4.52	.....	4.50	0.53	1.000	0.06	0.03
5158	5.43	5.41	.....	5.43	0.77	1.000	0.14	0.06
5184	0.52	1.08	.....	1.08	0.03	0.281	0.03	0.07
5190	1.88	1.89	.....	1.88	0.10	2.619e−03	0.02	0.06
5235	8.64	8.60	.....	8.64	2.04	1.000	0.52	0.41
5244	1.23	1.23	.....	1.23	0.04	0.927	0.04	-0.05
5261	0.64	0.64	.....	0.64	0.01	0.992	0.03	0.09
5263	9.04	9.10	8.94	9.04	2.12	1.000	0.08	-0.05
5298	3.44	3.45	.....	3.44	0.31	1.000	0.05	-0.03
5301	13.31	13.08	.....	13.31	4.60	1.000	0.06	0.03
5303	7.22	7.30	.....	7.22	1.46	1.000	0.10	0.34
5306	7.79	7.75	.....	7.79	1.58	1.000	0.10	0.07
5320	8.46	8.48	.....	8.46	1.86	1.000	0.14	0.04
5332	5.36	5.37	5.41	5.36	0.75	1.000	0.12	0.02
5336	1.35	1.35	.....	1.35	0.05	0.418	0.03	-0.03
5355	4.17	4.19	.....	4.17	0.45	1.000	0.33	0.88
5358	0.97	0.97	.....	0.97	0.02	1.000	0.45	0.01
5361	4.04	4.05	.....	4.04	0.45	1.000	0.06	0.09
5368	1.71	1.71	.....	1.71	0.08	0.993	0.03	0.00
5391	3.39	3.39	.....	3.39	0.33	1.000	0.04	0.28
5394	2.38	2.38	.....	2.38	0.15	0.999	0.05	0.26
5408	5.22	5.23	.....	5.22	0.78	0.000	0.02	-0.01
5413	9.95	9.96	.....	9.95	2.57	1.000	0.06	-0.02
5475	1.47	1.47	.....	1.47	0.06	1.000	0.04	0.05
5478	1.16	1.16	1.16	1.16	0.03	1.000	0.13	0.02
5482	1.46	1.46	.....	1.46	0.06	0.945	0.04	-0.03
5486	1.55	1.55	.....	1.55	0.07	1.000	0.04	-0.11
5491	7.64	7.56	.....	7.64	1.52	1.000	0.14	0.37
5495	4.45	4.48	.....	4.45	0.54	2.380e−03	0.02	-0.01
5505	5.22	5.19	.....	5.22	0.71	1.000	0.12	-0.12
5509	0.62	0.62	.....	0.62	0.01	1.000	0.03	0.03

Tab. 5.2:(continued)

Star	$P_{\rm Scargle}$	$P_{\rm CLEAN}$	$P_{\rm Rebull}$	$P_{\rm adopt}$	δP	$p_{\rm vari}$	$\Delta m_{\rm ptp}$	$\Delta(R_C - H\alpha)$
5529	10.48	10.64	10.51	10.48	2.85	1.000	0.21	0.04
5552	1.58	1.58	.....	1.58	0.07	0.474	0.06	0.66
5557	1.22	1.21	1.21	1.22	0.05	1.000	0.14	0.10
5574	1.21	1.21	.....	1.21	0.04	0.148	0.03	-0.13
5575	11.73	11.84	12.06	11.73	4.28	1.000	0.08	0.59
5580	5.15	5.15	.....	5.15	0.69	4.213e−03	0.03	0.01
5582	2.73	2.72	.....	2.73	0.21	0.985	0.04	-0.08
5610	3.92	3.95	.....	3.92	0.45	0.831	0.04	0.13
5612	8.64	8.72	.....	8.64	1.99	1.000	0.15	-0.01
5628	3.11	3.11	.....	3.11	0.20	0.998	0.04	0.39
5633	3.35	3.34	3.35	3.35	0.35	1.000	0.17	-0.01
5634	5.43	5.41	.....	5.43	0.81	1.000	0.10	0.15
5638	6.84	6.82	.....	6.84	1.23	1.000	0.08	0.78
5645	1.80	1.79	.....	1.80	0.09	1.000	0.09	0.05
5647	2.25	2.23	.....	2.25	0.14	0.933	0.03	0.00
5653	4.17	4.19	4.18	4.17	0.46	1.000	0.16	0.01
5663	1.96	1.95	.....	1.96	0.11	0.953	0.05	-0.09
5671	2.38	2.39	.....	2.38	0.15	1.000	0.18	0.01
5672	2.20	2.20	.....	2.20	0.13	0.819	0.03	-0.10
5673	8.28	8.26	8.49	8.28	1.78	1.000	0.50	0.13
5677	5.22	5.19	.....	5.22	0.87	1.000	0.34	0.05
5685	2.17	2.17	.....	2.17	0.13	0.492	0.02	-0.07
5687	4.40	4.42	4.41	4.40	0.60	1.000	0.06	0.01
5690	1.92	0.13	.....	1.97	0.11	0.932	0.03	0.61
5704	0.91	0.91	.....	0.91	0.02	0.838	0.03	0.01
5721	0.29	0.29	.....	0.29	0.00	5.930e−04	0.03	0.15
5732	2.17	2.17	.....	2.17	0.12	1.000	0.19	0.21
5750	5.15	5.15	.....	5.15	0.69	1.000	0.09	0.08
5762	4.26	4.27	.....	4.26	0.47	1.000	0.08	-0.02
5767	4.66	4.65	4.64	4.66	0.58	1.000	0.18	0.04
5768	1.30	1.30	.....	1.30	0.05	0.122	0.03	-0.02
5770	2.53	2.52	.....	2.53	0.27	0.193	0.03	0.03
5775	7.49	7.56	.....	7.49	1.46	1.000	0.07	0.04
5783	2.30	2.29	2.30	2.30	0.14	0.981	0.03	0.01
5785	3.63	3.61	.....	3.63	0.34	0.999	0.04	0.05
5786	3.11	3.09	.....	3.11	0.27	1.000	0.04	0.24
5791	0.91	0.92	11.58	0.91	0.02	1.000	0.08	0.05
5798	3.84	1.13	.....	1.13	0.03	1.000	0.04	-0.14
5803	2.16	2.17	2.18	2.16	0.15	0.891	0.04	0.03
5817	4.35	4.39	.....	4.35	0.49	1.000	0.15	0.01
5830	12.09	12.07	12.43	12.09	3.92	0.617	0.03	0.01
5831	4.95	4.90	.....	4.95	0.68	1.000	0.16	0.61
5837	1.12	1.11	.....	1.12	0.03	1.000	0.19	0.06
5838	8.84	8.84	8.90	8.84	2.03	1.000	0.16	0.02
5840	1.71	1.71	.....	1.71	0.08	0.199	0.03	-0.10
5845	2.50	1.66	.....	1.66	0.08	0.111	0.06	0.41
5847	1.30	1.30	.....	1.30	0.05	0.000	0.02	-0.05
5849	1.23	5.19	.....	1.32	0.05	1.000	0.09	0.01
5851	1.11	1.11	.....	1.11	0.03	0.997	0.05	0.07
5852	3.73	3.71	3.75	3.73	0.43	1.000	0.10	0.05
5853	3.96	4.00	.....	3.96	0.42	1.000	0.05	0.02
5855	12.88	12.81	12.66	12.88	4.31	1.000	0.28	0.04
5856	17.43	17.44	.....	17.43	8.11	1.000	0.04	0.04
5857	0.90	0.90	.....	0.90	0.02	1.000	0.07	0.04
5859	5.66	5.66	.....	5.66	0.87	0.085	0.03	0.09
5863	2.80	2.80	.....	2.80	0.21	0.148	0.02	0.03
5869	0.85	0.85	.....	0.85	0.02	1.000	0.10	0.10
5874	3.70	3.71	.....	3.70	0.43	1.000	0.27	0.11
5876	7.49	7.39	.....	7.49	1.46	1.000	0.08	0.03
5878	3.57	3.57	.....	3.57	0.33	1.000	0.06	-0.02
5879	1.83	1.84	.....	1.83	0.09	1.330e−03	0.03	-0.03
5880	9.95	9.96	.....	9.95	2.57	1.000	0.08	0.01
5883	3.66	3.67	3.66	3.66	0.35	1.000	0.09	0.00
5884	2.57	2.57	.....	2.57	0.18	0.995	0.05	0.01

Tab. 5.2:(continued)

Star	$P_{\rm Scargle}$	$P_{\rm CLEAN}$	$P_{\rm Rebull}$	$P_{\rm adopt}$	δP	$p_{\rm vari}$	$\Delta m_{\rm ptp}$	$\Delta(R_{\rm C}-{\rm H}\alpha)$
5896	1.84	1.85	.....	1.84	0.09	0.662	0.03	0.12
5897	1.90	1.90	.....	1.90	0.09	1.000	0.41	-0.05
5899	1.31	1.31	.....	1.31	0.04	1.000	0.10	0.03
5902	12.88	12.81	.....	12.88	4.31	1.000	0.05	0.07
5903	4.35	4.33	.....	4.35	0.51	0.999	0.03	-0.02
5905	8.46	8.48	.....	8.46	2.23	1.000	0.11	0.34
5906	1.50	1.51	.....	1.50	0.06	1.000	0.05	0.61
5907	4.21	4.27	.....	4.21	0.46	6.190e−04	0.02	0.00
5914	11.73	11.63	.....	11.73	3.67	1.000	0.07	-0.10
5924	3.00	2.99	.....	3.00	0.29	1.000	0.07	0.14
5927	2.55	2.55	.....	2.55	0.17	0.994	0.04	0.23
5932	3.16	3.17	.....	3.16	0.26	1.000	0.06	-0.09
5938	0.83	0.83	.....	0.83	0.02	1.000	0.05	0.07
5948	0.85	5.81	.....	5.81	0.88	1.000	0.39	0.23
5958	1.07	1.07	.....	1.07	0.03	0.123	0.02	-0.12
5967	10.77	10.64	.....	10.77	3.01	1.000	0.45	0.44
5968	9.48	9.66	9.61	9.48	2.41	1.000	0.07	0.05
5969	1.73	1.73	.....	1.73	0.08	1.556e−03	0.02	-0.12
5974	7.36	0.88	.....	0.88	0.02	1.000	0.04	0.02
5978	1.81	1.81	.....	1.81	0.09	0.076	0.02	0.56
5986	2.67	2.68	2.69	2.67	0.19	0.987	0.05	0.01
5987	1.97	1.99	.....	1.97	0.10	2.610e−04	0.02	-0.06
5990	1.18	1.18	.....	1.18	0.04	0.593	0.03	-0.13
5994	3.88	3.88	.....	3.88	0.39	0.997	0.04	-0.00
5999	2.55	2.55	.....	2.55	0.18	1.000	0.04	0.00
6008	1.32	1.32	.....	1.32	0.05	1.000	0.04	0.02
6013	10.48	10.46	10.35	10.48	2.85	1.000	0.16	-0.06
6014	1.59	1.59	.....	1.59	0.07	0.998	0.04	0.24
6019	0.65	0.64	.....	0.65	0.01	1.191e−03	0.02	-0.11
6022	1.73	1.73	.....	1.73	0.10	1.000	0.19	0.05
6024	9.71	9.81	.....	9.71	2.45	1.000	0.59	0.28
6031	3.92	3.90	.....	3.92	0.40	1.000	0.06	-0.05
6032	0.80	0.80	.....	0.80	0.02	1.000	0.06	0.39
6039	5.83	5.76	.....	5.83	0.88	1.000	0.29	0.37
6042	0.54	0.54	.....	0.54	0.01	1.000e−06	0.02	0.01
6043	10.77	10.64	.....	10.77	3.01	1.000	0.10	0.02
6045	1.75	1.76	.....	1.75	0.08	3.110e−04	0.02	-0.06
6055	5.92	5.98	.....	5.92	0.94	3.876e−03	0.03	0.02
6063	3.38	3.38	.....	3.38	0.30	1.000	0.13	0.19
6064	2.18	2.17	.....	2.18	0.13	0.000	0.01	-0.04
6067	2.93	2.92	2.94	2.93	0.27	1.000	0.12	0.01
6077	2.40	2.37	.....	2.40	0.16	6.221e−03	0.10	0.72
6079	5.22	5.23	.....	5.22	0.71	0.993	0.05	0.04
6081	0.68	0.68	0.68	0.68	0.01	1.000	0.09	-0.00
6102	9.04	9.10	11.08	9.04	2.12	1.000	0.19	0.24
6115	0.71	0.71	.....	0.71	0.01	2.700e−05	0.02	-0.17
6119	1.65	0.21	.....	1.65	0.08	0.754	0.03	0.10
6125	3.60	3.61	.....	3.60	0.36	1.000	0.14	0.27
6126	17.43	16.97	16.99	17.43	7.89	1.000	0.12	0.03
6136	2.25	2.24	2.23	2.25	0.13	0.101	0.03	-0.05
6139	1.61	1.61	.....	1.61	0.07	1.950e−04	0.01	-0.15
6145	0.45	0.45	0.45	0.45	0.01	1.000	0.19	0.10
6146	1.05	1.05	.....	1.05	0.03	5.100e−05	0.02	-0.11
6156	4.72	4.68	.....	4.72	0.58	1.000	0.24	0.00
6162	1.43	1.44	.....	1.43	0.05	0.999	0.05	-0.06
6163	2.09	2.09	.....	2.09	0.11	1.000	0.07	0.02
6165	3.85	3.90	3.91	3.85	0.57	1.000	0.10	0.07
6168	1.09	1.09	.....	1.09	0.03	2.061e−03	0.02	0.00
6172	1.76	1.76	.....	1.76	0.10	1.000	0.12	0.42
6175	4.17	4.19	4.17	4.17	0.45	1.000	0.10	0.76
6178	12.09	12.07	.....	12.09	3.80	1.000	0.12	0.03
6179	5.75	5.76	5.77	5.75	0.86	1.000	0.30	0.04
6181	2.38	2.36	.....	2.38	0.15	1.000	0.05	-0.06
6182	3.32	3.32	.....	3.32	0.30	1.000	1.84	0.76

Tab. 5.2:(continued)

Star	$P_{\rm Scargle}$	$P_{\rm CLEAN}$	$P_{\rm Rebull}$	$P_{\rm adopt}$	δP	$p_{\rm vari}$	$\Delta m_{\rm ptp}$	$\Delta(R_C - H\alpha)$
6201	1.44	1.44	0.72	1.44	0.05	1.000	0.20	0.02
6209	11.07	11.01	.....	11.07	3.18	1.000	0.13	-0.04
6210	0.84	0.84	5.41	0.84	0.02	2.215e−03	0.03	-0.05
6218	0.57	0.57	.....	0.57	0.01	6.000e−06	0.01	-0.11
6220	1.37	1.37	.....	1.37	0.05	1.000	0.06	-0.09
6228	8.28	8.26	.....	8.28	1.78	1.000	0.55	0.35
6245	0.61	0.61	.....	0.61	0.01	1.000	0.08	-0.02
6248	6.30	6.28	6.23	6.30	1.27	1.000	0.08	0.01
6253	1.76	1.77	.....	1.76	0.08	0.000	0.01	0.02
6255	4.66	4.65	.....	4.66	0.61	1.000	0.05	-0.01
6260	4.50	4.52	.....	4.50	0.55	8.000e−05	0.02	-0.12
6272	0.56	0.56	.....	0.56	0.01	0.000	0.03	-0.08
6288	9.25	9.10	9.26	9.25	2.22	0.580	0.04	0.02
6304	2.64	2.65	.....	2.64	0.19	0.692	0.03	-0.04
6307	1.38	1.38	.....	1.38	0.05	0.575	0.12	0.62
6308	0.97	0.97	.....	0.97	0.03	1.000	0.58	0.08
6316	2.43	2.42	.....	2.43	0.16	0.992	0.05	-0.02
6326	2.91	2.92	2.92	2.91	0.22	1.000	0.08	0.17
6327	6.51	6.54	.....	6.51	1.10	1.000	0.10	-0.04
6334	0.96	0.96	.....	0.96	0.02	0.920	0.05	-0.09
6340	1.45	1.46	1.47	1.45	0.05	8.765e−03	0.03	0.02
6342	7.64	7.66	7.75	7.64	1.52	1.000	0.11	-0.05
6344	0.71	0.71	.....	0.71	0.01	0.312	0.05	0.07
6349	1.24	1.24	.....	1.24	0.04	1.000	0.12	0.36
6383	0.91	0.91	.....	0.91	0.02	0.064	0.03	-0.16
6387	2.65	2.65	.....	2.65	0.19	1.000	0.14	0.30
6407	6.40	1.18	6.37	1.18	0.04	0.402	0.03	-0.02
6427	1.49	1.49	.....	1.49	0.06	0.000	0.02	-0.05
6428	1.13	1.13	.....	1.13	0.04	0.852	0.03	-0.04
6438	4.45	4.45	4.43	4.45	0.51	1.000	0.18	-0.02
6439	1.30	1.30	.....	1.30	0.04	0.165	0.05	-0.05
6451	1.32	4.08	.....	4.08	0.44	0.420	0.03	0.02
6476	8.46	8.60	.....	8.46	1.86	1.000	0.14	0.03
6486	2.07	2.07	.....	2.07	0.12	0.960	0.03	0.06
6503	12.09	12.31	13.06	12.09	3.81	0.057	0.04	-0.06
6517	4.50	4.48	.....	4.50	0.53	1.000	0.14	0.02
6519	6.51	6.47	.....	6.51	1.07	1.000	0.07	-0.06
6572	2.08	2.08	.....	2.08	0.12	0.501	0.05	-0.16
6577	5.08	5.10	.....	5.08	0.70	1.957e−03	0.02	0.03
6582	0.94	0.94	.....	0.94	0.02	0.791	0.04	-0.06
6585	3.30	3.32	.....	3.30	0.30	4.000e−06	0.02	-0.10
6592	0.67	0.67	.....	0.67	0.01	1.000	0.05	-0.17
6595	4.30	4.30	.....	4.30	0.48	1.000	0.11	0.08
6610	1.89	1.89	.....	1.89	0.10	0.965	0.03	-0.07
6642	8.11	8.15	.....	8.11	1.71	1.000	0.16	-0.02
6678	0.40	0.40	.....	0.40	0.00	0.918	0.02	0.06
6685	7.95	8.05	.....	7.95	1.64	1.000	0.06	-0.03
6699	0.78	0.78	.....	0.78	0.02	1.000	0.05	-0.06
6784	9.48	9.37	.....	9.48	2.34	1.000	0.15	0.07
6887	5.08	5.28	.....	5.08	0.67	0.538	0.04	0.11
6898	6.51	0.87	.....	0.87	0.02	1.000	0.05	0.02
6899	1.54	1.55	1.54	1.54	0.08	1.000	0.16	-0.04
6913	0.61	0.60	.....	0.61	0.01	0.507	0.04	-0.03
6987	3.22	3.20	.....	3.22	0.29	1.000	0.10	-0.06
6996	1.23	1.23	.....	1.23	0.04	1.000	0.06	0.01
7044	1.17	1.17	1.17	1.17	0.04	1.000	0.07	0.05
7049	5.92	5.87	5.89	5.92	0.95	1.000	0.06	-0.07
7103	4.13	4.13	4.10	4.13	0.58	1.000	0.06	-0.05
7297	5.02	5.06	5.06	5.02	0.68	1.000	0.13	-0.03
7303	2.79	2.79	2.78	2.79	0.21	1.000	0.07	-0.04
7401	4.26	4.24	1.76	4.26	0.48	1.000	0.05	0.09
7424	1.71	1.71	.....	1.71	0.08	0.632	0.03	-0.02
7451	2.28	1.77	.....	1.77	0.09	0.833	0.03	0.02
7487	1.71	1.71	.....	1.71	0.08	1.000	0.06	0.06

Tab. 5.2:(continued)

Star	$P_{\rm Scargle}$	$P_{\rm CLEAN}$	$P_{\rm Rebull}$	$P_{\rm adopt}$	δP	$p_{\rm vari}$	$\Delta m_{\rm ptp}$	$\Delta(R_{\rm C}-{\rm H}\alpha)$
7597	6.57	6.54	6.53	6.57	1.46	1.000	0.09	-0.06
7622	1.46	1.45	.....	1.46	0.06	0.142	0.02	0.02
7698	0.61	0.61	.....	0.61	0.01	2.790e−04	0.06	0.38
7714	4.45	4.48	4.58	4.45	0.51	1.000	0.06	0.19
7750	2.44	2.43	.....	2.44	0.16	6.490e−03	0.03	-0.00
7906	4.50	4.52	.....	4.50	0.55	1.000	0.04	0.07
7939	3.92	3.92	.....	3.92	0.40	1.000	0.08	0.05
7961	6.01	5.98	5.96	6.01	0.94	1.000	0.15	0.02
7974	0.88	0.88	.....	0.88	0.03	1.000	0.09	0.48
8235	0.34	0.25	.....	0.25	0.00	1.000	0.03	-0.08
8307	3.92	3.92	3.93	3.92	0.40	1.000	0.11	-0.08
8328	1.13	8.72	.....	8.72	1.98	1.000	0.14	0.13
8434	2.22	2.22	.....	2.22	0.14	1.000	0.06	-0.05
8518	3.38	3.39	3.40	3.38	0.30	1.000	0.05	-0.05
8595	1.17	1.17	1.17	1.17	0.04	1.000	0.07	0.13
8624	5.22	5.23	.....	5.22	0.76	1.000	0.07	0.12
8668	4.30	4.30	.....	4.30	0.48	1.000e−06	0.03	-0.04
8777	6.51	6.41	6.53	6.51	1.10	1.000	0.06	-0.03
8778	9.04	9.10	9.06	9.04	2.12	1.000	0.12	-0.01
8968	4.50	4.48	4.48	4.50	0.53	1.000	0.10	-0.05
9037	4.66	4.68	.....	4.66	0.60	0.114	0.04	-0.07
9083	3.27	3.27	.....	3.27	0.28	1.000	0.11	0.03
9228	2.14	2.13	.....	2.14	0.13	1.000	0.04	0.08
9279	0.68	0.68	.....	0.68	0.01	0.153	0.03	-0.04
9482	5.83	5.81	5.77	5.83	0.88	1.000	0.11	0.03
9685	3.41	3.43	3.41	3.41	0.30	1.000	0.05	-0.03
9773	1.73	1.73	.....	1.73	0.08	3.000e−06	0.03	-0.10

Tab. 5.3: All 184 irregular variable stars that passed both PMS tests and are therefore supposed to be PMS stars. The naming convention of the columns is the same as in Tab. 5.2.

Star	$p_{\rm vari}$	$\Delta m_{\rm ptp}$	$\Delta(R_{\rm C}-{\rm H}\alpha)$
67	1.000	2.17	-0.02
840	1.000	0.11	0.74
964	1.000	0.75	0.22
1720	1.000	0.13	0.03
2208	1.000	0.09	0.01
2229	1.000	0.85	0.23
2237	1.000	0.41	0.23
2284	1.000	1.03	-0.09
2285	1.000	0.11	-0.02
2344	0.999	0.06	-0.04
2456	1.000	0.13	0.00
2508	1.000	0.15	0.09
2825	1.000	0.29	0.97
2911	1.000	0.11	0.32
2948	1.000	0.18	1.02
3154	1.000	0.47	0.40
3248	1.000	0.37	0.00
3274	1.000	0.67	0.92
3355	1.000	0.24	0.10
3356	1.000	0.83	0.08
3370	1.000	0.58	1.22
3465	1.000	0.24	-0.13
3506	1.000	0.63	0.81
3558	1.000	0.53	0.36
3609	1.000	0.30	0.26
3637	1.000	0.15	0.62
3743	1.000	0.12	0.12
3766	1.000	0.30	-0.01
3767	1.000	0.54	1.32

Tab. 5.3:(continued)

Star	p_{vari}	Δm_{ptp}	$\Delta(R_C - H\alpha)$
3829	1.000	0.25	0.03
3844	1.000	0.22	1.42
3933	1.000	0.22	0.51
3992	1.000	0.24	0.09
4008	1.000	0.57	0.32
4052	1.000	0.30	0.71
4220	1.000	0.87	0.04
4232	1.000	0.08	0.31
4236	1.000	0.55	0.49
4280	1.000	0.16	0.03
4282	1.000	0.21	0.15
4313	1.000	0.18	0.05
4371	1.000	0.29	0.38
4392	1.000	0.68	0.38
4393	1.000	1.03	0.20
4470	1.000	0.09	0.01
4477	1.000	0.22	-0.01
4522	1.000	0.63	1.37
4538	1.000	0.08	0.22
4540	1.000	0.30	1.11
4542	1.000	0.38	0.45
4577	1.000	3.02	0.35
4663	1.000	1.23	0.31
4680	1.000	0.34	0.19
4776	1.000	0.21	0.54
4826	1.000	0.65	0.31
4937	1.000	0.08	-0.06
4945	1.000	0.24	1.25
4955	1.000	0.23	0.39
5048	1.000	0.47	0.71
5061	1.000	0.28	0.95
5114	1.000	1.93	0.97
5123	1.000	0.29	0.17
5150	1.000	0.10	1.01
5163	1.000	0.18	0.06
5195	1.000	0.69	0.20
5212	1.000	0.71	0.88
5236	1.000	0.18	0.08
5268	1.000	0.23	0.16
5274	1.000	0.16	0.25
5323	1.000	0.16	0.10
5339	1.000	0.96	0.61
5351	1.000	0.21	0.24
5365	1.000	0.10	-0.02
5416	1.000	0.16	1.60
5425	1.000	0.14	0.99
5429	1.000	0.29	0.05
5462	1.000	0.18	0.58
5463	1.000	0.49	0.71
5492	1.000	0.96	0.48
5514	1.000	0.17	0.12
5518	1.000	0.19	0.14
5520	1.000	0.75	0.03
5538	1.000	1.15	0.14
5542	1.000	0.85	0.25
5551	1.000	0.35	0.58
5571	1.000	0.17	-0.01
5578	1.000	4.26	-0.08
5591	1.000	0.07	-0.07
5630	1.000	0.19	0.28
5641	1.000	0.18	-0.01
5650	1.000	0.22	0.48
5661	1.000	0.31	1.49
5667	1.000	0.45	-0.08

Tab. 5.3:(continued)

Star	$p_{\rm vari}$	$\Delta m_{\rm ptp}$	$\Delta(R_{\rm C} - {\rm H}\alpha)$
5689	1.000	1.04	0.15
5692	1.000	0.19	0.11
5701	1.000	0.56	0.54
5714	1.000	0.18	0.96
5718	1.000	0.22	0.01
5722	1.000	0.40	0.70
5724	1.000	0.55	0.01
5727	1.000	0.29	-0.04
5737	1.000	0.25	0.02
5746	1.000	0.10	0.03
5760	1.000	0.18	0.20
5792	1.000	0.10	-0.14
5811	1.000	0.11	0.59
5814	1.000	0.25	0.04
5816	1.000	0.64	-0.01
5835	1.000	0.30	0.41
5844	1.000	0.25	0.79
5854	1.000	0.37	0.61
5861	1.000	0.10	0.84
5868	1.000	2.31	0.56
5881	1.000	0.34	0.47
5882	1.000	0.93	0.62
5890	1.000	0.26	1.17
5949	1.000	0.31	0.22
5952	1.000	0.16	-0.03
5953	1.000	0.10	0.04
5956	1.000	1.09	0.28
5966	1.000	0.20	0.44
5979	1.000	1.00	0.57
5980	1.000	0.12	0.06
5992	1.000	0.06	-0.13
6000	1.000	0.26	0.01
6003	1.000	0.27	0.11
6004	1.000	0.35	0.79
6033	1.000	0.57	0.54
6036	1.000	0.34	0.74
6107	1.000	0.25	-0.12
6117	1.000	0.11	1.05
6123	1.000	0.10	0.52
6127	1.000	0.25	0.13
6129	1.000	0.69	-0.01
6132	1.000	0.46	1.34
6135	1.000	1.09	0.33
6147	1.000	0.38	0.32
6159	1.000	0.22	0.82
6166	1.000	0.30	1.31
6171	1.000	0.41	-0.00
6173	1.000	0.26	0.00
6183	1.000	0.42	-0.10
6203	1.000	2.79	0.50
6204	1.000	0.05	0.06
6216	1.000	0.68	0.35
6219	1.000	0.76	0.65
6229	1.000	0.05	0.14
6232	1.000	0.10	0.06
6236	1.000	0.49	0.27
6242	1.000	1.22	-0.05
6251	1.000	0.15	1.06
6263	1.000	0.58	0.36
6270	1.000	0.77	0.01
6273	1.000	0.19	0.74
6285	1.000	0.50	-0.04
6291	1.000	0.46	1.35
6298	1.000	0.42	0.36

Tab. 5.3:(continued)

Star	$p_{\rm vari}$	$\Delta m_{\rm ptp}$	$\Delta(R_{\rm C}-{\rm H}\alpha)$
6339	1.000	0.27	0.40
6345	1.000	0.11	0.47
6376	1.000	0.51	1.22
6399	1.000	0.11	0.00
6461	1.000	0.07	-0.11
6467	1.000	0.25	0.10
6589	1.000	0.37	-0.01
6664	1.000	0.82	0.18
6680	1.000	0.15	0.94
7240	1.000	0.80	0.41
7418	1.000	0.09	0.07
7700	1.000	1.72	0.13
7857	1.000	0.05	-0.15
7873	1.000	0.10	0.78
8004	1.000	0.08	1.05
8144	1.000	0.67	0.14
8320	1.000	0.18	0.67
8334	1.000	0.31	0.03
8415	1.000	0.13	0.18
8457	1.000	0.36	0.08
8809	1.000	0.09	-0.07
8820	1.000	0.19	-0.02
9271	1.000	0.14	0.07
9563	1.000	0.11	0.09
9683	1.000	0.15	1.15
9688	1.000	0.13	-0.06
9809	1.000	0.54	-0.09

5.3 The Final Sample of Variable PMS Members

Fig. 5.3 and Fig. 5.4 show the spatial distribution of all PMS stars and non-cluster members, respectively. The latter were selected from the complete list of all 10554 stars in the field and represents all stars that *failed* at least one of the two PMS membership criteria described in the previous sections. This includes variable stars which failed one or both tests. From the spatial distribution of these non-PMS stars one can clearly identify the extent of the dust cloud located towards NGC 2264. When comparing Fig. 5.3 with Fig. 5.4 it is evident that most PMS stars are located in the region with the highest background extinction, i. e. close to the dense gas and dust out of which they have probably been formed.

In Fig. 5.5 I show the $I_{\rm C}$ vs $(R_{\rm C}-I_{\rm C})$ colour-magnitude diagram of all periodic and irregular variables. It is evident that the periodic variable PMS members are much more concentrated around a line parallel to the ZAMS than the irregular variable PMS members. The reason for this could be a smaller age range of the periodic variables and/or a higher variability of the irregular variables compared to the periodic variables. In addition a higher intrinsic extinction of the irregular variables due to circumstellar disks could yield larger scatter. In the following section the differences between the two subsamples will be discussed in more detail.

In Fig. 5.5 I also show the $I_{\rm C}$ vs $(R_{\rm C}-I_{\rm C})$ colour-magnitude diagram of all (169) previously known PMS stars in NGC 2264 which I could identify in my sample. It is evident that the new PMS variables I found extend to much fainter magnitudes than the previously known PMS stars, i. e. I found new PMS stars mainly in the low mass regime

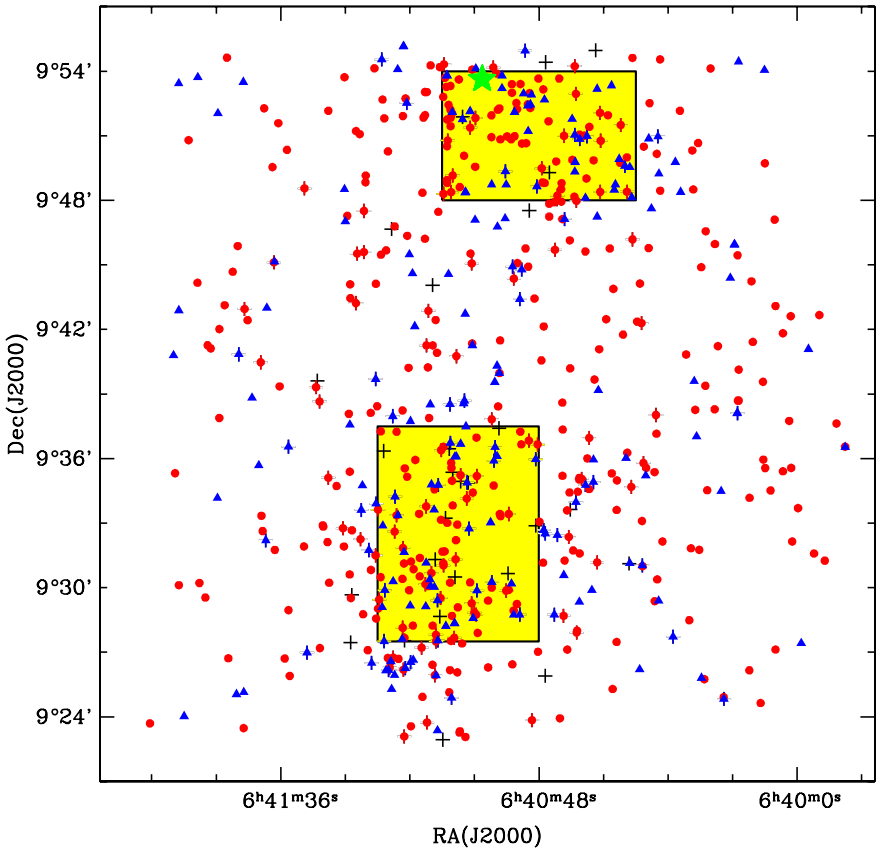

Fig. 5.3: Locations of all PMS variables from my survey which passed both tests including non-variable previously known PMS members. The symbols are the same as in Fig. 5.2. Also shown (indicated by the two boxes) are the two regions NGC 2264 N & S which were used to determine the PMS region in the CMD. The star in the northern box indicates the location of the bright star S Mon (V=4.7 mag).

which probably reaches down to the substellar limit of approximately I_C= 18.5 mag in NGC 2264.

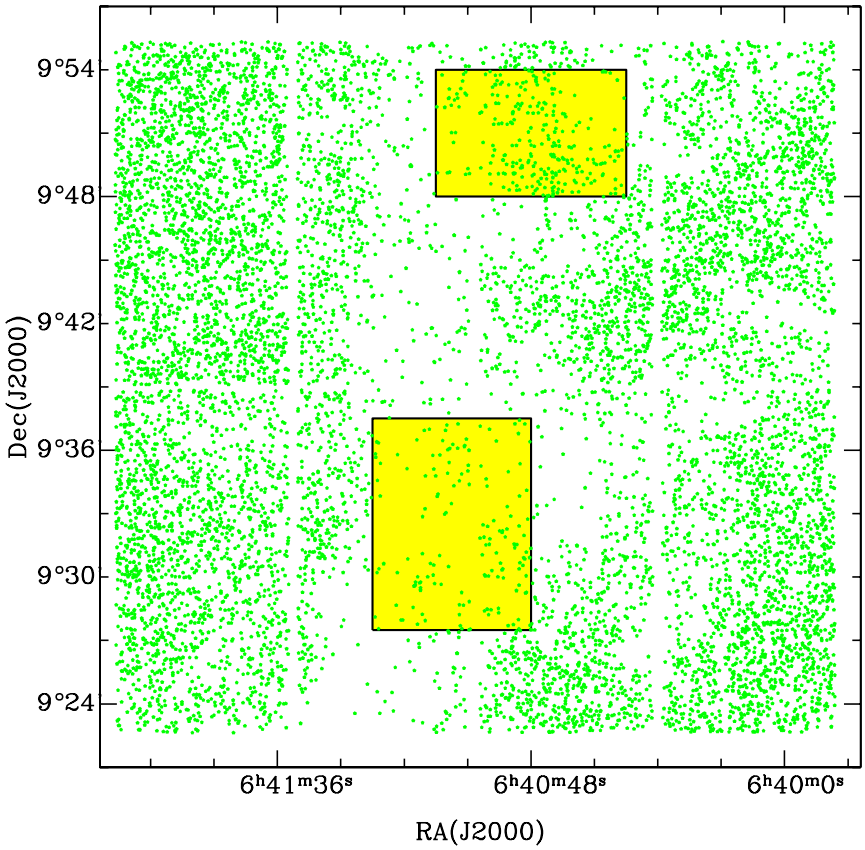

Fig. 5.4: Locations of all stars in the field that *failed* at least one of the two PMS membership criteria. I also show the two regions which were used for determination of the PMS region in the CMD.

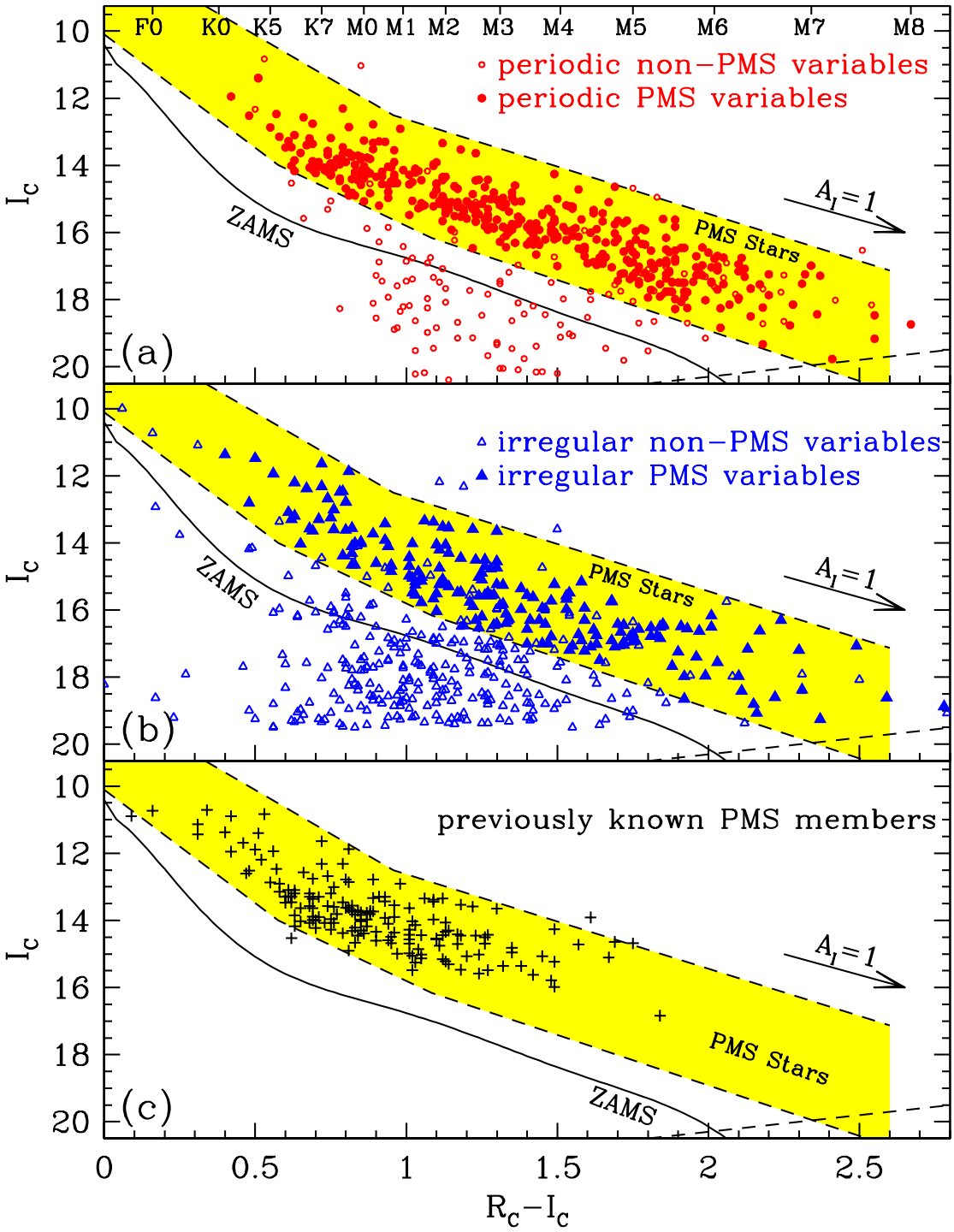

Fig. 5.5: The I_C vs $(R_C - I_C)$ colour-magnitude diagram for different samples of stars. Panel (a): All 543 periodic variables. The 405 periodic variables that passed both PMS tests are marked with filled circles while the periodic variables which did not pass both tests are marked by open circles. Some (bright) stars for which no $(R_C - H\alpha)$ colour was available (and hence did not pass the second test) are also marked by open circles. The PMS zone (defined and used for the first test) is indicated by the yellow region between the dashed lines. The solid line represents the ZAMS sequence. Panel (b): All 484 irregular variables. The 184 irregular variables which passed both PMS tests are indicated by filled triangles while the 300 variable stars which did not pass both tests are shown by open triangles. Panel (c): The CMD of the previously known PMS stars in the whole NGC 2264 field.

Chapter 6

The Nature of the Variability

In this section I investigate some general aspects of the stars' variability and investigate which differences in physical properties between periodic and irregular variables can be found. For this purpose I have to estimate the degree of variability, i. e. the peak-to-peak variation or the standard deviation in the light curve of each star. First, I determine the the peak-to-peak variation of the periodic variables.

6.1 The Peak-to-Peak Variation

For the determination of the peak-to-peak variation of the stars I have to account for statistical outliers (e. g. due to photometric noise and/or cosmic rays). Therefore, the difference of the maximum and minimum brightness in the light curve of a star may not be a reliable estimate of the stars' peak-to-peak variation. It is essential to calculate some kind of mean bright and faint magnitudes for each star, the difference between which yield the peak-to-peak variation of a star. However, the rotation periods of the stars vary from hours to weeks and, therefore, the determination of mean magnitudes in several *time* bins is complicated, because the optimal bin size would change from star to star. In addition the data points in the light curves are very unevenly sampled (see. Fig. 2.3) and also the number of data points in each (equally sized) time bin would highly vary from bin to bin. Therefore it is precarious to calculate the peak-to-peak variation of the stars by calculating the average brightness in equal sized time bins of the light curve.

In that regard the phased light curves provide a better tool for the determination of the peak-to-peak variation (at least for the periodic variables) because they are much more evenly sampled than the light curves in the time domain (see. Fig. 3.2). In addition it is lot easier to estimate the *mean* maximum and minimum brightness of the stars using the phased light curves because (in the sinusoidal case) the maximum brightness is achieved at phase 0.25 while the minimum brightness is located at a phase of 0.75. Therefore, the peak-to-peak variation of each periodic variable was calculated using the phased light curve of the star.

The procedure of determining the peak-to-peak variations of periodic variables is illustrated by Fig. 6.1. The phased light curve of each star was divided into 10 equally spaced phase bins of width 0.1 cycles. In each phase bin I calculated the median of the relative magnitudes which is called $\langle m_{\mathrm{rel}} \rangle_i$ for the ith bin. Finally the peak-to-peak variation of

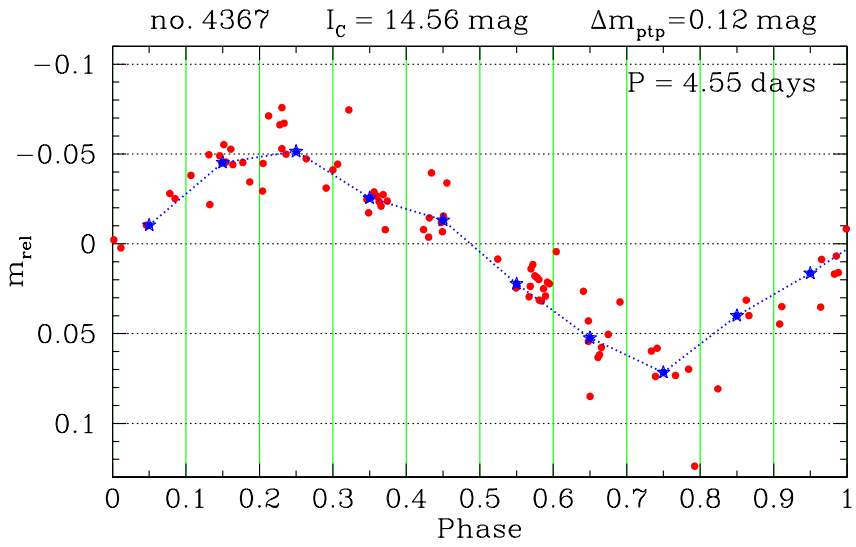

Fig. 6.1: The determination of the peak-to-peak variation, $\Delta m_{\rm ptp}$. The phased light curve (red dots) is divided into 10 equally spaced phase bins of 0.1 cycles width which are indicated by the green lines. The median magnitude in each of these bins is indicated by the blue stars. The peak-to-peak variation (0.12 mag for this star) is given by the difference of the maximum (here 0.07 mag) and minimum (here -0.051 mag) of these median magnitudes.

the star, $\Delta m_{\rm ptp}$, was calculated by subtracting the minimum of these median magnitudes, $\langle m_{\rm rel}\rangle_{\rm min}$, from the maximum of these median magnitudes, $\langle m_{\rm rel}\rangle_{\rm max}$, i. e.

$$\Delta m_{\rm ptp} = \langle m_{\rm rel}\rangle_{\rm max} - \langle m_{\rm rel}\rangle_{\rm min}. \tag{6.1}$$

I used the whole phased light curves for determining the peak-to-peak variation rather than two phase intervals centered at 0.25 cycles and 0.75 cycles where the expected maximum and minimum brightness is located respectively. In this way the determination of the peak-to-peak variation is independent of the phase zero point which may have been imprecisely determined for low signal-to-noise variations. The peak-to-peak variation of periodic variables are listed in column "$\Delta m_{\rm ptp}$" of Tab. 5.2 and Tab. D.1 for PMS members and non-PMS members respectively.

The determination of the peak-to-peak variation requires a different technique for non-periodic stars (i. e. all other stars which are not periodic variable including irregular variables) because phased light curves are not available for these stars. Therefore I determined the peak-to-peak variation of non-periodic stars as follows. In order to take statistical outliers into account I estimated the peak-to-peak variation of each non-periodic star with the difference of the third highest and third lowest data point in the light curve. For all non-periodic stars the peak-to-peak variations estimated this way are listed in column "$\Delta m_{\rm ptp}$" of Tab. 3.5. However, the listed peak-to-peak variations of periodic variables in this table were determined using the phased light curves as outlined above.

For periodic variables the determination of the peak-to-peak variations also with the

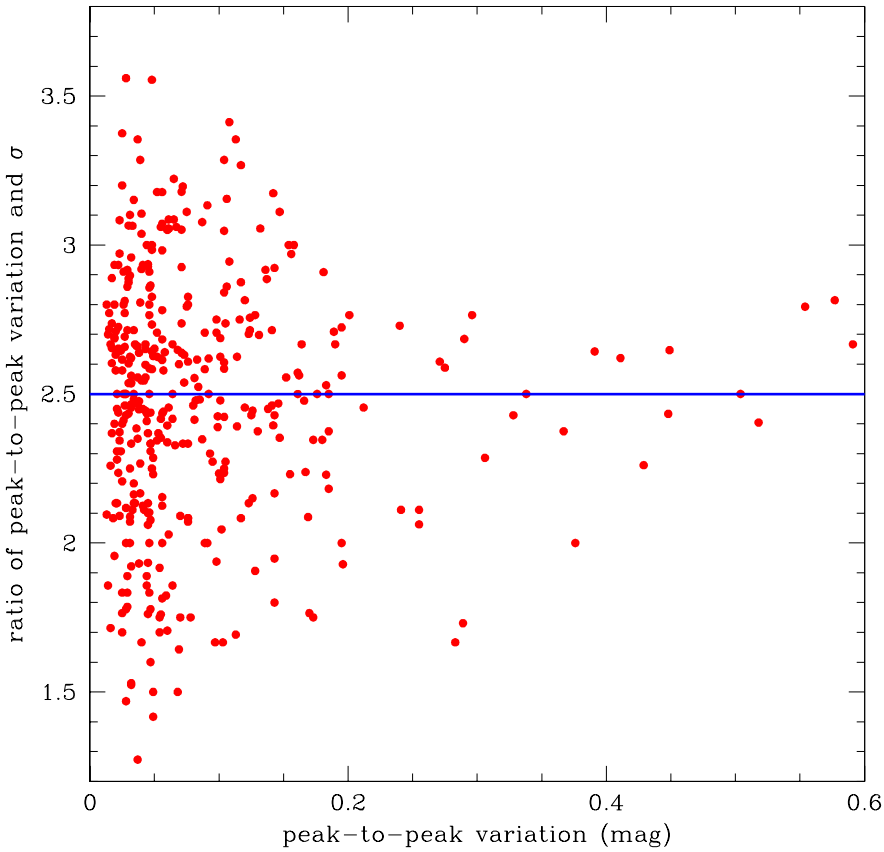

Fig. 6.2: The ratio of the peak-to-peak variation and the standard deviation (σ) for periodic variables as a function of the peak-to-peak variation. The blue line indicates the median ratio of 2.5, i. e. for periodic variables the peak-to-peak variation is typically 2.5 times the standard deviation.

second method (which was used for non-periodic stars) yields typically 0.02 mag higher than the method indicated by Fig. 6.1.

6.2 The Degree of Variability for Periodic and Irregular Variables

In this section I compare the degree of variability measured by the standard deviation, σ, in the light curves of the periodic variables with that of the irregular variables because the peak-to-peak variations of these two samples were determined in two different ways (see previous Sect.) and are therefore not comparable. The peak-to-peak variations of the periodic variables which were determined in the previous Section will be used in Sect. 9.

The standard deviation of all stars is listed in Table 3.5 and was calculated as described in Sect. 4.2. For the sample of periodic variables the peak-to-peak variation is typically 2.5 times the standard deviation (see Fig. 6.2) but this ratio can vary between 1.5 and 3.5 in some extreme cases. For the irregular variables the ratio of the peak-to-peak variation

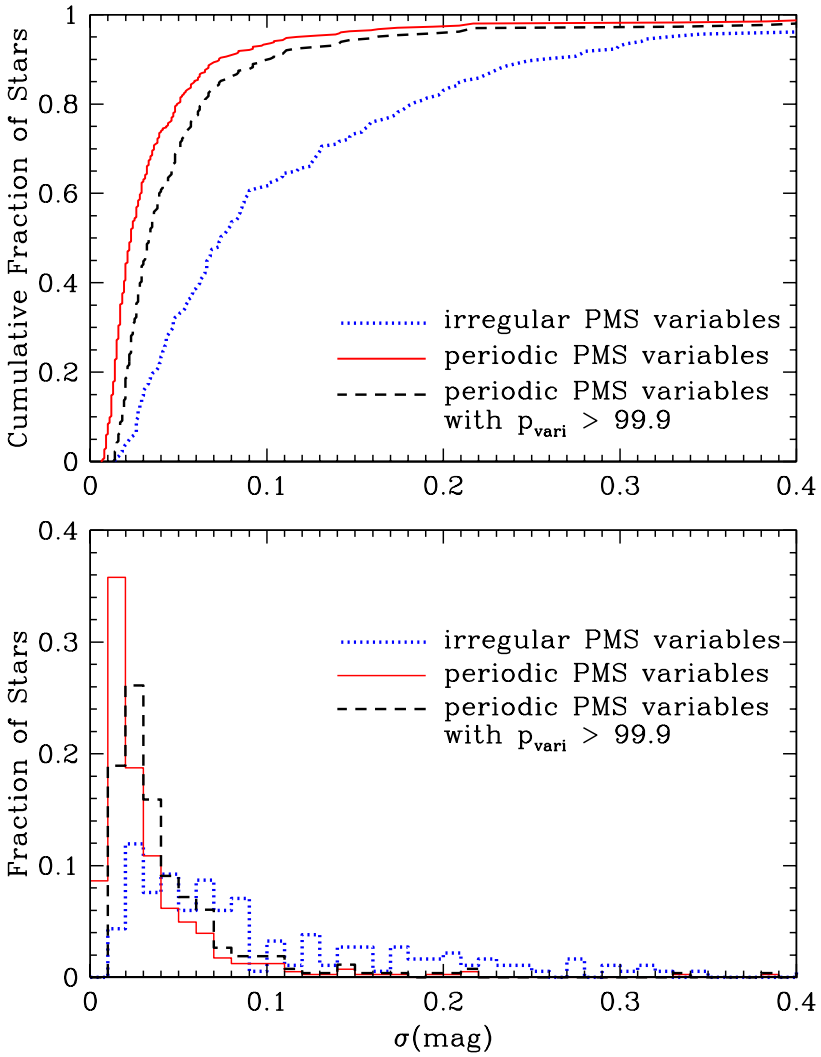

Fig. 6.3: Top panel: The red solid line and the blue dotted line shows the cumulative distribution of the standard deviation, σ, for all 405 periodic and 184 irregular variable PMS stars respectively. **Bottom panel:** The histogram of σ for the two different samples of stars in top panel.

and σ is typically 3 and varies between 2 and 5. The slightly different ratios for irregular and periodic variables can be explained by the different methods which were used for determining the peak-to-peak variation.

Fig. 6.3 shows the cumulative distribution of the standard deviation σ for all 405 periodic and 184 irregular PMS variables. It is evident from this plot that about half of the periodic variable stars have $\sigma \leq 0.02$ mag (solid red line) while only 5.4% (10/184) irregular variable stars show this small level of variability (dotted blue line). On the other hand only 2.7% of the periodic variable stars have $\sigma \geq 0.2$ mag but 14.7% of the irregular variable stars exceed this level, i. e. the fraction of stars with a small σ is always higher for the periodic variables.

This excess of periodic low amplitude stars is not surprising because the advantage of the periodogram analysis is that it is sensitive even for low amplitude variations. This

results from the fact that the power of the random scatter in the light curve due to photometric errors (white noise) is distributed over the whole frequency domain of the power spectrum. Therefore even low amplitude variations close to (and below) the photometric errors can be detected. The χ^2 test, on the other hand, is able to detect variability only if the variations in a light curve are inconsistent with the photometric errors. The cutoff level of a probability $p_{\rm vari}$= 99.9% corresponds to deviations of more than 3σ. In addition as already mentioned in Sect. 4.1 the sample of irregular variables is biased towards larger variations because of the conservative estimate of the photometric errors. Therefore one expect to find more periodic variables among the low amplitude variables compared to the irregular variables. However, the excess of irregular variables with large amplitude is significant and is not affected by this bias.

In order to take any bias resulting from the different variability analysis methods into account I selected only those 264 periodically variables which are also variable according to the χ^2 test (i. e. $p_{\rm vari} \geq$ 99.9%) and compared their distribution (which is also shown in Fig. 6.3) with that of the irregular variables. Again, I found that the two distributions are significantly different, as confirmed by a Kolmogorov-Smirnov test (Press et al., 1992) which shows that the probability that the two distributions are equivalent is less than 5×10^{-15}. The reduced periodic sample also shows an excess of periodic variables at low amplitudes. This implies that the degree of variability is typically larger for irregular variables compared with periodic variables.

A similar result was found in the ONC (Herbst et al., 2002) and in other T Tauri star associations (Herbst et al., 1994; Bouvier et al., 1995). They found that most irregular variables are CTTSs with larger peak-to-peak variations than periodic variables which are WTTSs in most cases. The latter have mostly peak-to-peak variations in $I_{\rm C}$ of less than 0.5 mag. In my sample this would correspond to standard deviations of σ = 0.1 to 0.3 mag. Herbst et al. (2002) furthermore concluded that the brightness variations of periodic WTTSs are mainly caused by cool spots and the observed maximum peak-to-peak variation of 0.5 mag was interpreted as the maximum possible brightness change which cool spots on the surface of a K or M star could cause. The periodic variables with peak-to-peak variations larger than 0.5 mag are believed to be due to hot surface spots resulting from mass accretion (see also Vrba et al., 1989, 1993; Fernàndez & Eiroa, 1996).

In my sample 2.5% of the periodic variables have peak-to-peak variations $\Delta m_{\rm ptp} \geq$ 0.5 mag and the interpretation outlined above suggests that the periodic variations of these stars could be mainly caused by hot spots while the periodicity of the remaining 97% is likely due to cool spots. In this case the majority of rotation periods was determined by brightness modulations caused by cool spots and the sample of periodic variables may contain mostly WTTSs. Assuming that the peak-to-peak variation of the irregular variables is typically three times the standard deviation (see above) 24% of the irregular variables have peak-to-peak variations $\Delta m_{\rm ptp} \geq$ 0.5 mag. In the presented picture the higher variability of the irregular variables suggests that a significant fraction of these stars are possibly CTTSs. In the following section I will investigate if there is further evidence for this interpretation.

The irregular variability of CTTSs can have various reasons. Often it is attributed to variable mass accretion resulting in hot spots which are not stable in brightness, size, and location over a few rotation periods (Bertout et al., 1988; Bertout, 1989; Bouvier & Bertout, 1989; Fernàndez & Eiroa, 1996). This interpretation is supported by the observed

correlation of the amplitude of the variability and the strength of the Hα emission in CTTSs (Vrba et al., 1989, 1993; Fernàndez & Eiroa, 1996). In addition flare-like activities can be an additional source of variability on short time scales (e. g. Bertout, 1989; Vrba et al., 1993; Herbst et al., 1994). In reality the situation is probably more complicated and it could well be that some WTTSs have small hot spots and that CTTSs have cool spots in addition to large hot spots. Vrba et al. (1989, 1993) demonstrated that the variability of CTTSs (both periodic and irregular) in their sample can be understood in terms of a changing pattern of cool and hot spots which are present simultaneously on the surfaces of these stars (see also Appenzeller & Dearborn, 1984). However, for CTTSs it is much more difficult and in many cases even impossible to detect periodic brightness modulations caused by cold spots because of the overlying "noise" from irregular variability.

6.3 The $H\alpha$ Emission Index

If the fraction of CTTSs is in fact higher among the irregular variables they should also show larger Hα emission than the periodic variables because CTTSs are defined by strong Hα emission, i. e. $W_\lambda(H\alpha) \geq$ 10 Å, (see Sect. 1.1) which is by definition not present in WTTS.

6.3.1 Definition of $\Delta(R_\mathrm{C} - \mathrm{H}\alpha)$

In order to investigate the Hα emission of the stars in the two samples I use the $(R_\mathrm{C} - \mathrm{H}\alpha)$ colour and define an Hα emission index $\Delta(R_\mathrm{C} - \mathrm{H}\alpha)$ of a star by the following equation:

$$\Delta(R_\mathrm{C} - \mathrm{H}\alpha) = (R_\mathrm{C} - H\alpha)_\mathrm{star} - (R_\mathrm{C} - H\alpha)_\mathrm{locus}, \tag{6.2}$$

where $(R_\mathrm{C} - \mathrm{H}\alpha)_\mathrm{star}$ is the instrumental colour of the star and $(R_\mathrm{C} - H\alpha)_\mathrm{locus}$ is the fit of the PMS/MS locus which is shown in the colour-colour diagram of Fig. 5.2 as a solid line (see also Eq. (5.1)). The Hα-index is a measure of the Hα emission of a star and corresponds to the vertical distance of the star from the solid line in Fig. 5.2.

In order to correlate the Hα-index with the Hα emission equivalent widths, $W_\lambda(H\alpha)$, of a star I used the full-width at half-maximum of the transmission curves of the applied R_C and Hα filters (1620 Å and 70 Å respectively) and estimated that equivalent widths of $W_\lambda(H\alpha)$= 10 Å corresponds approximately to Hα indices of 0.1. Therefore, stars with large Hα emission were selected if their Hα-index is larger than 0.1 mag, i. e. if

$$\Delta(R_\mathrm{C} - \mathrm{H}\alpha) \geq 0.1. \tag{6.3}$$

To simplify matters I call these stars CTTSs in the subsequent discussion although this specific PMS nature of the stars is not really proven by my analysis because the Hα-index is only a rough estimate of $W_\lambda(H\alpha)$. However, the stars selected in this way show most likely the properties of accreting PMS stars. Stars that failed the selection criterion of Eq. (6.3) are called WTTSs for the moment.

6.3.2 Comparison of $\Delta(R_\mathrm{C} - \mathrm{H}\alpha)$ with the Hα Emission Equivalent Width

In order to verify the classification of CTTSs and WTTSs according to Eq. (6.3) I compared the measured Hα-emission equivalent widths, $W_\lambda(H\alpha)$, of 151 (not necessarily periodic

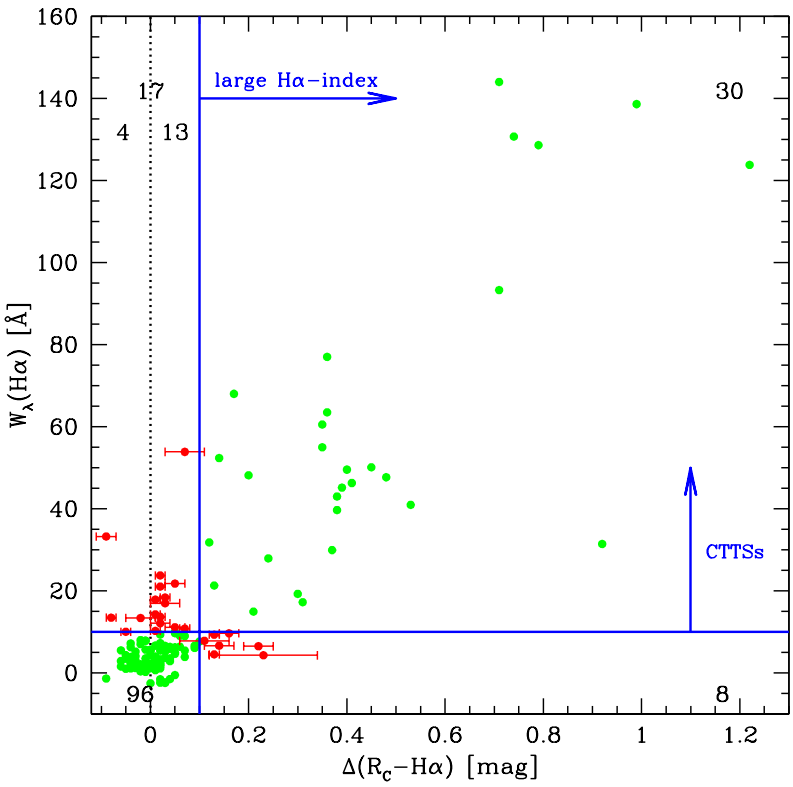

Fig. 6.4: The Hα-emission equivalent width $W_\lambda(H\alpha)$ as a function of the Hα-index, $\Delta(R_C - H\alpha)$, defined by Eq. (6.2). The blue vertical solid line has been placed at $\Delta(R_C - H\alpha) = 0.1$ mag which represents the selection criterion for stars with large Hα-emission (i. e. CTTSs). The blue horizontal solid line at $W_\lambda(H\alpha) \geq 10$ Å represents the classification of CTTSs commonly used in the literature. The vertical dotted line has been placed at $\Delta(R_C - H\alpha) = 0$ mag. The number of stars in each of the four quadrants defined by the solid lines are also given. Green symbols indicate that the classification of the stars agrees for both methods, while red symbols represent disagreement. For the latter stars also the photometric error $\delta(R_C - H\alpha)$ in the $(R_C - H\alpha)$ colour is indicated.

variable) TTSs from Rebull et al. (2002) with the calculated Hα-index of these stars. In Fig. 6.4 I show $W_\lambda(H\alpha)$ as a function of $\Delta(R_C - H\alpha)$ for all stars in this test sample. Stars with large Hα emission according to Eq. (6.3) are located right of the blue vertical solid line in this diagram while the stars with $W_\lambda(H\alpha) \geq 10$ Å are located above the blue horizontal solid line. These latter stars are CTTSs according to the commonly used definition.

The two blue solid lines divide the plane of the diagram in Fig. 6.4 into four quadrants. Both the Hα-emission equivalent width and the Hα-index selection criterion suggest that the 30 stars in the upper right and 96 stars in the lower left quadrant are CTTSs and WTTSs respectively (green symbols); i. e. for 126 stars (83.4%) the classifications resulting from the two different criteria agree. However, there are 25 stars in the upper left or lower right quadrant (red symbols) for which the classifications do not match. Since there are only 8 stars (5.3%) for which the Hα-index criterion suggests a classification as CTTSs but the stars are WTTSs according to $W_\lambda(H\alpha)$ measurement I conclude that the fraction

of erroneously classified CTTSs is negligible. The minimum equivalent width of these false detected CTTSs in the test sample is $W_\lambda(H\alpha)$= 4.3 Å.

There are 17 stars (11.3%) in the upper left quadrant, i. e. these stars are CTTSs according to the $W_\lambda(H\alpha)$ measurement but are classified as WTTSs according to the Hα-index. Most of these stars (13) are located right from the dotted line, i. e. they have a positive Hα-indices. In order to account for this relatively large contamination of selected WTTSs with stars that are actually CTTSs I will introduce later in Sect. 8.4.1 an additional sample of stars which I call "intermediate cases". For the moment all stars with $\Delta(R_C - H\alpha) \leq 0.1$ mag are called WTTSs but one has to keep in mind that about one tenth of these stars may actually be CTTSs.

I note that the fractions of erroneously classified CTTSs (5.3%) and erroneously classified WTTSs (11.3%) changes slightly to 7.6% and 8.8% respectively if out of the 151 stars in the test sample only those 91 stars are considered which are periodically variable according to my study. The reason for that is that most of the periodic variables are presumably WTTSs and the fraction of CTTSs is small among these stars (see below). In this (periodic) test sample only 20% (19/91) of the stars are CTTSs according to the $W_\lambda(H\alpha)$ data.

6.3.3 The Hα-index of Irregular and Periodic Variables

In Fig. 6.5 I show the cumulative distribution and the histogram of the Hα-index for periodic and irregular variables. It is evident that the Hα-index of the periodic variables is concentrated around zero and that only 22% of these stars have $\Delta(R_C - H\alpha) \geq 0.1$ mag. On the other hand the Hα-index of the irregular variables is distributed over a larger range and for 62% of the irregular variables it is above the critical level of 0.1 mag.

This supports the interpretation that the fraction of CTTSs among the irregular variables is higher than the fraction of CTTSs among the periodic variables and vice versa for the WTTSs (although some WTTSs may actually be CTTSs). In Sect. 7.3 I will quantify how strongly the sample of periodic variables is biased towards the WTTSs by comparing the fractions of CTTSs and WTTSs among the periodic variables with the expected fractions. However, first I look whether there is any correlation between the Hα-index and the degree of variability.

6.4 The Correlation between σ and the Hα-Index

In order to investigate the interpretation outlined in the previous section further I look for a correlation between the degree of variability of the stars and their Hα-index which is a measurement of their accretion and/or chromospheric activity (see Sect. 1.1). Fernàndez & Eiroa (1996) report a correlation of the Hα-emission (measured by $W_\lambda(H\alpha)$) and the amplitude of the variability (in the V-band) based on the study of 15 CTTS in the sense that the objects with the largest $W_\lambda(H\alpha)$ have the largest amplitudes. They conclude that the most active CTTSs show the largest degree of variability, while lower amplitude stars are less active. The same conclusion was drawn by Calvet, Cantó & Rodríguez (1983) based on the analysis of 12 stars.

In Fig. 6.6 I show σ and its median as a function of the Hα-index for periodic and

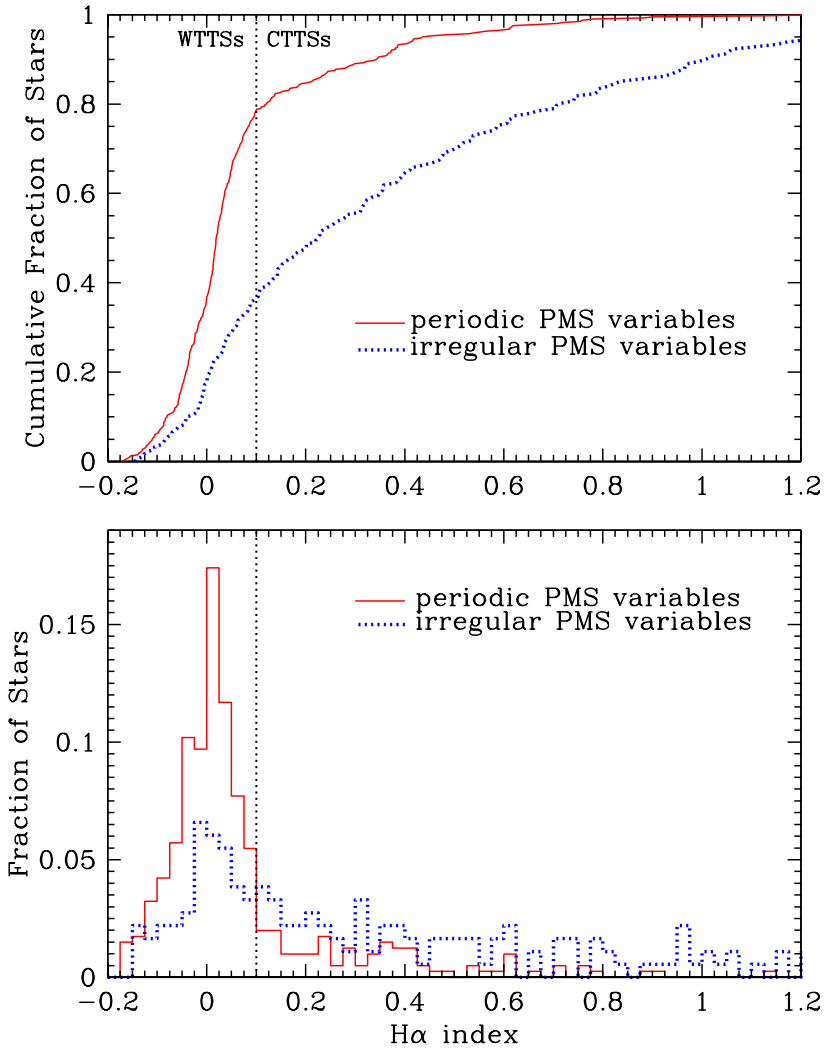

Fig. 6.5: Top panel: The cumulative frequency distribution of the Hα index, $\Delta(R_C - H\alpha)$, for all 405 periodic and 184 irregular variable PMS stars. The vertical dotted line indicates the classification criterion for WTTSs and CTTSs (see text). **(Bottom panel)**: The histogram of the Hα index for the two different samples of stars.

irregular variables respectively. It shows that for both samples there is an increase of the maximum σ with increasing Hα-index while in particular for the periodic variables the median σ increases with the Hα-index . The medians of σ for the periodic and irregular variables were calculated in fixed-sized bins of the Hα-index of width 0.075 mag and 0.2 mag respectively. Only bins with more than 14 data points are considered here. A Spearman rank-order correlation test (Press et al., 1992) indicates that the probability that the Hα-index and σ are not correlated is less than 6×10^{-28} if we use the joined sample of periodic and irregular variable stars. However, this high probability is dominated by the periodic sample. If only the periodic sample is used for this test the probability that σ and the Hα-index are not correlated is less than 9×10^{-15}. On the other hand the probability that σ and the Hα-index are not correlated for the irregular variables is only 0.137.

It is interesting that the variability of the periodic variables strongly correlates with the Hα-index while there is only weak evidence for such a correlation for the irregular

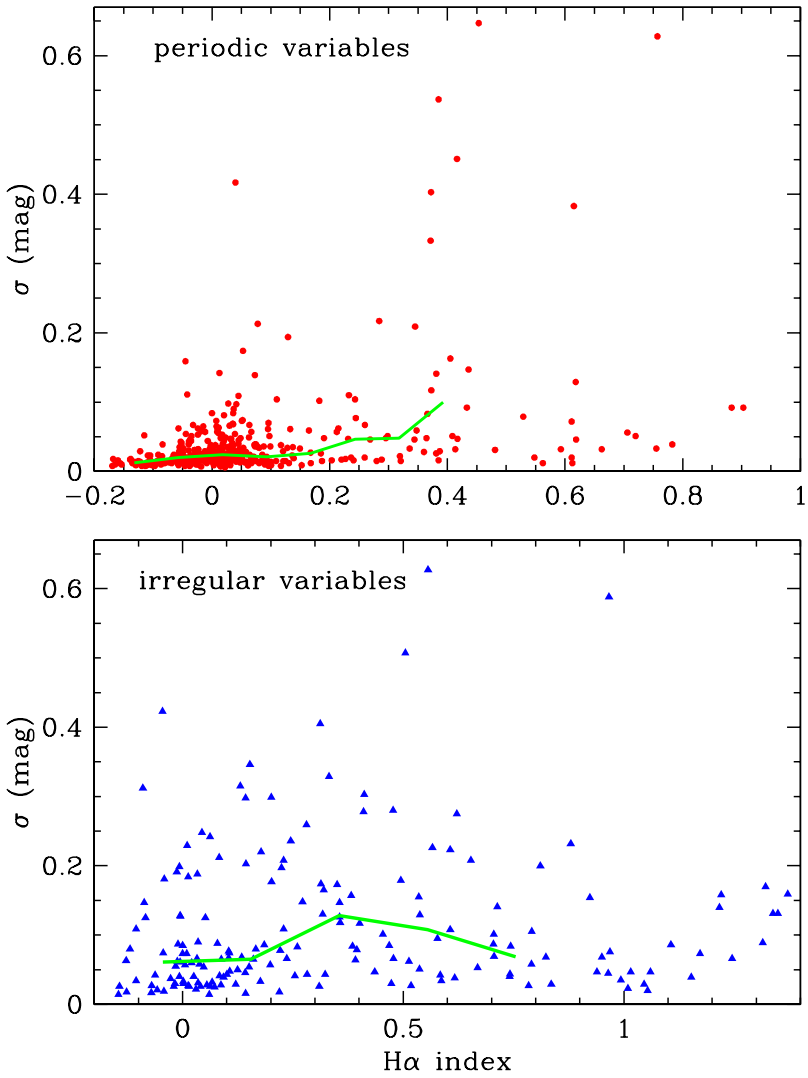

Fig. 6.6: The the degree of variability measured by the standard deviation σ as a function of $H\alpha$ index for all 405 periodic variable (**top panel**) and 184 irregular variable (**bottom panel**) PMS stars. The solid green lines represent the medians of σ for the periodic and irregular variables calculated in fixed sized bins of the Hα-index of width 0.075 mag and 0.2 mag respectively.

variables. One possible reason is that the sizes and numbers of cool spots (i. e. the total spot area) on periodic variables (WTTSs) are correlated with the chromospheric activity as in other active late type stars, i. e. periodic variables with more spots have more active regions on their surface and therefore stronger chromospheric Hα emission. For the irregular variables we see that there is a large scatter in the Hα, σ relation, and even low amplitude variables have large Hα indices. This could imply that there are many (irregular variable) CTTSs which have no large variations in their mass accretion rates. In addition these stars must have hot spot patterns which do not cause any large light modulations; e. g. accretion rings symmetric to the rotation axis (see e. g. Mahdavi & Kenyon, 1998).

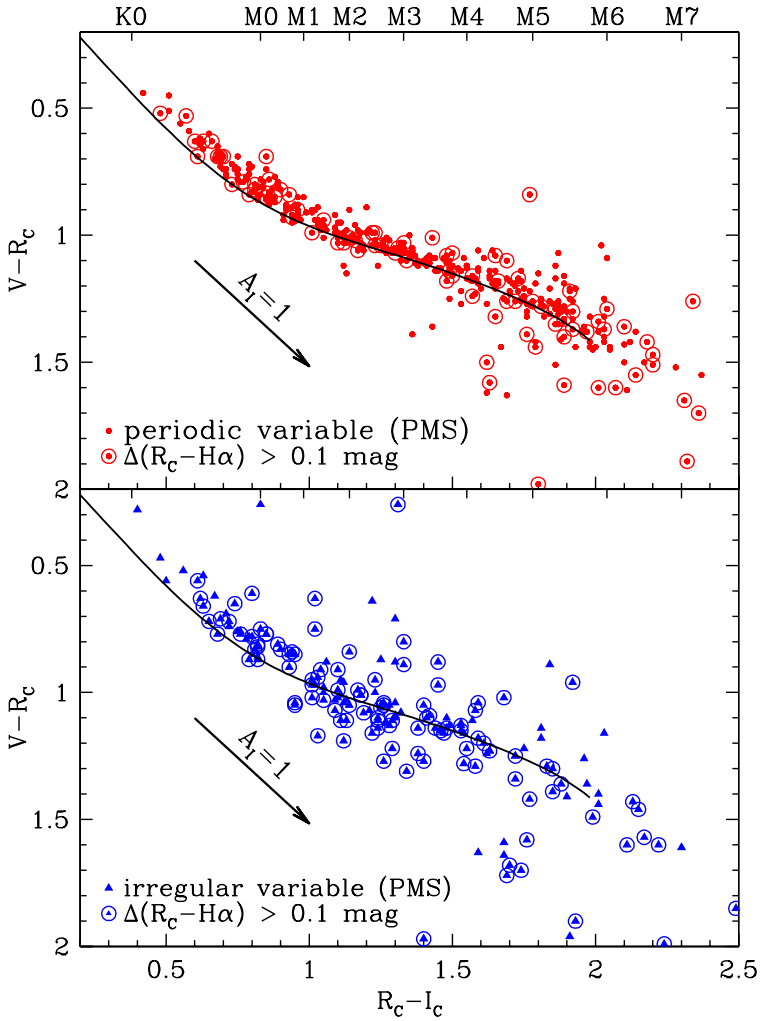

Fig. 6.7: The $(V - R_C)$ vs $(R_C - I_C)$ colour-colour diagram for periodic (top panel) and irregular variables (bottom panel) that passed both of our two PMS tests. Those stars which have an Hα-index$\geq$ 0.1 and therefore show the properties of accreting CTTSs are marked with a surrounding circle. The solid lines in both panels represents the ZAMS. The arrow length and direction indicates the mean reddening towards NGC 2264.

6.5 The $(V - R_C)$ vs $(R_C - I_C)$ Colour-Colour Diagram

In Fig. 6.7 I show the $(V - R_C)$ vs $(R_C - I_C)$ colour-colour diagram for periodic and irregular variables which passed both of the two PMS tests. The stars with an Hα-index of $\Delta(R_C - H\alpha) \leq 0.1$ are marked separately. It is evident that the scatter is much larger among the irregular variables compared to the periodic variables. Agreement with the ZAMS is good, although deviations due to the smaller log g values of the PMS stars are expected. The data points below the MS (i. e. with larger $(V - R_C)$ colours than a MS star) can be explained in both plots by embedded stars which are highly reddened with up to eight times the mean reddening. This interpretation is supported by the analysis of Rebull et al. (2002). They have determined an average $E(R_C - I_C) = 0.1 \pm 0.02$ mag in NGC 2264, but showed that some stars in NGC 2264 are reddened by up to $E(R_C - I_C)$= 1 mag.

Chapter 7

Completeness Level & Biases of the PMS sample

7.1 "Non-variable" PMS Members with Strong Hα Emission

Based on a periodic and irregular variability study I have selected a total number of 589 PMS members (405 periodic and 184 irregular variables) using the two selection criteria described in Sect. 5. However, there may exist low-amplitude PMS stars, for which I could detect no significant variability. Reasons for a small degree of variability in WTTSs could be a more or less equally distributed pattern of many spots causing only a small net modulation of the stellar brightness (see also Sect. 9.3) and in CTTSs there could be phases of relatively stable mass accretion. To simplify matters I call these stars "non-variable" PMS stars. In order to search for "non-variable" PMS stars both PMS tests described in Sect. 5 were applied to all stars which were not detected to be variable. As I will discuss in the following, "non-variable" PMS stars were selected if they passed both tests and have in addition strong Hα emission.

In Fig. 7.1 I show the $(R_{\rm C} - {\rm H}\alpha)$ vs $(R_{\rm C} - I_{\rm C})$ colour-colour-diagram for all "non-variable" stars which passed the two PMS selection criteria described in Sect.5.1 and Sect.5.2 respectively. The solid line in Fig. 7.1 represents the the PMS/MS locus while the dotted line represents an Hα-index of $\Delta(R_{\rm C} - {\rm H}\alpha) = 0.1$ mag (see Sect. 6.3.1).

I consider only stars as "non-variable" PMS members if they are located more than their photometric error $\delta(R_{\rm C} - {\rm H}\alpha)$ above the dotted line, i. e.

$$\Delta(R_{\rm C} - {\rm H}\alpha) \; -\delta(R_{\rm C} - H\alpha) \geq 0.1. \tag{7.1}$$

The stars which fulfil this condition are most likely CTTSs (see discussion in Sect. 6.3). This selection criterion was used since non-variable foreground MS stars are indistinguishable from "non-variable" WTTSs in the diagram of Fig. 7.1. 52 of the "non-variable" stars with $(R_{\rm C} - I_{\rm C}) \leq 2.5$ mag in Fig. 7.1 passed this additional selection criterion. Out of these "non-variable" PMS members 2 stars (no. 5941 = LkHα 55 and no. 6164 = W189) were classified as PMS stars prior to this study. Another 13 previously known "non-variable" PMS members (WTTSs) did not pass this additional test. The 50 newly found PMS stars are separately marked in Fig. 7.1 and listed in Table 7.1.

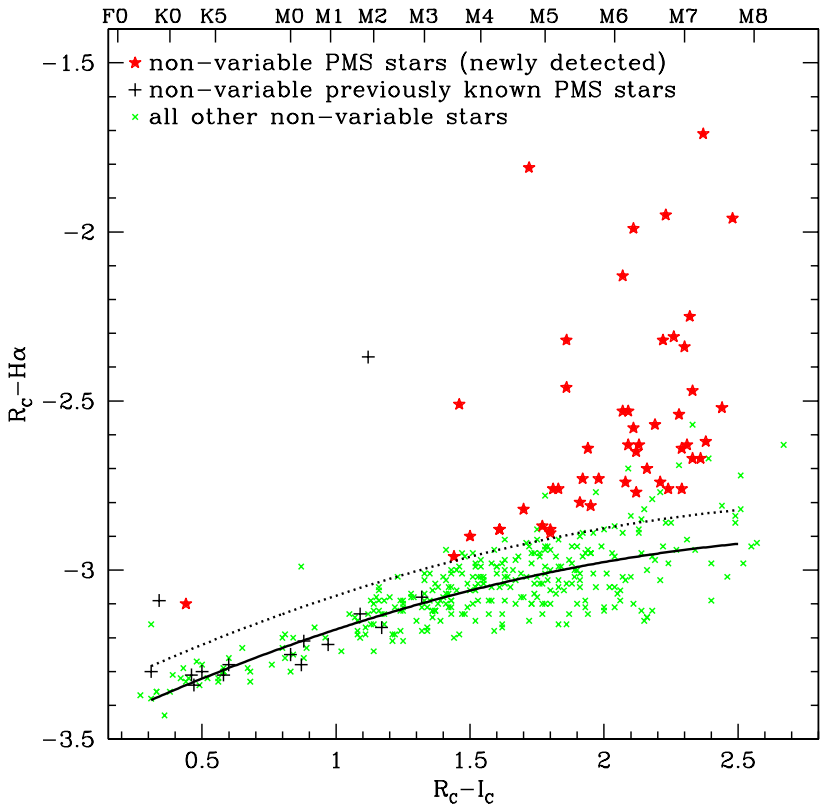

Fig. 7.1: The $(R_{\rm C} - {\rm H}\alpha)$ vs $(R_{\rm C} - I_{\rm C})$ colour-colour-diagram for all "non-variable" stars which passed the two PMS test (see Sect. 5) including previously known "non-variable" PMS members. The dotted line represents the selection criterion for "non-variable" PMS stars, i. e. an Hα-index of 0.1 mag. All "non-variable" stars which are located by more than their error in $(R_{\rm C} - {\rm H}\alpha)$ above the dotted line were classified as "non-variable" PMS stars.

From Fig. 7.1 it is evident that most (i. e. 83%) of the new "non-variable" PMS members have $(R_{\rm C} - I_{\rm C}) \leq 1.8$ mag. This can be understood if one considers that the photometric errors of these stars are typically larger compared with the bluer (i. e. brighter) stars. Therefore any variations in the light curves are harder to detect.

In total I have identified 641 PMS stars in NGC 2264; 405 periodic variable 184 irregular variables and 52 "non-variable" stars with strong Hα emission. Compared to the 182 previously known PMS stars and PMS candidates reported by Park et al. (2000) (not including 26 previously known massive OB stars) I have increased the number of known PMS stars in NGC 2264 by a factor of 3.5. As already mentioned in Sect. 5.3 most of the newly found PMS stars are low mass stars ($M \lesssim 0.25\,M_{\odot}$) with masses probably extending into the substellar regime (see also Fig. 8.1).

Tab. 7.1: New "non-variable" PMS stars in NGC 2264. The stars were selected from a sample of "non-variable" stars which passed both PMS tests and have in addition strong Hα emission of $\Delta(R_{\rm C}-{\rm H}\alpha)\ -\delta(R_{\rm C}-H\alpha) \geq 0.1$ (see text). P_{vari} is the probability that the star is variable according to the χ^2 test and $\Delta(R_{\rm C}-{\rm H}\alpha)$ is the Hα-index of the star. The other columns are the same as in Table 3.5.

Star	$\alpha(J2000)$	$\delta(J2000)$	$I_{\rm C}$	err	$(V-I_{\rm C})$	err	$(R_{\rm C}-I_{\rm C})$	err	$(R_{\rm C}-{\rm H}\alpha)$	err	$\Delta(R_{\rm C}-{\rm H}\alpha)$	σ	P_{vari}	cross id
156	6:39:15.84	9:46:34.1	17.84	0.01	3.32	0.05	1.98	0.03	-2.73	0.14	0.25	0.019	0.049	R1305
2163	6:40:10.41	9:51:15.2	17.33	0.01	3.03	0.01	1.80	0.01	-2.89	0.01	0.12	0.019	0.234	R1828
2727	6:40:16.67	9:40:23.0	17.15	0.01	3.06	0.01	1.77	0.01	-2.87	0.03	0.14	0.014	0.948	R2003
6:40:2	1.07	9:35:25.5	17.55	0.01	3.59	0.03	2.09	0.01	-2.63	0.19	0.33	0.01	2.920e−04	
9:2	1.32	9:48:26.5	19.00	0.03	...	...	2.26	0.03	-2.31	0.10	0.63	0.04	5.500e−05	
9:49:55.7	18.28	0.02	...	...	2.19	0.02	-2.57	0.05	0.38	0.014	0.328	R2324		
9:48:9.0	18.36	0.02	3.82	0.15	2.24	0.03	-2.76	0.05	0.19	0.019	0.021			
9:45:19.5	17.83	0.01	3.36	0.03	2.08	0.01	-2.74	0.04	0.23	0.010	0.281	R2397		
9:47:37.5	16.83	0.02	3.26	0.06	2.07	0.02	-2.13	0.07	0.84	0.017	0.993	R2401		
9:41:4.4	18.60	0.01	3.39	0.07	2.07	0.03	-2.53	0.06	0.44	0.017	5.000e−06			
9:50:20.2	16.79	0.01	2.62	0.01	1.50	0.01	-2.90	0.01	0.16	0.007	0.000			
16.2	19.42	0.03	...	...	2.28	0.05	-2.54	0.15	0.40	0.034	0.016			
33.6	16.73	0.01	3.02	0.01	2.80	0.01	-2.88	0.02	0.13	0.009	0.000	R2507		
17.71	0.04	3.06	0.01	2.81	0.01	-2.76	0.05	0.24	0.157	3.630e−04				
0.04	2.07	0.08	2.09	0.09	-2.53	0.18	0.43	0.035	3.100e−05					
0.03	...	...	2.38	0.09	-2.62	0.11	0.31	0.025	2.017e−03					
0.01	3.05	0.01	2.86	0.02	-2.46	0.02	0.54	0.007	0.000	R2959				
0.88	0.01	0.44	0.01	-3.10	0.06	0.24	0.014	0.000	Y2525,R2979 ,P67					
...	...	2.31	0.08	-2.63	0.17	0.31	0.040	9.026e−03						
...	...	2.23	0.07	-1.95	0.44	1.00	0.034	7.261e−03						
...	...	2.33	0.04	-2.67	0.09	0.27	0.019	2.000e−06						
...	...	2.30	0.05	-2.34	0.16	0.60	0.024	0.000						
...	...	2.48	0.07	-1.96	0.10	0.96	0.031	0.595						
3.14	0.09	1.86	0.02	-2.32	0.03	0.68	0.022	0.993						
...	2.22	0.05	-2.32	0.09	0.63	0.044	0.034							
0.02	2.70	0.01	-2.82	0.06	0.20	0.03	3.000	R3428						
0.02	-2.80	0.06	0.19	0.015	0.032	R3520								
0.02	-2.67	0.09	0.26	0.016	0.610	R3523								
0.02	-2.77	0.03	0.19	0.011	0.039									
0.01	-2.51	0.10	0.56	0.014	0.026	R3568								
0.03	-1.99	0.06	0.97	0.019	2.423e−03									

Tab. 7.1: (continued)

Star	$\alpha(J2000)$	$\delta(J2000)$	I_C	err	$(V-I_C)$	err	(R_C-I_C)	err	$(R_C-H\alpha)$	err	$\Delta(R_C-H\alpha)$	σ	P_{vari}	cross id
6154	6:41:12.75	9:32:28.7	17.51	0.01	3.31	0.03	1.95	0.01	-2.81	0.02	0.17	0.009	0.000	R3701
6169	6:41:13.11	9:24:36.9	16.44	0.01	2.79	0.01	1.61	0.01	-2.88	0.01	0.16	0.006	0.000	Y3810,R3716
6190	6:41:13.77	9:29:32.5	17.64	0.02	3.53	0.04	2.12	0.02	-2.65	0.03	0.31	0.009	3.940e−04	R3729
6302	6:41:17.35	9:31:52.8	18.18	0.02	3.62	0.09	2.29	0.02	-2.76	0.05	0.18	0.011	1.000e−06	
6306	6:41:17.38	9:35:56.5	19.28	0.03	...	...	2.44	0.05	-2.52	0.12	0.41	0.030	5.510e−04	
6354	6:41:18.66	9:49:2.7	18.20	0.01	3.31	0.04	1.92	0.01	-2.73	0.06	0.26	0.017	4.781e−03	
6355	6:41:18.69	9:32:52.7	19.03	0.02	...	...	2.32	0.07	-2.25	0.08	0.69	0.026	0.000	
6359	6:41:18.77	9:35:19.6	19.45	0.04	...	...	2.33	0.07	-2.47	0.16	0.47	0.033	3.219e−03	
6490	6:41:2.44	9:53:1.9	17.86	0.01	2.94	0.03	1.72	0.03	-1.81	0.04	1.21	0.018	0.430	
6:41:23.29	9:32:30.7	18.70	0.03	3.33	0.07	2.13	0.02	-2.63	0.06	0.33	0.012	5.210e−03		
1:24.02	9:26:53.0	17.61	0.01	3.08	0.03	1.83	0.01	-2.76	0.03	0.24	0.008	8.200e−05		
9:30:26.6	17.89	0.01	3.45	0.04	2.11	0.03	-2.58	0.05	0.38	0.014	0.024	R4001		
9:26:29.8	18.19	0.02	3.51	0.05	2.21	0.03	-2.74	0.05	0.21	0.012	8.000e−06	R4033		
9:28:7.7	19.22	0.03	...	...	2.16	0.03	-2.70	0.10	0.26	0.031	0.133			
9:53:58.5	17.14	0.01	3.23	0.02	2.94	0.02	-2.64	0.07	0.34	0.013	0.128			
48.6	19.39	0.03	...	...	2.37	0.08	-1.71	0.10	2.22	0.029	0.000			
2	0.01	2.77	0.02	1.61	0.01	-2.88	0.03	0.16	0.017	0.449				
1	2.56	0.01	1.44	0.01	-2.96	0.01	0.11	0.032	0.103	R4619				
3.49	0.13	2.29	0.03	-2.64	0.08	0.30	0.037	0.452						

7.2 Fraction of Variable PMS Stars and Completeness Level of the PMS Sample

In this section I estimate the fraction of variable PMS stars in the cluster. From this fraction I estimate the completeness level of the sample of variable PMS stars in NGC 2264. Therefore the central question in this section is: what fraction of PMS stars was detected through the photometric monitoring program and the adopted methods in selecting PMS stars?

The fraction of variable cluster members is given by

$$f_{\rm vari} = N_{\rm vari}/(N_{\rm vari} + N_{\rm non-vari}), \tag{7.2}$$

where $N_{\rm vari}$ is the number of variable (both periodic and irregular) and $N_{\rm non-vari}$ is the number of "non-variable" PMS stars in NGC 2264. These numbers (in particular $N_{\rm non-vari}$) are known for CTTSs since the PMS nature of these stars can be confirmed by an enhanced Hα emission. In addition one expects that there are also WTTSs (with no or weak Hα emission) which are "non-variable"; i. e. they have light modulations below the detection limit of this study. As mentioned above, in the $I_{\rm C}$ vs $(R_{\rm C} - I_{\rm C})$ colour-magnitude or $(R_{\rm C} - {\rm H}\alpha)$ vs $(R_{\rm C} - I_{\rm C})$ colour-colour diagrams these stars are indistinguishable from "non-variable" MS foreground stars. In order to estimate the number of "non-variable" WTTSs I therefore have to keep the relative contamination by foreground MS stars as low as possible. This is achieved by using only the two regions NGC 2264 N and S (see Sect. 5.2) for the analysis rather than the whole observed field. In order not to be affected in the following analysis by photometric errors I restrict myself to stars with $I_{\rm C} \leq 18.0$ mag and $(R_{\rm C} - I_{\rm C}) \leq 1.8$ mag. The latter criterion in particular was chosen to be less dependent of the adopted Hα-index which was used in the colour-colour diagram of Fig. 7.1 for selecting "non-variable" PMS stars.

Table 7.2 lists the number of variable and "non-variable" stars in each of the two regions which passed both PMS tests (see Sect. 5) and are in these colour and magnitude ranges. From the last column of this table it is evident that in the two regions NGC 2264 N and S about 74% of the PMS candidates (i. e. stars that passed the two tests) are variable. About half of the PMS candidates show periodic light modulations while only one fourth of the PMS candidates are irregularly variable. I note that these fractions are only rough estimates since I assumed that all stars in the two regions which passed both tests are indeed PMS stars. In particular I assumed that the contamination by non-members in the variable sample is negligible; i. e. all variables that passed both PMS test are actually PMS stars.

However, if I further assume that the two regions are representative for the whole cluster I can conclude that at least $f_{\rm vari} = 74\%$ of the PMS stars have been detected to be variable. This lower limit of the fraction of detected variable stars is not significantly higher if I consider only brighter stars; e. g. for stars with $I_{\rm C} \leq 16.0$ mag in NGC 2264 N and S I obtain a fraction of $f_{\rm vari} = 76\%$.

Since *all* PMS stars in the cluster are expected to be variable at some level my variability study is sensitive for detecting PMS stars with $I_{\rm C} \leq 18.0$ mag and $(R_{\rm C} - I_{\rm C}) \leq 1.8$ mag at a 74% level. As I will show in the following section the completeness level differs for WTTSs and CTTSs. While nearly all (95%) of the CTTSs are found to be variable only 68% of the WTTSs are found to be variable.

Tab. 7.2: The estimated fraction of variable stars in NGC 2264 N and S with $I_C \leq 18.0$ mag and $(R_C - I_C) \leq 1.8$ mag. Listed are numbers and fractions of periodic PMS variables (N_{p-vari}), irregular PMS variables (N_{i-vari}), "non-variable" PMS candidates ($N_{non-vari}$), the total number of all PMS candidates ($N_{PMS-total} = N_{p-vari} + N_{i-vari} + N_{non-vari}$), and the numbers and fractions of PMS variables ($N_{p-vari} + N_{i-vari}$) in the two concentrations of PMS stars NGC 2264 N and S (for a definition of the PMS candidates see text). The fractions were calculated relative to the total number of PMS star candidates ($N_{PMS-total}$) in the two regions.

sample of stars	North	South	North & South
$N_{PMS-total}$ ...	110	120	230 .....
$N_{non-vari}$	25 (22.7%)	36 (30.0%)	61 (26.5%)
N_{p-vari}	56 (50.9%)	54 (45.0%)	110 (47.8%)
N_{i-vari}	29 (26.4%)	30 (25.0%)	59 (25.7%)
variables	85 (77.3%)	84 (70.0%)	191 (73.5%)

In summary I conclude that the method of photometric monitoring is a very powerful tool for finding most PMS stars in the cluster since about three quarters of the whole PMS population in NGC 2264 (with $(R_C - I_C) \leq 1.8$ mag) could be identified this way. Therefore, my database of periodic and irregular variables should be a representative subset of the PMS stars in NGC 2264.

7.3 The Fraction of Periodic Variable CTTSs and WTTSs

In the following I estimate the fraction of periodic variables among the WTTSs and CTTSs in order to investigate how strongly the period distribution of NGC 2264 is biased by the non-detection of periods in these two groups of stars. Again I restrict the analysis to stars with $I_C \leq 18.0$ mag and $(R_C - I_C) \leq 1.8$ mag. Furthermore I consider in this section only stars that passed both PMS tests.

As already outlined in Chapter 6 the periodic variables are biased towards the WTTSs since it is much harder to detect periodically brightness modulations of CTTSs in the presence of a superimposed irregular variability. However, I will show below that this bias towards the WTTSs is partially compensated for the periodic sample due to those WTTSs with brightness modulations below the detection limit and which therefore have not been found.

As in Sect. 6.3 and Sect. 7.1 I regard all stars with enhanced Hα emission measured by the Hα-index as CTTSs. This is the case for $N_{CTTS} = 151$ stars in the whole region investigated. While 89 (59%) of these stars are irregularly variable only 49 (32%) are periodically variable and 13 (9%) are "non-variable". Thus only for about one third (49/151) of the CTTSs are periods detectable.

It is more difficult to estimate the total number of WTTSs in the cluster (N_{WTTS}) since "non-variable" WTTSs are indistinguishable from MS foreground stars in the I_C vs $(R_C - I_C)$ colour-magnitude and in the $(R_C - H\alpha)$ vs $(R_C - I_C)$ colour-colour diagram. However, with the result of the previous section (i. e. that about three-quarter of the PMS stars are variable) it is possible to estimate the total number of PMS stars in the cluster

($N_{\rm PMS}$) and since $N_{\rm PMS} = N_{\rm CTTS} + N_{\rm WTTS}$ I can determine $N_{\rm WTTS}$ indirectly.

Therefore I first estimate $N_{\rm PMS}$. In total 465 stars with $(R_{\rm C} - I_{\rm C}) \leq 1.8$ mag and $I_{\rm C} \leq 18.0$ mag are periodic or irregular variables. Since at least 73.5% of the PMS stars are variable (see Sect. 7.2) I obtain $N_{\rm PMS} = 465/0.735 \simeq 630$. With $N_{\rm WTTS} = N_{\rm PMS} - N_{\rm CTTS}$ I obtain $N_{\rm WTTS} \simeq 630 - 151 = 479$.

Of the periodic variables with $(R_{\rm C} - I_{\rm C}) \leq 1.8$ mag and $I_{\rm C} \leq 18.0$ mag 265 have a small Hα-index and are therefore classified as WTTSs. In addition 62 irregular variables are classified as WTTSs. Using these numbers I find that for at least 55% (265/479) of the WTTSs in NGC 2264 periods were detected and at least 13% (62/479) of the WTTSs I detected as irregular variables; i. e. in total for 68% of the WTTSs I have detected variability.

How do the measured period fractions of 55% and 32% for the WTTSs and CTTSs respectively influence the final period distribution? To answer this question let us first assume that the periods for *all* (estimated) 630 PMS stars in the cluster with $(R_{\rm C} - I_{\rm C}) \leq 1.8$ mag and $I_{\rm C} \leq 18.0$ mag could be measured. Using $N_{\rm CTTS} = 151$ and $N_{\rm WTTS} = 479$ (see above) I find that 24% (151/630) of the stars in NGC 2264 are CTTSs while the fraction of WTTSs is 76% (479/630). In my study 16% (49/314) of the periodic variables in these colour and magnitude ranges are classified as CTTSs and 84% (265/314) of the periodic variables are WTTSs. In Tab. 7.3 I summarise these results. From these numbers I conclude that the final period distribution is only slightly biased towards WTTSs in the sense that the periodic sample contains 9.5% more WTTSs than one would expect from the estimated composite of the cluster population.

Tab. 7.3: The estimated fractions of WTTSs and CTTSs among the total cluster population and the sample of periodic variables. Note that only stars with $(R_{\rm C} - I_{\rm C}) \leq 1.8$ mag and $I_{\rm C} \leq 18.0$ mag are considered.

sample of stars	WTTSs	CTTSs
estimated cluster population	76%	24%
periodic variables	84%	16%

Chapter 8

The Rotational Evolution of Low Mass Stars

In this section I present the rotation period distribution of NGC 2264 and compare it with that of the ONC because the ONC (aside from NGC 2264) is the only cluster PMS for which a statistical significant sample of rotation periods is known. One important aim is to examine the rotational evolution of low mass PMS stars (i. e. $0.1\,M_{\odot} \leq M \leq 1.5\,M_{\odot}$) in the context of disk-locking in oder to achieve a better understanding of their rotational evolution. For this purpose I also investigate to what degree there is ongoing disk-locking in NGC 2264. As it will be shown in the following Sections the invoked processes of magnetic stars-disk interaction are quite complex, which complicates simple interpretation of the period distributions in terms of disk-locked and not disk-locked stars.

For a comparison of the rotation period distributions it is essential to know the ages of the two clusters. However, the absolute ages depend strongly on the PMS evolution model used. As will be shown in Sect. 8.2.3 for the investigation of the rotational evolution it is sufficient to know the mean age ratio between the two clusters which should be better constrained. Therefore, I first determine the relative ages of NGC 2264 and the ONC in the following section.

8.1 The Age Ratio of NGC 2264 and ONC

The ages of the two clusters used in the literature are 1 Myr for the ONC (Hillenbrand, 1997) and 2–4 Myr for NGC 2264 (Park et al., 2000). These ages have been determined using several different PMS evolution models and are in some respects "*mean*" values of these different age estimates for each cluster. Using these numbers the age ratio of the two clusters is between two and four. However, the deduced ages are very model dependent and Park et al. (2000) demonstrated for NGC 2264 that different models lead to cluster ages ranging from 0.9 Myr up to 4.3 Myr, i. e. the estimated cluster ages differ by a factor of 4.8. Therefore, the ages of the two clusters which are used in the literature are not consistent and it is necessary that the age ratio of the clusters is determined for each model separately. In this way the the resulting age ratios are less affected by differences of the adopted PMS models (e. g. the zero point).

For the age determination of the ONC, Hillenbrand (1997) used the two PMS evolu-

Tab. 8.1: Estimated mean ages of NGC 2264 ($t_{\rm NGC\,2264}$) and the ONC ($t_{\rm ONC}$) taken from the literature. Ages were taken from Hillenbrand (1997) for the ONC and from Park et al. (2000) for NGC 2264. Listed are the PMS evolution model employed in the study from which the cluster age was taken (SF94 = Swenson et al., 1994; DM97 = D'Antona & Mazzitelli, 1994; BC98-I,II = Baraffe et al., 1998), the deduced cluster ages, and, if the same model was applied in both clusters, the resulting age ratio ($t_{\rm NGC\,2264}/t_{\rm ONC}$).

model	$t_{\rm ONC}$	$t_{\rm NGC\,2264}$	$\frac{t_{\rm NGC\,2264}}{t_{\rm ONC}}$
SF94	1.5 Myr	2.1 Myr	1.4
DM94	0.5 Myr	0.9 Myr	1.8
BC98-I	.....	4.3 Myr	...
BC98-II	.....	2.7 Myr	...

tion models by Swenson et al. (1994, hereafter SF94) and D'Antona & Mazzitelli (1994, hereafter DM94). These two PMS evolution models were also used for the age determination of NGC 2264 by Park et al. (2000). In addition Park et al. (2000) determined the age of NGC 2264 by employing two models of Baraffe et al. (1998, hereafter BC98-I and BC98-II). Tab. 8.1 summarises the results of the age determination of these studies in NGC 2264 and the ONC. For the models by SF94 and DM94 which were used in both studies also the resulting age ratios of the clusters are listed. The estimated ages of the ONC differ by a factor of three while the determined ages of NGC 2264 differ by a factor of 4.8 (or 2.3 considering only the models SF94 and DM94).

In order to get another independent determination of the age ratio of NGC 2264 and ONC I determined the mean ages of the clusters by adopting an improved PMS evolution model of D'Antona & Mazzitelli (1997, hereafter DM97). For the age determination of NGC 2264 I used the sample of 589 variable PMS stars (i. e. 405 periodic and 184 irregular variables) from the study presented here. This is a much larger data set compared to the 208 cluster members used by Park et al. (2000) for the age determination of NGC 2264. In Fig. 8.1 I show the observed $I_{\rm C}$ vs $(R_{\rm C} - I_{\rm C})$ colour-magnitude diagram of these 589 stars in NGC 2264. Individual dereddening of all stars in this sample is not possible because reddening, $E(R_{\rm C} - I_{\rm C})$, and extinction, $A_{I_{\rm C}}$, published by Rebull et al. (2002) are available only for about 180 of these stars. Therefore I calculated reddened isochrones and evolution tracks of the DM97 model by using the mean values $E(R_{\rm C} - I_{\rm C}) = 0.10 \pm 0.02$ and $A_{I_{\rm C}} = 0.25$ of the reddening and extinction towards NGC 2264 which were determined by Rebull et al. (2002) adopting $R = E(B-V)/A_V = 3.1$.

For the determination of the mean age of NGC 2264 I first calculated the median $I_{\rm C}$ magnitude in $(R_{\rm C} - I_{\rm C})$ colour bins of 0.1 mag width and determined the median age in each of these colour bins by applying the reddened isochrones of the DM97 model. The calculated median ages are listed in Tab. 8.2. The resulting mean age of NGC 2264 (i. e. the mean of the listed medians) is 1.0 ± 0.1 Myr.

The age of the ONC was calculated by using dereddened $I_{\rm C,0}$ and V_0 photometry of 785 cluster members with known spectral type in the colour range 0.55 mag $\leq (V - I_{\rm C})_0 \leq$ 2.05 mag taken from Hillenbrand (1997). The $I_{\rm C,0}$ vs $(V - I_{\rm C})_0$ colour-colour diagram of the ONC is shown in Fig. 8.1. Tab. 8.2 also lists the median ages of ONC stars calculated in 0.2 mag wide $(V - I_{\rm C})_0$ colour bins. The mean age of the ONC resulting from these medians is 0.5 ± 0.1 Myr.

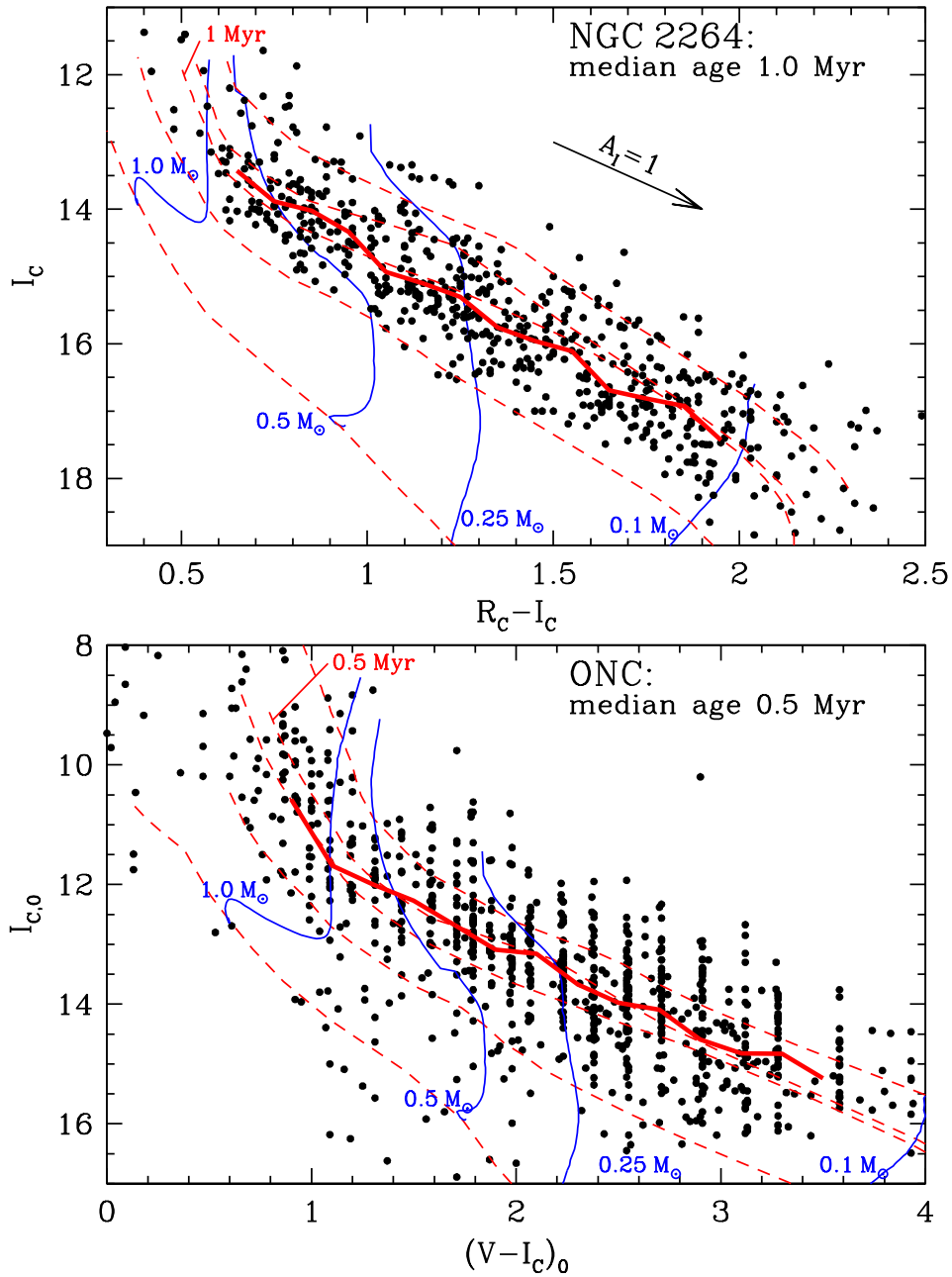

Fig. 8.1: Top panel: The colour-magnitude diagram of the 405 periodic and 184 irregular PMS variables in NGC 2264 found in this study. The red dashed lines are (0.1, 0.5, 1.0, 5.0, and 200 Myr) isochrones and the blue thin solid lines are evolution tracks for four different masses (0.1, 0.25, 0.5, and 1.0 $M_{\odot}$) by D'Antona & Mazzitelli (1997). The isochrones and evolution tracks were reddened using the mean reddening $E(R_{\rm C} - I_{\rm C}) = 0.1$ and extinction $A_{I_{\rm C}} = 0.25$ (Rebull et al., 2002). The red thick solid line is the median $I_{\rm C}$ magnitude of the stars calculated in different colour bins. **Bottom panel**: The colour-magnitude diagram of 785 individually dereddened ONC stars with known spectral type taken from (Hillenbrand, 1997). The solid and dashed lines are (unreddened) evolution tracks and isochrones respectively for the same masses and ages as in the top panel.

Tab. 8.2: Left: The median I_C magnitude in $(R_C - I_C)$ colour bins of 0.1 mag size for stars in NGC 2264, where the listed $(R_C - I_C)$ colours are the colour of the bin centres. Also listed are the number of data points per bin which was used for the determination of the median magnitude, the logarithm of the median age, and the median age of the stars in each bin. The median ages were derived employing reddened PMS evolution models by D'Antona & Mazzitelli (1997) assuming mean values of $E(R_C - I_C) = 0.1$ and $A_{I_C} = 0.25$. **Right**: The same for ONC stars. Listed are the median $I_{C,0}$ magnitudes in $(V - I_C)_0$ colour bins of 0.2 mag width. The dereddened photometric data were taken from Hillenbrand (1997).

NGC 2264					**ONC**				
$(R_C - I_C)$	median I_C	data points	log(age/yr)	age/Myr	$(V - I_C)_0$	median $I_{C,0}$	data points	log(age/yr)	age/Myr
0.65	13.43	25	5.8703	0.7	0.90	10.58	49	5.9906	1.0
0.75	13.88	34	5.8720	0.7	1.10	11.68	50	6.0511	1.1
0.85	14.02	45	5.7753	0.6	1.30	12.00	34	5.7625	0.6
0.95	14.34	28	5.8484	0.7	1.50	12.27	53	5.6537	0.5
1.05	14.93	34	6.0931	1.2	1.70	12.68	76	5.6975	0.5
1.15	15.10	51	6.0614	1.2	1.90	13.09	60	5.7684	0.6
1.25	15.30	55	6.0374	1.1	2.10	13.16	41	5.6442	0.4
1.35	15.76	33	6.1667	1.5	2.30	13.67	100	5.7687	0.6
1.45	15.96	39	6.0933	1.2	2.50	13.98	76	5.7386	0.5
1.55	16.11	35	6.0285	1.1	2.70	14.09	63	5.3040	0.2
1.65	16.69	34	6.1856	1.5	2.90	14.59	63	5.6326	0.4
1.75	16.81	41	5.9817	1.0	3.10	14.82	54	5.5719	0.4
1.85	16.92	41	5.9279	0.8	3.30	14.83	43	5.2723	0.2
1.95	17.43	27	5.8179	0.7	3.50	15.24	23	5.3356	0.2
mean age.....			5.9828	1.0 ± 0.1	mean age			5.6566	0.5 ± 0.1

The median and extreme values of the newly calculated cluster ages for the two clusters yield to an age ratio of $t_{\mathrm{NGC\,2264}} \;/\; t_{\mathrm{ONC}} = 2^{+0.75}_{-0.5}$. Taking also into account the numbers listed in Tab. 8.1 I conclude that the age ratio of the two clusters ($t_{\mathrm{NGC\,2264}} \;/\; t_{\mathrm{ONC}}$) previously estimated as 2–4 is actually more closer to two. Therefore I assume for the subsequent analysis that NGC 2264 is about twice as old than the ONC. I note that the absolute ages of the clusters may be somewhat larger than it is suggested by the analysis outlined above because the D'Antona & Mazzitelli models typically results in smaller ages compared with models by other authors.

8.2 The Rotation Period Distribution: From the ONC to NGC 2264

In this section I present the rotation period distributions of NGC 2264 and compare it with that of the ONC.

8.2.1 The Colour Dependence of the Rotation Periods in NGC 2264

As a first step I investigate how the period distribution in NGC 2264 depends on the colour of the stars. It is searched for a colour dependence instead of a mass dependence of the rotation periods because masses are only known from the analysis of Rebull et al. (2002) for about 150 of the 405 periodically variables. In addition the sample of stars with known

masses is biased towards the higher mass regime.

Fig. 8.2 shows both the period (P) and the angular velocity ($\omega = 2\pi/P$) as a function of the $(R_C - I_C)$ colour for all 405 periodically variable PMS stars. Also shown is the median of P and ω respectively. Both medians were calculated in equally spaced colour bins of 0.15 mag width. It is evident that the range covered by the angular velocity or period is very large for a given colour. However, as indicated by the medians there is apparently a change in both the angular velocity and period distribution which occurs at $(R_C - I_C) \approx 1.3$ mag. Stars redder than this colour (i.e. lower mass stars) rotates on average faster than the bluer stars (i.e more massive stars).

In order to investigate the different rotational properties of lower and higher mass stars in more detail I have divided the sample of 405 periodically variables into two samples. The first sample contains all stars with $(R_C - I_C) < 1.3$ mag while the second sample contains redder stars with $(R_C - I_C) > 1.3$ mag. From Fig. 8.1 or Fig. 8.5 it is evident that this division corresponds approximately to a spitting into stars with $M > 0.25\ M_\odot$ and $M < 0.25\ M_\odot$ respectively. I note, however, that this is only a rough mass estimate because reddening above or below average can shift higher mass stars into the redder or lower mass stars into the bluer regime.

8.2.2 The Rotation Period Distribution of NGC 2264 and the ONC

For the further analysis I use the two samples of higher and lower mass stars in NGC 2264 defined in the previous section. The left panel of Fig. 8.3 shows the histograms of the period distribution for each of these two samples. It is evident that the period distributions of the two samples are significantly different. The most obvious different is that higher mass stars with $(R_C - I_C) > 1.3$ mag show a bimodal period distribution while the period distribution of the lower mass stars with $(R_C - I_C) < 1.3$ mag is unimodal. In addition as already mentioned in the previous section the lower mass stars rotate much faster than the higher mass stars. The median rotation periods of the higher and lower mass stars (indicated by the vertical doted lines in Fig. 8.3) are 4.66 days and 1.88 days respectively; i. e. the lower mass stars rotate on average by a factor of 2.5 faster than the higher mass stars.

Fig. 8.3 (right panel) also shows a reproduction of the period distribution of the ONC by Herbst et al. (2001; 2002). As in NGC 2264 the period distribution for the ONC depends on the stellar mass. The distribution is bimodal for the higher mass stars with $M > 0.25\ M_\odot$ and unimodal for lower mass stars with $M < 0.25\ M_\odot$. Since in NGC 2264 a colour of $(R_C - I_C) = 1.3$ mag corresponds roughly to a mass of 0.25 $M_\odot$ the period distributions in in both clusters are unimodal for stars less massive than 0.25 $M_\odot$. The median rotation periods of the higher and lower mass stars in the ONC are 6.76 days and 3.33 days respectively. Thus, the lower mass stars in the ONC rotate an average by a factor of two faster than the higher mass ONC stars which is the same trend as in NGC 2264.

From Fig. 8.3 it is also rather obvious that the stars of both samples in NGC 2264 rotate much faster than the stars in the accordant samples in the ONC. For the same reason the related peaks in the histograms are located at shorter periods for NGC 2264: The peaks of the bimodal distribution of the higher mass stars in NGC 2264 are located at about 1 day and 4 days while the peaks in the corresponding distribution of higher mass ONC

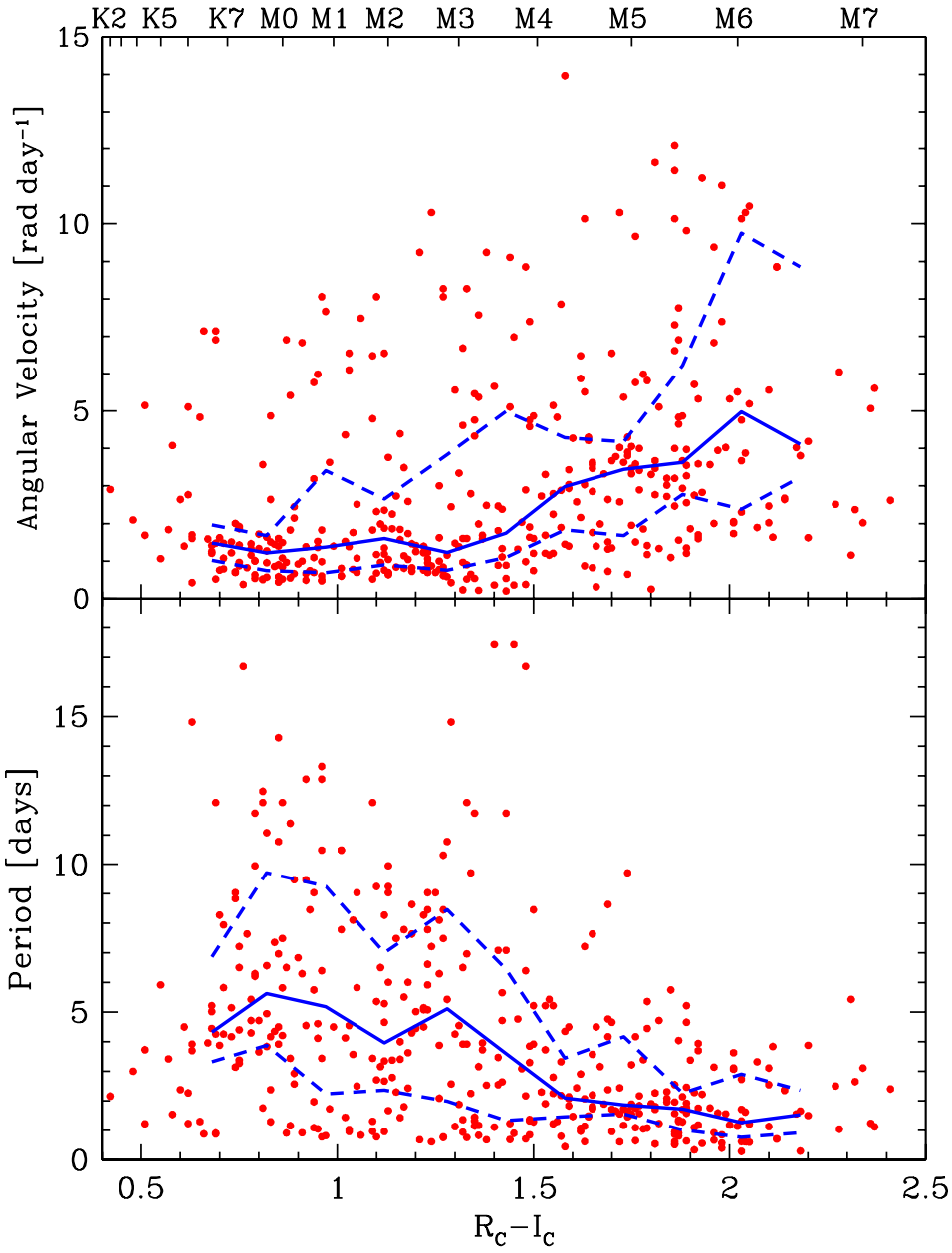

Fig. 8.2: Top panel: The angular velocity $\omega = 2\pi/P$ of the 405 periodically variable stars in NGC 2264 as a function of the $(R_C - I_C)$ colour. The blue solid line represents the median angular velocity calculated in fixed discrete colour bins of 0.15 mag width. The blue dashed lines represent the upper and lower quartiles in these bins. **Bottom panel**: The period P as a function of the $(R_C - I_C)$ colour for all periodically variables in NGC 2264. The blue solid and dashed lines are the median and the quartiles of the periods in colour bins of 0.15 mag width respectively.

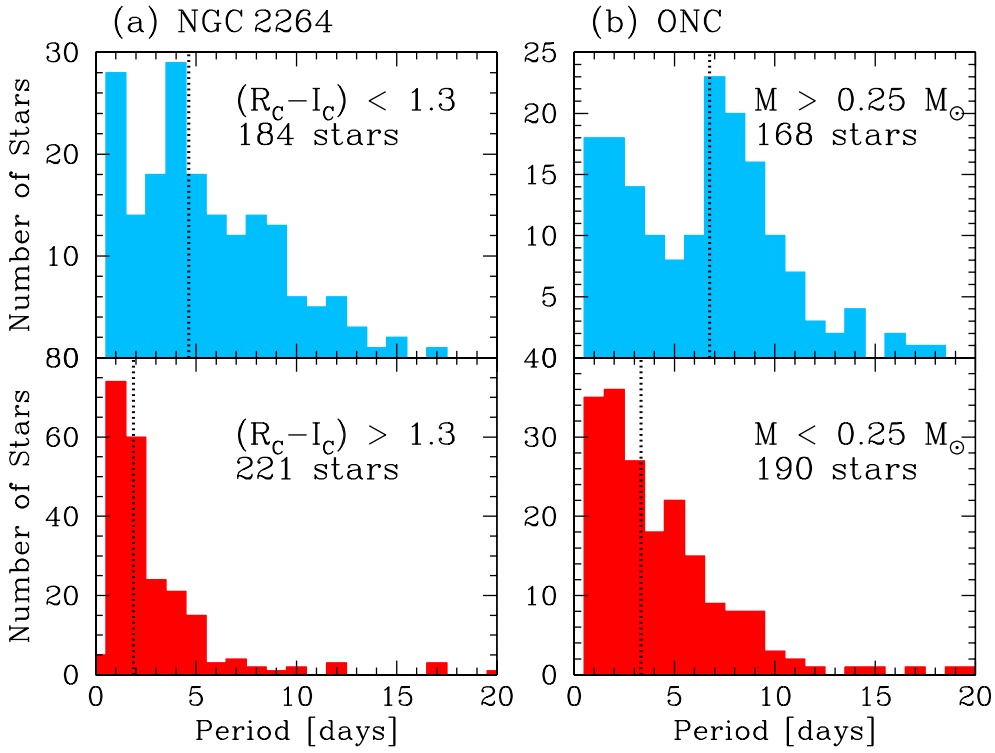

Fig. 8.3: **(a)** left panel: The period distribution for two different samples of periodically variable PMS stars in NGC 2264 (age: 2–4 Myr). The upper left histogram shows the period distribution for (higher mass) stars with $(R_C - I_C) < 1.3$ mag while the lower left histogram shows the period distribution for redder (lower mass) stars with $(R_C - I_C) > 1.3$ mag. This corresponds approximately to a devision into stars with $M > 0.25\ M_\odot$ (top) and $M < 0.25\ M_\odot$ (bottom). **(b)** right panel: The period distribution of periodically variable stars in the ONC (age: 1Myr) for two different *mass* regimes. The data are taken from Herbst et al. (2001; 2002).

stars are located at about 1.5 days and 7.5 days. The peaks of the unimodal distributions of lower mass stars in NGC 2264 and the ONC are located at periods of about 1 day and 1.5 days respectively.

The shorter median periods and the shift of the peaks to shorter periods in the distributions of NGC 2264 compared with the distributions of the ONC provide evidence for the spin-up of a significant fraction of the somewhat older PMS stars in NGC 2264. The median periods of the distribution indicate that the higher and lower mass stars in NGC 2264 spun up relative to the corresponding ONC stars by a factor of 1.5 and 1.8 respectively. This is consistent with the spin up calculated from the shift of the peaks which indicates that the stars in NGC 2264 spun-up relative to the stars in the ONC by a factor of 1.5–1.9 (i. e. 1.5 days compared to 1 day and 7.5 days compared to 4 days). As I will show in the following section this amount of spin-up is consistent with expectations based on PMS contracting models and conservation of angular momentum.

However, the ratio of the median periods for the higher mass stars and lower mass stars in the which is 2.5 in NGC 2264 and 2.0 in the ONC, indicates that the lower mass stars in NGC 2264 spun up faster than the higher mass stars or equivalently some higer mass stars in NGC 2264 spun up less fast or did not spin up at all. Since it is expected

that some stars in NGC 2264 are still disk-locked (see below) this can be explained by a larger fraction of disk-locked stars among the higher mass stars.

8.2.3 Spin-up with Conserved Angular Momentum

In this section I examine whether for most stars their spin-up from the age of the ONC to the age of NGC 2264 described above is consistent with conservation of angular momentum. I assume that the rotational evolution of the stars in both clusters can be described by:

1. full convection (polytropic structure),
2. rigid rotation, and
3. homologous contraction.

The first assumption is supported by detailed PMS models e. g. of Krishnamurthi et al. (1997) which show that the total moment of inertia of TTSs younger than 2 Myr is equal to the moment of inertia in the convective envelope of the stars if they are less massive than 0.9 $M_\odot$. According to their analysis, a minimum of 97% of the total moment of inertia is in the convective envelope if the stars are less massive than 0.9 $M_\odot$ and younger than 4 Myr or if the stars are less massive than 1.2 $M_\odot$ and younger than 2 Myr (see their Fig. 2). From Fig. 8.1 it is evident that almost all stars in the sample used here fulfil these conditions, i. e. their total angular momentum in almost completely in the convective envelope. Although real PMS stars may not be rigid rotators their actual rotational evolution is sufficiently similar and therefore the accuracy of the following discussion is adequate for the order of magnitude estimate I wish to make. I note that point 3 is actually not an independent assumption since the assumption of full convection at all stages is equivalent to assuming a homologous structure.

It is well known that the luminosity of solar-like stars in the early PMS phase is generated almost entirely by gravitational contraction with nearly constant effective temperature (e. g. Hayashi, 1966; Kippenhahn & Weigert, 1994). According to the virial theorem one half of the released gravitational energy $E_{\rm grav}$ heats up the interior of the star while the other half is radiated, i. e.

$$L = -\frac{1}{2}\frac{dE_{\rm grav}}{dt}. \tag{8.1}$$

Assuming that the stars in both clusters could be represented by polytropes their gravitational energy is given by (e. g. Kippenhahn & Weigert, 1994):

$$E_{\rm grav} = -\frac{3}{5-n}\frac{GM^2}{R}, \tag{8.2}$$

where M and R are the stellar mass and radius respectively, G is the gravitational constant and n is the *polytropic index* which is defined by a pressure (P) density (ρ) relation of $P \propto \rho^{1+1/n}$. Since $L = 4\pi R^2 \sigma T_{\rm eff}^4$ and using the polytropic index $n = \frac{3}{2}$ of a fully convective star Eqs. (8.1) and (8.2) yield:

$$4\pi R^2 \sigma T_{\rm eff}^4 = -\frac{1}{2}\frac{{\rm d}\left(\frac{3GM^2}{3.5R}\right)}{{\rm d}t}. \tag{8.3}$$

For constant mass M one gets

$$\frac{\mathrm{d}R}{\mathrm{d}t} = -\frac{28\pi R^4 \sigma T_{\mathrm{eff}}^4}{3GM^2}. \tag{8.4}$$

The integration of Eq. (8.4) (assuming $T_{\mathrm{eff}} \approx$ const.) yields

$$\frac{1}{R^3} - \frac{1}{R_0^3} = \frac{28\pi\sigma T_{\mathrm{eff}}^4}{GM^2}\, t, \tag{8.5}$$

where R_0 is the radius at the onset of star formation, i. e. at the birthline at $t = 0$. Since $R_0^3 \gg R^3$ for the PMS stars in both clusters one can neglect the second term on the left hand side of Eq. (8.5). If the effective temperature, T_{eff}, is assumed to be constant I finally get $R \propto t^{-1/3}$.

I now calculate the evolution of the rotation period as a function of the stellar radius if angular momentum is conserved. The specific angular momentum of a star is given by

$$j = \frac{J}{M} = \frac{I\omega}{M}, \tag{8.6}$$

where J is the total angular momentum, I is the moment of inertia and $\omega = 2\pi/P$ the angular velocity of a star which rotates with period P. The moment of inertia can be written as $I = k^2 R^2 M$, where k is the radius of gyration which is $k = 0.45$ for a $n = 3/2$ polytrope (e. g. Ruciński, 1988). One finally obtains for the specific angular momentum

$$j = \frac{2\pi k^2 R^2}{P}. \tag{8.7}$$

Therefore, if the angular momentum of a contracting PMS star is conserved (i. e. $j =$ const) the star will spin up as $P \propto R^2$.

Putting together the results above it follows that low-mass stars spin up with

$$P \propto t^{-2/3} \tag{8.8}$$

if angular momentum is conserved. In Sect. 8.1 we estimated that the mean age ratio of stars in NGC 2264 and the ONC is $t_{\mathrm{NGC\,2264}} \,/\, t_{\mathrm{ONC}} \approx 2$. Therefore, if angular momentum is conserved it is expected that the stars in NGC 2264 have on average spun up by a factor of

$$\frac{P(t_{\mathrm{NGC\,2264}})}{P(t_{\mathrm{ONC}})} = \left(\frac{t_{\mathrm{NGC\,2264}}}{t_{\mathrm{ONC}}}\right)^{-\frac{2}{3}} \approx 1.6 \tag{8.9}$$

relative to stars in the ONC. This is in agreement with the mean spin-up of 1.5–1.75 measured in Sect. 8.2.2 by comparing the location of the peaks in the observed period distributions.

In summary, the spin up of NGC 2264 stars relative to the stars in the ONC indicated by the shift of the peaks in the period distributions of the two clusters is consistent with conservation of angular momentum. I note, however, that this conclusion is valid only for the majority of the stars in NGC 2264, since there is evidence that a certain fraction of stars in NGC 2264 (e. g. about 20% of the higher mass stars) maintain a lower rotation rate even as they have aged from the ONC (see Fig. 8.4). These stars are probably still locked to their disks and therefore lose angular momentum.

8.2.4 Angular Momentum Loss by Magnetic Star-Disk Interaction

Beside the two rotational evolution scenarios mentioned above one has to consider a third possible evolution scenario which is a intermediate case of the spin up with conserved angular momentum and disk-locking at a constant rotation period. As I will argue below it is likely that some stars indeed lose angular momentum but are not locked at a constant rotation period. For those stars disk-locking is imperfect and therefore I call this scenario in the subsequent discussion "imperfect" disk-locking.

"Imperfect" disk-locking can be understood as follows. Hartmann (2002) argued that disk-locking is not instantaneous and it takes a time ($\tau_{\rm D}$) until disk-locking is achieved. This time $\tau_{\rm D}$ is determined by the rate at which angular momentum is removed from the inner disk and is given by

$$\tau_{\rm D} \gtrsim 4.5 \times 10^6 \text{ yr } f \frac{M_{0.5}}{\dot{M}_{-8}} \tag{8.10}$$

(Equation (8) in Hartmann, 2002), where $M_{0.5}$ is the stellar mass in units of 0.5 $M_\odot$, $\dot{M}_{-8}$ is the mass accretion rate in units of 10^{-8} $M_\odot$ yr^{-1} and f is the angular velocity of the star in units of the breakup velocity.

Using Eq. (8.10) for a 0.5 $M_\odot$ star in the ONC with the typical mass accretion rate of 10^{-8} $M_\odot$ yr^{-1} one obtains that disk-locking should be very rare in the first 0.5 Myr – 1 Myr as long as $f \gtrsim 0.1 - 0.2$. These values agree with the observed f values of the fast rotating ($P \approx 2$ days) higher mass stars of $M \approx 0.5$ $M_\odot$ in the ONC (Herbst, Bailer-Jones & Mundt, 2001). For the fast rotating ($P \approx 1$ days) lower mass stars in the ONC the f values are somewhat larger (i. e. $f \approx 0.65$ for a 0.1 $M_\odot$ star) (Herbst, Bailer-Jones & Mundt, 2001). Therefore, the product of f and M in Eq. (8.10) is approximately constant for the two mass regimes. However, Rebull et al. (2000) report a mass dependence of the mass accretion rate of the ONC stars in the sense that lower mass stars have typically smaller $\dot{M}$. According to their Fig. 24 the mass accretion rate scales approximately as $\dot{M} \propto M^2$ for stars with 0.15 $M_\odot < M <$ 1 $M_\odot$. Hence, the disk-locking time scale could be much larger for lower mass stars. Note that this assumes that the magnetic field structure is equal for both mass regimes. As it will be discussed in Chapter 9 it could be that the topology of the magnetic fields of the lower mass stars differs from that of the higher mass stars which could also cause longer disk-locking time scales τ_D for the lower mass stars.

Form the estimates of $\tau_{\rm D}$ it is also evident that some stars in the ONC (age: ~ 1 Myr) have not been able to achieve disk-locking until now. Thus, the presence of fast rotators in the ONC are in principle explainable by locking times which are larger than their ages. Stars with "imperfect" disk-locking should also show disk indicators such as a large infrared excess. Therefore "imperfect" disk-locking could also explain the presence of fast rotating stars with large infrared excesses which were reported by Herbst et al. (2002). Since the accretion rate decreases on average with increasing age it is also possible that some stars are unable to achieve disk-locking until the age of NGC 2264.

As also discussed by Hartmann (2002) there is probably a wide range of mass accretion rates in the TTSs phase; i. e. stars with high $\dot{M}$ will be locked within 10^5 yr while others may take 10^7 yr to achieve disk-locking. Also this whole consideration depends strongly on the initial conditions (rotation rate, radius, $\dot{M}$) at which the young star has left the protostellar phase and has entered the TTS phase at the birthline. During the protostellar phase with very high $\dot{M}$ values the star was presumably disk-locked but with much higher rotation period. In addition one should keep in mind that mass accretion in young stars

is a highly variable process on a broad range of time scales and FU Orionis stars are an extreme example of highly variable mass accretion (e. g. Hartmann & Kenyon, 1996).

Those stars which interact magnetically with their disks but have ages which are smaller than the disk-locking time scale $\tau_{\rm D}$ are not disk-locked at a constant rotation period. However, as long as the magnetic star-disk interaction exists, it continuously removes angular momentum from the stars but on such low rates that disk-locking of the contracting stars is not yet possible. As a result these stars are braked in the spin up and rotate with periods shorter than the disk-locking period but larger than the periods of stars which spin up conserving angular momentum. "Imperfect" disk-locking can last as long as the magnetic star-disk interaction exists; i. e. as long as the stellar age is smaller than the dissipation time of the circumstellar disks. It is also feasible that the rotational evolution of a star is first determined by "imperfect" disk-locking but disk-locking becomes effective later and the star is locked at a fixed rotation period. Also a evolution in the reverse order is possible; i. e. a disk-locked star evolves into a stage of "imperfect" disk-locking.

8.2.5 The Period Distribution in the Context of Disk-Locking

In this section I discuss the period distributions of NGC 2264 and the ONC in more detail. Since NGC 2264 is twice as old as the ONC and (under the assumption that the initial conditions were similar in both clusters) the period distributions of the ONC represent an earlier evolution stage of the rotational properties of PMS stars than the distributions of NGC 2264. In Sect. 8.2.3 it was shown that the shift of the peaks in the period distributions of NGC 2264 relative to those in the ONC (see Fig. 8.3) is consistent with conservation of angular momentum; i. e. the stars which build up the peaks evolve from the ONC to NGC 2264 with constant angular momentum. In the following I first concentrate on the discussion of the higher mass stars with $M \gtrsim 0.25\ M_{\odot}$. The lower mass stars will be considered afterwards.

Higher Mass Stars

In the ONC, Herbst et al. (2002) have interpreted the bimodality of the period distribution of higher mass stars in the range $M > 0.25\ M_{\odot}$ as an effect of the magnetic interaction of the young stars with their circumstellar disks, i. e. as a result of disk-locking. Based on the observed slow rotators in the ONC they adopted a normal distribution for the locking angular velocity ($\omega_{\rm lock}$) with mean 0.8 rad/day and standard deviation 0.2 rad/day (corresponding to $P_{\rm lock} = 7.85^{+2.62}_{-1.57}$ days).

This assumption is supported by the fact that the measured rotation period of CTTSs – i. e. accreting stars with inner circumstellar disks – in other associations peaks at a period of about 8 days (Bouvier, Forestini & Allain, 1997, and references therein). Most of these stars are located in the Taurus molecular cloud complex. Thus, according to the interpretation of Herbst et al. (2002), the higher mass ONC stars with $P \gtrsim 6$ days (i. e. the stars which build up the second peak in the period distribution) are still magnetically locked into co-rotation with their disks or have just been released from them. They have estimated that about 40% of the higher mass stars in the ONC could still be locked to their disk. This interpretation is also supported by measurements of the infrared excess of the stars in the ONC: Herbst et al. (2002) report a (weak) correlation of the infrared excess and the rotation period of the stars in the sense that stars with circumstellar disks

rotate with longer periods than stars without disks.

From Fig. 8.3 it is evident that there is a gap in the period distribution of the higher mass ONC stars with periods between 4 days and 5 days. As I will outline in the following it is very unlikely that the stars with shorter periods (i. e. the stars of the first peak) have ever been magnetically locked to their disk. Let us first assume that the stars of the first peak (at 1.5 days) have also been locked to their disks in the past with a locking period of about 8 days and released from their disks at earlier times. Subsequently these stars spun up conserving angular momentum. Using Eq. 8.9 and adopting a cluster age of 1 Myr it follows that these stars released from their disks when they were younger than 0.1 Myr and it would have taken about 0.9 Myr to cross the gap in the period distribution. Note that this duration which is needed to cross the gap is a lower limit because angular momentum loss would reduce the spin up. However, as it was shown in the previous Sect. it is very unlikely that the higher mass ONC stars have been disk-locked when they were younger than 0.1 Myr, since the time which is needed for these stars to achieve disk-locking ($\tau_{\rm D}$) is about 0.5 – 1.0 Myr and may even be longer in some extreme cases.

Another possibility which could explain the presence of fast rotators (i. e. the first peak) in the period distribution of the higher mass ONC stars is that these stars are locked with a different locking period. However, as it was also shown by Hartmann (2002) locking periods of the higher mass stars which differ (for a given age) by a factor of four are very unlikely (see also Sect. 8.4.2).

Note that the fact that there is a first *peak* in the period distributions of the ONC and NGC 2264 at about two and one days respectively is only a binning effect. All fast rotating stars with periods shorter than 1.5 days will fall into the first two bins and therefore produce a bimodal period distribution which is not present in the period distribution on a logarithmic scale which is shown in Fig. 8.4. However, the discussion presented above does not depend on the presence of the *bimodal* distribution but just on the fact that there are fast rotating stars.

NGC 2264 represents a later state in the rotational evolution of the stars and there are two possible explanations for the presence of the second peak in the period distribution of the higher mass stars:

1. It is possible that the stars with rotation periods of $P \gtrsim 4$ days are still locked to their disks but the typical locking period $P_{\rm lock}$ in NGC 2264 is generally shorter than that in the ONC. If this is true these stars should show disk indicators such as enhanced Hα emission or infrared excess. As I will show below this is not the case.

2. It is more likely that the stars with $P \gtrsim 4$ days have been locked in the past with a locking period similar to the locking period in the ONC and released from their disks presumably when they were at the age of the ONC stars. Now these stars spin up conserving angular momentum or with a moderate loss of angular momentum in a "imperfect" disk-locking scenario. Both would result in a shift of the second peak towards shorter periods (see Sect. 8.2.3).

Under the assumption that decoupling is a statistical process one expects that in NGC 2264 compared with the ONC more of the slow rotators have decoupled from their disks while others are still disk locked at a 8 day period. The shift of the second peak is first evidence for this decoupling. Further evidence is given by the period distributions of

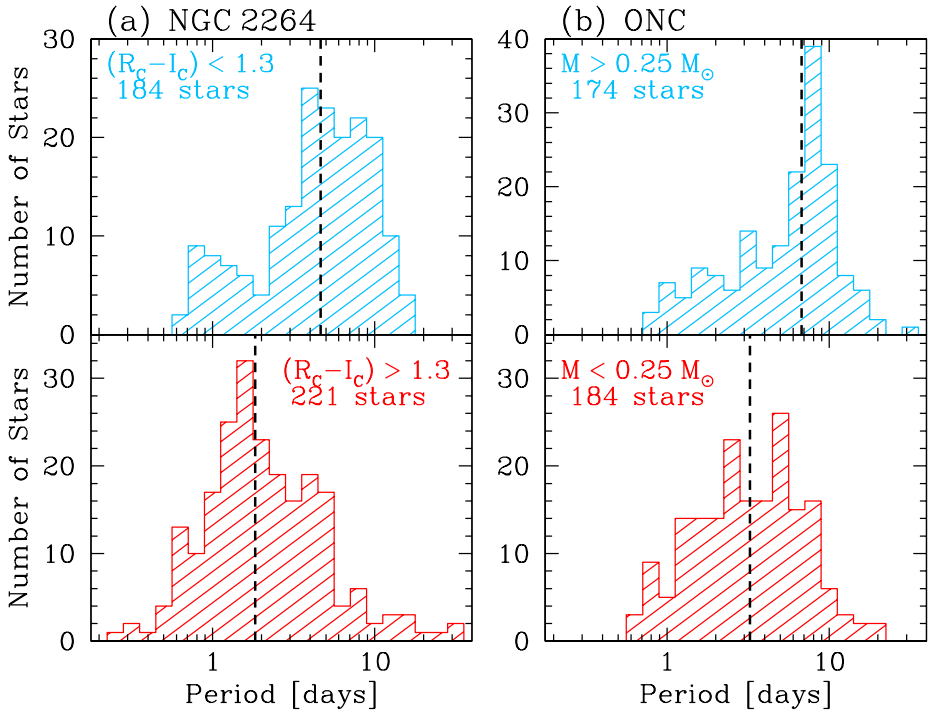

Fig. 8.4: Same as in Fig. 8.3 but in logarithmic scale. The dotted lines in each panel represent the median of $\log(P)$.

the higher mass stars in the ONC and NGC 2264 on a logarithmic scale which is shown in the top panels of Fig. 8.4. On a logarithmic scale stars with different periods which spin up by conserving angular momentum do always maintain their distance from each other; i. e. a group of stars which spins up with conserved angular momentum will also conserve the width of the period distribution in the histogram of Fig. 8.4. The width of the peak in the histogram for the ONC (centered at 8 days) is much smaller than the width of distribution of slow rotating stars in NGC 2264. This suggests that a fraction of stars does not spin up and is disk-locked while the stars with shorter periods spin up conserving angular momentum. The number of stars with long rotation period (i. e. $P \gtrsim 2$ days) indicates that about 20%–30% of the stars in NGC 2264 could still be locked to their disks.

In Fig. 8.3 the first peak of the period distribution of higher mass stars in NGC 2264 ($P < 1.5$ days) can be explained by a spin up of stars. These stars are the counterparts of the higher mass stars in the first peak of the ONC. The spin up of some of these stars can be explained by "imperfect" disk-locking.

Lower Mass Stars

In Fig 8.3 the periods of the lower mass stars in NGC 2264 are distributed over a much smaller range than in the ONC. Most stars seem to spin up with conserved angular momentum as already outlined above (Sect. 8.2.3) on the basis of the peak locations in the ONC and NGC 2264. However, evidence for angular momentum conservation of most PMS stars is not only provided by the shift of the peak in the period distribution but also from the widths of the period distribution on logarithmic scale. As shown in Fig. 8.4 the width

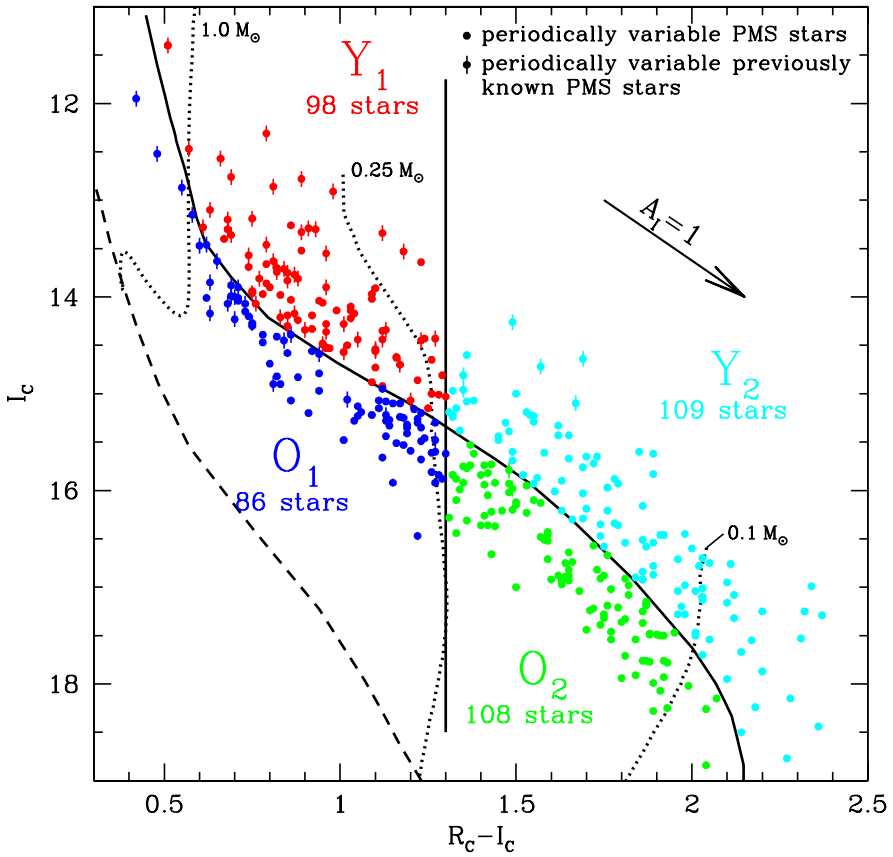

Fig. 8.5: The colour-magnitude diagram of the periodic variables in NGC 2264 which were divided into the four sub-samples (Y_1, O_1, Y_2, and O_2). The solid vertical line at $(R_C - I_C) = 1.3$ mag (which corresponds approximately to $M = 0.25\ M_\odot$) represents the devision into higher and lower mass stars. The second solid line is a reddened 1 Myr isochrone of D'Antona & Mazzitelli (1997) which I used for a division into younger (Y_1 and Y_2) and older (O_1 and O_2) stars. Different symbol colours indicate the classification of the stars into the for sub-samples. Also shown is the number of stars in each of the four sub-samples. The dotted lines reddened represent 0.1, 0.25, and 1.0 $M_\odot$ evolution tracks. The dashed line represents the ZAMS.

of the logarithmic period distribution of the lower mass stars is similar in both clusters. However, there is a more pronounced peak between 1.5 days and 2 days in the histogram of NGC 2264 in Fig. 8.4. Such a peak is not present in the histogram for the ONC where the logarithmic period distribution seems to be more flat. This could very well indicate that spin up of some lower mass stars with "imperfect" disk-locking is happening; i. e. without this braking one would observe more stars with $P \leq 1.5$ days.

In the following Sections I investigate whether there is further evidence for the interpretation of the period distributions I suggest here or if other explanations are possible. In addition, the period distribution in the ONC has recently been interpreted by Barnes (2003) as a result of different rotational morphology and a resulting different magnetic structure of the stars which he called the "convective sequence" and the "interface sequence". I will discuss this aspect in Chapter 9 in more detail where I also investigate the dependence of the peak-to-peak variation from the rotation period.

8.3 Young and Old PMS Stars in NGC 2264

In the previous section I found evidence that the spin-up of most PMS stars from the age of the ONC (1–1.5 Myr) to the age of NGC 2264 (2–4 Myr) can be described by conservation of angular momentum. In this section I investigate whether a similar result can be found using only stars in NGC 2264. Therefore the period distributions of sub-samples of the cluster stars with different mean ages will be compared.

As the first step each of the two samples of higher and lower mass PMS stars defined in Sect. 8.2 was divided into two sub-samples of younger and older stars (see Fig 8.5). A star was classified as young or old according to its location relative to a reddened 1 Myr isochrone of the DM97 model in the I_C vs $(R_C - I_C)$ colour-magnitude diagram of Fig 8.5. Stars above and below the 1 Myr isochrone are called young and old stars respectively. The different sub-samples are indicated in Fig. 8.5 by different symbol colours.

In this way the higher mass stars with $(R_C - I_C) < 1.3$ mag were divided into the sub-samples Y_1 and O_1 with 98 young and 86 old stars, respectively. Correspondingly the lower mass stars with $(R_C - I_C) > 1.3$ mag were divided into the sub-samples Y_2 and O_2 which contain 109 young stars and 108 old stars respectively. 4 stars with $(R_C - I_C) > 2.5$ mag were excluded from the analysis.

8.3.1 Spatial Distribution of Young and Old Stars

I first investigate the spatial distribution of the stars in the four sub-samples. Fig. 8.6 shows the spatial positions of the young and old stars separately. It is evident that the younger stars in the upper panels of Fig. 8.6 show a larger spatial concentration compared with the older stars in the plots of the lower row. For Y_1 and Y_2 there are two concentrations apparent which we called NGC 2264 N and NGC 2264 S in Chapter 5 (see Figs. 5.3 and 5.4). These two concentrations were already mentioned by Sagar et al. (1988) as points of maximum stellar density. The northern concentration is near the O7 Ve star S Mon which is the most massive star in the cluster.

The larger spatial scatter of the older stars in both mass regimes is coincident with the theory that stars form in dense clouds close together and migrate from their birthplace with increasing age. If we assume a distance of 760 pc (Sung, Bessel & Lee, 1997) for NGC 2264 a star with a projected tangential velocity of 1 km/sec ($\approx$ 1 pc/Myr) moves $4.5'$ within 1 Myr. The observed velocity dispersion of cluster members in the proper motion study by Vasilevskis, Sanders & Balz (1965) is somewhat larger. For the stars with a cluster membership probability of more than 0.95 they observed a dispersion (one sigma) in the cential proper motions (μ_x,μ_y) of $0\farcs15$ and $0\farcs16$ for μ_x and μ_y respectively which corresponds to $25'$ per 1 Myr. Therefore, the larger scatter of the older stars could be explained by the migration of the stars with a typical projected velocity of a few km/sec on a time scale of a few Myr.

When comparing the spatial distributions of the subsamples Y_1 and Y_2 in Fig. 8.6 there is a tendency that the higher mass stars in Y_1 are more concentrated than the lower mass stars in Y_2. This could be a result of a higher tangential velocity of the lower mass stars.

From the left hand panels of Fig. 8.6 it is also evident that both concentrations of PMS stars in NGC 2264 (i. e. NGC 2264 N & S) contain young and old stars. Therefore there

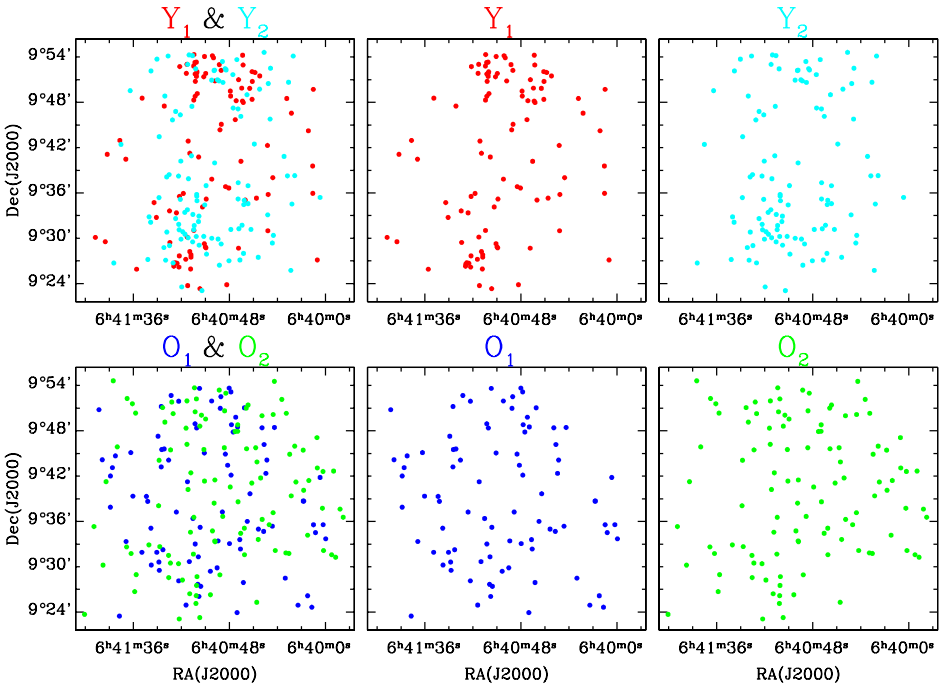

Fig. 8.6: Top panels: The spatial positions of young NGC 2264 stars in the sub-samples Y_1 (young higher mass stars) and Y_2 (lower mass stars young). The left panel shows the positions of stars of the combined sub-samples (i. e. all young stars) while the middle and right panels show the positions of the stars in Y_1 and Y_2 separately. The colours are the same as in Fig. 8.5. **Bottom panels**: The same as in the upper row but for old stars in the sub-samples O_1 (higher mass stars) and O_2 (lower mass stars).

is no evidence for an age difference between these two concentrations, i. e. star formation in the two concentrations happened roughly at the same time.

8.3.2 Period Distribution of Young and Old Stars

Fig. 8.7 shows the histograms of the period distribution for the four different sub-samples Y_1, Y_2, O_1, and O_2. Note that the upper left histogram of Fig. 8.3 (higher mass stars in NGC 2264) is the sum of the two histograms for Y_1 and O_1. The lower left histogram of Fig. 8.3 is the sum of the histograms for Y_2, O_2.

The result of Sect. 8.2 that lower mass stars rotate on average faster than higher mass stars is also apparent from Fig. 8.7. For both young and old stars the peaks of the distributions for the higher mass stars (left hand panels) are located at longer periods than the peaks of the distributions for lower mass stars in the right hand panels. In addition the median periods (indicated by the dashed line in Fig. 8.7) of the higher mass stars are in both cases larger than the median periods of the corresponding samples of the lower mass stars.

There no evidence for a spin-up of the older stars in NGC 2264 compared with the younger stars. In contrast the median periods for both the lower and the higher mass

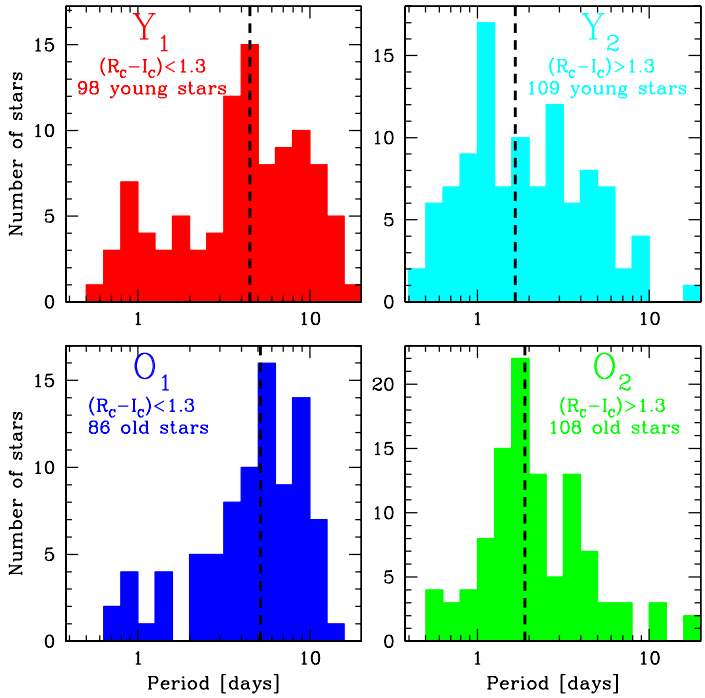

Fig. 8.7: The period distribution of stars in the four sub-samples Y_1, Y_2, Y_1, and Y_2 on logarithmic scale. The colours are the same as in Fig. 8.5. The histograms for higher mass stars are on the left hand side while the histograms for lower mass stars are on the right hand side. The vertical dashed lines indicate the median period for each sample.

stars are slightly shorter for the younger stars: The higher mass stars in the samples Y_1 and O_1 have median rotation periods of 4.48 days and 5.15 days respectively. In the case of the lower mass stars the median rotation periods are 1.66 days for the sample Y_2 and 1.89 days for the stars in O_2.

A Kolmogorov-Smirnov test (Press et al., 1992), however, yields a probability of 0.4 that the distribution Y_1 and O_1 are equivalent; i. e. they are not significantly different. For the lower mass stars this test indicates that there is only probability of 4×10^{-3} that the distributions Y_2 and O_2 are equivalent. Hence, there is evidence that the two distributions are significantly different. The same is evident from the fraction of fast rotating stars in the two samples. For the lower mass stars the fractions of fast rotating stars with periods shorter than 1.3 days are 37% and 17% for the younger and older stars respectively.

In addition, for the lower mass stars the width of the logarithmic period distribution (i. e. the number of neighbouring bins with more than say 5 stars) is smaller in the case the older stars. Together with the result that the peak in the logarithmic period distribution of the young stars is located at about 1 day while the corresponding peak for the older stars is located at about 2 days this indicates that the some older stars are braked to longer rotation periods while others spun up compared with the young stars.

In summary, for the lower mass stars I find that the fraction of fast rotating stars is higher for the younger stars. *This is the opposite from what one would expect from a contracting PMS model.* In such a scenario the older stars should rotate with shorter rotation

periods than the younger stars if the stars spin up with conserved angular momentum according to $P \propto t^{-2/3}$.

I have no satisfactory explanation for this unexpected behaviour. A possible reason could be that the age spread of the stars is not as big as it is indicated by the scatter of the stars in the colour-magnitude diagram (Fig. 8.5) and if the identified young stars are contaminated with old stars and vise versa. A further reason for the enhanced scatter could be the variability of the stars. This interpretation is supported by the fact that the irregular variables which show typically larger brightness variations than periodic variables (see Sect. 6.2) also show a larger scatter in the colour-magnitude diagram (see Fig. 5.5). An additional reason for a misleading age determination of the fast rotating stars could be a large fraction of non-resolved binary stars. This would lead to brighter absolute magnitudes of the variables which results in a younger estimated age. In this scenario the fast rotating young stars would actually be fast rotating older binary stars.

Despite the possible contamination of the young subsample with older stars (and vice versa) and a much smaller age difference than indicated by the colour-magnitude diagram it is quite likely from the spatial distribution of the stars (see Sect. 8.3.1 above) that the stars in the sub-samples Y_1 and Y_2 are indeed *on average* younger than the stars in the sub-samples O_1 and O_2. Therefore, a possible more satisfactory explanation for the period distributions in Fig. 8.7 could be "imperfect" disk-locking. In this scenario some of the rapid rotators in Y_1 and Y_2 will be braked when they reach the age of the samples O_1 and O_2 respectively.

8.4 Disk-locking in NGC 2264

8.4.1 The Hα-emission as a disk-locking indicator

In this section I investigate what fraction of the periodic variables in NGC 2264 show evidence for the presence of disk-locking. In the disk-locking scenario (described e. g. by Shu et al., 1994) angular momentum is transported via magnetic field lines from the PMS star to the circumstellar disk which loses angular momentum via a disk wind (see also Fig. 1.2). A common feature of all models is the presence of mass accretion onto the star. It is generally believed that large Hα emission equivalent widths of $W_\lambda(H\alpha) > 10$ Å are a result of the increased mass accretion onto the star (see Sect. 1.1).

In order to verify the disk-locking scenario, other authors (e. g. Herbst et al., 2002) looked for a correlation between the rotation period and the infrared excess of the stars as a disk indicator. As already mentioned in Sect. 8.2.5 for the ONC there is evidence that slow rotators have on average a larger infrared excess than fast rotors (Herbst et al., 2002). This was interpreted as evidence for disk-locking. However, Herbst et al. (2002) also report rapidly rotating stars with large $(I-K)$ excesses and slow rotators with small infrared excesses.

A large infrared excess of a star is an indicator for the presence of circumstellar dust which may be connected with the presence of a circumstellar gas disk but it is not necessarily an indicator for current mass accretion which is believed to be highly variable in TTSs. Therefore, even if some ONC stars have large infrared excesses they are not necessarily coupled to their disks and fast rotation periods are possible. Beside the infrared excess the presence of strong Hα emission is a different and possibly better indicator for *ongoing*

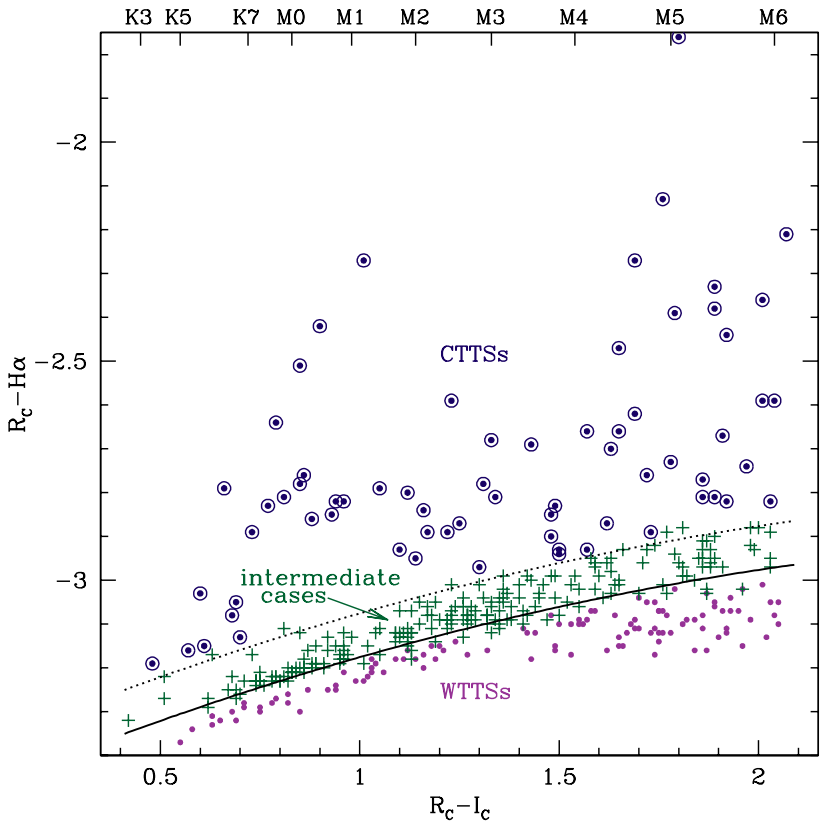

Fig. 8.8: The $(R_C - H\alpha)$ vs $(R_C - I_C)$ colour-colour diagram of all 405 periodic variables. The classification of periodic variable CTTSs (⊙), WTTSs (•), and intermediate cases (+) was done according to the location of the stars in this diagram. The solid line represents the PMS/MS locus (see Sect. 5.1). The dotted line represents a Hα-index of $\Delta(R_C - H\alpha) = 0.1$ mag. Only stars which are located more than their photometric error $\delta(R_C - H\alpha)$ above that line were classified as CTTSs while stars which are located more than $\delta(R_C - H\alpha)$ below the solid line were classified as WTTSs. All other stars are classified as intermediate cases.

disk-locking of a star. Fortunately there is no strong nebular Hα emission in NGC 2264 which is a serious difficulty in the ONC and prevents accurate determination of the stars' Hα emission.

Since chromospheric activity of the stars can also produce significant Hα emission (see Sect. 1.1) the presence of such emission is not a unambiguous sign of mass accretion in particular close to an Hα emission equivalent width of $W_\lambda(H\alpha) = 10$ Å. Therefore, in the ideal case both indicators – large infrared excess *and* large Hα emission – should be used for the selection of disk-locked stars. However, because of the lack of spectra and spectral types for a large amount of periodic variables in NGC 2264 Hα emission equivalent widths and infrared excesses are only available from the literature for a small subsample of these stars. Therefore I have to deal here with the Hα-index which as a measure for the strength of the Hα emission. This Hα-index , $\Delta(R_C - H\alpha)$, is defined Sect. 6.3 by Eq. (6.2).

In Sect. 6.3.2 I have selected stars with strong Hα emission if $\Delta(R_C - H\alpha) > 0.1$ mag. These stars were called CTTSs while the stars which did not fulfil this criterion were called WTTSs. However, it was also demonstrated that the classification of the WTTSs is

uncertain because some WTTSs with small (positive) Hα-indices could actually be CTTSs. In order to avoid such uncertainties I introduce here a new classification of stars which I call "intermediate cases" and is defined as follows.

In the subsequent discussion stars are called WTTS only if

$$\Delta(R_{\rm C} - {\rm H}\alpha) \; + \delta(R_{\rm C} - {\rm H}\alpha) \leq 0.0 \text{ mag},$$

where $\delta(R_{\rm C} - {\rm H}\alpha)$ is the photometric error of the $(R_{\rm C} - {\rm H}\alpha)$ colour. In addition stars are called CTTSs only if

$$\Delta(R_{\rm C} - {\rm H}\alpha) \; - \delta(R_{\rm C} - {\rm H}\alpha) \geq 0.1 \text{ mag} \; .$$

The stars which are neither CTTSs nor WTTSs according to these definitions are called "intermediate cases". Fig. 8.8 shows the location of these three samples in the $(R_{\rm C} - {\rm H}\alpha)$ vs $(R_{\rm C} - I_{\rm C})$ colour-magnitude diagram. According to the above definition stars are only called CTTSs if they are located more than their photometric error, $\delta(R_{\rm C} - {\rm H}\alpha)$, above the dotted line (which represents a Hα-index of 0.1). Analogous, stars are called WTTSs if they are located more than their photometric error below the solid line, i. e. below the PMS/MS locus with zero Hα-index. This explains the presence of green crosses (intermediate cases) above and below the lines in Fig. 8.8.

Since the photometric errors for stars with $(R_{\rm C} - I_{\rm C}) \geq 2.1$ mag are relatively large and the PMS/MS locus is poorly defined in this magnitude range, for the further analysis only the 381 stars with $(R_{\rm C} - I_{\rm C}) \leq 2.1$ mag are considered. Of these 381 stars I classified 68 stars as CTTSs, 109 stars as WTTSs, and 204 stars as intermediate cases.

8.4.2 The Dependence of the Period Distribution from the Hα-Index

In this section I present and discuss the period distributions of the different sub-classes of PMS stars (CTTSs, WTTSs, and intermediate cases) defined in the previous section. According to the standard model, disk-locking is always connected with ongoing accretion onto the star. Therefore, it is expected that most CTTSs (not WTTSs) are locked to their disks. However, the presence of accretion and corresponding strong Hα-emission is only evidence for disk-locking at the present time; it does not indicate that a star has been locked in the past.

Fig. 8.9 shows the period distributions of stars in the three samples for higher mass stars with $(R_{\rm C} - I_{\rm C}) < 1.3$ mag (in total 184 stars) and lower mass stars with $(R_{\rm C} - I_{\rm C}) > 1.3$ mag (197 stars) separately. Fig. 8.10 shows the cumulative period distributions of the higher and lower mass stars but only for CTTSs and WTTSs.

It is evident that the period distribution of the higher mass CTTSs looks quite different from that of the WTTSs although the statistics are poor. According to a (binning independent) Kolmogorov-Smirnov test (Press et al., 1992) there is only a probability of 0.02 that the two distributions are equivalent. From Fig. 8.9 it is also evident that in both mass regimes the CTTSs rotate with longer periods on average than the WTTSs.

The period distribution of the higher mass CTTSs in the upper left hand panel of Fig. 8.9 is rather flat compared with that of the WTTSs in the upper right hand panel. This shows that the few stars in NGC 2264 which could be still disk locked show a different period distribution than the stars without disks. In addition the period distribution of

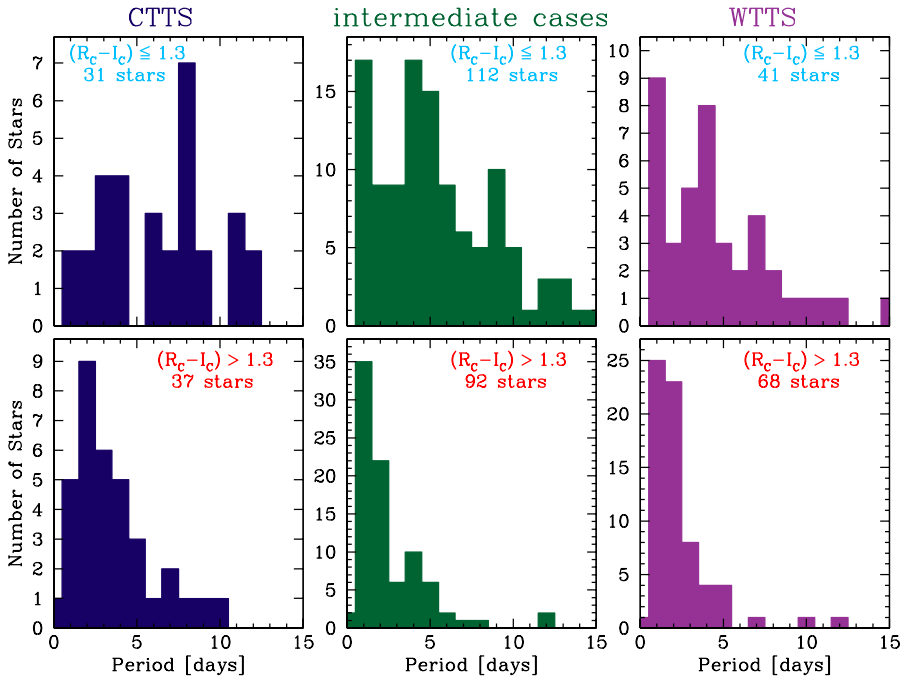

Fig. 8.9: The period distributions for the three different subclasses of PMS stars (i. e. CTTSs, WTTSs, and intermediate cases) shown in Fig. 8.8. Each of these subsamples is divided into higher mass stars with $(R_C - I_C) \leq 1.3$ mag (top panels) and lower mass stars $(R_C - I_C) > 1.3$ mag (bottom panels). The colours are the same as in Fig. 8.8.

the CTTSs shows a peak at 8 days, a noteworthy agreement with the commonly adopted locking period of these stars (see Sect. 8.2.5). There are also a few CTTSs with rotation periods shorter than 5.5 days. These stars could be either locked CTTSs with a shorter locking period of CTTSs with "imperfect" disk-locking.

Let us now discuss the lower mass stars. The period distributions of the lower mass stars (lower panels in are Fig. 8.9) show a evolution sequence from the CTTSs via the intermediate cases to the WTTSs in the sense that the width of the distributions decreases from the left to the right panel. This also indicates that WTTSs rotates faster on average than CTTSs. A Kolmogorov-Smirnov test results in a probability of less than 0.001 that the distributions for the CTTSs and WTTSs are equivalent.

One interesting difference between the higher and lower mass stars is that the period distribution of the lower mass CTTSs peaks at about 2–3 days. The possible reason for this finding could be a shorter locking period of the lower mass stars compared with the higher mass stars. If this is true the locking period for lower mass stars is about 2–3 days rather than 8 days. This would explain the lack of the 8 day peak in the period distributions of the lower mass stars in Fig. 8.3.

In the following I investigate how the different locking periods of the higher and lower mass stars can be explained. According to the model of Shu et al. (1994), the locking period $P_{\rm lock}$, of a given star depends on the stellar mass (M), radius (R), mass accretion rate ($\dot{M}$), and surface magnetic field strength (B). In their model $P_{\rm lock}$ is equal to the

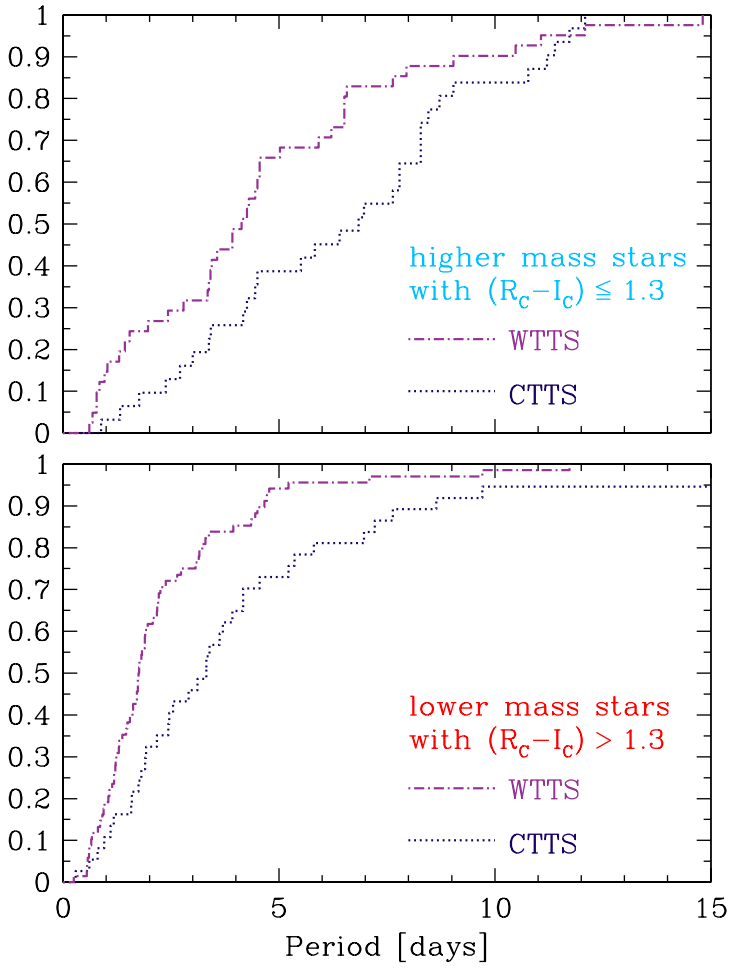

Fig. 8.10: The cumulative period distribution for CTTSs and WTTSs. The top panel shows the distributions for higher mass stars with $(R_C - I_C) \leq 1.3$ mag while the lower panel shows the distributions for lower mass stars with $(R_C - I_C) > 1.3$ mag.

Keplerian period, P_K of the inner disk, which is truncated at a radius R_T, i. e.

$$P_{lock} = P_K(R_T) \propto \left(\frac{R_T^3}{M}\right)^{1/2}. \tag{8.11}$$

With the usual assumption that the stellar magnetic field has a closed global structure which can be modelled approximately by an aligned dipole magnetic field with surface strength B (Königl, 1991) the truncation radius is given by

$$R_T \propto \left(\frac{B^4 R^{12}}{M\dot{M}^2}\right)^{1/7}. \tag{8.12}$$

Inserting Eq. (8.12) into Eq. (8.11) we obtain for the locking period

$$P_{lock} \propto \frac{B^{6/7} R^{18/7}}{M^{5/7}\dot{M}^{3/7}} \tag{8.13}$$

(e. g. Shu et al., 1994).

Although very little known in particular about $\dot{M}$ and B, there is evidence for a power-law mass dependence of $\dot{M}$ in NGC 2264 (Rebull et al., 2002) and the Orion flanking fields (Rebull et al., 2000) in the form of $\dot{M} \propto M^{\gamma}$ with $\gamma \approx 2$. In addition it would be surprising if lower mass stars have a much weaker magnetic field B than the higher mass stars because they rotate much faster. If one therefore assumes that the locking period depends only weakly on B for a mass range of $0.1 - 0.3\ M_{\odot}$ its value is mainly determined by the ratio $R^{18/7} M^{-11/7}$. According the PMS evolution tracks by D'Antona & Mazzitelli (1997) the stellar radius of lower mass stars at the age of NGC 2264 depends on the stellar mass roughly as $R \propto M^{4/5}$. Using these approximations in Eq. 8.13 I obtain that the locking period of the lower mass stars in NGC 2264 depends on mass as $P_{\rm lock} \propto M^{18/35} \approx \sqrt{M}$. Hence, the locking period of a $0.25\ M_{\odot}$ star is a factor of about 1.6 larger than the locking period of a $0.1\ M_{\odot}$ star; i. e. the changes in mass, mass accretion rate, and stellar radius without invoking any change of B are not sufficient to explain the suggested changes in locking period.

For higher mass stars there is a weaker mass-radius dependence and therefore also the locking period is less mass dependent. According to the evolution models for stars at the age of NGC 2264 by D'Antona & Mazzitelli (1997) the factor $R^{18/7} M^{-11/7}$ in Eq. 8.13 varies between a $0.3\ M_{\odot}$ star and a $0.5\ M_{\odot}$ star by 20% but there is basically no mass dependence of this factor for stars with masses larger than $0.5\ M_{\odot}$. Thus the small (1σ) scatter in the locking periods of the higher mass stars of $P_{\rm lock} = 7.85^{+2.62}_{-1.57}$ days (see Herbst et al., 2002) may be a result of the small dependence of $R^{18/7}/M^{5/7}$ on mass in this mass range.

As outlined above the locking period of the lower mass stars might be 2–3 days. However, such a short locking period contradicts the corresponding period distribution observed in the ONC where more than half of the stars rotate with period larger than 3 days. One could imagine two different scenarios in the context of "imperfect" disk-locking for explaining this discrepancy. First, not all stars which interacts with their disks at present time and thus have a large Hα-index are indeed locked to their disks. Second, disk-locking was still "imperfect" at the age of the ONC but the stars were able to achieve disk-locking at the age of NGC 2264.

8.5 Possible Angular Momentum Evolution Scenarios

In this section I summarise the basic features of the three possible processes, namely disk-locking, "imperfect" disk-locking, and stellar spin up with conserved angular momentum, which likely determine the rotational evolution of TTSs. This will be done on the basis of Fig. 8.11 which schematically depicts these three different rotational evolution scenarios for higher and lower mass stars.

The main result of the previous discussion is that disk-locking is or was present for the **higher mass stars** in NGC 2264 with $(R_{\rm C} - I_{\rm C}) \leq 1.3$ mag (i. e. $M \geq 0.25\ M_{\odot}$). The top panel of Fig. 8.11 illustrates the rotational evolution of typical higher mass stars. The locking period of these stars is expected to be about 8 days which is suggested by the period distributions in Figs. 8.3 and 8.4. Also the analysis of the Hα-index suggests these locking periods.

The solid blue and the dashed red line in the upper panel of Fig. 8.11 illustrates the rotational evolution of two typical higher mass stars. Both are locked with a rotation period of about 8 days. While the first star (blue line) is locked for a longer time (i. e. several Myr) and is still locked at the age of NGC 2264 the second star (red line) decouples from its disk roughly at the age of the ONC. After their decoupling they spin up in both cases towards the main sequence with (nearly) constant angular momentum since angular momentum loss due to Skumanich-like winds is negligible on the time scales considered here.

As it was shown, it is possible to explain the presence of fast rotators among the higher mass stars in the ONC and NGC 2264 (i. e. the first peak in the period distributions) by "imperfect" disk-locking. The orange dotted line in Fig. 8.11 depicts the rotational evolution of such fast rotators: As long as the stars interact magnetically with their disks they lose some angular momentum but they still spin up with decreasing radius. Once the star-disk interaction breaks down the stars spin up conserving angular momentum.

The three outlined scenarios result in a large scatter of rotation periods at the ZAMS which is observed in several ZAMS clusters (e. g. Bouvier, Forestini & Allain, 1997, see also Chapter 1). In order to explain the observed rotation distributions on the ZAMS (in particular the presence of some slow rotators) disk-locking times of at least 10 Myr are required for a few stars (Barnes et al., 2001, see also Fig. 1.1).

I concluded that ("perfect") disk-locking is not very important for the rotational evolution of most **lower mass** stars since most of the lower mass stars apparently spin up from the ONC to NGC 2264. Most of the spin up of these stars can be explained by "imperfect" disk-locking. Hence, the fraction of stars with "imperfect" disk-locking may be larger for the lower mass stars compared with the higher mass stars and only some lower mass stars are disk-locked. The locking periods of these stars are certainly shorter than for the higher mass stars and show a larger scatter. Based on the analysis of the Hα-index I have estimated that the locking period of the lower mass stars is typically about 2–3 days.

The lower panel of Fig. 8.11 illustrates these possible rotational evolution scenarios of low mass stars. The solid blue line and the dashed red line represent disk-locked stars with different decoupling times. For the dashed line it is also assumed that disk-locking is "imperfect" until the star is slightly older than the age the ONC while it is able to achieve disk-locking afterwards. As described for the higher mass stars it is possible that some stars are never disk-locked and the phase of "imperfect" disk-locking is followed by a spin up with conserved angular momentum. This evolution is indicated by the dotted orange line in the bottom panel of Fig. 8.11.

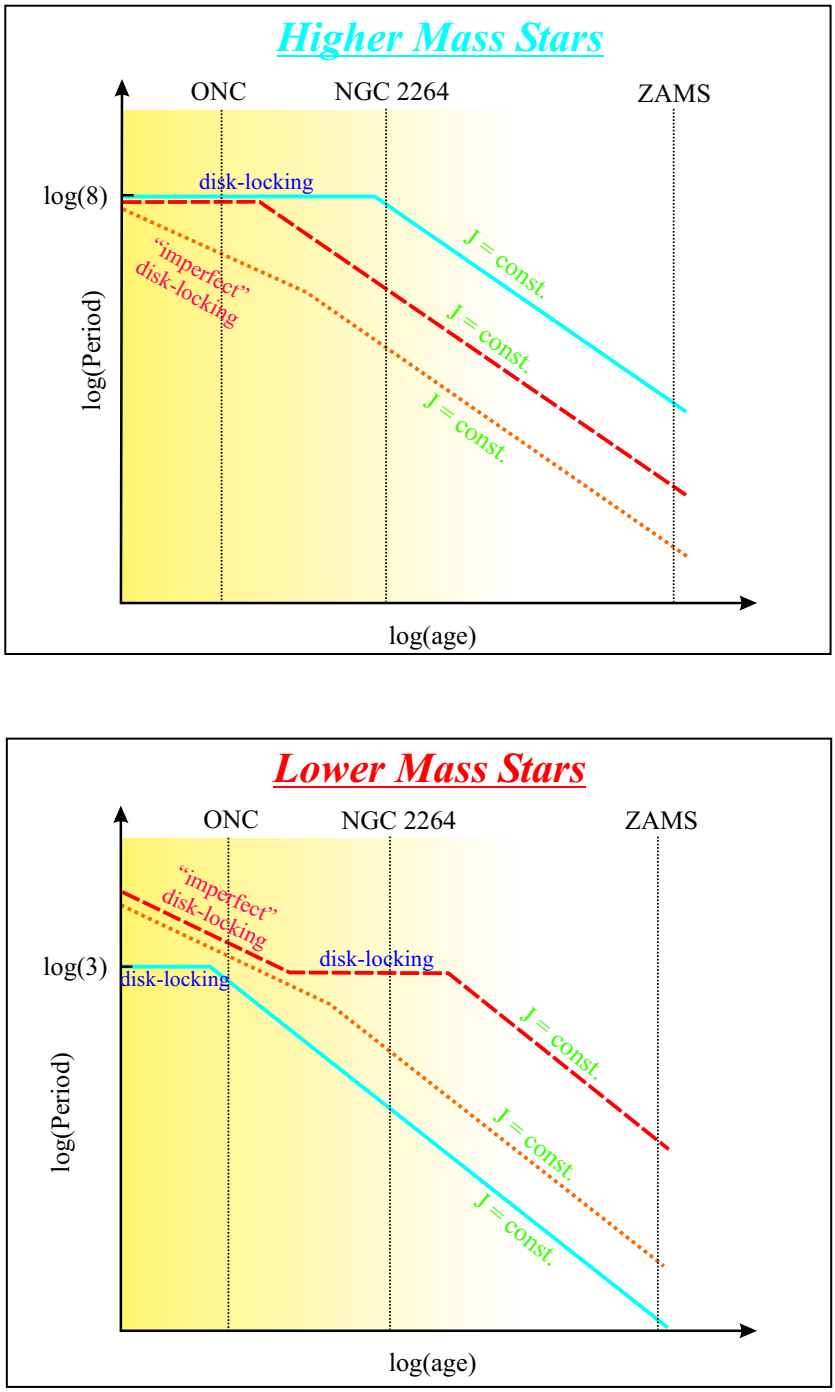

Fig. 8.11: Schematic diagram of the time evolution of the rotation period for higher and lower mass stars in different evolution scenarios. See text for a detailed description.

Chapter 9

Rotation & Magnetic Fields

9.1 The Colour Dependence of the Peak-to-Peak Variation

In this section I investigate whether the peak-to-peak variation of the periodic variables depend on the colour of the stars. The peak-to-peak variation of all periodic variables was determined by using the phased light curves as described in Sect. 6.1. As I will outline below this investigation give rise to rather surprising results.

Fig. 9.1 shows the peak-to-peak variation as a function of the $(R_C - I_C)$ colour for different sub-samples of the periodic variables. In the top panel all 405 periodic variables are shown. From this diagram it is evident that the peak-to-peak variation of the of redder (i. e. lower mass) stars with $(R_C - I_C) \gtrsim 1.3$ mag is typically below 0.06 mag while the bluer (i. e. higher mass) stars typically occupy a larger range of peak-to-peak variations, i. e. $\gtrsim 0.2$ mag and even more in some extreme cases. In the middle panel of Fig. 9.1 only the peak-to-peak variations of 89 stars with large Hα-indices of $\Delta(R_C - H\alpha) > 0.1$ mag (i. e. strong Hα emitters) are shown. It is evident that these stars show a large scatter in their peak-to-peak variations. A comparison with the top panel shows that in particular for stars with $(R_C - I_C) \gtrsim 1.5$ mag the large peak-to-peak variations of more than 0.06 mag are mostly produced by stars with $\Delta(R_C - H\alpha) > 0.1$ mag. The bottom panel of Fig. 9.1 shows the peak-to-peak variations for the remaining (316) stars with weak Hα emission, i. e. $\Delta(R_C - H\alpha) \leq 0.1$ mag. From this panel it is even more evident that the peak-to-peak variations of the lower mass stars with $(R_C - I_C) \gtrsim 1.5$ mag cover a smaller range than the peak-to-peak variations of stars with $(R_C - I_C) \lesssim 1.3$ mag. For stars with $1.5 > (R_C - I_C) > 1.3$ the peak-to-peak variation seem to decrease more or less linear with increasing colour.

This trend can be quantified by using the cumulative frequency distributions of the peak-to-peak variation for higher and lower mass stars. In the top and bottom panel of Fig. 9.2 I show these distributions for strong and weak Hα emitters respectively (i. e. for TTSs and WTTSs, respectively). For both samples the discrimination between higher and lower mass stars was set at a colour of $(R_C - I_C) = 1.4$ mag; i. e. higher mass stars are bluer and lower mass stars are redder than this colour. This dividing colour was chosen since it represents the mean of the transition zone between the regions with large and small scatter in the peak-to-peak variations. Note that the colour of $(R_C - I_C) = 1.4$ mag corresponds approximately to an spectral type of M3–M4.

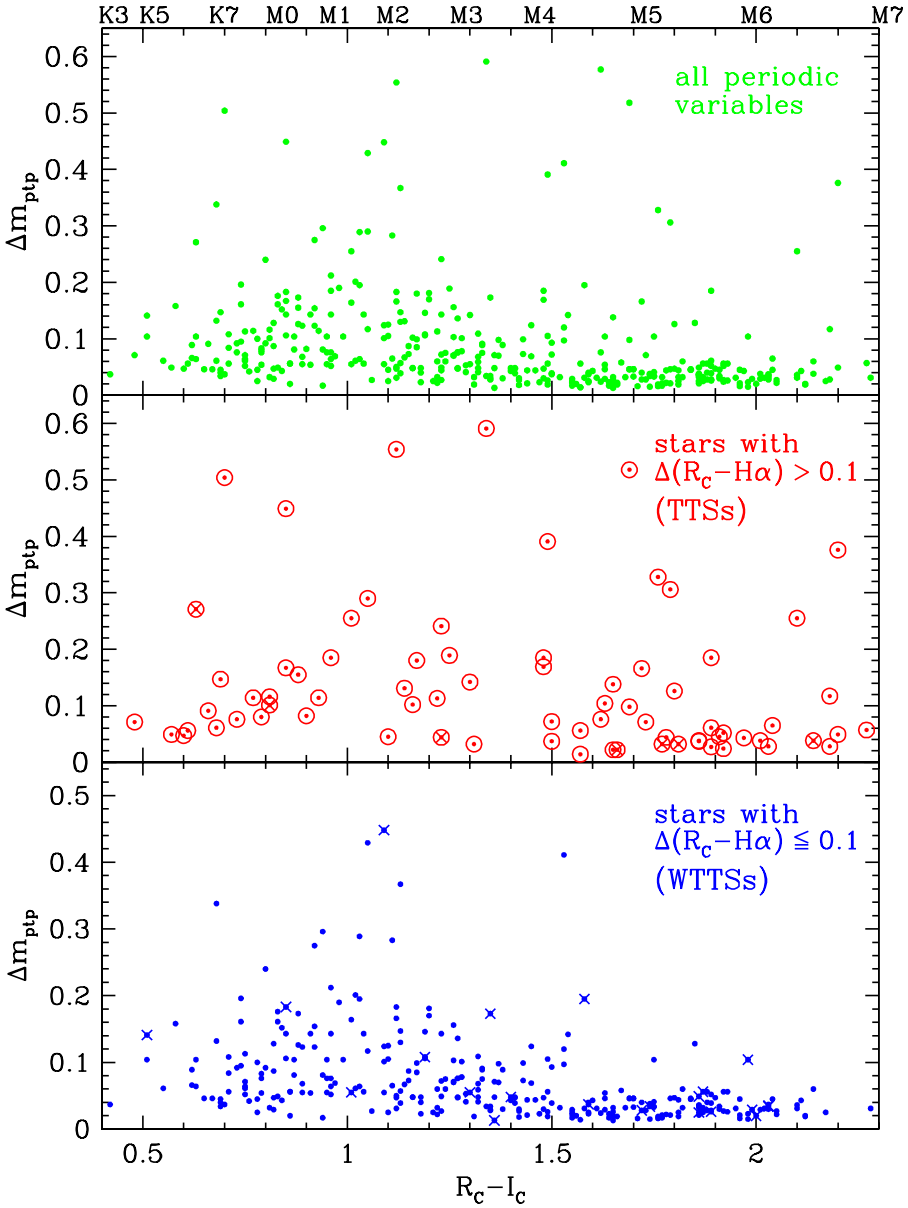

Fig. 9.1: The peak-to-peak variation, $\Delta m_{\rm ptp}$, of the periodic variables as a function of the $(R_{\rm C} - I_{\rm C})$ colour of the stars. In the top panel all periodic variables are shown. The diagram in the middle panel contains only stars with strong Hα emission (TTSs) indicated by a large Hα-index of $\Delta(R_{\rm C} - {\rm H}\alpha) > 0.1$ mag. In the bottom panel only stars with weak Hα emission (WTTSs) corresponding to $\Delta(R_{\rm C} - {\rm H}\alpha) \leq 0.1$ mag are shown. In both the middle and bottom panel those stars with large photometric errors which could shift a star below or above the discrimination level of 0.1 mag are marked by a cross.

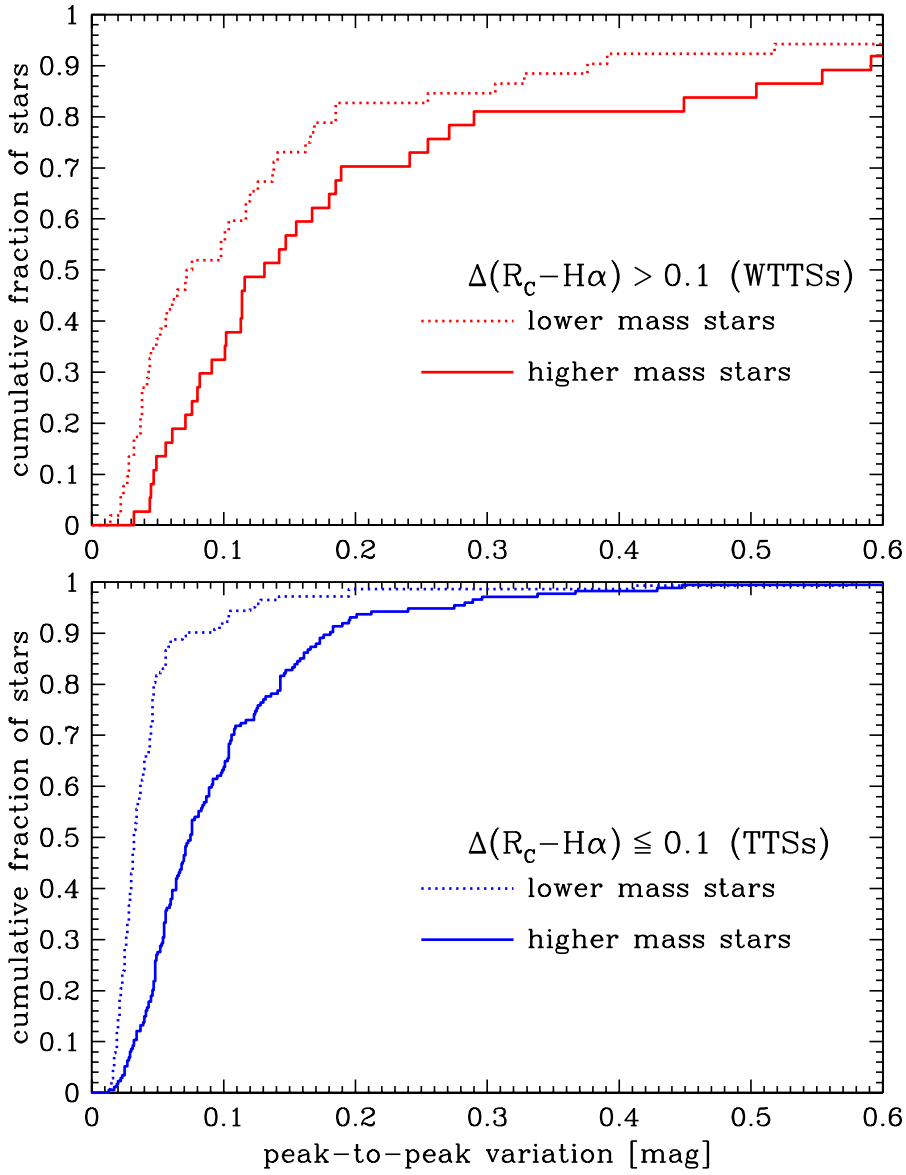

Fig. 9.2: The cumulative frequency distribution of the peak-to-peak variation, $\Delta m_{\rm ptp}$, for periodic variables with strong and weak Hα emission. The top panel shows the cumulative distribution for stars with a large Hα-index of $\Delta(R_{\rm C} - {\rm H}\alpha) > 0.1$ mag for higher mass stars with $(R_{\rm C} - I_{\rm C}) \leq 1.3$ mag and lower mass stars with $(R_{\rm C} - I_{\rm C}) > 1.3$ mag separately. The bottom panel shows the same for periodic variables with weak Hα emission and correspondingly smaller Hα-index of $\Delta(R_{\rm C} - {\rm H}\alpha) \leq 0.1$ mag.

The median peak-to-peak variations of the higher and lower mass stars with strong Hα emission are 0.13 mag and 0.07 mag respectively. For stars with weak Hα emission the median peak-to-peak variations are 0.08 mag for the higher mass stars and 0.03 mag for the lower mass stars. Therefore in both samples the higher mass periodic variables have peak-to-peak variations which are on average twice as large as those of the lower mass stars. In addition for weak Hα emitters it is also evident from Fig. 9.2 that about 90% of the lower mass stars with $(R_{\rm C} - I_{\rm C}) > 1.4$ mag have peak-to-peak variations only of ≤ 0.06 mag while only 38% of the higher mass stars have such small peak-to-peak variations.

The result that the lower mass stars show a distribution of the peak-to-peak variation which clearly differs from that of the higher mass stars (which is most obvious for the weak Hα emitters) is confirmed by a Kolmogorov-Smirnov test (Press et al., 1992). For both, stars with strong and weak Hα emission there is only probability of 0.03 and 2×10^{-24} respectively that the distribution for higher and lower mass stars are equivalent.

I emphasis that the smaller peak-to-peak variations of the faster rotators (i. e. the lower mass stars) are very surprising as I will outline in the following: The surface magnetic activity in late type stars is strongly correlated with the rotation period through a dynamo process. The usual interpretation in this framework (of a $\alpha - \omega$ dynamo model) is that the magnetic activity on the stellar surface scales with the internal magnetic flux which results from the action of differential rotation and turbulent convection (e. g. Bouvier, 1997). It is further assumed that internal differential rotation increases with the surface rotation. Thus, for fast rotators an enhanced magnetic surface activity is expected which is believed to cause larger surface spots and larger brightness variations.

As it was shown in Sect. 8.2 the lower mass stars in NGC 2264 rotate much faster on average than the higher mass stars in the cluster. Hence, *larger* peak-to-peak variations of the lower mass stars are expected, just the opposite to what is observed in NGC 2264. Therefore, the situation may not be quite as simple as assumed in the model described above. In the following Sections this will be discussed in more detail.

As it is outlined in Chapter 6 it is likely that the periodic brightness variations of the stars with larger Hα-indices are produced by hot surface spots, while cool spots are expected to be the source for the periodic brightness modulations of the stars with weak Hα emission. The stars with strong Hα emission often show irregular variability which was interpreted as a result of non-stable mass accretion. Therefore, their peak-to-peak variations are expected to be more variable between individual rotational cycles. In contrast the peak-to-peak variations of the stars with weak Hα emission (WTTSs) are expected to be much more stable over several rotation periods. The cool surface spots on the WTTSs should be mostly determined by the stellar properties while the magnetic field of CTTSs could be influenced by the presence of the circumstellar disk. For simplifying the subsequent discussion I therefore only consider stars with $\Delta(R_{\rm C} - {\rm H}\alpha) \leq 0.1$ mag (which are mostly WTTSs).

9.2 Peak-to-Peak Variation and Angular Velocity

In this section I discuss the dependence of peak-to-peak variations from the stellar rotation rate measured by the angular velocity $\omega = 2\pi/P$. Fig. 9.3 shows the measured peak-to-peak variation, $\Delta m_{\rm ptp}$, as a function of ω for higher mass stars with $(R_{\rm C} - I_{\rm C}) \leq 1.4$ mag

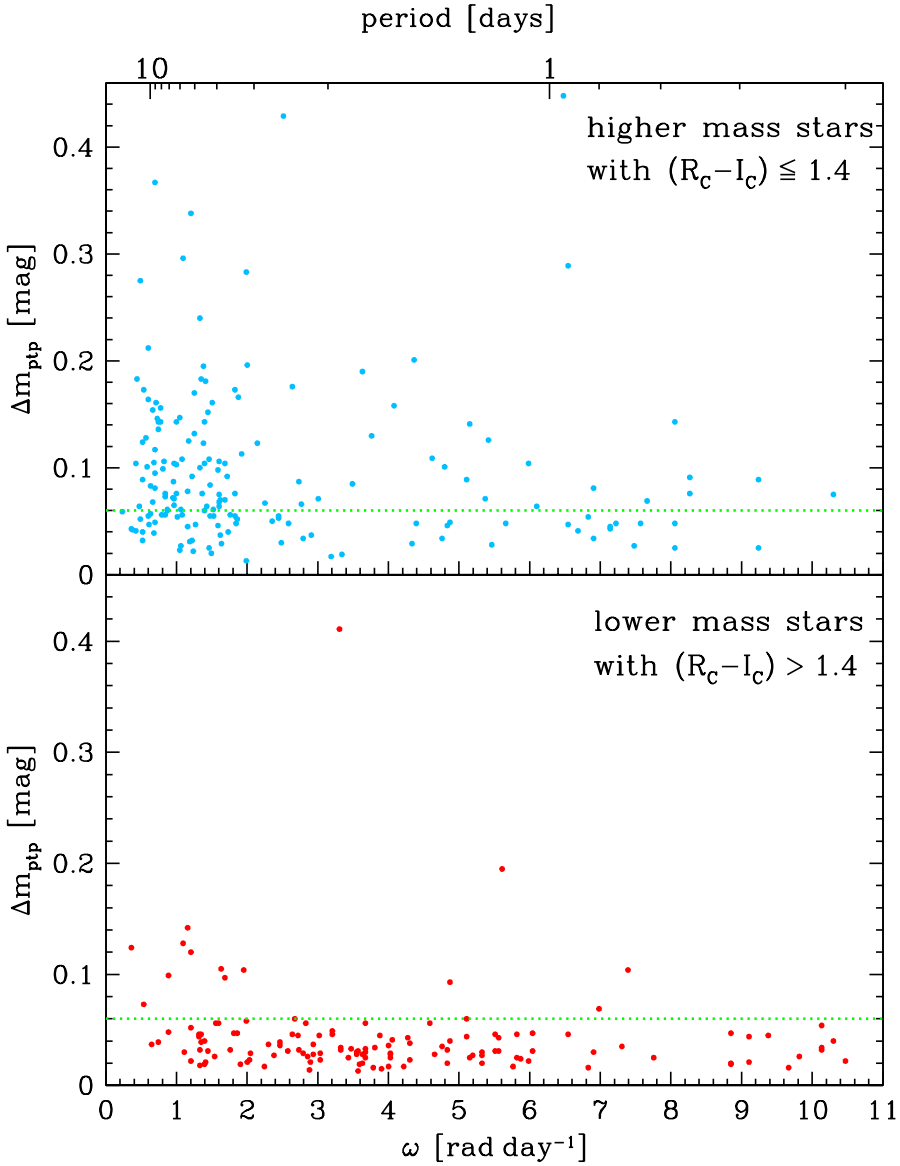

Fig. 9.3: The peak-to-peak variation of the periodic variables with a Hα-index of $\Delta(R_{\rm C} - {\rm H}\alpha) \leq 0.1$ mag (WTTSs) as a function of the angular velocity, ω. The top panel shows $\Delta m_{\rm ptp}$ of higher mass stars with $(R_{\rm C} - I_{\rm C}) \leq 1.4$ mag, while the bottom panel shows $\Delta m_{\rm ptp}$ only for lower mass with $(R_{\rm C} - I_{\rm C}) > 1.4$ mag. The green dotted line represents a peak-to-peak variation of 0.06 mag which is interpreted as the typical upper limit of the peak-to-peak variation for lower mass stars.

and lower mass stars with $(R_C - I_C) > 1.4$ mag separately. Fig. 9.3 shows only stars which have a small Hα-index of $\Delta(R_C - H\alpha) \leq 0.1$ mag.

For the lower mass stars there is an apparent upper limit of the peak-to-peak variations of $\Delta m_{ptp} = 0.06$ mag at least for the fast rotators. This limit is indicated by the horizontal dashed green line in the bottom panel of Fig. 9.3. The same line is also drawn in the diagram for the higher mass stars in the upper panel. It is further evident that most of the higher mass stars have an angular velocity of $\omega \lesssim 2.0$ rad day^{-1}. Most (9 out of 14) of the lower mass stars which exceed the limit of $\Delta m_{ptp} = 0.06$ mag have also $\omega \leq 2.0$ rad day^{-1}. Therefore there is a general trend that the peak-to-peak variation of the stars with $\omega < 2.0$ rad day^{-1} is higher on average than the peak-to-peak variation of faster rotating stars.

I note that the fraction of lower mass stars which exceeds $\Delta m_{ptp} = 0.06$ mag depends on the used colour cut in the sense that it is higher (15%) for a colour cut of $(R_C - I_C) = 1.3$ mag and lower (7%) for a colour cut of $(R_C - I_C) = 1.5$ mag (see also bottom panel of Fig. 9.1). This increase is mainly caused by stars with $\omega < 2.0$ rad day^{-1} because the number of stars with $\Delta m_{ptp} = 0.06$ mag in this angular velocity range changes from 15 to 5 for a colour cut of $(R_C - I_C) = 1.3$ mag and $(R_C - I_C) = 1.5$ mag respectively, while the corresponding numbers of faster rotating stars with such a large peak-to-peak variation changes only from 10 to 5. This could indicate that most of the stars classified as lower mass stars which have large peak-to-peak variations and slow angular velocities are actually higher mass stars which are reddened more than average and therefore have been shifted in the lower mass colour regime.

The obviously different behaviour of the lower and higher mass stars regarding the level of the peak-to-peak variation naturally pose the question which physical processes are responsible for the observed effects. As mentioned in the previous Section, it would be surprising if the faster rotating lower stars have much weaker magnetic fields than the slower rotating higher mass stars. Therefore this simple explanation is inadequate and other possible explanations are necessary. In addition it is very surprising that the change from large to small peak-to-peak variations appears to happen rather abruptly at a colour of $(R_C - I_C) \approx 1.4$ mag (i. e. at a spectral type of M3 – M4) and an angular velocity of $\omega \approx 0.2$ rad day^{-1}. In the following section I discuss possible reasons for this sudden change in the observed peak-to-peak variations.

9.3 Reasons for the Smaller Peak-to-Peak Variations of the Lower Mass Stars

Since it is extremely unlikely that my results can be explained by differences in the inclination angles of the rotation axes between slow and fast rotators one has to invoke different spot patterns on the stellar surface to explain the differences in the peak-to-peak variations between the two samples.

How different spot patterns could explain the differences in the peak-to-peak variations is illustrated in Fig. 9.4. Large peak-to-peak variations can be most easily explained by correspondingly large spots or spot groups located at relatively low stellar latitudes (see Fig. 9.4a). Herbst et al. (1994) argued on the basis of observed light curves of WTTSs that the maximum possible peak-to-peak variations resulting from cool surface spots are

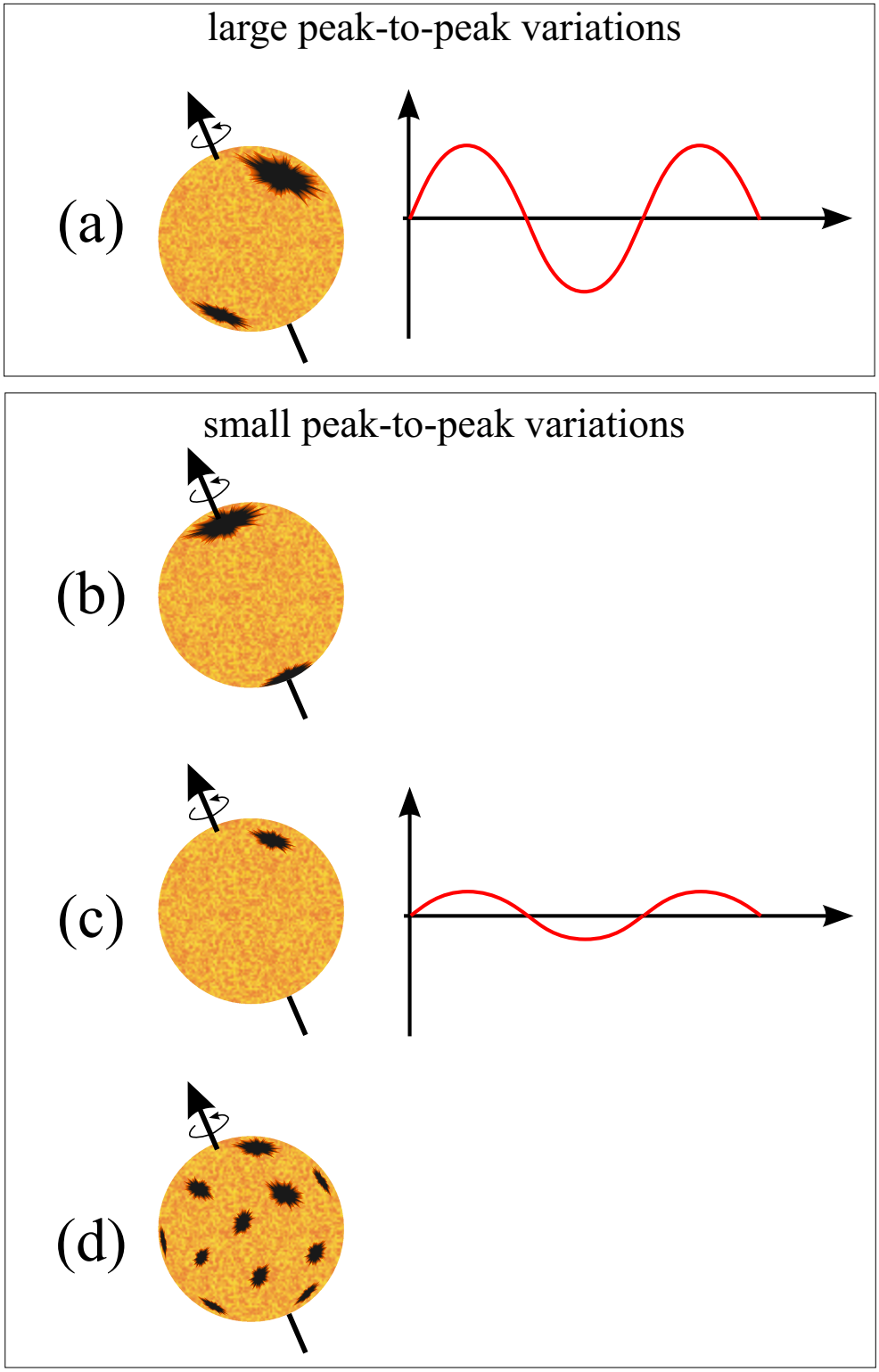

Fig. 9.4: Schematic illustration of possible spot patters which produce large and small peak-to-peak variations.

0.5 mag in I. In NGC 2264 I observed maximum peak-to-peak variations of 0.45 mag in I_C for stars with $\Delta(R_C - H\alpha) \leq 0.1$ mag (i. e. stars which have most likely cool spots). About 97% of these stars have peak-to-peak variations below 0.2 mag in I_C. Observations of late K and early M type TTSs suggest that about 20% – 30% of the stellar surface can be covered by such spots (Vrba et al., 1989, 1993; Bouvier & Bertout, 1989). The colour variations of these stars further suggest effective spot temperatures which are typically 500 – 1000 K below that of the stellar photospheres.

Possible spot patters to explain the small peak-to-peak variations are shown in Fig 9.4b–d. First, small peak-to-peak variations of a spotted star can be produced by a two spot pattern for which the spots are located close to the rotation axis at large latitudes (see panel (b) of Fig. 9.4). This would be the case for a perfect bipolar magnetic field which is aligned with the rotation axis. However, there is no obvious reason that the lower mass stars have a different alignment a bipolar magnetic field than the higher mass stars.

Second, it is possible that the spot pattern is the same as for the stars with large peak-to-peak variations but the spot(s) itself is of smaller relative size and therefore the spot-photosphere contrast is small (see Fig. 9.4c). However, it would be surprising if the spot on lower mass stars have a smaller relative size than those on higher mass stars since the former rotate faster on average than the latter (see previous Sect.). Therefore one would expect larger magnetic surface flux for the lower mass stars resulting in a larger (total) spotted area. Hence, it is unlikely that a single or few small spots produce the observed behaviour of the peak-to-peak variations.

Maybe the most realistic spot pattern which could explain the observed differences in the peak-to-peak variations of higher and lower mass stars is shown in Fig. 9.4d. It consists of many small spots or spot groups which are relatively evenly distributed over the whole stellar surface and gives rise to small peak-to-peak variations. Although the individual spots are small the total spot area may be as large as one single spot in case (a). Therefore the total magnetic flux on the stellar surface may be comparable with that of a bipolar magnetic field and more distributed over the whole surface.

If panel (a) and (d) of Fig. 9.4 actually describe most realistically the spot pattern on the higher and lower mass stars than it is clear that the pattern suddenly changes for spectral types later than M3–M4. The main reason may be a change in the magnetic field topology since the cool spots are believed to be the "footprints" of the magnetic field on the stellar surface. In the following section I discuss possible reasons for such a change.

9.4 Different Magnetic Field Topologies

It is widely accepted that the magnetic fields of late type stars result from basically two different kinds of dynamo mechanisms. First, it is believed that large-scale magnetic fields are produced in an interface layer at the base of the convection zone and above the radiative core of the stars (e. g. Spiegel & Weiss, 1980) and the resulting dynamo is of $\alpha\Omega$-type. Beside this shell like dynamo turbulent dynamos are at work in stars with thick convection zones and this latter dynamo type is the only possible type in fully convective stars (Durney, de Young, & Roxburgh, 1993). These latter stars are therefore not expected to have large-scale magnetic fields. The turbulent dynamo must be of another kind and is likely of the α^2-type (Steenbeck & Krause, 1969; Küker & Rüdiger, 1999).

TTSs are expected to be fully convective during their early evolution stages. When these stars contract toward the MS the radiative core forms and the stars evolves no longer along the (convective) Hayashi tracks in the HR-diagram but follow the (radiative) Henyey tracks. Küker & Rüdiger (1999) argued that at the time when the star branches off the convective track the mechanism of field generation changes from the α^2 to the $\alpha\Omega$ due to the strong rotational shear between the radiative core and the convection zone.

These different dynamo mechanisms must have an impact on the magnetic field topology and therefore must also leave their imprint in the spot pattern on the stellar surface. Since shell-like dynamos on the one hand produce large scale magnetic fields it could be that the spot pattern of these stars consists only of a few large spots (or spot groups) as it is indicated in panel (a) of Fig. 9.4. Turbulent dynamos on the other hand might be unable to produce such large-scale magnetic fields. Therefore the spot pattern could also have a small-scale nature as it is illustrated in panel (d) of Fig. 9.4. If this is true than the observed change in the peak-to-peak variation would result from a sudden change of the topology of the magnetic field resulting from a abrupt change of the dynamo mechanism.

However, as mentioned above low mass TTSs stars are generally expected to be fully convective in the early evolution stages. PMS evolution models by D'Antona & Mazzitelli (1997) or Krishnamurthi et al. (1997) suggest that at the age of NGC 2264 stars with masses $M \lesssim 0.9\ M_{\odot}$ are still fully convective. Hence, one would expect that stars below this mass have magnetic fields which are generated by turbulent dynamos, while for higher mass stars the shell dynamo mechanism dominates. With the interpretation presented above this contradicts the observation that the change of the peak-to-peak variation appears at about $0.3\ M_{\odot}$ (corresponding to a spectral type of M3–M4). It is interesting that this spectral type agrees with the limit below which stars reach the MS as fully convective stars; i. e. these stars never evolve a radiative core. If the presented interpretation of the peak-to-peak variations is true this could indicate that at the age of NGC 2264 a shell-like dynamo is already inherent in stars with $M \gtrsim 0.3\ M_{\odot}$.

9.5 The Impact of a Changing Magnetic Field Topology on the Rotational Evolution

As outlined in the previous section there is evidence for a change in the magnetic field topology from the higher mass stars to the lower mass stars. Since the magnetic field plays a decisive role in the disk-locking scenario (see Chapter 8) one has to discuss the impact of the changing magnetic field topology on the rotational evolution of the stars.

Recently, Barnes (2003) has proposed that different dynamo processes are responsible for the observed bimodal period distribution of the higher mass stars in the ONC. For stars with a shell dynamo on the one hand and stars a turbulent dynamo on the other hand he proposed two different rotational sequences which he called the "interface" (I) and the "convective" (C) sequence respectively. He further suggested that the bimodality of the period distribution in the ONC "represents an early glimpse ... perhaps even the first incarnation of the I and C sequences".

In order to investigate these ideas further I show in Fig. 9.5 the period (on logarithmic scale) as a function of the $(R_{\rm C} - I_{\rm C})$ colour for the stars with weak Hα emission (i.e. $\Delta(R_{\rm C} - {\rm H}\alpha) \leq 0.1$ mag). These stars were divided into two subsamples according to the

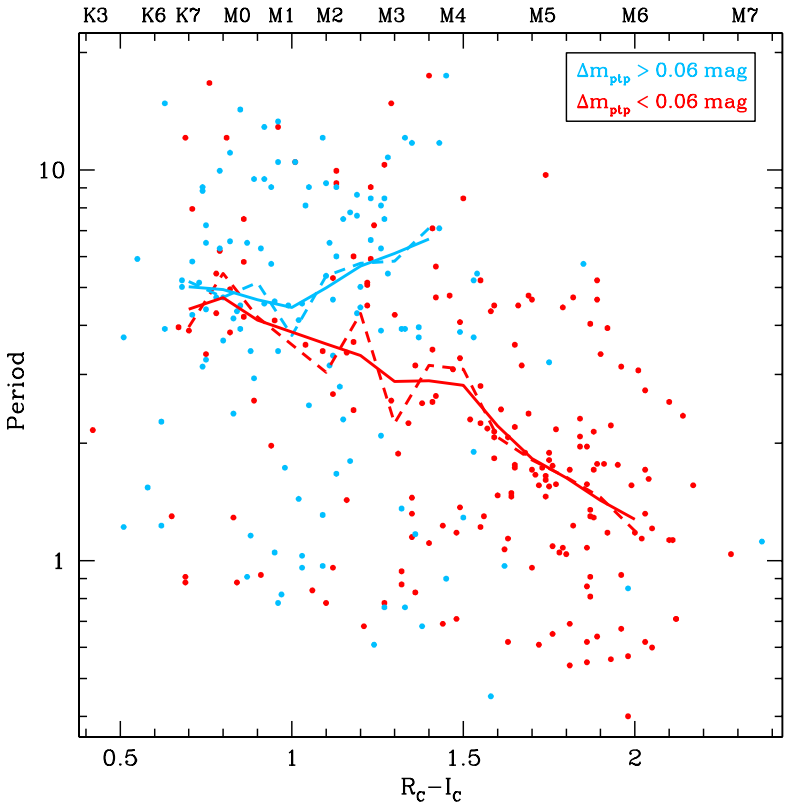

Fig. 9.5: The period of the stars with weak Hα-emission ($\Delta(R_{\rm C} - {\rm H}\alpha) \leq$ 0.1 mag) as a function of the $(R_{\rm C} - I_{\rm C})$ colour. Blue symbols represent stars with $\Delta m_{\rm ptp}>$ 0.06 mag while red symbols represent stars with $\Delta m_{\rm ptp}<$ 0.06 mag. The red and blue dashed lines represent the median periods of the stars with peak-to-peak variations above and below 0.06 mag respectively. These medians for both samples were calculated in $(R_{\rm C} - I_{\rm C})$-bins of width 0.1 mag. The solid lines represent smoothed median curves.

green line in Fig. 9.3, namely into stars with $\Delta m_{\rm ptp}>$ 0.06 mag and $\Delta m_{\rm ptp}<$ 0.06 mag respectively. For each of these two samples I calculated the median rotation period in fixed sized $(R_{\rm C} - I_{\rm C})$ bins of width 0.1 mag. The resulting medians for both samples are shown as the dashed lines in Fig. 9.5. The solid lines in this figure represent smoothed median curves. The blue and the red solid line are comparable with the I and C sequences shown in Fig. 2 or Fig. 6 of of Barnes (2003).

If the bimodal distribution of the higher mass stars would result from the two different sequences (as proposed by Barnes, 2003) and if the division into the interface and convective sequence is equivalent to the division into stars with small and large peak-to-peak variations (as proposed by Fig. 9.5 and the discussion in the previous section) than one would expect different rotation period distributions for the (higher mass) stars with large and small peak-to-peak variations respectively. Therefore I show these period distributions of the higher mass stars with $\Delta(R_{\rm C} - {\rm H}\alpha) \leq$ 0.1 mag for large and low peak-to-peak variations in the top panel of Fig. 9.6.

Although the period distributions of the two samples of higher mass stars differs in some detail they are not significantly different from each other. A Kolmogorov-Smirnov test (Press et al., 1992) yields a probability of 0.36 that the two samples are equivalent. The period distribution of stars with large peak-to-peak variations shows a small excess for

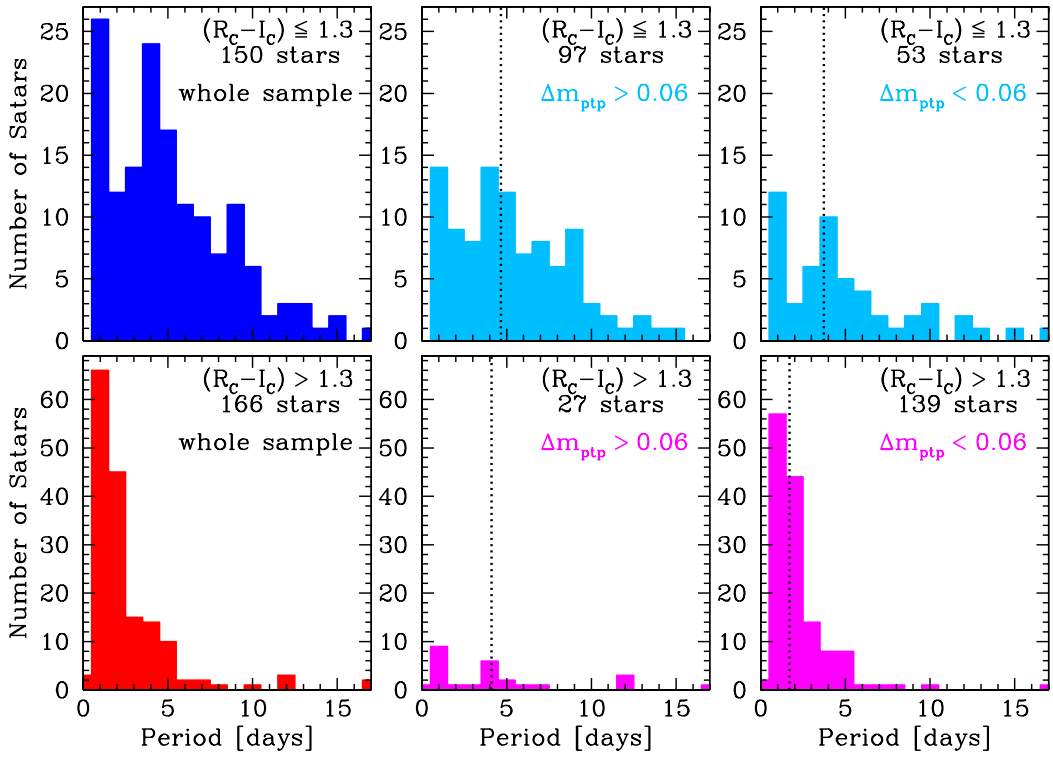

Fig. 9.6: Period distributions for stars with weak Hα-emission (i. e. $\Delta(R_{\rm C} - {\rm H}\alpha) \leq$ 0.1 mag). **Top panels:** Histograms for higher mass stars with $(R_{\rm C} - I_{\rm C}) \leq$ 1.3 mag. In the left panel the period distribution of all these stars are shown. The middle and right panel show the distributions for stars with large ($\Delta m_{\rm ptp} >$ 0.06 mag) and small ($\Delta m_{\rm ptp} <$ 0.06 mag) peak-to-peak variations respectively. The dotted line represent the median rotation period in each sample. **Bottom panels:** The same for the lower mass stars with $(R_{\rm C} - I_{\rm C}) >$ 1.3 mag.

periods between 5 and 10 days compared with distribution of the stars with small peak-to-peak variations. However, the bimodality of the period distribution is apparent for both samples, although more clearly for the stars with low peak-to-peak variations. Therefore it is unlikely that the bimodality of the period distribution for the higher mass stars in NGC 2264 results straightforward from the adopted two different dynamo mechanisms. A further interesting difference between the two samples is the larger fraction of stars with very short periods ($\leq$ 1.5 days) for the stars with $\Delta m_{\rm ptp} <$ 0.6 mag.

For the sake of completeness I show the corresponding period distributions of the lower mass stars in the bottom panels of Fig. 9.6. Since almost all stars in this mass regime have peak-to-peak variations of $\Delta m_{\rm ptp} \leq$ 0.06 mag these distributions are only of limited significance. However, the distribution of the lower mass stars with $\Delta m_{\rm ptp} >$ 0.06 mag shows a kind of bimodal distribution. This could indicate that the speculation mentioned above is true, i. e. that these stars are actually higher mass which are reddened more than average.

The discussion in this section leads to the conclusion that it is very unlikely that the bimodal period distribution of the higher mass stars reflects the two different samples of stars with large and small peak-to-peak variations respectively. The different dynamo

mechanisms which are probably responsible for large or small peak-to-peak variations, might also be responsible for the different rotational behaviour of the higher and lower mass stars, i. e. the shorter rotation periods of stars with spectral later than M3 compared with stars of earlier spectral type. Since the disk-locking process discussed in the previous Chapter 8 depends strongly on the magnetic field of the stars, the different magnetic field topologies suggested for the lower mass stars could result in a much longer time time scale τ_{D} by which disk-locking is finally achieved.

Chapter 10

Summary & Future Prospects

10.1 The underlying data set

For this thesis an extensive photometric monitoring program has been carried out in the area of the young open cluster NGC 2264. In total about 10500 stars in the magnitude range between I_C= 9.8 mag and I_C= 21 mag were monitored over a total time interval of more than two months. All of these stars have been checked for both periodic and irregular variability using two different periodogram techniques and a χ^2-test respectively.

Two PMS tests were applied to the sample of variable stars in order to reject variable stars which are obviously not PMS stars from the further analysis. This two selection criteria yield a total of 589 variable stars which are most likely PMS stars. The location of the variables in the colour-magnitude diagram (Fig. 8.1) suggests that they cover a mass range from about 1.2 $M_\odot$ probably down into the substellar regime. Out of the 589 variable PMS stars 405 show periodic brightness modulations while 184 stars are irregularly variable. In addition I have detected 52 non-variable PMS stars in NGC 2264 with strong Hα-emission. This numbers mean that I was able to increased the number of known PMS stars in NGC 2264 by a factor of 3.5 and the number of published rotation periods in NGC 2264 by more than a factor of ten.

Thanks to this study in NGC 2264 there exists now a second cluster aside the ONC for which a statistically significant number of rotation periods is known. Such a large data set is of particular importance for the analysis presented here because it is possible to divide the total sample of stars in various sub-samples (e. g. samples of different masses, ages, or Hα-emission strength) and investigate the rotational properties of these different samples.

As a first result I found that the degree of variability (measured by the standard deviation of the stars) is typically larger for the irregular variables. The analysis of the Hα-index demonstrated that the irregular variables additionally show stronger Hα-emission on average than periodic variables. I concluded that the fraction of CTTSs is much larger among the irregular variables compared with the periodic variables and vice versa for the WTTSs.

I have estimated how much the sample of periodic variables in the range of $(R_C - I_C) \leq 1.8$ mag and $I_C \leq 18.0$ mag is biased towards the WTTSs. Therefore I compared the estimated fraction of WTTSs among the complete cluster population with the fraction of WTTSs among the periodic variables. I note that WTTSs and CTTSs were defined

here as stars with small Hα-index (i. e. $\Delta(R_{\rm C} - {\rm H}\alpha) < 0.1$ mag) and large Hα-index (i. e. $\Delta(R_{\rm C} - {\rm H}\alpha) > 0.1$ mag) respectively. I found that the bias of the periodic variables towards the WTTSs is partially canceled due to those WTTSs for which no periods could be detected probably because of small amplitudes in their brightness variations. The expected composite of the periodic sample (i. e. the estimated composite of the whole cluster population) is of 76% WTTSs and of 24% CTTSs. The periodic sample itself is composed of WTTSs by 84% and of CTTSs by 16%. Hence, compared with the expected value the fraction of WTTSs among the periodic variables is by about 10% too large. However, this is only a small bias towards the WTTSs and the discussion of the rotational properties which is based on the periodic sample should therefore be a representative for the whole cluster.

10.2 The rotational evolution young stars

The rotational evolution of young stars with masses of $0.1\ M_{\odot} \lesssim M \lesssim 1.2\ M_{\odot}$ was discussed on the basis of the extensive data set which I obtained for NGC 2264 and on the basis of rotation periods of stars in the somewhat younger ONC measured by Herbst et al. (2002). NGC 2264 and the ONC are to date the only PMS clusters for which statistically significant samples of PMS stars with known rotation period are available.

First of all it was necessary to determine the age ratio of the two clusters. The age ratio deduced from the ages given in the literature is $2 - 4$ (with a best estimate of 3), but I have shown that the age ratio of the clusters is probably somewhat smaller than that. Although it is hard to estimate the error on the age ratio I concluded that it is probably in the range of $1.5 - 2.75$ with the most probable value of about 2.

I found that the period distribution of NGC 2264 is mass dependent and bimodal for stars with $M \gtrsim 0.3\ M_{\odot}$ while the period distribution of lower mass NGC 2264 stars with $M \lesssim 0.3\ M_{\odot}$ is unimodal. In addition the lower mass stars rotate faster on average than the higher mass stars. Hence, the period distribution of the stars in NGC 2264 is similar to the period distribution of the ONC reported by Herbst et al. (2002). The interesting difference of the distributions in both clusters is that the peaks of NGC 2264 are at shorter periods compared with the related peaks of the ONC. This is immediately connected with the result that the higher and lower mass stars in NGC 2264 rotate faster on average than the stars in the corresponding mass regimes of the ONC. I concluded that most stars in NGC 2264 spun up compared with the stars in the ONC and I have shown that this spin up can be explained by conservation of angular momentum and gravitational contraction of the stars. Contrary I was not able to detect a significant spin up between younger and older stars in NGC 2264 which is probably due to uncertain age determinations of the individual stars.

However, there is evidence that a certain fraction of stars in NGC 2264 (e. g. about 20%–30% of the higher mass stars) maintain a relatively low rotation rate beside the fact that they have aged from the ONC. This led me to the conclusion that disk-locking is and was present among the higher mass in NGC 2264. Evidence for the presence of disk-locking among the higher mass stars is provided by the period distribution on a logarithmic scale or by the period distribution of stars with strong Hα-emission measured by a large Hα-index (i. e. CTTSs). The period distribution of these stars suggest a locking-period of about 8 days which is consistent with this commonly adopted locking period (e. g. by

Herbst et al., 2002).

For the rotational evolution of the lower mass stars from the age of the ONC to the age of NGC 2264 disk-locking seems to play only a minor role because most of these stars are fast rotators and probably spin up with conserved angular momentum or with only moderate angular momentum loss. Based on the period distribution of lower mass CTTSs I concluded that if the lower mass stars are indeed disk-locked their locking period must be shorter than that of the higher mass stars, namely about 2–3 days. The rotational evolution of the lower mass stars is probably determined by the scenario which I called "imperfect" disk-locking. This scenario is characterised by a disk-star interaction which removes angular momentum from the stars but not enough to lock the star to a constant rotation period.

Different magnetic field topologies of the higher and lower mass stars could explain the apparently different rotational behaviour of the two samples. I found that the peak-to-peak variations of the lower mass periodic variables which were classified as WTTSs are in almost all cases below 0.06 mag and therefore significantly smaller than the peak-to-peak variations of the corresponding higher mass stars. The latter have typical peak-to-peak variations of $\Delta m_{\rm ptp} \lesssim 0.2\,mag$ but up to 0.6 mag in some extreme cases. These differences in the peak-to-peak variations of higher and lower mass stars are very surprising. I concluded that the different behaviour results from entirely different spot patterns which are present on the surfaces of higher and lower mass stars respectively.

I further argued that these entirely different spot patterns result from different dynamo processes which are at work in higher and lower mass stars respectively. According to this interpretation higher mass stars on the one hand have large scale magnetic fields resulting from shell dynamos (e. g. of $\alpha\omega$-type). The magnetic fields of lower mass stars on the other hand are of small scale structure and could be produced by turbulent dynamo processes (e. g. of α^2-type). I concluded that these different magnetic field structures of higher and lower mass stars affect the rotational evolution of the two samples in the sense that it is unlikely that lower mass stars are able to achieve disk-locking disk-locking when they are at the age of the ONC or NGC 2264.

10.3 Outlook

I have outlined that the adopted methods of selecting PMS stars in NGC 2264 are extremely efficient. In particular variability itself is probably one of the best indicators for youth of the stars. However, additional data such as spectroscopic measurements of the Li I and Hα equivalent width for all variable stars might improve the results. In addition, with knowledge of the spectral type of each variable star individual dereddening is possible. Using a dereddened CMD or the HR diagram this would yield a more accurate mass and age determination and thus to a better division into higher and lower mass stars. In particular the rotational evolution of PMS stars in NGC 2264 (i. e. differences between young and old stars) would be better constrained since uncertainties of the age determination might be smaller. Hence, a future goal is to obtain spectra for the whole sample of variables I found in NGC 2264 with a resolution sufficient to determine the spectral type, the Hα, and Li I equivalent width. Large amounts of spectra could be obtained using multi-object spectrographs such as MOSCA on the 3.5m telescope of the Calar Alto observatory.

Another goal is to improve the selection of disk-locked candidates. As already outlined in Sect. 8.4.1 in the ideal case both large Hα emission *and* large infrared excess should be used for the selection of disk-locked stars. Therefore, nearly simultaneous observations of NGC 2264 in the J, H, and K-bands are necessary to determine different infrared excesses. The infrared camera Ω2000 of the 3.5m telescope on Calar Alto is the ideal instrument for such observations because of the large area on the sky (about $15' \times 15'$) which it covers. I have tried to obtain infrared images of the cluster, but the observations were clouded out completely.

Regarding the rotational evolution of low mass stars it appears necessary to obtain more rotation periods of stars which are slightly older than the two clusters considered here; i. e. to obtain statistically significant samples of stars with known rotation periods. In particular for stars less massive than about 0.3 $M_{\odot}$ more rotation rates are needed to investigate their rotational evolution until they reach the main sequence. Hence, extensive photometric monitoring programs which are sensitive down into the substellar regime have to carried out. Possible targets for such programs are the clusters NGC 1333 (1 Myr), IC 348 (2 Myr), ρ Oph (2 Myr), NGC 6611 (3 Myr), NGC 2362 (5 Myr), IC 2602, IC 2391, and NGC 1960 (all about 30 Myr).

In order to improve our knowledge about the initial conditions of the rotational evolution in the PMS phase, more rotation rates of protostars (class I objects) are necessary. However, photometric monitoring of these deeply embedded objects is complicated because they are expected to be highly irregularly variable due to their large mass accretion rates. In addition such programs have to carried out in the infrared. A better strategy to obtain rotation rates of protostars might be using high-resolution near-infrared spectra in order to determine $v \sin i$ values for these objects, a method which was successful employed in the past e. g. by Greene & Lada (2002a).

Finally $v \sin i$ measurements of all periodic variables provide the possibility to calculate (inclination dependent) radii of the stars using the measured rotation periods; i. e. calculating $R (\sin i) = v(\sin i)P/2\pi$. This would allow us to check the radius predictions of PMS evolution models.

Appendix

Appendix A

Error Correction Functions

The errors we used for applying the χ^2-test were corrected using the following transformations.

Aperture Photometry with 8 pixel Aperture Size

5 sec Exposures

Fit of standard deviation σ in the light curve:

$$S(I_{\mathrm{C}}) = \begin{cases} 0.015 & , \quad I_{\mathrm{C}} < 14.22 \\ e^{0.529 \times I_{\mathrm{C}} - 11.718} & , \quad I_{\mathrm{C}} \geq 14.22 \end{cases} \tag{A.1}$$

Fit of the median error $\overline{\delta m_{\mathrm{rel}}}$ in the light curve:

$$M(I_{\mathrm{C}}) = \begin{cases} 0.005 & , \quad I_{\mathrm{C}} < 13.91 \\ e^{0.694 \times I_{\mathrm{C}} - 14.956} & , \quad I_{\mathrm{C}} \geq 13.91 \end{cases} \tag{A.2}$$

Resulting error correction factor:

$$C(I_{\mathrm{C}}) = \begin{cases} 3.0 & , \quad I_{\mathrm{C}} < 13.91 \\ e^{-0.694 \times I_{\mathrm{C}} + 10.756} & , \quad 13.91 \leq I_{\mathrm{C}} < 14.22 \\ e^{-0.166 \times I_{\mathrm{C}} + 3.238} & , \quad 14.22 \leq I_{\mathrm{C}} \end{cases} \tag{A.3}$$

50 sec Exposures

Fit of standard deviation σ in the light curve:

$$S(I_{\mathrm{C}}) = \begin{cases} 0.011 & , \quad I_{\mathrm{C}} < 16.33 \\ e^{0.764 \times I_{\mathrm{C}} - 16.988} & , \quad I_{\mathrm{C}} \geq 16.33 \end{cases} \tag{A.4}$$

Fit of the median error $\overline{\delta m_{\mathrm{rel}}}$ in the light curve:

$$M(I_{\mathrm{C}}) = \begin{cases} 0.005 & , \quad I_{\mathrm{C}} < 15.94 \\ e^{0.827 \times I_{\mathrm{C}} - 18.477} & , \quad I_{\mathrm{C}} \geq 15.94 \end{cases} \tag{A.5}$$

Resulting error correction factor:

$$C(I_{\mathrm{C}}) = \begin{cases} 2.2 & , \quad I_{\mathrm{C}} < 15.94 \\ e^{-0.827 \times I_{\mathrm{C}} + 13.967} & , \quad 15.49 \leq I_{\mathrm{C}} < 16.33 \\ e^{-0.063 \times I_{\mathrm{C}} + 4.435} & , \quad 16.33 \leq I_{\mathrm{C}} \end{cases} \tag{A.6}$$

500 sec Exposures

Fit of standard deviation σ in the light curve:

$$S(I_{\mathrm{C}}) = \begin{cases} 0.01 & , \quad I_{\mathrm{C}} < 17.55 \\ e^{0.809 \times I_{\mathrm{C}} - 18.815} & , \quad I_{\mathrm{C}} \geq 17.55 \end{cases} \tag{A.7}$$

Fit of the median error $\overline{\delta m_{\mathrm{rel}}}$ in the light curve:

$$M(I_{\mathrm{C}}) = \begin{cases} 0.005 & , \quad I_{\mathrm{C}} < 17.38 \\ e^{0.857 \times I_{\mathrm{C}} - 20.188} & , \quad I_{\mathrm{C}} \geq 17.38 \end{cases} \tag{A.8}$$

Resulting error correction factor:

$$C(I_{\mathrm{C}}) = \begin{cases} 2.0 & , \quad I_{\mathrm{C}} < 17.38 \\ e^{-0.857 \times I_{\mathrm{C}} + 15.583} & , \quad 17.38 \leq I_{\mathrm{C}} < 17.55 \\ e^{-0.047 \times I_{\mathrm{C}} + 1.374} & , \quad 17.55 \leq I_{\mathrm{C}} \end{cases} \tag{A.9}$$

Aperture Photometry with 20 pixel Aperture Size

5 sec Exposures

Fit of standard deviation σ in the light curve:

$$S(I_{\mathrm{C}}) = \begin{cases} 0.006 & , \quad I_{\mathrm{C}} < 13.59 \\ e^{0.709 \times I_{\mathrm{C}} - 14.231} & , \quad I_{\mathrm{C}} \geq 13.59 \end{cases} \tag{A.10}$$

Fit of the median error $\overline{\delta m_{\mathrm{rel}}}$ in the light curve:

$$M(I_{\mathrm{C}}) = \begin{cases} 0.005 & , \quad I_{\mathrm{C}} < 12.86 \\ e^{0.761 \times I_{\mathrm{C}} - 15.651} & , \quad I_{\mathrm{C}} \geq 12.86 \end{cases} \tag{A.11}$$

Resulting error correction factor:

$$C(I_{\mathrm{C}}) = \begin{cases} 1.2 & , \quad I_{\mathrm{C}} < 12.86 \\ e^{0.709 \times I_{\mathrm{C}} - 8.932} & , \quad 12.86 \leq I_{\mathrm{C}} < 13.59 \\ e^{-0.053 \times I_{\mathrm{C}} + 4.21} & , \quad 13.59 \leq I_{\mathrm{C}} \end{cases} \tag{A.12}$$

50 sec Exposures

Fit of standard deviation σ in the light curve:

$$S(I_{\mathrm{C}}) = \begin{cases} 0.006 & , \quad I_{\mathrm{C}} < 14.80 \\ e^{0.675 \times I_{\mathrm{C}} - 15.113} & , \quad I_{\mathrm{C}} \geq 14.80 \end{cases} \tag{A.13}$$

Fit of the median error $\overline{\delta m_{\mathrm{rel}}}$ in the light curve:

$$M(I_{\mathrm{C}}) = \begin{cases} 0.005 & , \quad I_{\mathrm{C}} < 15.30 \\ e^{0.716 \times I_{\mathrm{C}} - 16.257} & , \quad I_{\mathrm{C}} \geq 15.30 \end{cases} \tag{A.14}$$

Resulting error correction factor:

$$C(I_{\mathrm{C}}) = \begin{cases} 2.2 & , \quad I_{\mathrm{C}} < 14.80 \\ e^{0.675 \times I_{\mathrm{C}} - 9.814} & , \quad 14.80 \leq I_{\mathrm{C}} < 15.30 \\ e^{-0.041 \times I_{\mathrm{C}} + 1.145} & , \quad 15.30 \leq I_{\mathrm{C}} \end{cases} \tag{A.15}$$

500 sec Exposures

Fit of standard deviation σ in the light curve:

$$S(I_{\mathrm{C}}) = \begin{cases} 0.01 & , \quad I_{\mathrm{C}} < 16.77 \\ e^{0.809 \times I_{\mathrm{C}} - 18.815} & , \quad I_{\mathrm{C}} \geq 16.77 \end{cases} \tag{A.16}$$

Fit of the median error $\overline{\delta m_{\mathrm{rel}}}$ in the light curve:

$$M(I_{\mathrm{C}}) = \begin{cases} 0.005 & , \quad I_{\mathrm{C}} < 15.96 \\ e^{0.857 \times I_{\mathrm{C}} - 20.188} & , \quad I_{\mathrm{C}} \geq 15.96 \end{cases} \tag{A.17}$$

Resulting error correction factor:

$$C(I_{\mathrm{C}}) = \begin{cases} 2.0 & , \quad I_{\mathrm{C}} < 15.96 \\ e^{0.842 \times I_{\mathrm{C}} - 13.434} & , \quad 15.96 \leq I_{\mathrm{C}} < 16.77 \\ e^{-0.010 \times I_{\mathrm{C}} + 0.848} & , \quad 16.77 \leq I_{\mathrm{C}} \end{cases} \tag{A.18}$$

Appendix B

Definition of the PMS Zone in the Colour-Magnitude Diagram

The PMS zone in the colour-magnitude diagram is shown in Fig. 4.8. The borders of this region are indicated by the dashed lines which are given by the following equations:

Upper borderline:

$$I_{\mathrm{C}} = \begin{cases} 5.22 \times (R_{\mathrm{C}} - I_{\mathrm{C}}) + 7.5 & , \quad I_{\mathrm{C}} \leq 0.958 \\ 2.82 \times (R_{\mathrm{C}} - I_{\mathrm{C}}) + 9.8 & , \quad I_{\mathrm{C}} > 0.958 \end{cases}$$

Lower borderline:

$$I_{\mathrm{C}} = \begin{cases} 6.63 \times (R_{\mathrm{C}} - I_{\mathrm{C}}) + 10.1 & , \quad & & I_{\mathrm{C}} & \leq & 0.576 \\ 4.30 \times (R_{\mathrm{C}} - I_{\mathrm{C}}) + 11.5 & , \quad 0.576 & < & I_{\mathrm{C}} & \leq & 1.085 \\ 3.01 \times (R_{\mathrm{C}} - I_{\mathrm{C}}) + 12.9 & , \quad 1.085 & < & I_{\mathrm{C}} & & \end{cases}$$

Appendix C

Calibrations

In this Chapter I give the calibrations used for labeling the spectral types in the colour-magnitude and colour-colour diagrams. In addition I describe the determination of the colour – spectral type and colour – bolometric correction calibration. These latter two calibrations were used for the transformation of the PMS evolution tracks by D'Antona & Mazzitelli (1997) from the L vs $T_{\rm eff}$ plane into the $I_{\rm C}$ vs $(R_{\rm C}-I_{\rm C})$ plane.

The calibrations were determined by using photometric measurements of ZAMS stars with known spectral type reported by Johnson (1966), Leggett (1992) (only the measurements of young disk stars were used), Kirkpatrick & McCarthy (1994), and Bessel (1991) (used only for $T_{\rm eff}$ – $(R_{\rm C}-I_{\rm C})$ calibration). If necessary the measurements were transformed from the Johnson V,R,I into the Cousins V,R,I system by applying the transformation equations given by Bessel (1983); i. e.

$$\begin{aligned}(R-I)_{\rm C} &= 0.840\,(R-I)_{\rm J}+0.035, \text{ for F} - \text{K dwarfs}\\ (R-I)_{\rm C} &= 1.045\,(R-I)_{\rm J}-0.094, \text{ for M dwarfs.}\end{aligned}$$

The spectral type calibration is indicated by the red line in the top panel of Fig. C.1 and was obtained by fitting a polynomial to the shown measurements. The Johnson (1966) measurements were only used for spectral types earlier than M0. The bottom panel of Fig. C.1 indicates how the ZAMS in the $I_{\rm C}$ vs $(R_{\rm C}-I_{\rm C})$ colour-magnitude diagram was determined. Only the measurements reported by Johnson (1966) and Leggett (1992) were used for the calculation of the ZAMS locus which is indicated by the red line in that figure.

The evolution tracks and isochrones of the adopted PMS evolution models (which were given in the HR diagram) were transformed into the colour magnitude diagram as follows. Any given point in the $L_{\rm bol}$ vs $T_{\rm eff}$ plane was transformed into both the $I_{\rm C}$ vs $(R_{\rm C}-I_{\rm C})$ plane and the $I_{\rm C}$ vs $(V-I_{\rm C})$ in two steps:

First the effective temperature, $T_{\rm eff}$, was transformed into the appropriate colour by adopting a relationship between the colour and the effective temperature. For the $I_{\rm C}$ vs $(V-I_{\rm C})$ colour-magnitude diagram I used the transformation equations given by Hillenbrand (1997) (see her Appendix C). For the $I_{\rm C}$ vs $(R_{\rm C}-I_{\rm C})$ colour-magnitude diagram I determined the relationship between the effective temperature, $T_{\rm eff}$, and the $(R_{\rm C}-I_{\rm C})$ colour by using the data shown in Fig. C.2. The red and blue lines in this figure represent a two component polynomial fit which is given by:

$$(R_{\rm C}-I_{\rm C}) = 34.843-16.569\times\log(T_{\rm eff})+1.964\times[\log(T_{\rm eff})]^2$$

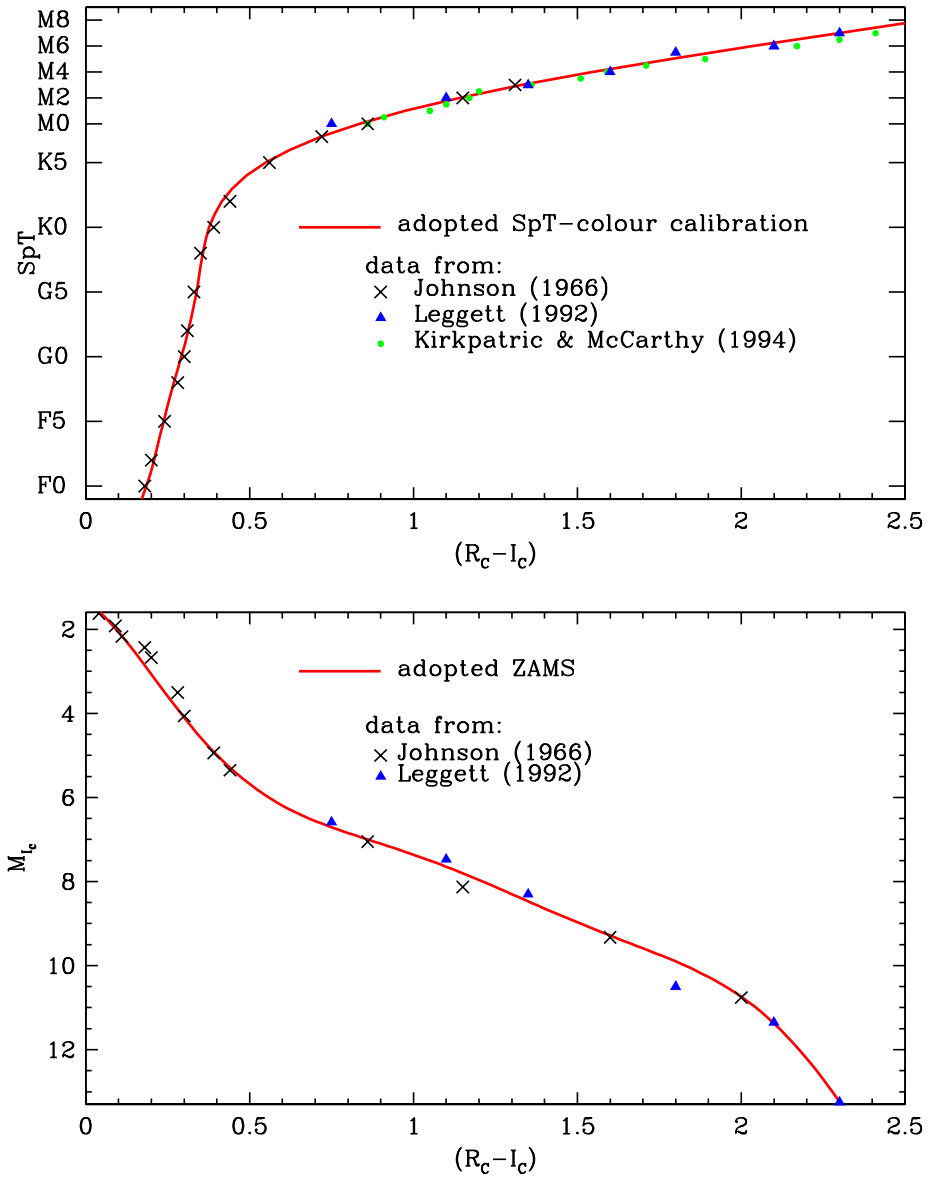

Fig. C.1: Top panel: The spectral type of ZAMS stars as a function of the colours. The different symbols represent the photometric data taken from the different authors. The red solid line indicates the adopted calibration. **Bottom panel:** The adopted ZAMS in the $I_{\rm C}$ vs $(R_{\rm C} - I_{\rm C})$ colour-magnitude diagram. The symbols are the same as in the top panel.

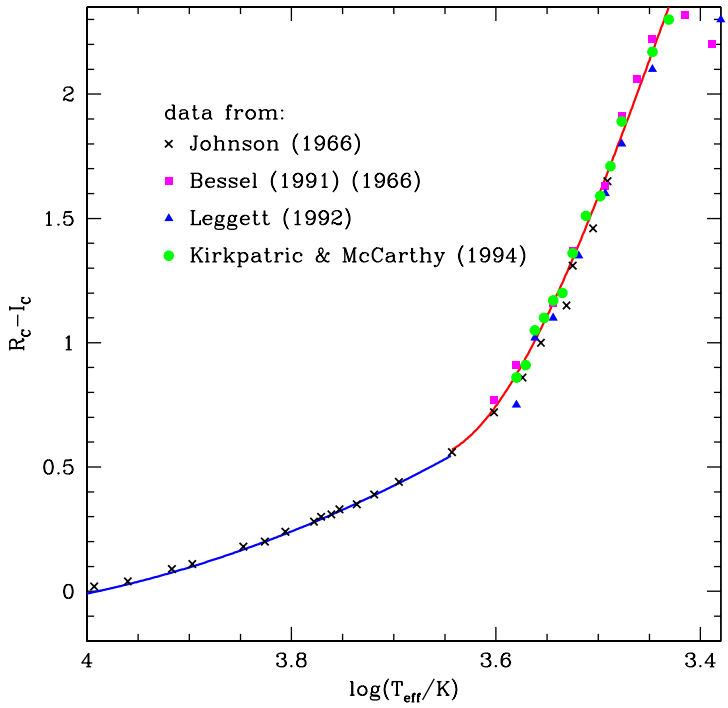

Fig. C.2: Adopted relationship between the effective temperature, $T_{\rm eff}$, and the $(R_{\rm C} - I_{\rm C})$ colour of the stars. The symbols represent data taken from different studies.

$$\text{for} \quad \log(T_{\rm eff}) > 3.643$$

$$(R_{\rm C} - I_{\rm C}) = -0.003 + 0.002 \times \log(T_{\rm eff}) - 0.072 \times [\log(T_{\rm eff})]^2 + 0.699 \times [\log(T_{\rm eff})]^3$$
$$\text{for} \quad \log(T_{\rm eff}) \leq 3.643.$$

Second the luminosity was transformed into the absolute $I_{\rm C}$-magnitude by using the equation

$$I_{\rm C} = 4.75 - 2.5 * log(L_{\rm bol}/L_{\odot}) - {\rm BC}_{I_{\rm C}}(T_{\rm eff}),$$

where ${\rm BC}_{I_{\rm C}}$ is the bolometric correction for the $I_{\rm C}$-band which was determined for a given effective temperature as follows. The transformation equations given by Hillenbrand (1997) (given in her Appendix C) were used for calculating the bolometric correction for the V-band, ${\rm BC}_V$. Together with the already determined $(V - I_{\rm C})$ colour this added up to ${\rm BC}_{I_{\rm C}}$, i. e.

$${\rm BC}_{I_{\rm C}} = (V - I_{\rm C}) + {\rm BC}_V \ .$$

Appendix D

Rejected Periodic Variables

In the following Table we list all periodic variables which were rejected from the analysis because they *failed* at least one of the two PMS tests described in Sect. 5.1 (test I) and Sect. 5.2 (test II).

Tab. D.1: All 129 periodic variable stars which were rejected from the further analysis. The columns 1–8 are the same as in Tab. 5.2. In the additional column at the end (failed test) we list the number of the PMS test which was failed by the star.

Star	$P_{\rm Scargle}$	$P_{\rm CLEAN}$	$P_{\rm Rebull}$	$P_{\rm adopt}$	δP	$p_{\rm vari}$	ptp-vari	$\Delta(R_{\rm C}-{\rm H}\alpha)$	failed test
538	3.19	3.20	.....	3.19	0.27	0.000	0.04	-5.96	II
553	0.28	0.28	.....	0.28	0.00	0.010	0.18	-0.26	I,II
587	0.24	0.24	.....	0.24	0.00	0.019	0.13	-0.15	I,II
716	0.17	0.17	.....	0.17	0.00	0.491	0.17	-5.85	I,II
769	0.21	0.21	.....	0.21	0.00	$1.000e-06$	0.16	-0.00	I
787	0.81	0.81	.....	0.81	0.02	$3.130e-04$	0.04	-0.19	I,II
790	2.07	2.06	.....	2.07	0.12	1.000	0.10	-0.22	I,II
1088	0.20	0.25	.....	0.20	0.00	0.022	0.11	-0.08	I
1167	1.70	1.70	.....	1.70	0.08	0.000	0.03	-0.32	II
1178	1.21	1.20	.....	1.21	0.04	0.017	0.06	-0.17	I,II
1267	1.35	1.35	1.35	1.35	0.05	0.377	0.05	-0.02	I
1411	0.81	0.81	.....	0.81	0.02	0.309	0.06	-0.14	I,II
1427	0.77	0.77	.....	0.77	0.02	0.994	0.11	-0.26	I,II
1450	1.24	1.23	.....	1.24	0.04	0.163	0.04	-0.19	I,II
1460	1.05	1.05	.....	1.05	0.03	0.011	0.06	-0.15	I,II
1525	0.54	0.54	.....	0.54	0.01	0.074	0.07	0.19	I
1605	1.53	1.54	1.57	1.53	0.06	1.000	0.08	-0.23	II
1609	4.95	4.94	.....	4.95	0.64	$4.230e-04$	0.05	-0.25	II
1840	0.53	0.53	.....	0.53	0.01	$1.589e-03$	0.51	-5.91	I,II
1872	1.16	1.16	.....	1.16	0.04	$8.641e-03$	0.14	-0.13	I,II
1963	0.21	0.21	.....	0.21	0.00	0.000	0.05	-0.23	I,II
1980	1.12	1.11	.....	1.12	0.03	$9.488e-03$	0.28	-0.23	I,II
2063	8.84	8.97	.....	8.84	2.16	0.477	0.05	-0.23	I,II
2079	1.23	1.23	.....	1.23	0.05	1.000	0.12	8.53	I
2106	0.18	0.18	.....	0.18	0.00	$2.300e-05$	0.28	-5.94	I,II
2303	0.28	0.28	.....	0.28	0.00	1.000	0.24	-0.18	I,II
2439	1.04	1.04	.....	1.04	0.03	$6.200e-05$	0.36	-5.95	I,II
2496	1.05	1.05	.....	1.05	0.03	$1.820e-04$	0.15	-0.22	I,II
2575	0.30	0.30	.....	0.30	0.00	$6.000e-06$	0.22	-0.10	I
2714	0.39	0.40	.....	0.40	0.00	$1.300e-05$	0.04	-0.17	I,II
2719	2.91	2.89	.....	2.91	0.23	1.000	0.06	-0.18	I,II
2792	0.12	0.14	.....	0.14	0.00	$5.000e-06$	0.07	-0.31	I,II
2831	2.50	2.51	.....	2.50	0.17	1.000	0.15	1.49	I
2916	0.49	0.49	.....	0.49	0.01	$4.580e-04$	0.22	-5.90	I,II
2976	1.78	1.78	.....	1.78	0.09	0.972	0.06	1.14	I
3033	0.95	0.95	.....	0.95	0.02	$2.000e-06$	0.03	-0.20	I,II
3070	2.40	2.39	2.36	2.40	0.15	0.991	0.08	-0.01	I

Tab. D.1: (continued)

Star	P_{Scargle}	P_{CLEAN}	P_{Rebull}	P_{adopt}	δP	p_{vari}	ptp-vari	$\Delta(R_{\mathrm{C}} - \mathrm{H}\alpha)$	failed test
3245	2.20	2.19	.....	2.20	0.13	1.000	0.07	-0.22	I,II
3269	1.35	1.36	.....	1.35	0.05	1.000	0.08	-5.99	II
3318	1.10	1.10	.....	1.10	0.03	$1.619e-03$	0.13	-0.72	I,II
3377	0.95	0.95	.....	0.95	0.02	$2.000e-06$	0.03	-0.30	II
3594	2.78	2.78	.....	2.78	0.24	0.029	0.08	-0.33	II
3627	0.54	0.54	.....	0.54	0.01	0.748	0.06	-0.18	I,II
3640	1.13	1.13	.....	1.13	0.05	0.999	0.05	-0.17	I,II
3658	0.53	0.53	.....	0.53	0.01	1.000	0.10	-0.14	I,II
3815	1.71	1.71	.....	1.71	0.08	0.841	0.06	-0.50	II
3854	3.44	3.43	.....	3.44	0.33	0.013	0.12	-0.61	II
3858	0.59	0.59	.....	0.59	0.01	1.000	0.18	-0.51	II
3897	4.17	4.16	.....	4.17	0.48	$2.622e-03$	0.05	-0.50	II
3900	4.21	4.19	.....	4.21	0.49	1.000	0.73	1.07	I
3927	2.41	2.41	.....	2.41	0.16	$2.450e-04$	0.04	-0.51	II
3948	4.89	4.90	.....	4.89	0.66	0.000	0.08	0.04	I
3960	0.59	0.60	.....	0.60	0.01	$3.130e-04$	0.19	-5.89	I,II
3975	0.51	0.50	.....	0.51	0.01	$2.910e-04$	0.21	2.87	I
4022	0.69	0.69	.....	0.69	0.01	$3.300e-05$	0.04	-0.43	II
4107	0.16	0.16	.....	0.16	0.00	0.035	0.34	-0.42	I,II
4168	7.35	7.47	.....	7.35	1.49	1.000	0.71	1.74	I
4193	4.12	4.13	.....	4.12	0.53	1.000	0.15	-0.11	I,II
4238	4.04	4.10	.....	4.04	0.45	$1.000e-05$	0.06	-0.27	I,II
4458	1.04	1.04	.....	1.04	0.03	0.000	0.03	-0.28	I,II
4597	1.59	1.59	.....	1.59	0.07	$1.690e-04$	0.08	-0.24	I,II
4814	2.31	2.31	.....	2.31	0.15	0.178	0.12	-0.32	I,II
4845	7.49	7.47	.....	7.49	1.50	0.000	0.02	-0.19	II
4850	0.18	0.18	.....	0.18	0.00	0.000	0.03	-0.19	II
4885	0.74	0.74	.....	0.74	0.02	0.972	0.08	-5.69	II
4908	1.90	1.90	.....	1.90	0.10	1.000	0.06	-0.27	II
4954	1.59	1.59	.....	1.59	0.07	0.198	0.04	-0.20	II
5018	1.40	3.43	.....	3.43	0.33	0.000	0.03	-0.40	II
5160	2.16	2.16	.....	2.16	0.12	0.515	0.04	-0.16	II
5183	6.20	6.22	.....	6.20	1.06	0.013	0.10	0.52	I
5224	0.26	0.26	.....	0.26	0.00	1.000	0.09	-0.48	II
5227	0.14	0.14	.....	0.14	0.00	$9.320e-04$	0.28	-0.63	I,II
5228	0.39	0.39	.....	0.39	0.00	0.543	0.04	-0.32	II
5255	0.70	2.41	.....	0.70	0.01	0.033	0.06	-0.41	II
5321	0.89	0.89	.....	0.89	0.02	$1.000e-06$	0.03	-0.11	I
5378	3.07	1.40	.....	3.07	0.26	$2.474e-03$	0.04	-0.22	II
5388	1.57	1.57	.....	1.57	0.07	0.457	0.21	0.29	I
5548	0.46	0.46	.....	0.46	0.01	0.672	0.06	0.01	I
5613	6.61	6.61	.....	6.61	1.23	0.212	0.07	-0.67	II
5622	1.13	1.14	.....	1.13	0.04	0.763	0.05	-6.00	II
5679	6.61	6.75	.....	6.61	1.21	1.000	0.09	-0.40	II
5680	2.82	2.82	.....	2.82	0.23	1.000	0.28	-0.36	II
5810	9.71	9.51	.....	9.71	2.45	1.000	0.11	0.11	I
5824	8.84	8.72	.....	8.84	2.16	1.000	0.07	-0.36	II
5871	0.84	0.84	.....	0.84	0.02	0.700	0.09	-0.25	II
5926	8.84	8.84	.....	8.84	2.03	1.000	0.14	0.20	I
5960	0.55	0.55	.....	0.55	0.01	0.000	0.27	2.87	I
6001	6.01	5.98	5.99	6.01	1.00	1.000	0.17	-0.35	II
6012	4.35	4.33	.....	4.35	0.52	1.000	0.72	-0.43	II
6093	0.96	0.96	.....	0.96	0.02	0.000	0.03	-0.58	I,II
6101	0.46	0.46	.....	0.46	0.01	0.994	0.10	0.38	I
6293	2.71	2.72	.....	2.71	0.20	$5.800e-05$	0.03	-0.27	II
6362	5.15	5.06	.....	5.15	0.73	$5.650e-04$	0.03	-0.27	II
6370	0.63	0.63	.....	0.63	0.01	1.000	0.06	-0.25	II
6388	0.17	0.17	0.17	0.17	0.00	1.000	0.67	-0.22	II
6491	0.15	0.15	.....	0.15	0.00	1.000	0.41	-0.05	I
6573	1.07	1.07	.....	1.07	0.03	1.000	0.06	0.00	I
6597	6.61	6.61	.....	6.61	1.21	$2.305e-03$	0.03	-0.32	II
6643	1.09	1.09	.....	1.09	0.03	$5.000e-06$	0.04	-0.29	I,II
6998	0.35	0.35	.....	0.35	0.00	0.977	0.12	-0.35	II
7019	0.18	0.18	.....	0.18	0.00	$4.380e-04$	0.33	-5.93	I,II

Tab. D.1: (continued)

Star	P_{Scargle}	P_{CLEAN}	P_{Rebull}	P_{adopt}	δP	p_{vari}	ptp-vari	$\Delta(R_{\mathrm{C}} - \mathrm{H}\alpha)$	failed test
7167	1.12	1.12	.....	1.12	0.03	0.372	0.06	-0.29	II
7215	11.07	11.01	.....	11.07	3.35	0.000	0.03	-0.30	II
7481	0.36	0.36	.....	0.36	0.00	1.000	0.41	-0.33	I,II
7596	4.12	4.10	.....	4.12	0.46	1.000	0.09	-0.19	II
7600	0.25	0.25	.....	0.25	0.00	$2.351e-03$	0.08	-0.35	I,II
7960	2.64	2.64	.....	2.64	0.18	$1.780e-04$	0.04	-0.24	I,II
8186	0.25	0.25	.....	0.25	0.00	$2.000e-06$	0.05	-0.34	I,II
8211	0.14	0.14	.....	0.14	0.00	0.998	0.36	-5.85	I,II
8219	0.95	0.95	.....	0.95	0.03	0.064	0.10	-0.19	I,II
8226	1.11	1.11	.....	1.11	0.03	1.000	1.60	-5.83	I,II
8314	0.34	0.34	.....	0.34	0.00	0.032	0.40	-5.86	I,II
8374	0.18	0.18	.....	0.18	0.00	0.564	0.25	-5.90	I,II
8406	17.43	17.44	.....	17.43	8.40	1.000	0.17	0.10	I
8627	4.40	4.39	.....	4.40	0.54	$4.000e-06$	0.03	-0.14	I,II
8851	1.18	1.18	1.19	1.18	0.06	0.949	0.07	-5.68	II
8874	1.13	1.14	.....	1.13	0.04	0.880	0.04	-0.14	I,II
8940	1.19	1.20	.....	1.19	0.04	$3.910e-04$	0.05	-0.19	II
8959	0.25	0.25	.....	0.25	0.00	$5.146e-03$	0.05	-0.07	I
9540	6.51	6.41	.....	6.51	1.17	$2.212e-03$	0.03	-0.22	I,II
9546	0.78	0.78	.....	0.78	0.02	$3.000e-06$	0.04	-0.23	I,II
9590	0.25	0.25	.....	0.25	0.00	0.000	0.04	-0.23	I,II
9622	1.32	1.32	.....	1.32	0.05	$4.500e-05$	0.12	0.15	I
9637	5.08	5.06	.....	5.08	0.71	0.321	0.06	-0.17	I,II
9652	0.29	0.29	.....	0.29	0.00	0.000	0.12	-0.23	I,II
9665	0.14	0.14	.....	0.14	0.00	$3.570e-04$	0.23	-5.91	I,II
9741	0.14	0.14	.....	0.14	0.00	0.036	0.35	-5.84	I,II
9772	0.11	0.11	.....	0.11	0.00	1.000	0.65	-5.82	I,II
9789	6.62	6.61	3.27	6.62	1.14	1.000	0.16	-0.11	II

Bibliography

Allain, S., Bouvier, J., Prosser, C., Marshall, L. A., & Laaksonen, B. D. 1996, A&A305, 498

Ambartsumian, V. A., in Stellar Evolution and Astrophysics, Acad, Sci., Armenian SSR, Erevan

André, P., Montmerle, T. 1994, ApJ, 420, 837

André, P., Ward-Thompson, D., Barsony, M. 1993, ApJ, 406, 122

Appenzeller, I., Dearborn, D. S. P. 1984, ApJ, 278, 689

Appenzeller, I. & Mundt, R. 1989, A&A Rev., 1, 291

Attridge, J. M. & Herbst, W. 1992, ApJ, 398, L61

Bachiller, R. 1996, ARA&A, 34, 111

Bailer-Jones, C. A. L., Mundt, R. 2001, A&A367, 218

Baraffe, I., Chabrier, G., Allard, F., Hauschildt, P. H. 1998, A&A337, 403

Barnes, S. ApJ, 586, 464

Barnes, S., Sofia, S., & Pinsonneault, M.. 2001, ApJ, 548, 1071

Barnes, S., Sofia, S., Prosser, C.F., & Stauffer, J. R. 1999, ApJ, 516, 263

Barsony, M. 1995, in: Clouds, Cores, amd Low Mass Stars, ed. Clemens, D. P., Barvainis, R., p. 197, San Francisco: ASP

Bertout, C., 1989, ARA&A27, 351

Bertout, C., Basri, G., Bouvier, J. 1988, ApJ, 330, 350

Bessel, M. S. 1983, PASP, 95, 480

Bessel, M. S. 1991, AJ, 101, 662

Blandford, R. D., & Payne, D. G. 1982, MNRAS, 199, 883

Blitz, L. 1993, in Protostars and Planets III, eds. Levy, E. & Lunine, J., pp. 125-161, Tucson, Univ. Ariz. Press

Bodenheimer, P. 1995, ARA&A33, 199

Bouvier, J. 1997, in "Cool stars in Clusters and Associations", eds. Pallavicini, R. & Micela, G. Mem. Soc. Astron. Ital., 68

Bouvier, J. & Bertout, C. 1989, A&A, 211, 99

Bouvier, J., Bertout, C., Benz, W., & Mayor, M. 1986, A&A, 165, 110

Bouvier, J., Cabrit, S., Fernandez, M., Martin, E. L., Matthews, J. M. 1993, A&A272, 176

Bouvier, J., Covino, E., Kovo, O., Martin, E. L., Matthews, J. M., Terranegra, L., Beck, S. C. 1995, A&A, 299, 89

Bouvier, J., Forestini, M. & Allain, S. 1997, A&A326, 1023

Brault, J.W. & White, O. R. 1971, A&A, 13, 169

Cabrit, S. Edwards, S., Strom, S. E., Strom, K. M. 1990, ApJ, 354, 687

Calvet, N., Cantó, J., & Rodríguez, L. F. 1983, ApJ 268, 739

Calvet, N., Hartmann, L. 1992, ApJ, 386, 239

Camenzind, M. 1990, Reviews in Modern Astronomy 3, 234

D'Antona, F. & Mazzitelli, I. 1994, ApJS, 90, 467

D'Antona, F. & Mazzitelli, I. 1997 in "Cool stars in Clusters and Associations", eds. Pallavicini, R. & Micela, G. Mem. Soc. Astron. Ital., 68 (isochrones: http://www.mporzio.astro.it/∼dantona/prems.html)

Deeming, T. J. 1975, Ap&SS36, 137

Durney, B. R., de Young, D. S., Roxburgh, I. W. 1993, Solar Physics, 145, 207

Edwards, S., Strom, S. E., Hartigan, P., Strom, K. M., Hillenbrand, L. A., et al. 1993, AJ, 106, 372

Eislöffel, J., Mundt, R., Ray, T. P., Rodríguez, L. F. 2000, in Protostars and Planets IV, ed. V. Mannings, A. P. Boss, & S. S. Russell (Tucson: Univ. Arizona Press), 815

Feigelson, E. D., & Montmerle, T. 1999, ARA&A, 37, 363

Fernandez, M. & Eiroa, C. 1996, A&A, 310, 143

Flaccomio, E., Micela, G., Sciortino, S., Damiani, F., Favata, F. Harnden, R. & Schachter, J. 2000, A&A, 355, 651

Flaccomio, E., Micela, G., Sciortino, F., Favata, Corbally, C. & Tomaney, A. 1999, A&A, 345, 521

Ghosh, P., Lamb, F. K. 1979b, ApJ, 232, 259

Ghosh, P.; Lamb, F. K. 1979b, ApJ, 234, 296

Goldsmith, P. F. & Arquilla, R. A. 1985, In Protostars and Planets II, ed. Black, D. & Matthews, M. S., pp. 137-149, Tucson, Univ. Ariz. Press

Goodman, A., Benson, P., Fuller, G., Myers, P. 1993, ApJ, 406, 528

Greene, T. P. & Lada, C. J. 1997, AJ, 114, 2157

Greene, T. P. & Lada, C. J. 2002, AJ, 124, 2185

Greene, T. P. & Lada, C. J. 2002, PASP, 115, 505

Hartmann, L. 2002, ApJ, 566, L29

Hartmann, L. 1998, Accretion Processes in Star Formation, Cambridge: Cambridge Univ. Press

Hartmann, L. W., Hewett, R. Stahler, S., & Mathieu, R. D. 1986, ApJ, 309, 275

Hartmann, L. W., & Kenyon, S. J. 1996, ARA&A, 34, 207

Hayashi, C. 1966, ARA&A, 4, 171

Hayashi, C., Hoshi, R., Sugimoto, D. 1962, Prog. Theor. Phys. Suppl., Vol. 22

Herbig, G. 1962, Adv. Astron. Astrophys., 1, 47

Herbig, G. 1957, ApJ, 125, 612

Herbig, G. 1954, ApJ, 119, 483

Herbst, W., Bailer-Jones, C. A. L., Mundt, R., Meisenheimer, K. & Wackermann, R. 2002, A&A, 396, 513

Herbst, W., Bailer-Jones, C. A. L., Mundt, R. 2001 ApJ, 554, L197

Herbst, W., Herbst, D. K., Grossman, E. J. & Weinstein, D., 1994, AJ, 108, 1906

Herbst, W., Maley, J. A., Williams, E. C. 2000, AJ, 120, 349

Hillenbrand, L. A. 1997 AJ, 113, 1733

Hirth, G. H., Mundt, R., & Solf, J. 1997, A&AS, 124, 437

Hoffmeister, C. 1965 *Veröff. der Sternwarte Sonneberg*, 6, 97

Horne, J. H. & Baliunas, S. L. 1986, ApJ, 302, 757

James, D. J., & Jeffries, R. D. 1997, MNRAS, 292, 252

Johnson, H. L. 1966, ARA&A4, 193

Joy, A. H. 1945, ApJ110, 424

Kawaler, S. D. 1988, ApJ, 333, 236

Kearns, K. E. & Herbst, W. 1998, AJ, 116, 261

Kearns, K. E.; Eaton, N. L., Herbst, W., & Mazzurco, C. J. 1997, AJ, 114, 1098

Kippenhahn, R., Weigert, A. 1994, *Stellar Structure and Evolution*, Springer-Verlag, Berlin

Kirkpatrick, J. D. & McCarthy Jr., A. W. 1994, AJ, 107, 333

Königl, A. 1991, ApJ 370, L39

Königl, A. 1989, ApJ, 342, 208

Krishnamurthi, A., Terndrup, D. M., Pinsonneault, M. H., Sellgren, K., Stauffer, J. R., et al. 1998, ApJ, 493, 914

Krishnamurthi, A., Pinsonneault, M. H., Barnes, S., Sofia, S. 1997, ApJ, 480, 303

Küker, M. & Rüdiger, G. 1999, A&A, 346, 922

Lada, C. J., 1991, in: The Physics of Star Formation and Early Evolution, eds. Lada, C. J. & Kylafis, N. D., p. 329, kluwer, Dordrecht

Lamm, M. H., Bailer-Jones, C. A. L., Mundt, R., Herbst, W., Scholz, A. 2003, submittet to A&A

Lamm, M. H., Bailer-Jones, C. A. L., Mundt, R., Herbst, W. 2003, in preperation

Lamm, M. H., Bailer-Jones, C. A. L., Mundt, R., Herbst, W. 2003, in preperation

Leggett, S. K. 1992, ApJS, 82, 351

Mahdavi, A., & Kenyon, J. S. 1998, AJ, 497, 342

Marcy, G. W. 1980, AJ, 85, 230

Monet, D. , Bird A., Canzian, B., Dahn, C., Guetter, H., et al. 1998, The USNO-A2.0 Catalogue

Mundt, R., & Eislöffel, J. 1998, AJ, 116, 860

Muzerolle, J., Calvet, N., & Hartmann, L. 2001, ApJ, 550, 944

Najita, J., Edwards, S., Basri, G., & Carr, J. 2000, in Protostars and Planets IV, ed. V. Mannings, A. P. Boss, & S. S. Russell (Tucson: Univ. Arizona Press), 457

Ogura, K., 1984, PASJ, 36, 139

Ostriker, E., & Shu, F. H. 1995, ApJ, 447, 813

Palla, F. 2001, ASP Conf. Ser., 243, 525,

Palla, F. & Stahler, S. W. 2000, ApJ, 540, 255

Palla, F. & Stahler, S. W. 1999, ApJ, 525, 772

Palla, F. & Stahler, S. W. 1990, ApJ, 360, L47

Park, B., Sung, H., Bessel, M. & Kang, Y. 2000, AJ, 120, 894

Press, W. H., Teulolsky, S. H., Vetterling, W. T. & Flannery, B. P. 1992, Numerical Recipies in C, (Cambridge University Press)

Prosser, C. F. & Grankin, K. 1997 CfA preprint 4539

Prosser, C. F. et al. 1993 PASP, 105, 1407

Queloz, D., Allain, S., Mermilliod, J.-C., Bouvier, J., & Mayor, M. 1998, A&A, 335, 183

Radick, R. R., Thompson, D. T., Lockwood, G. W., Duncan, D. K., & Baggett, W. E. 1987, ApJ, 321, 459

Rebull, L. M., Makidon, R. B., Strom, S. E., Hillenbrand, L. A., Birmingham, A., Patten, B. M., Jones, B. F., Yagi, H. & Adams, A. T. 2002, AJ, 123, 1528

Rebull, L. M. 2001, AJ, 121, 1676

Rebull, L. M., Hillenbrand, L. A., Strom, S. E., Duncan, D. K., Patten, B. M., Pavlovsky, C. M. Makidon, R., Adams, M. T. 2000, AJ, 119, 3026

Roberts, D. H., Lehar, J., & Dreher, J. W 1987, AJ, 93, 968

Ruciński, S. M. 1988, AJ, 95, 1895

Rydgen A. E., & Vrba, F. J. 1983, ApJ, 267, 191

Sagar, R., Myakutin, V. I., Piskunov, A. E. & Dluzhnevskaya, O. B. 1988, MNRAS, 234, 831

Scargle, J. D. 1982, ApJ, 263, 835

Shu, F. H., Najita, J., Ostriker, E., Wilkin, F. Ruden, S. P. & Lizano, S. 1994, ApJ 429, 781

Shu, F. H., Lizano, S., Ruden, S. P., & Najita, J. 1988, ApJ, 328, L19

Shu, F. H., Adams, F. C., Lizano, S. 1987, ARA&A, 25, 23

Skumanich 1972, ApJ, 171, 565

Soderblom, D. R., Jones, B. F., & Fischer, D. 2001, ApJ, 563, 334

Spiegel, E. A., & Weiss, N. O. 1980, Nature, 287, 616

Spitzer, L. Jr. 1978, *Physical Processes in the Interstellar Medium*, New York, Wiley

Stahler, S. W. 1983, ApJ, 274, 822

Stassun, K. G.; Mathieu, R. D., Mazeh, T., Vrba, F. J. 1999, AJ, 117, 2941

Stauffer, J., & Hartmann, L. W. 1987, ApJ, 318, 337

Steenbeck, M., & Krause, F. 1969, Astron. Nachr., 291, 49

Strom, K., et al. 1990, ApJ, 362, 168

Sung, H., Bessel, M. S. & Lee, S.-W. 1997, AJ, 114, 2644

Swenson, F. J., Faulkner, J. Rogers, F. J., & Iglesias, C. A. 1994, ApJ, 425, 286

Terndrup, D. M., Pinsonneault, M., Jeffries, R. D., Ford, A., Stauffer, J. R., & Sills, A. 2002, ApJ, 576, 950

Terndrup, D. M., Stauffer, J. R., Pinsonneault, M. H., Sills, A., Yuan, Y., et al. 2000, AJ, 119, 1303

Vasilevskis, S., Sanders, W. L., & Balz, A. G. A. 1965, AJ, 70, 10

Vrba, F. J., Rydgren, A. E., Chugainov, P. F., Shakovskaya, N. I., Bruce Weaver, W., 1989, AJ, 97, 483

Vrba, F. J., Chugainov, P. F., Bruce Weaver, W., Stauffer, J. S. 1993, AJ, 106, 4

Van Leeuwen, F. & Alphenaar, P. 1982, ESO Messenger 28, 15

Vogel, S. S. & Kuhi, L. V. 1981, ApJ, 245, 960

Walker, M. F. 1956, ApJS, 2, 365

Walter, F. M. 1986, ApJ, 306, 573

Wardle, M., & Königl, A. 1993, ApJ, 410, 218

Weber, E. D. & Davis, L. 1967, ApJ, 148, 217

Wenzel, W. 1956, *Veröff. der Sternwarte Sonneberg*, 219, 1

Acknowledgements

It is a pleasure to thank those people who contributed in various ways to the success of this thesis.

Mein besonderer Dank gilt meinem Betreuer Reinhard Mundt, der mir mit seinem reichen Erfahrungschatz stets zur Seite stand, es nie an Unterstützung hat mangeln lassen und mir viele hilfreiche Anregungen gegeben hat. Die hervorragende Arbeitsatmosphäre und die Tatsache, dass er stets ein offenes Ohr für meine Probleme hatte, haben wesentlich zum Gelingen dieser Arbeit beigetragen. Vielen Dank für die gute Zusammenarbeit, die ich sehr genossen habe.

Auch Coryn Bailer-Jones gebührt besonderer Dank, denn ohne ihn wäre es mir nicht möglich gewesen, mich zügig in die Arbeit mit den verschiedenen Programmen zur Datenreduktion und Datenanalyse einzuarbeiten. Ferner danke ich ihm für die ausgiebigen Diskussionen, für die ihm auch das Wochenende nicht zu schade war, und dafür, dass er Teile dieser Arbeit Korrektur gelesen hat.

Furthermore, I am grateful to our collaborator Bill Herbst, for sharing his great experience in the field with me. His helpful suggestions on my work in different stages have certainly improved these great results. I am also deeply grateful that he made it possible for me to watch the German soccer team playing against Cameroon during the last World Cup while I was staying at Wesleyan University. I also thank Luisa Rebull and Eric Young for making their unpublished data available to me.

Bei Herrn Prof. Dr. Appenzeller bedanke ich mich dafür, dass er sich zur Zweitkorrektur dieser Arbeit bereit erklärt hat.

Ich danke ebenfalls den Direktoren des MPIA, die mir die Möglichkeit zur Promotion eröffnet haben und mit der Bereitstellung der finanziellen Mittel sicherstellten, dass ich einerseits die nötigen Beobachtungen durchführen und andererseits die gewonnenen Ergebnisse auf verschiedenen Tagungen präsentieren konnte. In diesem Zusammenhang danke ich Frau Schleich für die reibungslose Organisation der damit verbundenen Reisen.

Dank meines (wechselnden) internationalen Bürokollegiums, das fast ausschließlich aus "Theoristen" bestand, konnte ich nicht nur meine Kenntnis über das Universum und seine Bestandteile erweitern, sondern auch Einblicke in andere, mir bisher nicht vertraute, Kulturkreise gewinnen. So brachte uns Sami das arabische Leben und Helmut das bayrische Leben näher. Ich danke euch beiden sowie Markus W. und Sabine für das entspannte Raumklima.

Ich danke meinen Eltern die mich in den letzten Jahren auf vielfältige Weise unterstützt haben. Gleiches gilt auch für meine Großeltern, denen es leider nicht vergönnt war, die Fertigstellung dieser Arbeit zu erleben. Schließlich danke ich dem wichtigsten Menschen in meinem Leben. Danke Nicole, dass du da bist.

Die Beobachtungen, die dieser Arbeit zugrunde liegen, wurden mit dem ESO/MPG 2.2-m-Teleskop auf La Silla in Chile durchgeführt. Die Bilddatenreduktion und Bilddatenanalyse wurde mit dem Softwarepaket IRAF durchgeführt. IRAF wurde von der "IRAF programming group" der National Optical Astronomy Observatories (NOAO) in Tucson (Arizona) entwickelt.